Magnetic Phase Diagram of the Frustrated Kondo Lattice on the Zigzag Ladder

Dissertation with the aim of achieving a doctoral degree
at the Faculty of Mathematics, Informatics
and Natural Sciences

**Department of Physics
of Universität Hamburg**

submitted by
Matthias Peschke, M.Sc.
born October 25, 1988 in Lüneburg, Germany

Hamburg
2019

Kurzfassung

Das Phasendiagramm des Kondo-Gitter Modells ist auf einer eindimensionalen frustrierten Zickzack-Leiter mit Hopping-Amplituden t_1 entlang der Sprossen und t_2 entlang der Beine untersucht. Als Methoden sind die Dichtematrix Renormierungsgruppe (DMRG) und *variational uniform matrix product state* (VUMPS) verwendet. Die Konkurrenz zwischen indirektem magnetischen Austausch, dem Kondo-Effekt und der geometrischen Frustration führt zu einem vielfältigen Phasendiagramm: Bei halber Füllung und starkem J bildet der Grundzustand einen Kondo-Isolator mit kommensurablen oder inkommensurablen kurzreichweitigen Spinkorrelationen. Der kommensurabel-inkommensurabel Phasenübergang ist perturbativ erklärbar und findet für $J = \infty$ bei $t_2 = 0{,}5 t_1$ statt. Für ein schwächeres J führt die geometrische Frustration zu einem spontanen Bruch der Translationssymmetry des Grundzustands an einer kritischen Grenzlinie $J_c^{\dim}(t_2)$. Der resultierende dimerisierte Grundzustand zeichnet sich durch alternierende ferro- und antiferromagnetischen Korrelationen entlang der Sprossen aus. Er ist nicht störungstheeoretisch erklärbar, aber das Modell mit klassichen Spins kann hierfür herangezogen werden – die gleiche Spindimerisierung tritt auch hier auf. Durch den Symmetriebruch nimmt die geometrische Frustration ab und eröffnet die Möglichkeit für eine quasi-langreichweitig geordnete Spinspirale mit Wellenvektor $Q = \frac{\pi}{2}$. Diese Phase ist durch eine zweite kritische Linie $J_c^{\mathrm{mag}}(t_2)$ separiert. Die quasi-langreichweitig geordnete Spinspirale bei schwachem J mit lückenlosen Spinanregungen über dem zweifach entarteten Grundzustand ist ungewöhnlich und nicht auf eine effektive reine Spintheorie zurückzuführen. Das Modell ist ein Isolator bei halber Füllung. Im lochdotierten Bereich und für negatives t_2 ist der Grundzustand ferromagnetisch für ausreichend starkes J. Im Gegensatz zur gewöhnlichen Kondo-Kette ($t_2 = 0$), in der die Phasenlinie $J_c^{\mathrm{FM}}(n)$ monoton ist, stellt die Phasenlinie der frustrierten Leiter eine Kuppelform dar. Dieses ist einer van Hove Singularität in der freien Zustandsdichte zugeordnet. Im elektrondotierten Bereich zerstört das übernächste Nachbar-Hopping t_2 den Ferromagnetismus bei $J = \infty$. Trotzdem ist der Grundzustand bei mittleren Werten von J und Elektronen-Konzentrationen um $n \approx 1{,}5$ ferromagnetisch. Im schwachen J-Bereich bei $n = \frac{N}{L} = 1{,}5$ entwickelt der Grundzustand ungewöhnliche Cluster mit Wellenvektor $Q = \frac{\pi}{4}$, was einer Wellenlänge von $\lambda = 8$ Gitterplätzen entspricht.

Schlagwörter: DMRG, VUMPS, Kondo-Gitter Modell, geometrische Frustration, eindimensionale Vielteilchensysteme

Abstract

The phase diagram of the Kondo lattice model on a one-dimensional frustrated zigzag ladder with hoppings t_1 along the rungs and t_2 along the legs is investigated by employing the density-matrix renormalization group (DMRG) and the variational uniform matrix product state (VUMPS) approach. The competition between indirect magnetic exchange, the Kondo effect and the geometrical frustration generates a rich phase diagram: at half-filling and strong J, the ground state is a Kondo insulator with either commensurate or incommensurate short-range spin correlations dependent on the degree of frustration. The commensurate-incommensurate phase transition is understood perturbatively and happens at $t_{2,c}^{\mathrm{comm}} = 0.5t_1$ in the infinite-J limit. For weaker J, the geometrical frustration leads to a spontaneous break of the translational symmetry in the ground state at a critical line $J_c^{\mathrm{dim}}(t_2)$. The resultant dimerized ground state is characterized by alternating ferro- and antiferromagnetic spin correlations along the rungs of the ladder. It is not accessible perturbatively but is explained by the model with classical spins in which the same spin-dimerization is observed. The break of the translational symmetry alleviates the geometrical frustration and paves the way for quasi-long-range spiral magnetic order with wave-vector $Q = \frac{\pi}{2}$. This phase is separated by a second critical line $J_c^{\mathrm{mag}}(t_2)$. The quasi-long-range ordered spin spiral at weak J with gapless spin excitations on top of the twofold degenerate dimerized ground state is unconventional and cannot be explained by an effective spin-only theory. The model is found to be an insulator at half-filling. In the hole-doped regime and for negative t_2, the ground state is ferromagnetic for sufficiently strong J. In contrast to the ordinary Kondo chain ($t_2 = 0$) where the transition line $J_c^{\mathrm{FM}}(n)$ is monotone, the transition line for the frustrated Kondo ladder has a dome structure which is attributed to a van Hove singularity in the noninteracting density of states. In the electron-doped regime, the next-nearest neighbour hopping t_2 destroys the ferromagnetism at $J = \infty$. However, at intermediate values of J, the ground state is still ferromagnetic for specific electron concentrations about $n \approx 1.5$. In the weak-J limit and $n = \frac{N}{L} = 1.5$, the ground state exhibits unconventional clusters with a wave-vector $Q = \frac{\pi}{4}$, i.e. a wavelength of $\lambda = 8$ lattice sites.

Key words: DMRG, VUMPS, Kondo lattice model, geometrical frustration, one-dimensional many-body systems

Contents

Contents

CHAPTER 1

Introduction

> The whole is greater than the sum of its parts.
>
> *(Aristoteles)*

It is a fascinating phenomenon that featureless building blocks can develop complex and manifold properties, which exceed their own features by far. This phenomenon appears nearly everywhere in science and is also found in everyday life. A living system is built of simple molecules and constitutes a primary example for the emergence of complexity. Fashion is another example for the emergence of collective phenomena. Here, the basic building blocks are the humans in a specific community and the mutual interaction results from the ambition to imitate each other. It was, e.g, fashionable for men in the 19th century to wear hats but this trend stopped spontaneously in the mid of the 20th century.

It is of particular interest in physics to develop microscopic theories for the building blocks which are able to capture this emergence of complexity. Crucial ingredients for a microscopic theory are the interactions amongst the basic building blocks which are the heart of the many-body problem. In solid-state physics, one is not faced with the problem of determining the fundamental interactions and particles, but is tasked with a solution of known equations which describe the many-body problem. A solid is composed of nuclei and electrons which interact via the Coulomb interaction. Although this problem sounds simple, it is highly complex. It constitutes another prime example for the emergence of complexity from many nearly featureless objects, which mutually interact with each other. In fact, this theory is able to capture various collective properties of solids like magnetism [1], (high-temperature) superconductivity [2, 3], or Mott-insulators [4–6]. This complexity is not found in the formulation of the theory, but it is found in its solution. Therefore, physicists have been trying to develop methods and approximations for the solution of the general solid-state problem for the last 100 years. Still, some collective phenomena are not understood, with the most famous example being the high-temperature superconductivity [3]. Major approximations were the development of fundamental model systems, which capture the strongly interacting many-body problem but simplify the chemical composition of the solids. Examples are the single band Hubbard model [7], the periodic Anderson model [8] and the Kondo lattice model [9]. These simplified model systems, however, also build complex many-body problems for which general solutions are not available. In particular, this is the case for systems with frustration, i.e. for systems for which no *easy* arrangement exists so that all interactions are satisfied simultaneously. Frustration can be caused by the geometry of the system, which is referred to as geometrical frustration.

In general, frustration can be the trigger for unconventional phases of matter like spin-liquids [10, 11] and was also suggested by ANDERSON [12] as a key ingredient for high-temperature superconductivity. The unconventional phases appear because in a frustrated system many ground state candidates with different properties lie very close in energy. In the resultant complex energy landscape unconventional states can also be the lowest in energy under specific circumstances. Hence, it has been (and still is) of importance to develop numerical methods for exact solutions of those model systems.

A milestone was the development of the density-matrix renormalization group (DMRG) by S. R. WHITE [13]. This method allows an exact treatment of one-dimensional lattice models. From a modern perspective, the DMRG method falls into the class of tensor network methods [14]. Another class of methods are diagrammatical expansions of the Green's function or the self energy. For the latter, the primary example is the dynamical mean-field theory (DMFT) [15, 16]. It was proven to be exact in infinite dimensions [17] but it fails for low-dimensional quantum systems in which frustration has its strongest impact. Other substantial progress was brought by quantum Monte Carlo (QMC) methods [18–20]. In principal, QMC can be used in any dimension but for systems with frustration, it is plagued by the numerical sign problem [21]. For that reason, the detailed impact of frustration on the phases of solids is not entirely understood from the theoretical side.

The aim of this thesis is to systematically analyse the role of frustration in a quasi-one-dimensional strongly correlated quantum lattice model by employing the DMRG method. As the model system serves the Kondo lattice, to which a more detailed introduction is devoted in the following section. A brief introduction for tensor network methods is given afterwards.

1.1 The Kondo model for lattices with geometrical frustration

The Kondo lattice model (KLM) contains conduction electrons which are described by a single band $\varepsilon(\boldsymbol{k})$. The conduction electron system is coupled locally via the orbital spin operator $\boldsymbol{s}_i = \sum_{\tau\tau'} c_{i\tau}^\dagger \boldsymbol{\sigma}_{\tau\tau'} c_{i\tau'}$ to localized moments with spin quantum number $S = 1/2$. The Hamiltonian can be written in a mixed momentum-space real-space notation:

$$H = \sum_{\boldsymbol{k}\sigma} \varepsilon(\boldsymbol{k}) c_{\boldsymbol{k}\sigma}^\dagger c_{\boldsymbol{k}\sigma} + J \sum_i \boldsymbol{S}_i \boldsymbol{s}_i. \tag{1.1}$$

An important feature of this model is that the different localized moments are not coupled directly to each other but only via the conduction electron system. Therefore, the KLM is a paradigm model for indirect magnetic interactions. In specific cases, it is possible to derive an explicit spin-spin interaction for these indirect magnetic interactions. In the general case, however, it is not possible to build a Hamiltonian theory for the local moments only. A famous example for an effective spin-only theory is the weak-J regime in which the RKKY theory [9, 22, 23] applies. In this case, the low-energy Hamiltonian represents a Heisenberg model [24] with long-range interactions J_{ij} determined by the static susceptibility $\chi_{ij}(\omega = 0)$ of the noninteracting conduction electron system. For bipartite (not frustrated) lattices, the susceptibility oscillates between the two sublattices, so that the resultant effective model favors antiferromagnetic alignment between the localized moments. This antiferromagnetic alignment competes with the onsite singlet formation between conduction electrons and localized moments

[25]. Adding geometrical frustration to this competition as a third competitor gives rise to interesting and unconventional phases. The reason is that the possible trade-offs for the system are much richer as compared to spin-only systems. Since the effective magnetic interactions are not written down in the Hamiltonian, but emerge through the conduction electrons, the geometrical frustration can lead to an unconventional feedback of the conduction electrons which changes the effective interactions. The material CePdAl is a candidate for a frustrated Kondo lattice system. In fact, the material shows an unconventional partially ordered ground state which does not belong to any standard heavy-fermion class [26, 27].

Fig. 1.1 shows three different possible trade-offs with which a triangular KLM could respond to the geometrical frustration.

1. Fig. 1.1(a): 120° alignment of the local moments. In this case, the conduction electron system does not change the indirect magnetic interactions. This ground state is found in the spin-1/2 Heisenberg model on the two-dimensional triangular lattice [28].

2. Fig. 1.1(b): Partial ordering of the local moments. This case represents a compromise between antiferromagnetic ordering of the local moments and singlet formation between the two different species. Two of the three localized moments form a nonlocal RKKY singlet while the third moment is in a singlet state with its conduction electron partner. Since the moments are partially screened by the conduction electron system, this phase is called partial Kondo screening (PKS) [29]. This ground state breaks the translational symmetry of the Hamiltonian in Eq. (1.1).

3. Fig. 1.1(c): Qualitative change of the indirect magnetic interactions. In this case, the conduction electron system changes the effective interactions. One out of the three bonds of the triangle receives a ferromagnetic interaction while the remaining two bonds can be antiferromagnetic without any frustration. This ground state also breaks the translational symmetry of the Hamiltonian in Eq. (1.1).

A primary goal of this work is to unveil which trade-off is the lowest in energy for the frustrated one-dimensional zigzag ladder.

(a) 120° phase   **(b)** PKS phase   **(c)** Dimerized phase
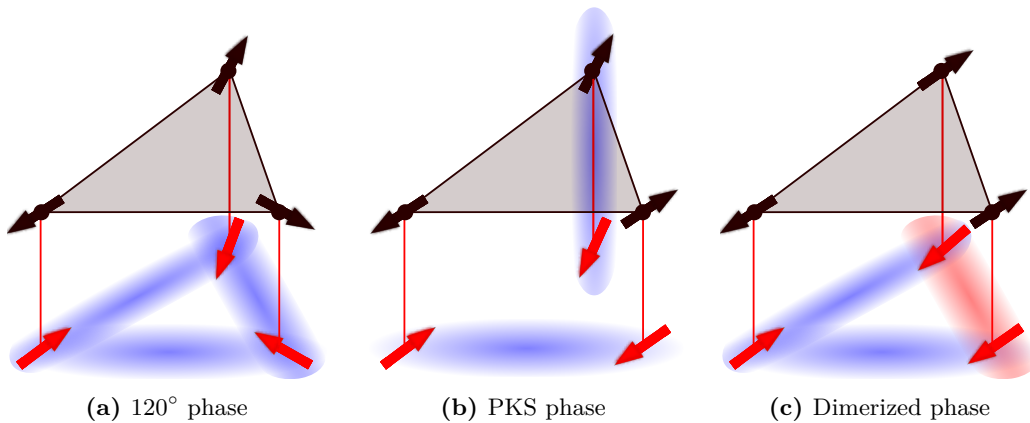
Figure 1.1: Sketches of different possible ground states of a triangular Kondo lattice. The black layer represents the conduction electron system and the red arrows display the local moments. Blue (red) clouds denote antiferromagnetic (ferromagnetic) correlations.

1.2 Tensor network methods for quantum many-body problems

The quantum many-body problem can be boiled down to the diagonalization of the Hamiltonian of the system. This provides the eigenstates and eigenenergies from which one can calculate all desired quantities. The Hilbert space dimension, however, grows exponentially with the system size, so that the diagonalization is also an exponentially hard problem. However, all eigenstates also provide an exponential amount of information and one is usually interested in either the ground state or low lying excited states. Nevertheless, the determination of the ground state remains an exponentially hard problem. To make progress regardless of that, one needs a subset of the full Hilbert space in which the ground state is located and one needs to be able to parameterize this subset directly. With this at hand one can determine the ground state by solving an optimization problem in the restricted subset. Hence, the following major questions are crucial for the efficient determination of the ground state:

1. Which criteria define an appropriate subset of the full Hilbert space in which the ground state is located and which is substantially smaller than the full Hilbert space?

2. How can one parameterize this subset directly?

3. Can one optimize the parameters of the ansatz efficiently?

The first question can be answered by deeply analysing the entanglement structure of ground states from short-range Hamiltonians [30–32]. From this it follows that the correct criterion is given by the entanglement properties of the states. E.g., for one-dimensional gapped Hamiltonians, it was proven that the ground state obeys an *area law* [30], i.e. the entanglement entropy of a sub-chain with respect to the remaining system scales with the area of the sub-chain, which itself is constant. For critical gapless systems, the entanglement entropy scales logarithmically with the size of the sub-chain [33–36]. Similar results were obtained for higher-dimensional systems [32]. One should emphasize that the subset of states in the Hilbert space which obey an area law is substantially smaller than the full Hilbert space. In fact, it constitutes a null set in the Hilbert space.

The second question is the point where tensor networks come into play. A tensor network is constructed to parameterize states with a definite entanglement structure [37, 38]. As a primary example serve matrix product states (MPS, see Fig. 1.2(a) for a sketch of an MPS) [14, 39, 40] as they reproduce the same area law as ground states from gapped and short-range one-dimensional Hamiltonians. With the parameterization of quantum states as MPS, one is able to target the relevant subset of the Hilbert space directly. For critical one-dimensional systems, the entanglement scaling of MPS does not fit the scaling of a corresponding ground state. The multi-scale renormalization ansatz (MERA) [41, 42] is an extended one-dimensional tensor network which provides the correct entanglement scaling for one-dimensional critical systems. Higher dimensional generalizations are also available where the most famous one is the projected entangled pair state (PEPS) [43–45] (see Fig. 1.2(b)).

The third question is equally important because only if one is able to optimize the suited ansatz efficiently, can one benefit from the tensor network. In the case of MPS, there are quite efficient algorithms for the optimization of the variational parameters in the MPS. First and foremost the density-matrix renormalization group (DMRG) is an efficient algorithm for optimizing MPS [14]. The DMRG algorithm has already been used before it was connected with MPS

(a) Matrix product state (MPS)   **(b)** Projected entangled pair state (PEPS)
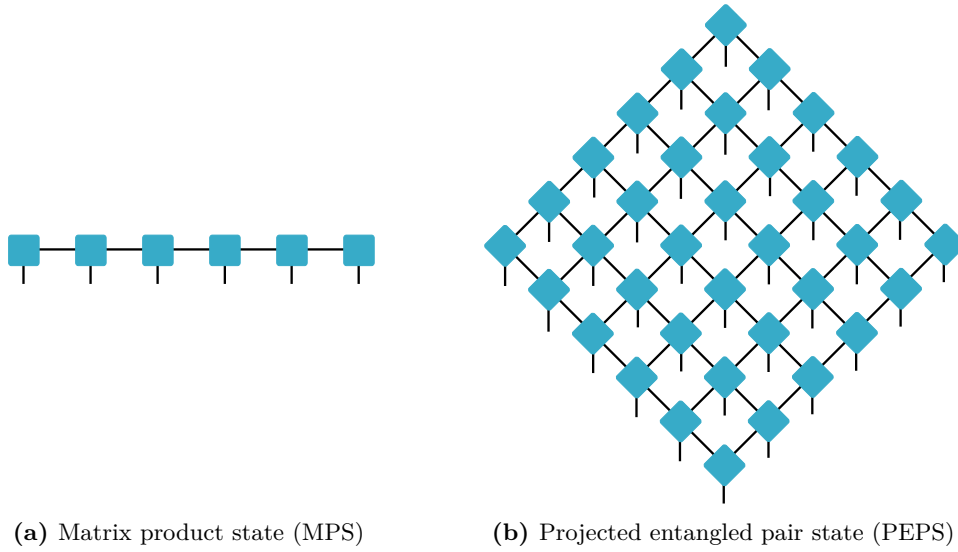
Figure 1.2: Sketches of different tensor network states.

[13, 46]. More recently, a variational method was suggested which optimizes MPS directly in the thermodynamic limit. The method is called the variational uniform matrix product state algorithm (VUMPS) [47]. Both optimization algorithms are extensively used for this work. In the case of other tensor networks, the efficient optimization is a much more involved task so that their success is limited as compared to MPS. However in the last years, substantial progress has been achieved for the optimization of PEPS [48–53].

1.3 Structure of this work

The structure of the present work is as follows: Chap. 2 introduces matrix product states (MPS) which constitute the variational space for the numerical methods used in this thesis. It covers both finite and infinite MPS and also introduces the concept of matrix product operators. Two optimization algorithms are discussed in Chap. 3. First, the single-site density-matrix renormalization group and second the variational uniform matrix product state approach. In Chap. 4, I discuss in detail how to gain efficiency with the incorporation of global symmetries. Therein is a detailed introduction to representation theory. Chap. 5 contains a detailed introduction to the Kondo lattice model and its symmetries. Additionally, two perturbative approximations are presented. Afterwards, I give an in-depth analysis of the half-filled frustrated one-dimensional Kondo zigzag ladder in Chap. 6 and Chap. 7 collects results for the same model away from half-filling. Finally, I present a summary and an outlook for future perspectives in Chap. 8.

CHAPTER 2

Matrix product states

Matrix product states (MPSs) are a versatile variational ansatz for one-dimensional quantum lattice models. They were firstly proposed by FANNES et al. [39] and later connected to the density-matrix renormalization group [14, 40]. In this chapter, I give a detailed introduction to MPS starting with the formal definition in Sec. 2.1. Afterwards, I will discuss a possible interpretation of MPS as a renormalization scheme in Sec. 2.2. An important structure of MPS is the gauge freedom which will be addressed in Sec. 2.3. I will also cover uniform MPS in the thermodynamic limit in Sec. 2.4 and present the basic entanglement structure of MPS in Sec. 2.5. The related structure of matrix product operators (MPOs) is discussed in Sec. 2.6 and finally I will present different arithmetic operations involving both MPSs and MPOs in Sec. 2.7.

2.1 Definition

Consider a Hilbert space $\mathcal{H}$ which is obtained by an L-times tensor product of local Hilbert spaces $\mathcal{H}_{\text{loc}}^{(i)}$:

$$\mathcal{H} = \bigotimes_{i=1}^{L} \mathcal{H}_{\text{loc}}^{(i)} \tag{2.1}$$

This situation generally occurs if one deals with a lattice system where each site of the lattice is equipped with a local quantum system with dimension d_i. The resulting many-body Hilbert space $\mathcal{H}$ has then dimension $d = \prod_{i=1}^{L} d_i$ and is spanned by the canonical tensor-product basis $|\sigma_1, \ldots, \sigma_L\rangle$ which is obtained from the local basis elements $|\sigma_i\rangle$ of $\mathcal{H}_{\text{loc}}^{(i)}$. A generic state in $\mathcal{H}$ is then determined by d coefficients, one for each basis element:

$$|\Psi\rangle = \sum_{\boldsymbol{\sigma}} T^{\sigma_1 \cdots \sigma_L} |\sigma_1 \cdots \sigma_L\rangle \tag{2.2}$$

A MPS is a state in a many-body Hilbert space of the following form:

$$|\Psi\left[\{A\}\right]\rangle = \text{tr} \sum_{\boldsymbol{\sigma}} \boldsymbol{A}^{\sigma_1}(1) \cdots \boldsymbol{A}^{\sigma_L}(L) |\sigma_1 \cdots \sigma_L\rangle \tag{2.3}$$

Here $A(i) \in \mathbb{A}_i := \mathbb{C}^{\chi_{i-1} \times d_i \times \chi_i}$ is a single ($\chi_{i-1} \times d_i \times \chi_i$)-tensor or alternatively a collection of $d_i = \dim\left(\mathcal{H}_{\text{loc}}^{(i)}\right)$ matrices of size $\chi_{i-1} \times \chi_i$ labeled by $\boldsymbol{A}^{\sigma_i}$ with $\chi_L = \chi_0$. The tensors $A(i)$

are called the *site tensors* of the MPS and χ_i describes the *bond* or *auxiliary* dimension of the MPS. The precise definition for the A-tensor as a multi-linear form reads:

$$A(l): \quad \mathbb{C}^{\chi_{l-1}} \otimes \mathbb{C}^{d_l} \otimes \mathbb{C}^{\chi_l *} \to \mathbb{C} \tag{2.4}$$
$$|i_{l-1}\rangle \otimes |\sigma_l\rangle \otimes \langle i_l| \mapsto A^{\sigma_l}_{i_{l-1}i_l},$$

where the components $A^{\sigma_l}_{i_{l-1}i_l}$ are given by the action on the canonical basis of $\mathbb{C}^{\chi_{l-1}} \otimes \mathbb{C}^{d_l} \otimes \mathbb{C}^{\chi_l *}$. It is obvious from this equation that I do not use the convention for upper indices being contravariant and lower indices beeing covariant. Instead, I use the convention to write the physical indices as upper indices and the auxiliary indices as lower indices. I will also identify the components with the tensor itself, whenever this is convenient. Throughout this thesis, I use the convention that the rank-3 site tensors are written as non-bold symbols A while the site matrices $\boldsymbol{A}^\sigma$ (or any other matrix) are written with bold symbols. To indicate the dependence of the state $|\Psi\rangle$ on the set of A-tensors $\{A(i)\}_{i=1,\dots,L}$, I use curly brackets around the A-tensors. In the case of translation-invariant A-tensors, the curly brackets are omitted and the state is referred to as an *uniform* MPS (uMPS). An uMPS depends on a single A-tensor only, which is placed at every site of the lattice. It is convenient to use a graphical notation for the A-tensors:

$$A^\sigma_{ij} = \quad \overset{i}{\underset{\sigma}{\boxed{A}}}\overset{j}{} \tag{2.5}$$

Here, the rank-3 tensor is visualized as a box with three legs, one for each index. This graphical notation can be used for general tensors including scalars, vectors, or higher-rank tensors. For example, a general state in the canonical basis of the multi-site Hilbert space can be written as in Eq. (2.2), which leads to the identification

$$T^{\sigma_1\cdots\sigma_L} = \operatorname{tr} \boldsymbol{A}^{\sigma_1}(1)\cdots\boldsymbol{A}^{\sigma_L}(L) \tag{2.6}$$

In a graphical notation this becomes:

$$\boxed{\begin{array}{ccc} & T & \\ \sigma_1 & \cdots & \sigma_L \end{array}} = \overparen{\boxed{A}-\boxed{A}-\cdots-\boxed{A}-\boxed{A}}_{\sigma_1\ \ \ \sigma_2\ \ \ \ \ \ \sigma_{L-1}\ \ \ \sigma_L}, \tag{2.7}$$

which visualizes the whole state $|\Psi[\{A\}]\rangle$, or more precisely the components for the canonical basis. What can be also seen in Eq. (2.7) is how to visualize tensor contractions in the graphical notation: if two tensors get contracted over several indices, one connects all legs of such index pairs. The trace operation is visualized by connecting two legs of the same tensor.

Eq. (2.6) or (2.7) also shows that any MPS is equivalent to a state in the canonical basis by evaluating the matrix products and the trace in Eq. (2.3) first. An arbitrary state in the form of Eq. (2.2) can also be written as an MPS, but the concrete form of the A-tensors is not unique. A possible decomposition can be achieved by the following procedure:

1. Reshape the tensor $T^{\sigma_1\cdots\sigma_L}$ into a $d \times d^{L-1}$ matrix by combining the indices $\sigma_2\cdots\sigma_L$ into a multi-index Σ.

2. Perform a singular value decomposition (SVD, see Appendix Chap. A) on the reshaped tensor:

$$T^{\sigma_1 \Sigma} = \sum_{i=1}^{\chi_1} U^{\sigma_1 i} S^{ii} V^{i\Sigma} \tag{2.8}$$

3. Set $A_{0,i}^{\sigma_1} = U^{\sigma_1 i}$ and $\tilde{T}^{i\sigma_2 \cdots \sigma_L} = S^{ii} V^{i\Sigma}$ by decomposing the multi-index Σ back into $\sigma_2 \ldots \sigma_L$.

4. Reshape the tensor $\tilde{T}$ into a $d \cdot \chi_1 \times d^{L-2}$ matrix by combining the indices i and σ_2 into a multi-index I and the indices $\sigma_3 \cdots \sigma_L$ into a multi index Σ.

5. Perform a SVD on the reshaped tensor:

$$\tilde{T}^{I\Sigma} = \sum_{j=1}^{\chi_2} U^{Ij} S^{jj} V^{j\Sigma} \tag{2.9}$$

6. Set $A_{i,j}^{\sigma_2} = U^{Ij}$ by decomposing the multi-index I back into i and σ_2 and $\tilde{\tilde{T}}^{j\sigma_3 \cdots \sigma_L} = S^{jj} V^{j\Sigma}$ by decomposing the multi-index Σ back into $\sigma_3 \ldots \sigma_L$.

7. Iterate this procedure by going back to step 4.

This procedure gives an exact representation of an arbitrary state in an MPS formulation. In the general case, the auxiliary bond dimensions χ_i then grow exponentially with the system size L. The procedure can also be used to obtain an approximation for the state as an MPS by taking in steps 3 and 6 only the $\chi_{\max}$ largest singular values. This fixes the bond dimension to a cutoff value $\chi_{\max}$ but introduces a truncation error which is the sum of all discarded singular values.

The states in Eq. (2.3) define a subspace $\mathcal{M}$ of the full Hilbert space $\mathcal{H}$:

$$\mathcal{M} = \{|\Psi[\{A\}]\rangle \mid A(i) \in \mathbb{A}_i\} \tag{2.10}$$

The set $\mathcal{M}$ depends on the bond dimensions χ_i and does *not* form a linear subspace of $\mathcal{H}$, since the sum of two MPSs has in general different bond dimensions $\tilde{\chi}_i$. The MPS is a natural map from the space of parameters $\mathbb{A} = \bigoplus_i \mathbb{A}_i$ into $\mathcal{M}$. The map is not injective because of two reasons: firstly, there is a natural gauge freedom in the parametrization, and secondly *singular A*-tensors are not excluded in the definition of $\mathbb{A}_i$. Singular A-tensors are tensors which can be compressed to a smaller bond dimension $\tilde{\chi} < \chi$ without changing the state. To make this more explicit: with the definition above, one actually has $\mathcal{M}_{\{\chi\}} \subset \mathcal{M}_{\{\tilde{\chi}\}}$ for two sets of bond dimensions $\{\chi\}$ and $\{\tilde{\chi}\}$ with $\chi_i > \tilde{\chi}_i$ all $i = 1, \ldots, L$. The singular parametrization leads to conceptual as well as numerical problems. Hence, it would be desirable to restrict the A-tensors to a subset $\mathcal{A} \subset \mathbb{A}$ which only contains elements which are non-singular.

For an MPS with open boundary conditions, this can be obtained with help of the density matrices $\boldsymbol{L}(i)$ and $\boldsymbol{R}(i)$ which are recursively defined:

$$\boldsymbol{L}(i+1) = \sum_{\sigma_i} \boldsymbol{A}^{\dagger\sigma_i}(i)\boldsymbol{L}(i)\boldsymbol{A}^{\sigma_i}(i), \qquad \boldsymbol{L}(1) = 1 \tag{2.11}$$

$$\boldsymbol{R}(i-1) = \sum_{\sigma_i} \boldsymbol{A}^{\sigma_i}(i)\boldsymbol{R}(i)\boldsymbol{A}^{\dagger\sigma_i}(i), \qquad \boldsymbol{R}(L) = 1 \tag{2.12}$$

and can be computed with a computational cost scaling as $\mathcal{O}(\chi^3)$. The set $\mathcal{A}$ can then be defined as an open subset of $\mathbb{A}$ for which all density matrices have full rank. Since $\boldsymbol{L}(i)$ and $\boldsymbol{R}(i)$ are per definition positive matrices, this is equivalent to asking for strictly positive definite density-matrices. By restricting to the set $\mathcal{A}$, one gets a better variational set:

$$\mathcal{M} = \{|\Psi[\{A\}]\rangle \mid A \in \mathcal{A}\} \tag{2.13}$$

Although the map defined by the MPS is still not injective, the remaining ambiguity is the gauge freedom which will be discussed in Sec. 2.3.

In the case of periodic boundary conditions, one can assume that the state is described by a uMPS with bond dimension χ. The respective restriction of the parameter space is described in Sec. 2.4 for uMPS in the thermodynamic limit.

2.2 Interpretation of matrix product states

An MPS as defined in the last section is a special parametrization of a general state $|\Psi\rangle$ in the Hilbert space $\mathcal{H}$. As will be discussed later, this parametrization is an efficient variational ansatz for several optimization problems. A more physical interpretation of the introduced A-tensors is also possible. Here, the A-tensors define a renormalization group (RG) scheme, to iteratively renormalize the low-energy basis of the system. To see this, one can write the matrix multiplications in the MPS explicitly and then change the order of summation (open boundaries assumed):

$$|\Psi\rangle = \sum_{\boldsymbol{\sigma}} \sum_{i_1,\dots,i_{L-1}} A^{\sigma_1}_{1,i_1}(1)A^{\sigma_2}_{i_1,i_2}(2)\cdots A^{\sigma_{L-1}}_{i_{L-2},i_{L-1}}(L-1)A^{\sigma_L}_{i_{L-1},1}(L) |\boldsymbol{\sigma}\rangle \tag{2.14}$$

Collecting only the relevant terms for the summation over σ_1, one obtains:

$$|i_1\rangle = \sum_{\sigma_1} A^{\sigma_1}_{i_1}(1) |\sigma_1\rangle \tag{2.15}$$

The site tensor on site 1 transforms the local basis at site 1 into an effective state space $\mathcal{I}_1$. Performing this iteratively until the site l one obtains an effective state space $\mathcal{I}_l$ consisting of the states:

$$|i_l\rangle = \sum_{\sigma_l,i_{l-1}} A^{\sigma_l}_{i_{l-1},i_l}(l) |i_{l-1}\sigma_l\rangle \tag{2.16}$$

Here, it becomes obvious that the site tensor $A(l)$ is a map which combines the effective state space $\mathcal{I}_{l-1}$ with the local Hilbert space $\mathcal{H}_{\text{loc},l}$ at site l into an effective state space $\mathcal{I}_l$[1]:

$$A : \quad \mathcal{I}_{l-1} \otimes \mathcal{H}_{\text{loc},l} \to \mathcal{I}_l \tag{2.17}$$
$$|i_{l-1}\rangle \times |\sigma_l\rangle \mapsto \sum_{i_l} A^{\sigma_l}_{i_{l-1} i_l} |i_l\rangle$$

If $\dim(\mathcal{I}_l) < \dim\left(\mathcal{I}_{l-1} \otimes \mathcal{H}^{(l)}_{\text{loc}}\right)$ this map is a truncation. In a RG picture the A-tensors should be chosen in such a way that the low-energy sector of the Hilbert space is kept.

2.3 Gauge freedom and canonical forms

The MPS in Eq. (2.3) is not unique in the sense that different A-tensors lead to the same physical state. In other words the map Ψ:

$$\Psi : \quad \mathcal{A} \longrightarrow \mathcal{M}$$
$$A \longmapsto |\Psi[\{A\}]\rangle$$

is not injective. The transformations G on elements $A \in \mathcal{A}$, which leave the state unchanged, introduce a gauge freedom. This gauge freedom allows to require certain constraints on the A-tensors.

Consider an arbitrary invertible $\chi_i \times \chi_i$ matrix $\boldsymbol{C}(i)$ and the matrix product $\boldsymbol{A}^{\sigma_i}(i)\boldsymbol{A}^{\sigma_{i+1}}(i+1)$ as a part of Eq. (2.3) between the matrices at site i and $i+1$. One can insert $\boldsymbol{C}(i)^{-1}\boldsymbol{C}(i)$ between the two matrices and then multiply $\boldsymbol{C}(i)^{-1}$ to the left and $\boldsymbol{C}(i)$ to the right to obtain different matrices $\tilde{\boldsymbol{A}}^{\sigma_i}(i)$ and $\tilde{\boldsymbol{A}}^{\sigma_{i+1}}(i+1)$ while leaving the product and hence the whole state invariant. Therefore the gauge transformations for MPSs are:

$$\boldsymbol{A}^{\sigma_i}(i) \to \boldsymbol{A}^{\sigma_i}(i)\boldsymbol{C}(i)^{-1} \qquad \boldsymbol{A}^{\sigma_{i+1}}(i+1) \to \boldsymbol{C}(i)\boldsymbol{A}^{\sigma_{i+1}}(i+1), \tag{2.18}$$

for $\boldsymbol{C}(i)$ being an element of the general linear group $\text{GL}(\chi_i)$. These gauge transformations can be inserted at every bond in the MPS. Consequently, the gauge group G is the direct product $G = \prod_i \text{GL}(\chi_i)$. The group G has a right action on the parameter space $\mathbb{A}$:

$$\mathbb{A} \otimes G \to \mathbb{A}$$
$$(\{A_i\}_{i=1,\dots,L}, \{\boldsymbol{C}_i\}_{i=1,\dots,L}) \mapsto \{A_i^G\}_{i=1,\dots,L}, \quad A_i^G = \sum_\sigma \boldsymbol{C}(i-1)\boldsymbol{A}^\sigma \boldsymbol{C}(i),$$

which can also be restricted to the space $\mathcal{A}$. This group action allows to define a principal fiber bundle $\Psi : \mathcal{A} \to \mathcal{M}$ only if the group action is *free*. To ensure this, one needs to quotient out the stabilizer subgroup of G which is given by all scalar multiples of the identity matrix at every site. One advantage from this mathematical structure is that the set $\mathcal{M}$ is then known to be a smooth complex manifold.

---

[1] Notice that this map is of course canonically isomorphic to Eq. (2.4) but the physical intuition behind the definition here is important.

For uMPSs, all site tensors $A(i)$ are equal, so that one can write the gauge transformation as $\boldsymbol{A}^{\sigma} \to \boldsymbol{C}\boldsymbol{A}^{\sigma}\boldsymbol{C}^{-1}$ for any invertible $(\chi \times \chi)$ matrix $\boldsymbol{C}$. Hence, the gauge group is in this case $G = \mathrm{GL}(\chi)$ and again obtaining a *free* group action, one requires the quotient with the stabilizer subgroup which results in this case in the projective linear group $\mathrm{PGL}(\chi)$. This again leads to the structure of a principal fiber bundle with the trivialization given by the map Ψ. The manifold character of $\mathcal{M}$ will be used to derive variational principles for uMPSs in the thermodynamic limit.

Beside the structural information from the gauge group, the gauge freedom can be used to transform the MPS into canonical forms where the A-tensors fulfill certain constraints. These constraints can substantially improve numerical algorithms. For the *right canonical* form, one requires that every site fulfills:

$$\mathbb{1} = \sum_{\sigma_i} \boldsymbol{A}^{\sigma_i} (\boldsymbol{A}^{\sigma_i})^{\dagger} \tag{2.19}$$

$$\tag{2.20}$$

If a single A-tensor fulfills this condition, it is called *right-normalized* and will be written as A_R. In the graphical notation, I will use orange-colored boxes for right-normalized tensors. For the *left canonical* form, one requires that every site fulfills:

$$\mathbb{1} = \sum_{\sigma_i} (\boldsymbol{A}^{\sigma_i})^{\dagger} \boldsymbol{A}^{\sigma_i} \tag{2.21}$$

$$\tag{2.22}$$

If a single A-tensor fulfills this condition, it is called *left-normalized* and will be written as A_L. In the graphical representation, yellow boxes are used.

A combination of these two canonical forms is called the *mixed gauge* representation. This is characterized by one center site (the *pivot* site p) and all A-tensors to the left being left-normalized, and all A-tensors to the right being right-normalized. The *pivot* site tensor is referred to as A_P and can also be brought into a left- or right-normalized form which leads to

the center-matrix representation of the MPS:

$$|\Psi\left[\{A\}\right]\rangle = \sum_{\boldsymbol{\sigma}} \boldsymbol{A}_L^{\sigma_1}(1)\cdots\boldsymbol{A}_L^{\sigma_p}(p)\boldsymbol{P}\boldsymbol{A}_R^{\sigma_{p+1}}(p+1)\cdots\boldsymbol{A}_R^{\sigma_L}(L)\left|\boldsymbol{\sigma}\right\rangle, \tag{2.23}$$

where $\boldsymbol{P}$ is the center-matrix (or the super block wavefunction in original DMRG) and is a result of the normalization procedure of A_P. For details, see Sec. 2.7.1. An uMPS in the *mixed gauge* representation is characterized by the tensors $(A_L, A_R, A_P, \boldsymbol{P})$. The translational invariance of the state then shows up in the fact that the *pivot* site can be shifted to arbitrary positions in the chain because one has the conditions:

$$\boldsymbol{A}_P^{\sigma} = \boldsymbol{P}\boldsymbol{A}_R^{\sigma} = \boldsymbol{A}_L^{\sigma}\boldsymbol{P} \tag{2.24}$$

2.4 Uniform matrix product states in the thermodynamic limit

The MPSs from Sec. 2.1 are defined on a finite lattice with L sites. The A-tensors in the MPS can be chosen site-dependent or uniform, i.e site-independent. The site-dependent A-tensors are suited to describe inhomogeneous systems or systems with open boundary conditions. On the other hand, uniform MPSs (uMPSs) constitute a natural choice for translational invariant systems. In solid state physics, these systems appear naturally, as a lattice is per definition a periodic object. When considering finite systems, the translational invariance can only be reflected when periodic boundary conditions are applied. Although finite uMPS are a good ansatz for the simulation of lattice systems with periodic boundary conditions, the optimization procedures are not efficient. There exist no algorithms which scale as $\mathcal{O}(\chi^3)$, which is the typical scaling for open-boundary MPS methods. The reason is that the recursive definition of boundary matrices (or density matrices) is not possible, since there is no boundary anymore. For example the computation of expectation values of local operators can be performed with a computational cost of $\mathcal{O}(\chi_{\min}^2\chi_{\max}^3)$. For uMPSs one has $\chi_{\min} = \chi_{\max} = \chi$ and hence a cost of $\mathcal{O}(\chi^5)$. The additional cost is connected with the fact that the correlations in a periodic system can travel along *two* different paths corresponding to the two directions on a ring. To overcome this problem and to develop efficient algorithms for uMPS, one can examine the uMPS directly in the thermodynamic limit $L \to \infty$, since then there is only a single path for the development of correlations. Therewith, it is possible to reestablish the $\mathcal{O}(\chi^3)$ scaling. The algorithms however, need to be adapted accordingly to avoid possible divergencies. In this subsection, I will introduce uMPS in the thermodynamic limit and will present some results for the manifold of uMPS which are important to derive the variational algorithms later. uMPS and its geometrical structure are analysed in detail in Ref. [54, 55].

Consider first a lattice with $L = 2N + 1$ sites labeled from $-N$ to $+N$. A uMPS in the thermodynamic limit $N \to \infty$ is then formally defined as

$$|\psi\left[A\right]\rangle = \sum_{\boldsymbol{\sigma}} \mathrm{tr}\left[\boldsymbol{V}\prod_{n\in\mathbb{Z}}\boldsymbol{A}^{\sigma_n}\right]|\boldsymbol{\sigma}\rangle = \sum_{\boldsymbol{\sigma}} \mathrm{tr}\left[\boldsymbol{V}\cdots\boldsymbol{A}^{\sigma_{-1}}\boldsymbol{A}^{\sigma_0}\boldsymbol{A}^{\sigma_1}\cdots\right]|\boldsymbol{\sigma}\rangle. \tag{2.25}$$

Here $\boldsymbol{V}$ is a $\chi \times \chi$ boundary matrix. An important result is that when choosing the A-tensors from a suitable restricted open subset $\mathcal{A} \in \mathbb{A}$, all observables are independent of the boundary matrix V. As already discussed in Sec. 2.1, one needs to exclude singular A-tensors for which

some matrices do not have full rank. For uMPS however, there is a second requirement which ensures that the uMPS can be properly normalized and is independent of the boundaries. A central object of uMPS is the transfer matrix $T_{A^\dagger}^A = \sum_\sigma \boldsymbol{A}^{\dagger\sigma} \otimes \boldsymbol{A}^\sigma$, which defines two maps on the auxiliary space $\mathbb{C}^{\chi\times\chi}$ of the uMPS:

$$T_{A^\dagger}^A : \quad \boldsymbol{x} \longmapsto \sum_\sigma \boldsymbol{A}^{\dagger\sigma} \boldsymbol{x} \boldsymbol{A}^\sigma \tag{2.26}$$

$$\tilde{T}_{A^\dagger}^A : \quad \boldsymbol{x} \longmapsto \sum_\sigma \boldsymbol{A}^\sigma \boldsymbol{x} \boldsymbol{A}^{\dagger\sigma} \tag{2.27}$$

If one interprets matrices in $\mathbb{C}^{\chi\times\chi}$ as vectors, these maps can be more conveniently written as $T_{A^\dagger}^A \, |x\rangle$ and $\langle x| \, T_{A^\dagger}^A$. It is obvious from the definition that these maps are positive. With the help of $T_{A^\dagger}^A$, one can formulate the restrictions for the parameter space to obtain well defined uMPS. An element $A \in \mathbb{A}$ is in $\mathcal{A}$ if:

1. The transfer matrix $T_{A^\dagger}^A$ has a non-degenerate largest eigenvalue ω^{max} so that the spectral radius is $\varrho(T) = |\omega^{max}|$. This way, all other eigenvalues lie strictly in the circle with radius $\varrho(T)$ on the complex plain.

2. The left $\langle l|$ and right $|r\rangle$ eigenvectors corresponding to ω^{max} interpreted as $\chi \times \chi$-matrices are strictly positive definite. That also implies that they have full rank.

If both conditions are fulfilled, one can renormalize the A-tensor so that $\omega^{max} = 1$. The left and right eigenvectors then correspond to fixed points of the transfer matrix and the uMPS has norm 1. One can then show that expectation values are independent of the boundary matrix V [54–56]. Another implication is that uMPSs build from A-tensors of $\mathcal{A}$ are exponentially clustering. This implies that two-point correlation functions decay exponentially with the distance. This can be seen by a simple calculation, which also helps to make the transfer matrix as a central object more familiar. With the help of the definition of the transfer matrix T one can write for the expectation value of the correlation function of a local operator O_i:

$$\langle O_i O_j \rangle = \langle l| \, T_{O_i} T^{|j-i|} T_{O_j} \, |r\rangle , \tag{2.28}$$

where the dominant eigenvectors $\langle l|$ and $|r\rangle$ of the transfer matrix T are already included for the left and right infinite parts of the expectation value and T_{O_i} is a generalized transfer matrix with the operator included:

$$T_{O_i} = \sum_{\sigma\sigma'} O_i^{\sigma\sigma'} \boldsymbol{A}^\sigma \otimes \boldsymbol{A}^{\dagger\sigma'} \tag{2.29}$$

To proceed, one can perform an eigen-decomposition of the transfer matrix T:

$$T = |r\rangle \langle l| + \sum_\alpha \lambda_\alpha |\lambda_\alpha\rangle \langle \lambda_\alpha| \tag{2.30}$$

Inserting this decomposition in Eq. (2.28), one directly obtains the disconnected part $\langle O_i \rangle \langle O_j \rangle$

of the correlation function and a connected part:

$$\langle O_i O_j \rangle = \langle l | T_{O_i} | r \rangle \langle l | T_{O_j} | r \rangle + \sum_\alpha \lambda_\alpha^{|i-j|} \langle l | T_{O_i} | \lambda_\alpha \rangle \langle \lambda_\alpha | T_{O_j} | r \rangle \tag{2.31}$$

By the restriction to the set $\mathcal{A}$, all eigenvalues λ_α have $|\lambda_\alpha| < 1$, and hence the connected part of the correlation function decays exponentially. The correlation length ξ and also the pitch angle Q of the correlations are determined by the second largest eigenvalue λ_2 as $\xi = \frac{1}{\ln |\lambda_2|}$ and $Q = \arg(\lambda_2)$.

After restricting to the open subset $\mathcal{A} \subset \mathbb{A}$, one can define a principal fiber bundle for uMPS in the thermodynamic limit with total space $\mathcal{A}$, base space $\mathcal{M}$ and trivialization Ψ. The fibers are given by the gauge group $\mathrm{PGL}(\chi)$ introduced in Sec. 2.3. This of course implies that $\mathcal{M}$ (and also $\mathcal{A}$) are smooth complex manifolds. As the set $\mathcal{M}$ serves as the variational set for various algorithms, its tangent space is of importance for deriving the variational conditions. An intuitive way to obtain a tangent element at the point $|\Psi[A]\rangle$ is the derivative with respect to the parameters A. This derivative would naturally appear for any optimization problem on the set $\mathcal{M}$, so it is a useful task to analyse the structure of the tangent vectors in some detail. By the product rule for derivatives, one obtains a tangent vector $|\Phi[B,A]\rangle$ as a linear combination of the derivatives with respect to all parameters parametrized by a tensor $B \in \mathbb{C}^{\chi \times d \times \chi}$:

$$|\Phi[B,A]\rangle = B^I \frac{\partial}{\partial A^I} |\Psi[A]\rangle = \sum_{n \in \mathbb{Z}} \sum_{\boldsymbol\sigma} \mathrm{tr}\left[\cdots \boldsymbol{A}^{\sigma_{n-1}} \boldsymbol{B}^{\sigma_n} \boldsymbol{A}^{\sigma_{n+1}} \cdots \right] |\boldsymbol\sigma\rangle \tag{2.32}$$

Here I lists all entries of the A-tensor, hence it is a collective index $I = (i,j,\sigma)$. The notation suggests that the elements $\frac{\partial}{\partial A^I} |\Psi[A]\rangle$ build a basis of the tangent space $T\mathcal{M}_{|\Psi[A]\rangle}$ at the point $|\Psi[A]\rangle$. This, however, is not the case because of the gauge freedom in the MPS representation. In fact, $\frac{\partial}{\partial A^I} |\Psi[A]\rangle$ forms an overcomplete basis. One can see this immediately, when looking at the (complex) dimensions of $\mathcal{A}$, $\mathcal{M}$ and $\mathrm{PGL}(\chi)$. $\mathcal{A}$ is an open subset of $\mathbb{A}$, so as a manifold the dimension is $\dim \mathcal{A} = \chi^2 \cdot d$. Hence, its tangent space $T\mathcal{A}_A$ is a $\chi^2 \cdot d$-dimensional vector space which can be identified with $\mathbb{A}$. $\mathrm{PGL}(\chi)$ is a Lie group and given by the quotient of $\mathrm{GL}(\chi)$ with its center subgroup of matrices proportional to the identity. The dimension of $\mathrm{GL}(\chi)$ is $\dim \mathrm{GL}(\chi) = \chi^2$ and its center has dimension 1 so that one gets $\dim \mathrm{PGL}(\chi) = \chi^2 - 1$. Since locally, one can write $\mathcal{A} = \mathrm{PGL}(\chi) \times \mathcal{M}$, due to the fiber bundle structure, one gets $\dim \mathcal{M} = \chi^2(d-1)+1$. The tangent space $T\mathcal{A}_A$ of the total space of the bundle then decomposes pointwise in a direct sum of a vertical $V\mathcal{A}_A$ and a horizontal $H\mathcal{A}_A$ subspace:

$$T\mathcal{A}_A = V\mathcal{A}_A \oplus H\mathcal{A}_A \tag{2.33}$$

The derivative of the bundle projection Ψ at a given point A is a map between $T\mathcal{A}_A$ and $T\mathcal{M}_{|\Psi[A]\rangle}$. Its nullspace then directly determines the vertical subspace $V\mathcal{A}_A$. Instead the horizontal subspace $H\mathcal{A}_A$ is not uniquely determined but needs an additional structure of the bundle. The structure is called a *principal connection* and is quite technically defined as a Lie algebra valued 1-form ω acting on $T\mathcal{A}_A$ so that the kernel of ω is the horizontal subspace $H\mathcal{A}_A$. Of course, this 1-form has to satisfy different conditions. In a more practical way, one understands this as a gauge fixing condition for the elements $B \in T\mathcal{A}_A \sim \mathbb{A}$. One can directly check that the gauge transformations for tangent elements B at the point A are of the following

form:

$$\boldsymbol{B}^{\sigma} \to \boldsymbol{B}'^{\sigma} = \boldsymbol{B}^{\sigma} + \boldsymbol{A}^{\sigma}\boldsymbol{X} - \boldsymbol{X}\boldsymbol{A}^{\sigma} \tag{2.34}$$

with $\boldsymbol{X}$ a $\chi \times \chi$-matrix. These are gauge transformations in the sense that $|\Phi[B,A]\rangle = |\Phi[B',A]\rangle^1$. This gauge freedom can be used to require, e.g., the *left* gauge fixing condition for the elements B:

$$0 = \sum_{\sigma} \boldsymbol{A}_L^{\dagger\sigma}\boldsymbol{B}^{\sigma} = \sum_{\sigma} \boldsymbol{B}^{\dagger\sigma}\boldsymbol{A}_L^{\sigma}. \tag{2.35}$$

There is a very useful way to parametrize the B-tensors so that they are automatically in the *left gauge*. To obtain the parametrization one might recognize that Eq. (2.35) is fulfilled for any operator acting on the nullspace of A_L. A_L can be interpreted as a $(\chi d) \times \chi$ matrix which can be extended to a $(\chi d) \times (\chi d)$ unitary matrix. The additional $\chi(d-1)$ columns correspond to the nullspace and are referred to as N_L. For N_L one then has:

$$\tag{2.36}$$

Eq. (2.36) is equivalent to Eq. (2.35), so one can set $\boldsymbol{B}^{\sigma} = \boldsymbol{N}_L^{\sigma}\boldsymbol{X}$ as a parametrization for B. X is a $\chi(d-1) \times \chi$ matrix which directly parametrizes tangent elements in the *horizontal* subspace or equivalently tangent vectors in $T\mathcal{M}_{|\Psi[A]\rangle}$. Before, the dimension of of $T\mathcal{M}_{|\Psi[A]\rangle}$ was evaluated to $\dim T\mathcal{M}_{|\Psi[A]\rangle} = \chi^2(d-1) + 1$, which would be a mismatch to the $\chi(d-1) \times \chi$-dimensional parametrization. However, X parametrizes the part of $T\mathcal{M}_{|\Psi[A]\rangle}$ which is orthogonal to $|\Psi[A]\rangle$. For later applications of the tangent space, this is particularly useful because it can be used as the space of the new search direction, in first order. On the other hand, the space along the MPS direction is physically irrelevant, since the physical content of a state does not change if the state is multiplied by a scalar.

At the end of this section, I want to discuss a basic optimization problem, which will be useful for all later algorithms. Consider an arbitrary state $|\Theta\rangle \in \mathcal{H}$ and a uMPS $|\Psi[A]\rangle$. One can then introduce the tangent space projector $\mathcal{P}_{|\Psi[A]\rangle}$ which performs an orthogonal projection of the state $|\Theta\rangle \in \mathcal{H}$ onto the tangent space $T\mathcal{M}_{|\Psi[A]\rangle}$. Orthogonality is here defined by the standard inner product of the Hilbert space. This task can be converted into an optimization problem, by searching the tangent element $|\Phi[B(\boldsymbol{X}),A]\rangle$ such that the overlap with $|\Theta\rangle$ is maximized or by minimizing the distance to the tangent elements $|\Phi[B(\boldsymbol{X}),A]\rangle$:

$$\min_{\boldsymbol{X}} \||\Theta\rangle - |\Phi[B(\boldsymbol{X}),A]\rangle\| \tag{2.37}$$

Eq. (2.37) can be multiplied out which leads to the overlap between two tangent vectors.

---

1   This essentially means that $\boldsymbol{A}^{\sigma}\boldsymbol{X} - \boldsymbol{X}\boldsymbol{A}^{\sigma}$ parametrizes the vertical subspace $V\mathcal{A}_A$, since one has $|\Phi[B,A]\rangle = 0$ for $B \in V\mathcal{A}_A$

Here, it becomes visible that it is crucial to parametrize the tangent elements by the matrix $\boldsymbol{X}$ because otherwise the overlap is singular [55]. With the parametrization, however, one simply has:

$$\left\langle \Phi[B^\dagger(\boldsymbol{X}^\dagger),A^\dagger] \,\middle|\, \Phi[B(\boldsymbol{X}),A] \right\rangle = 2\pi\delta(0)\operatorname{tr}\boldsymbol{X}^\dagger\boldsymbol{X} \tag{2.38}$$

so that the minimization problem (2.37) becomes quadratic. Note that there is still a diverging term in the overlap in Eq. (2.38) but this will drop out during all computations. The solution to Eq. (2.37) is:

$$2\pi\delta(0)\boldsymbol{X} = \frac{\partial}{\partial\boldsymbol{X}^\dagger}\left\langle \Phi[B^\dagger(\boldsymbol{X}^\dagger),A^\dagger] \,\middle|\, \Theta \right\rangle \tag{2.39}$$

Here, the diverging factor $\delta(0)$ drops out if $|\Theta\rangle$ is translation-invariant. Now the last step is to construct the resulting state $|\Phi[B(\boldsymbol{X}),A]\rangle$ from the solution for $\boldsymbol{X}$ (2.39) via $\boldsymbol{B}^\sigma = \boldsymbol{N}_L^\sigma\boldsymbol{X}$ and Eq. (2.32). Afterwards, one can directly deduce the corresponding tangent space projector

$$\mathcal{P}_{|\Psi[A]\rangle} = \sum_n \sum_{\boldsymbol{\sigma},\boldsymbol{\sigma}'} \left[\cdots \boldsymbol{A}_L^{\dagger\sigma_{n-1}} \boldsymbol{N}_L^{\dagger\sigma_n} \boldsymbol{N}_L^{\sigma'_n} \boldsymbol{A}_L^{\sigma'_{n-1}} \cdots \right] \left[\cdots \boldsymbol{A}_R^{\sigma'_{n+2}} \boldsymbol{A}_R^{\sigma'_{n+1}} \boldsymbol{A}_R^{\dagger\sigma_{n+1}} \boldsymbol{A}_R^{\dagger\sigma_{n+2}} \cdots \right] |\boldsymbol{\sigma}'\rangle \langle\boldsymbol{\sigma}| \tag{2.40}$$

This formula can be put in a slightly different form which is more useful for the upcoming algorithms. The projector $\boldsymbol{N}_L^{\dagger\sigma}\boldsymbol{N}_L^{\sigma'}$ can be rewritten as $\mathbb{1}\delta_{\sigma\sigma'} - \boldsymbol{A}_L^{\dagger\sigma}\boldsymbol{A}_L^{\sigma'}$ so that the tangent space projector consists of two different parts.

$$\begin{aligned}
\mathcal{P}_{|\Psi[A]\rangle} = \sum_n \sum_{\boldsymbol{\sigma},\boldsymbol{\sigma}'} \Bigg\{ &\left[\cdots \boldsymbol{A}_L^{\dagger\sigma_{n-1}} \mathbb{1}\delta_{\sigma_n\sigma'_n} \boldsymbol{A}_L^{\sigma'_{n-1}} \cdots \right] \left[\cdots \boldsymbol{A}_R^{\sigma'_{n+1}} \boldsymbol{A}_R^{\sigma'_n} \boldsymbol{A}_R^{\dagger\sigma_n} \boldsymbol{A}_R^{\dagger\sigma_{n+1}} \cdots \right] \\
&- \left[\cdots \boldsymbol{A}_L^{\dagger\sigma_{n-1}} \boldsymbol{A}_L^{\dagger\sigma_n} \boldsymbol{A}_L^{\sigma'_n} \boldsymbol{A}_L^{\sigma'_{n-1}} \cdots \right] \left[\cdots \boldsymbol{A}_R^{\sigma'_{n+1}} \boldsymbol{A}_R^{\sigma'_n} \boldsymbol{A}_R^{\dagger\sigma_n} \boldsymbol{A}_R^{\dagger\sigma_{n+1}} \cdots \right] \Bigg\} |\boldsymbol{\sigma}'\rangle \langle\boldsymbol{\sigma}|
\end{aligned} \tag{2.41}$$

This lengthy formula can be written more convenient by using the graphical notation:

$$\mathcal{P}_{|\Psi[A]\rangle} = \sum_n \qquad\qquad\qquad\qquad\qquad\qquad\qquad - \tag{2.42}$$

2.5 Area law

In the previous sections, MPSs were described as a variational ansatz for obtaining groundstates of one-dimensional Hamiltonians by minimizing the energy of the MPS. Variational ansätze are found at the heart of most numerical methods. When optimizing a variational ansatz, one obtains the optimal state in the variational space but it is a priori completely unknown if this state is a good approximation to the true groundstate of the system. For the MPS ansatz however, there exists the famous *area law* which states that the true ground state of one-dimensional *gapped* systems lies in the space of the MPSs. This is a remarkable result, since it guarantees that if one is able to find the optimal MPS representation for a state, this will be indeed the groundstate of the system. To give an overview over this theorem, I will first introduce the concept of entanglement in quantum mechanics.

Entanglement in quantum mechanics is a property of states in a system G consisting of two subsystems A and B. *Consisting of* means that the Hilbert space of G is obtained by the tensor product of the Hilbert spaces of A and B:

$$\mathcal{H}_G = \mathcal{H}_A \otimes \mathcal{H}_B \tag{2.43}$$

For any state $|\Psi\rangle \in \mathcal{H}_G$ one can then decide if it is an entangled state or not. The relevant quantity is the partial trace over the projector $|\Psi\rangle\langle\Psi|$ with respect to the degrees of freedom of

one part of the system, which is called the reduced density matrix ϱ_A:

$$\varrho_A = \text{tr}_B |\Psi\rangle \langle\Psi| \tag{2.44}$$

The partial trace is over all states in $\mathcal{H}_B$ so that ϱ_A is an operator acting in $\mathcal{H}_A$. ϱ_A fulfills all requirements to be a density operator: it is Hermitian, positive semidefinite and has $\text{tr}_A \, \varrho_A = 1$. Then the state $|\Psi\rangle$ is not entangled if and only if $\varrho_A = \varrho_A^2$. In other words, the state is not entangled if ϱ_A describes a pure state, whether $|\Psi\rangle$ is entangled if ϱ_A describes a mixed state. Note that this definition is independent of the basis in the two subsystems A and B. There exist different measures for the strength of entanglement [57, 58]. The most common measure is the von Neumann entropy S_{vN} or the more general Renyi entropy S_{R} [59] of the reduced density-matrix ϱ_A:

$$S_{\text{vN}} = -\text{tr}_A \left[\varrho_A \ln \varrho_A \right] \tag{2.45}$$

$$S_{\text{R}}^{(\alpha)} = \frac{\alpha}{1-\alpha} \log \left[\text{tr}_A \, \varrho_A^\alpha \right] \tag{2.46}$$

For $\alpha \to 1$, S_{R} is identical with S_{vN}. The state $|\Psi\rangle$ is not entangled if $S_{\text{vN}} = 0$ while it is entangled otherwise. And the larger the entropy, the larger the entanglement in the state.

This quite general framework for entanglement is relevant in the context of *area laws* if the bipartition of a system is spatial. Hence, one assumes that the system G is d-dimensional and one cuts out a subsystem C and measures the entanglement between C and $G \setminus C$. See Fig. 2.1 for an example of bipartitions for one- and two-dimensional lattice system. The subsystem C has a d-dimensional volume $\mathcal{V}_C$ and a $(d-1)$-dimensional surface $\mathcal{S}_C = \partial\mathcal{V}_C$ and it is of particular interest how the entanglement depends on $\mathcal{V}_C$ and $\mathcal{S}_C$. A state $|\Psi\rangle$ of the system G is said to fulfill an *area law* if the entanglement scales with the surface $\mathcal{S}_C$ while it is said to fulfill a *volume law* if it scales with the volume $\mathcal{V}_C$. For a state $|\Psi[\{A\}]\rangle$ in a MPS representation with bond dimensions $\{\chi_i\}_{i=1,\dots,L}$ on a one-dimensional lattice with L sites, one can easily compute the entanglement for a bipartition as depicted in the left of Fig. 2.1. Note that it is convenient to divide the one-dimensional chain into two chains by cutting at a given site p rather cutting the chain at two sites, because in this case, there would be disconnected parts. However, this has no impact on the entanglement scaling. The volume of the subsystem C is then directly related to the length L of the chain. So it will be important how the entanglement scales with the chain length. Suppose the state $|\Psi[\{A\}]\rangle$ is in the *mixed-gauge* representation with the pivot site p coinciding with the site of the cut. Then the summation over A_L defines an orthonormal basis $|L_i\rangle$ for the left part of the system and the summation over A_R defines an orthonormal basis $|R_j\rangle$ for the right part of the system:

$$|L_i\rangle = \left(\sum_{\sigma_1 \dots \sigma_p} \boldsymbol{A}_L^{\sigma_1}(1) \cdots \boldsymbol{A}_L^{\sigma_p}(p) |\sigma_1 \dots \sigma_p\rangle \right)_i \tag{2.47}$$

$$|R_i\rangle = \left(\sum_{\sigma_{p+1} \dots \sigma_L} \boldsymbol{A}_R^{\sigma_{p+1}}(p+1) \cdots \boldsymbol{A}_R^{\sigma_L}(L) |\sigma_{p+1} \dots \sigma_L\rangle \right)_j \tag{2.48}$$

Here one takes only the i-th (j-th) component from the matrix products and open boundaries
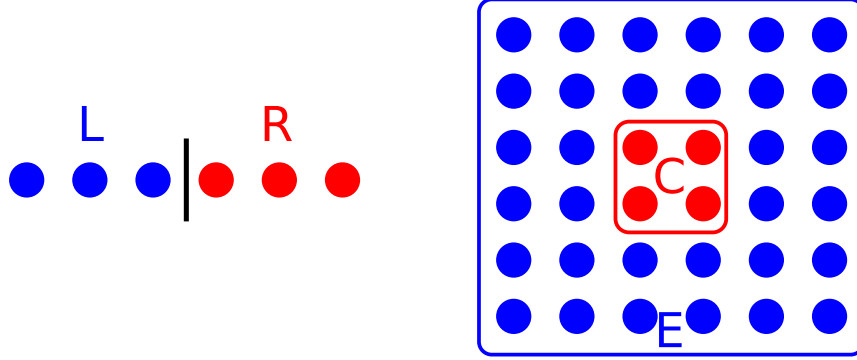
Figure 2.1: Bipartitions of a one- and a two-dimensional lattice. Left: A chain of length $L = 6$ divided into two parts L and R of size $L_S = \frac{L}{2}$. The boundary of the subsystem (either L or R) is zero-dimensional and hence does not scale with L_S. Right: A two-dimensional $L \times L$ lattice with $L = 6$, for which a subsystem C of size $L_S \times L_S$ ($L_S = 2$) is cut out. The boundary of the subsystem scales linearly with L_S.

are assumed so that $\boldsymbol{A}_L^{\sigma_1}(1)$ and $\boldsymbol{A}_L^{\sigma_L}(L)$ are row- and column-vectors respectively. The state is then entirely determined by the center matrix $\boldsymbol{P}$ at the pivot site p and can be written as:

$$|\Psi\rangle = \sum_{i,j=1}^{\chi_p} P_{ij} |L_i\rangle |R_j\rangle \tag{2.49}$$

This formula makes explicit that the *mixed gauge* representation is well-suited to compute the entanglement for a bipartition at the pivot site and is called the Schmidt decomposition of the state $|\Psi\rangle$. The projector $|\Psi\rangle \langle\Psi|$ and the partial trace over either the left or right space can be readily obtained from this Schmidt decomposition:

$$\varrho_L = \boldsymbol{P}\boldsymbol{P}^\dagger \tag{2.50}$$

$$\varrho_R = \boldsymbol{P}^\dagger \boldsymbol{P}, \tag{2.51}$$

and the singular values Σ of $\boldsymbol{P}$ allow to compute the entanglement entropy efficiently:

$$S_{\text{vN}} = -\sum_{i=1}^{\chi_p} \Sigma_i^2 \log \Sigma_i^2 \tag{2.52}$$

The resulting entanglement entropy (2.52) is independent of the chain length L and is bounded by the bond dimension χ_p as $S_{\text{vN}}^{\max} = \ln \chi_p$. Recognizing that the surface $\mathcal{S}$ for the subsystem of the one-dimensional system is zero-dimensional and consequently a constant independent of L, it becomes clear that MPSs fulfill an *area law*. In contrast, the situation is different if the MPS parametrizes a state on a two-dimensional lattice, for example the system in the right part of Fig. 2.1. For this parametrization, one has to choose a one-dimensional snake through the two-dimensional lattice. The surface of the subsystem C scales linearly with the total number of sites L (the volume scales as L^2). On the other hand, the entanglement of the MPS does not change compared to the previous case, hence it is again a constant bounded by the bond dimension. In this sense, MPS for two-dimensional systems does not fulfill an *area law*. The

generalizations of MPS, called projected entangled pair states (PEPS) [43–45], however, fulfill the *area law* in two dimensions.

The entanglement structure of MPSs is obtained quite simply as demonstrated in the paragraph above. A rather non-trivial task is the same entanglement analysis for groundstates of Hamiltonians. The central result is that in one dimension they also obey the *area law* if they contain only local interactions and if the ground state is clearly separated in their spectrum, i.e. they have a finite spectral gap. This result proves that MPSs are well-suited for simulating one-dimensional quantum systems and are the basis of the success of all MPS-related methods. The prove is quite lengthy, so I will refer the interested reader to Ref. [30, 37] and references therein.

2.6 Matrix Product Operators

For the optimization of the variational parameters in an MPS, an efficient computation of expectation values with a Hamilton operator $\langle \Psi | H | \Psi \rangle$ is mandatory. The general structure of MPSs can be transferred to arbitrary operators acting in the Hilbert space $\mathcal{H}$. The d-dimensional local Hilbert space can be interpreted as a $\tilde{d} \times \tilde{d}$ space of local operators. With this identification, one can write e.g. the Hamilton operator in the following form:

$$H = \mathrm{tr} \sum_{\boldsymbol{\sigma}, \boldsymbol{\sigma}'} \boldsymbol{W}^{\sigma_1 \sigma_1'}(1) \cdots \boldsymbol{W}^{\sigma_L \sigma_L'}(L) \, |\boldsymbol{\sigma}\rangle \langle \boldsymbol{\sigma}'| \,, \tag{2.53}$$

where $\boldsymbol{W}^{\sigma_i \sigma_i'}(i)$ are $\chi_{i-1} \times \chi_i$ matrices and χ describes the bond dimension of the matrix product operator (MPO). Many of the properties of MPSs can therefore be transferred to MPOs and used for algorithms on MPOs [60]. One can also represent the basic building block $\boldsymbol{W}^{\sigma_i \sigma_i'}$ in a graphical notation. Since it is a rank-4 object, it is represented by a box with four legs:

$$W_{ij}^{\sigma\sigma'} = \quad\begin{array}{c} \sigma' \\ i \boxed{W} j \\ \sigma \end{array} \tag{2.54}$$

The MPO-form of the operators is particularly useful for Hamiltonians with short-range interactions. These operators can be represented exactly in this formalism with small bond dimension χ. However, some long-range interactions can be represented quite efficiently with moderate bond dimensions [61–63] as well.

As an example, one can examine the MPO representation of a simple operator containing only a nearest-neighbor hopping-like term in the form $H = \sum_{\langle i,j \rangle} X_i Y_j + \mathrm{h.c.}$. In the case that $[X_i, Y_j] = 0$ at least for i and j being nearest neighbors, this operator can be represented with bond dimension $\chi = 4$:

$$W_i = \begin{pmatrix} \mathbb{1} & 0 & 0 & 0 \\ X_i & 0 & 0 & 0 \\ Y_i^\dagger & 0 & 0 & 0 \\ 0 & Y_i & X_i^\dagger & \mathbb{1} \end{pmatrix} \tag{2.55}$$

Here, every entry in the W-tensor is an operator acting on the local physical state.

2.7 Arithmetics for matrix product states

For any algorithm which operates with MPSs and MPOs several operations have to be performed as efficiently as possible. Here, I present the most common of them. Some algorithms are *direct* in the sense that resulting objects are directly calculated from the original objects and others are *variational* in the sense that a random MPS is optimized to be the result of the given computation.

2.7.1 Direct algorithms

MPS addition

The sum of two finite MPSs can be obtained easily. However, an important conceptional point is that the sum of two MPSs has a different bond dimension than the original ones. Therefore the sum operation will leave the manifold of MPS with bond dimension χ (see discussion of the manifold properties for MPS Sec. 2.4). To actually compute the sum of two MPS $|\Psi[\{A\}]\rangle$ and $|\Phi[\{B\}]\rangle$, one has to calculate the direct sum of the A-tensors and the B-tensors. The resulting MPS $|\Xi[\{C\}]\rangle$ then has tensors:

$$\boldsymbol{C}^{\sigma}(l) = \boldsymbol{A}^{\sigma}(l) \oplus \boldsymbol{B}^{\sigma}(l) \tag{2.56}$$

and hence the resulting MPS has a bond dimension given as the sum of the original bond dimensions. This can be often reduced again by a compression algorithm ([14]). For example in the trivial case of $|\Psi[\{A\}]\rangle = |\Phi[\{B\}]\rangle$ a simple scaling factor of 2 is enough, resulting in an MPS with the same bond dimension.

MPS sweeping

MPSs can be brought into canonical forms by taking use of the gauge symmetry as described in Sec. 2.3. The mixed-canonical form in particular simplifies several algorithms. Consider a normalized MPS $|\Psi[\{A\}]\rangle$ with arbitrary A-tensors. The *mixed gauge* representation for a given site p – which acts as the *pivot* site in several algorithms later – is characterized by A-tensors left from p being left-normalized while A-tensors right from p being right-normalized. Bringing an MPS into this *mixed gauge* representation is a standard task in any MPS implementation. First, consider a finite MPS $|\Psi[\{A\}]\rangle$. Here the procedure is as follows:

1. Bring all A-tensors into the left-normalized form up to the site p in an iterative procedure starting from site $l = 1$ until $l = p - 1$. Reshape the A-tensor at site l by combining the incoming auxiliary index i and the physical index into a composite index $(i\sigma)$ to obtain a rectangular matrix $\tilde{\boldsymbol{A}}$ with matrix elements:

$$\tilde{A}_{(i\sigma)j} = A^{\sigma}_{ij}(l) \tag{2.57}$$

   Then perform a QR decomposition (Chap. A) of $\tilde{\boldsymbol{A}}$ to obtain an orthogonal matrix $\boldsymbol{Q}$ and an upper triangular matrix $\boldsymbol{R}$. Reshape the matrix $\boldsymbol{Q}$ back into the form of the A-tensors

to obtain a left-normalized site tensor at site l:

$$A_L{}^\sigma_{ij}(l) = Q_{(i\sigma)j} \qquad (2.58)$$

Finally, multiply the matrix R into $A(l+1)$.

In a similar way, one can right-normalize the tensors to the right of p, by starting at the right end $l = L$ of the chain. The difference is that the tensors have to be reshaped by combining the physical σ and the right auxiliary index j into a combined index, namely by setting:

$$\tilde{A}_{i(\sigma j)} = A^\sigma_{ij}(l) \qquad (2.59)$$

Afterwards, one has to perform a LQ decomposition of $\tilde{\boldsymbol{A}}$. Here one can use standard algorithms for the QR decomposition by using $\tilde{\boldsymbol{A}}^\dagger$.

The *mixed gauge* representation naturally leads to the pivot site p (often also called center site), which often needs to be shifted by one site. In MPS language this procedure is called a *sweepstep*. When the pivot site of an MPS is at site p and should be shifted to $p+1$, one simply makes the procedure for left-normalization only for the site $l = p$. If instead the pivot site should be shifted to $p-1$, one performs a single right-normalization step at the site $l = p$.

Note that instead of the QR decomposition, one can also perform a SVD decomposition (Chap. A) of the reshaped A-tensor and multiply the singular values together with left (right) isometry into the next (previous) site. This has the advantage that one is able to truncate the MPS simultaneously by taking only the χ_{trunc} largest singular values.

In the case of uMPSs, the above algorithms are not applicable and one has to tackle the problem in a different manner. The starting point here is a uMPS $|\Psi[A]\rangle$ in the uniform gauge with a single A-tensor placed at every site of the infinite lattice. Now, one needs to find a gauge transformation $\boldsymbol{L}$ so that $\boldsymbol{A}^\sigma_L := \boldsymbol{L}A^\sigma\boldsymbol{L}^{-1}$ is left-normalized. The corresponding gauge transformation can be found by decomposing the left dominant eigenvector $|l\rangle$ of the transfer matrix $T^A_{A\dagger}$ as $|l\rangle = \boldsymbol{L}^\dagger\boldsymbol{L}$. This can be directly checked by plugging the obtained A_L in the condition for left-normalization Eq. (2.21). From a numerical point of view, however, this is not stable, since one has to compute the matrix square-root-like decomposition (Cholesky decomposition). In exact arithmetic this is no problem, since the fixed point for a proper uMPS is strictly positive definite. However, there might be very small eigenvalues which make the numerical decomposition unstable. Additionally, one has to compute the matrix-inverse from $\boldsymbol{L}$ which is also numerically unstable. A better choice is an iterative procedure based on the equation:

$$\boldsymbol{A}^\sigma_L\boldsymbol{L} = \boldsymbol{L}\boldsymbol{A}^\sigma, \qquad (2.60)$$

where one starts with a random $\boldsymbol{L}$ and performs iterative QR decompositions of $\boldsymbol{L}A^\sigma$ (after appropriate reshaping) into $\boldsymbol{A}^\sigma_L\boldsymbol{L}$ until $\boldsymbol{L}$ is converged. With a similar algorithm, one can also find the gauge transformation $\boldsymbol{R}$ so that $\boldsymbol{A}^\sigma_R := \boldsymbol{R}^{-1}\boldsymbol{A}^\sigma\boldsymbol{R}$ is right-normalized. Now, one can perform these gauge transformations at the left (right) of an arbitrary pivot site p and therewith left- (right)-normalize all tensors to the left (right) of p. To the left (right) of the pivot site, the gauge transformation $\boldsymbol{L}$ ($\boldsymbol{R}$) remains, and needs to be multiplied in the A-tensor

at site p to give the pivot-site tensor A_P:

$$\boldsymbol{A}_P^\sigma = \boldsymbol{L}\boldsymbol{A}^\sigma \boldsymbol{R} \tag{2.61}$$

The pivot-matrix $\boldsymbol{P}$ is then also easily obtained by $\boldsymbol{P} = \boldsymbol{L}\boldsymbol{R}$. In summary one obtains the three A-tensors and the pivot-matrix $(A_L, A_R, A_P, \boldsymbol{P})$ which describe the uMPS in the *mixed gauge*.

MPS overlap

Given two finite MPS $|\Psi[\{A\}]\rangle$ and $|\Phi[\{B\}]\rangle$ with open boundary conditions, the overlap between both can be calculated by contracting the whole network depicted in Fig. 2.2. The most efficient way is to contract the network from left to right (or right to left). Therefore, one introduces a matrix $\boldsymbol{L}$ which is recursively defined as the left boundary of the network at site l:

$$\boldsymbol{L}(l+1) = \sum_{\sigma_l} \boldsymbol{B}^{\sigma_l\dagger}(l)\boldsymbol{L}(l)\boldsymbol{A}^{\sigma_l}(l) \tag{2.62}$$

with the initial condition $\boldsymbol{L}(1) = 1$. In an analogous manner one may define a right boundary matrix $\boldsymbol{R}$. The scalar product $\langle\Phi[\{B^\dagger\}]\,|\,\Psi[\{A\}]\rangle$ is then given by $\langle\Phi[\{B^\dagger\}]\,|\,\Psi[\{A\}]\rangle = \operatorname{tr}\boldsymbol{L}(l+1)\boldsymbol{R}(l)$ which is independent of the site index l.

When dealing with uMPS $|\Psi[A]\rangle$ and $|\Phi[B]\rangle$, the above procedure is not useful because of the diverging number of lattice sites. The relevant quantity for the overlap here is the rank-4 transfer matrix T:

$$T_{B^\dagger}^A = \sum_\sigma \boldsymbol{B}^{\sigma\dagger} \otimes \boldsymbol{A}^\sigma \tag{2.63}$$

The scalar product is then the infinite power of this transfer matrix:

$$\langle\Phi[B^\dagger]\,|\,\Psi[A]\rangle = \lim_{N\to\infty} T^N, \tag{2.64}$$

so that the dominant eigenvalue of the transfer matrix determines the overlap. For properly normalized states, the dominant eigenvalue λ of T either has norm $|\lambda| = 1$ or $|\lambda| < 1$. In the first case the overlap is 1 and in the second case it is zero. This is actually an example of Anderson's orthogonality catastrophe [64], which states that in one dimension, two states are either orthogonal or equal in the thermodynamic limit.
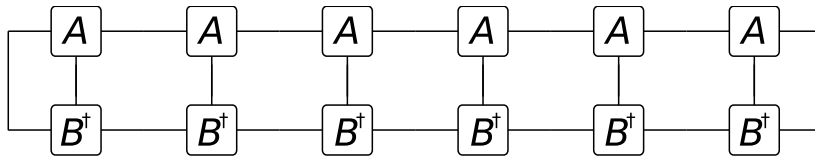

Figure 2.2: The overlap network of two MPS $|\Psi[\{A\}]\rangle$ and $|\Phi[\{B\}]\rangle$.

MPS-MPO expectation value

Another common task is to evaluate the expectation value of some operator O in a state described by a finite MPS $|\Psi[\{A\}]\rangle$. A slightly more general operation is to calculate the overlap matrix element with two different MPSs $|\Psi[\{A\}]\rangle$ and $|\Phi[\{B\}]\rangle$. Again this can be done by contracting the corresponding network from left to right (or from right to left). In this case, it is a similar network as depicted in Fig. 2.2 but with the MPO W-tensors included. And in a completely analogous manner, one defines boundary tensors for the left boundary at site l as:

$$\boldsymbol{L}_{b_l}(l+1) = \sum_{\sigma_l,\sigma_l',a_l} \boldsymbol{B}^{\sigma_l\dagger}(l)\boldsymbol{L}_{a_l}(l)\boldsymbol{A}^{\sigma_l'}(l)W_{a_lb_l}^{\sigma_l\sigma_l'}(l) \tag{2.65}$$

Here a_l and b_l are the left and right auxiliary spaces of the MPO W-tensors, respectively, and Eq. (2.65) has to be evaluated for each value of the index $b_l = a_{l+1}$. This formula is easier to understand in the graphical notation:

$$\tag{2.66}$$

The right boundary can be calculated by a similar formula and one obtains for the overlap matrix element:

$$\langle\Phi[\{B^\dagger\}]\,|\,O\,|\,\Psi[\{A\}]\rangle = \mathrm{tr}\sum_{b_l}\boldsymbol{L}_{b_l}(l+1)\boldsymbol{R}_{b_l}(l) \tag{2.67}$$

In the case of uMPSs, this is again a non-trivial task, since one has to be very careful with potentially diverging terms. Because of that, I want to focus only on expectation values of operators. For example the Hamilton operator H (the extensive operator for the total energy) will clearly have a diverging expectation value. Normally, one is only interested in the density of these expectation values $\langle h\rangle = \frac{1}{\mathbb{Z}}\langle H\rangle$ which is well defined in the thermodynamic limit. Let us first look at the particularly easy case where the operator O is a sum of local operators O_i. The density expectation value o is then the expectation of a local operator at an arbitrary site i. It is then most easily obtained in the *mixed gauge* representation of the state $|\Psi[A]\rangle$:

$$o = \mathrm{tr}\sum_{\sigma\sigma'}O_i^{\sigma\sigma'}\boldsymbol{A}_C^{\sigma\dagger}\boldsymbol{A}_C^{\sigma'} \tag{2.68}$$

This idea can be continued to cases where the operator consists of a sum of operators which only have support on a finite number of lattice sites. For example for a two-site Hamiltonian of

the form $H = \sum_i h_{i,i+1}$, one obtains for the energy density:

$$h = \text{tr} \sum_{\sigma_1\sigma_2\sigma_3\sigma_4} h_{i,i+1}^{\sigma_1\sigma_2\sigma_3\sigma_4} \boldsymbol{A}_C^{\sigma_1\dagger} \boldsymbol{A}_C^{\sigma_2} \boldsymbol{A}_R^{\sigma_3} \boldsymbol{A}_R^{\sigma_4\dagger} \tag{2.69}$$

For general operators, one needs to solve the fixed point equation of the transfer matrix $T_{A^\dagger}^A(W)$. However, as mentioned above, this will lead to a diverging expectation value, so that one has to substract a constant shift term at each step in the iterative solution of the fixed point equation to obtain a finite result. This procedure is described in Sec. 3.2.1 for the Hamiltonian represented as an MPO.

2.7.2 Variational algorithms

Variational algorithms are very typical for MPSs, stemming from the fact that MPSs constitute a very flexible variational ansatz for quite general optimization problems.

Optimization of the overlap

The first example is to find a state $|\Phi([\{B\}])\rangle$ which minimizes the distance to a given state $|\Psi[\{A\}]\rangle$:

$$\min_{\{B\}} \left\| |\Psi[\{A\}]\rangle - |\Phi[\{B\}]\rangle \right\|^2 \tag{2.70}$$

The site tensors in $|\Phi[\{B\}]\rangle$ should be obtained variationally by this condition. The global optimal truncation of an MPS $|\Psi[\{A\}]\rangle$ is an application of this algorithm when one chooses $|\Phi[\{B\}]\rangle$ to have a smaller bond dimension than $|\Psi[\{A\}]\rangle$.

In principle Eq. (2.70) fixes the B-tensors, but it is not easy to solve this minimization problem exactly, because of the non-quadratic dependence of the cost-function on the parameters. A standard procedure for MPS algorithms solves this issue. Transform the global optimization problem into a local one for only a single B-tensor at site p. Then solve this local optimization problem again and again at each site in the lattice while sweeping from site to site. To derive the equations for a local update is a rather simple task, since the cost-function depends quadratically on the single tensor $B(p)$ in this case. Hence a simple derivative leads to the equation:

$$\boldsymbol{B}_P^{\sigma_p}(p) = \boldsymbol{L}\boldsymbol{A}^{\sigma_p}(p)\boldsymbol{R}, \tag{2.71}$$

which is only valid if $|\Phi[\{B\}]\rangle$ is in the *mixed gauge* with the pivot site at site p (indicated by the subscript P in the above equation). $\boldsymbol{L}$ and $\boldsymbol{R}$ are the left and right boundaries of the overlap network between $|\Psi[\{A\}]\rangle$ and $|\Phi[\{B\}]\rangle$ as in Eq. (2.62). This equation has now to be solved multiple times for all lattice sites until convergence is reached. The convergence quality is easily obtained by the distance between both states as in Eq. (2.70). During the sweeping procedure (shifting of the pivot site), one has to make sure that the according boundary tensors are known. A more detailed description of the algorithm is available in Sec. 3.1.

This sweeping algorithm can not be performed when dealing with uMPSs in the thermodynamic limit. In this case, one has the same cost-function but both states depend only on a single

tensor:

$$\min_B \left\| |\Psi[A]\rangle - |\Phi[B]\rangle \right\|^2 \tag{2.72}$$

This equation looks rather similar to Eq. (2.37) and in fact it can be solved with the tangent space projector from Eq. (2.41). Here it is strictly necessary that the tangent space is parametrized properly to avoid any diverging terms. The optimal condition from Eq. (2.72) can be written with the tangent space projector:

$$\mathcal{P}_{|\Psi[A]\rangle} |\Phi[B]\rangle = 0 \tag{2.73}$$

From the precalculations for the projector (2.41) the solution follows readily and is given by the condition:

$$A'_P = B_L P', \tag{2.74}$$

where A'_P and P' are the results of the two different parts of the tangent space projector. Eq. (2.74) can be used to develop iterative methods for optimizing the overlap. See, e.g. Ref. [56].

CHAPTER 3

Variational matrix product states

In this section I want to present the algorithms for MPSs, which can be used to obtain a groundstate approximation for a given Hamilton operator H. In fact these algorithms are related to the ones presented in Sec. 2.7 but are treated in an extra section because of their outstanding importance. As a fundamental criterion for the optimization on uses the Ritz principle known from quantum mechanics.

The algorithms for finite MPSs are called density-matrix renormalization group (DMRG) methods because they are deeply related to the traditional DMRG algorithm without MPS [13, 46]. The DMRG methods are well established as a standard tool for the solution of strongly correlated one-dimensional quantum many-body systems. An extensive review is written by ULRICH SCHOLLWÖCK [14] for example. As already discussed for the optimization of the overlap for finite MPS, the key idea is to convert the global optimization problem into a local optimization problem for a small number of A-tensors instead of optimizing all A-tensors simultaneously. The method which is equivalent to the traditional DMRG algorithm is the *two-site* algorithm – called 2sDMRG – where at each step, two A-tensors are optimized. For hard problems, 2sDMRG is numerically too expensive, i.e. the algorithm can not be applied if the auxiliary bond dimension χ of the MPS is too high ($\chi \sim 10.000$). Instead the *single site* DMRG (1sDMRG) is numerically quite efficient so that tensors with bond dimension $\chi \sim 10.000 - 100.000$ (only with the use of symmetries) can be simulated. In this algorithm, only one A-tensor is optimized per step. This, however, has the disadvantage that the optimization procedure is likely to get stuck in a local minimum. To overcome this issue, several ideas were presented to add non-local information to the local optimization of a single A-tensor [65–67]. For the computations in this thesis, I only use the 1sDMRG algorithm which is presented in some detail in the Sec. 3.1.

The DMRG algorithms as described above work for a fixed system size L. Often, one is interested in the thermodynamic limit $L \to \infty$, which can then be obtained by a finite-size scaling analysis in $1/L$. Another possibility is to develop algorithms which work directly in the thermodynamic limit. These methods must work with translation-invariant states, namely uMPSs. However, the idea of optimizing a single tensor only while leaving the others untouched would immediately break the translational invariance. Still, already the traditional DMRG algorithm was used for infinite systems from the beginning, see [13]. Here, the idea is to grow the lattice at each iteration step by adding two sites in the center of the chain and then absorbing the two sites into the environment. With this procedure one always deals with an environment-site-site-environment configuration. For this configuration the two-site

DMRG algorithm can be applied with the same steps as for finite systems. At some point, the environments do not change anymore when additional sites are absorbed and a fixed point is reached. The reached state is believed to be the groundstate in the thermodynamic limit. The optimization procedure does not always work this way in the thermodynamic limit, but reaches the limit only when convergence is reached. The iDMRG algorithm can also be performed with MPSs using various optimizations [68].

Another method for infinite systems is the infinite time-evolving block decimation (iTEBD) in imaginary time [69, 70]. Here, the uMPS is time-evolved by a Trotter decomposition of the time-evolution operator in imaginary time to reach the groundstate. This algorithm works directly in the thermodynamic limit, but besides the bad convergence properties for imaginary-time propagation, it is also limited to Hamilton operators which can be Trotter-decomposed. Recent developments try to overcome these issues. For example in [71] the convergence speed is accelerated by recycling parts of the environment. In [72], an extension to long-range interactions is developed. But still, the additional Trotter error and the comparably slow convergence speed for the imaginary time evolution make this method suboptimal.

A third method was recently introduced by ZAUNER-STAUBER et al. [47]. In this approach, the minimization problem (the Ritz principle) is solved directly with global updates of the uMPS at each iteration. It is called variational uMPS (VUMPS) approach and is described in Sec. 3.2.

3.1 1sDMRG

The Ritz principle states that the ground state of a Hamiltonian minimizes the energy functional, which in terms of MPSs is given by:

$$E(\{A^\dagger\},\{A\}) = \frac{\langle \Psi[\{A^\dagger\}] \, | \, H \, | \, \Psi[\{A\}] \rangle}{\langle \Psi[\{A^\dagger\}] \, | \, \Psi[\{A\}] \rangle} \tag{3.1}$$

This minimization problem, however, turns out to be very complex since the energy expectation value depends a highly non-linear manner on all the A-tensors and hence on the parameters. The same problem was already addressed in the optimization of the overlap (see Sec. 2.7) and the same trick can be applied: Fix all A-tensors except the one at site p. Then the energy expectation value depends quadratically on $A(p)$ and a solution leads to a locally optimized tensor at site p. This, however, is by far not a global minimum and when using this procedure it is necessary to sweep through the lattice and optimize again and again each tensor at one site while keeping all others fixed. When convergence is reached, one has a good chance to be at the global minimum, however, this is not guaranteed and one could also get stuck somewhere in a local one. To derive the precise equations for the optimization step of a single tensor, one can rewrite Eq. (3.1) for the case of varying a single tensor only:

$$E(A^\dagger(p),A(p)) = \frac{\langle \Psi\left[A^\dagger(p)\right] \, | \, H \, | \, \Psi\left[A(p)\right] \rangle}{\langle \Psi\left[A^\dagger(p)\right] \, | \, \Psi\left[A(p)\right] \rangle} \tag{3.2}$$

The numerator and denominator of the minimization can be calculated efficiently with appropriate boundary tensors for the corresponding networks. For the numerator, one needs the

boundaries as in Eq. (2.65) to write:

$$\langle \Psi[A^\dagger(p)] \, | \, H \, | \, \Psi[A(p)] \rangle = \text{tr} \sum_{a_p,b_p} \sum_{\sigma_p,\sigma_p'} W^{\sigma_p \sigma_p'}(p)_{a_p b_p} \boldsymbol{L}_{a_p}(p) \boldsymbol{A}^{\sigma_p'}(p) \boldsymbol{R}_{b_p}(p) \boldsymbol{A}^{\dagger \sigma_p}(p) \tag{3.3}$$

For the denominator, one needs the boundaries as in Eq. (2.62):

$$\langle \Psi[A^\dagger(p)] \Psi[A(p)] \rangle = \text{tr} \sum_{\sigma_p} \boldsymbol{L}(p) \boldsymbol{A}^{\sigma_p}(p) \boldsymbol{R}(p) \boldsymbol{A}^{\dagger \sigma_p}(p) \tag{3.4}$$

This term simplifies even more in the *mixed gauge* representation with *pivot* site p, since one then has $\boldsymbol{L}(p) = \boldsymbol{R}(p) = \mathbb{1}$. For the minimization of the expression in Eq. (3.2) one has to take the derivative with respect to $A^\dagger(p)$ which corresponds to omitting $A^\dagger(p)$ in the above equations. Setting $\frac{\partial}{\partial A^\dagger(p)} \left(E(A^\dagger(p), A(p)) \right) = 0$, one obtains the equations for the local optimization of $A(p)$:

$$\sum_{a_p,b_p} \sum_{\sigma_p'} W^{\sigma_p \sigma_p'}(p)_{a_p b_p} \boldsymbol{L}_{a_p}(p) \boldsymbol{A}^{\sigma_p'}(p) \boldsymbol{R}_{b_p}(p) = E \boldsymbol{A}^{\sigma_p}(p) \tag{3.5}$$

which is in this form only valid if the MPS is in the *mixed gauge* representation with *pivot* site p. The visualization of Eq. (3.5) again facilitates the readability:

$$\tag{3.6}$$

Eq. (3.6) states that $A(p)$ is an eigenstate of an effective Hamilton operator H_{eff} with minimal energy. Hence it is an ordinary eigenvalue equation for the effective Hamilton operator H_{eff} and can be solved by Krylov-based methods since only the extremal eigenvalue is of importance. For these methods, the complexity is solely determined by the application of the effective Hamilton operator on a state. Eq. (3.5) shows that this can be done with a complexity $\mathcal{O}(d \cdot \chi^3 \cdot \chi_W)$ as long as the MPO matrices $\boldsymbol{W}^{\sigma \sigma'}$ are sparse.

This single update of a local tensor $A(p)$ must then be embedded in an algorithm which traverses through the lattice and optimizes one tensor after the next. Such an algorithm is presented in Alg. 1. The basic operations of this algorithm are:

1. LOCALUPDATE(p,L,R,H) : Local optimization of the tensor $A(p)$ as the groundstate of the effective Hamiltonian by a Krylov-based eigensolver. The effective Hamiltonian is build up from the environments L and R and the W-tensor at site p from the Hamiltonian H. The effective matrix-vector multiplication is computed by Eq. (3.5)

2. SWEEPSTEP($p,direction$): Shifting of the pivot site p to either $p + 1$ or $p - 1$ depending

---

Algorithm 1 1sDMRG algorithm

1: **procedure** GROUNDSTATE(Hamiltonian H,energyPrecision ϵ_E,statePrecision ϵ_S,fluctuations α_F)
2:     $|\Psi[\{A\}]\rangle$,L,R ← INITIALIZE()
3:     $direction$ ← $RIGHT$
4:     $halfsweepRange$ ← $\{1,\ldots,L\}$
5:     E_{old} ← 1000
6:     **while** $\Delta E > \epsilon_E$ and $\Delta S > \epsilon_S$ **do**
7:         **for** $p \in halfsweepRange$ **do**
8:             E_{curr},$A(p)$ ← LOCALUPDATE(p,L,R,H)   ▷ Eq. 3.5
9:             $|\Psi[\{A\}]\rangle$ ← ENRICH(p,$direction$,α_F)   ▷ Sec. 3.1.1
10:            $|\Psi[\{A\}]\rangle$ ← SWEEPSTEP(p,$direction$)   ▷ Sec. 2.7.1
11:            L,R ← UPDATEENVIRONMENT(p,$direction$)   ▷ Eq. 2.65
12:        $direction$ ← flip
13:        **if** $direction = LEFT$ **then**
14:            $halfsweepRange$ ← $\{L-1,\ldots 1\}$
15:        **else if** $direction = RIGHT$ **then**
16:            $halfsweepRange$ ← $\{2,\ldots L\}$
17:        ΔE ← $|E_{curr} - E_{old}|$
18:        ΔS ← STATEERROR($|\Psi[\{A\}]\rangle$,H)   ▷ Sec. 3.1.2
19:        E_{old} ← E_{curr}
20:    **return** E_{curr},$|\Psi[\{A\}]\rangle$

---

on the direction (Sec. 2.7.1)

3. UPDATEENVIRONMENT(p,$direction$): Update of the left or right boundary tensor depending on the direction (2.65). The other boundary can be reused since one part of the network does not change through SWEEPSTEP(p,$direction$)

A suitable initial configuration is an MPS with random A-tensors in the *mixed-gauge* representation, so that the pivot site is at one of the edges of the one-dimensional lattice (either $p = 1$ or $p = L$). Additionally, the boundary tensors $L(l)$ and $R(l)$ should be precalculated for each site so that for each boundary the pivot site matches the given l. A corresponding routine INITIALIZE() should be available.

The algorithm Alg. 1 is complete in the sense that it can be used to solve simple systems. Two subtleties are however necessary for a faster convergence and an accurate error estimation. Since each optimization step involves only a single A-tensor, the algorithm is likely to get stuck in a local minimum. This problem can be circumvented with an ENRICH()-function (line 9 in Alg. 1) and will be discussed in the next subsection while the error estimation (essentially the STATEERROR()-function in line 18 in Alg. 1) is discussed afterwards.

3.1.1 Fluctuations and subspace expansion

The 1sDMRG algorithm is numerically quite efficient, since the Krylov based eigensolver can operate in an effective Hilbert space of moderate size. This stems from the fact that only

the parameters of a single A-tensor enter the optimization procedure. On the other hand, the variational space for a single optimization is rather small, so that the algorithm might be stuck in a local minimum. Additionally, the algorithm works at fixed bond dimensions $\{\chi_l\}_{l=1,\dots,L}$ and is not able to enlarge them dynamically. Both problems are of particular importance if symmetries are encoded in the algorithm, since the correct bond dimensions in the different symmetry blocks are not known in advance. In the past, several expansion schemes were developed which address both problems by mixing non-local information into the optimization problem. The non-local information is often called *fluctuations* and controlled in magnitude by an additional parameter α_F. At the beginning, density-matrix fluctuations were suggested already for the traditional DMRG method [65]. In the MPS form, the whole algorithm can be built up without constructing the reduced density-matrix at any time so that density-matrix fluctuations are not ideal because the reduced density-matrix would need to be computed. This can be an expensive calculation for challenging problems requiring a very high bond dimension χ. Therefore a better way is to expand the A-tensors in the MPS directly and introduce subspace expansion schemes [66]. A quite efficient expansion scheme was recently suggested in Ref. [67].

Let us start by defining what a subspace expansion looks like. Consider a tensor P with dimensions $\chi_{i-1} \times d \times \tilde{\chi}$, then the expanded form of the $\chi_{i-1} \times d \times \chi_i$ $A(i)$-tensor is:

$$\boldsymbol{A}^\sigma(i) \to \tilde{\boldsymbol{A}}^\sigma(i) = \boldsymbol{A}^\sigma(i) \oplus_{\mathrm{col}} \boldsymbol{P}^\sigma \tag{3.7}$$

The sign $\oplus_{\mathrm{col}}$ is meant to indicate that the direct sum is only for the column spaces, since the row spaces of the matrices are equal. The expanded tensor $\tilde{A}(i)$ therefore has dimensions $\chi_{i-1} \times d \times (\chi_i + \tilde{\chi})$. To not destroy the matrix multiplications in the state $|\Psi[\{A\}]\rangle$, one needs to resize the row-space of $A(i+1)$ accordingly. To achieve this, one adds a properly resized zero-matrix:

$$\boldsymbol{A}^\sigma(i+1) \to \tilde{\boldsymbol{A}}^\sigma(i+1) = \boldsymbol{A}^\sigma(i+1) \oplus_{\mathrm{row}} \boldsymbol{0}^\sigma \tag{3.8}$$

This expansion would destroy any normalization of the A-tensor, but this can be restored by the sweeping procedure. The central question then is how to choose the P-tensor. A randomly chosen tensor would expand the A-tensors but would also kick the algorithm away from the optimum. Ideally, the P-tensor expands the A-tensor and simultaneously pushes the state into the direction of the minimum. In Ref. [66], it was proven that the current residual $(H - E)|\Psi[\{A\}]\rangle$ fulfills these requirements. However, this is a numerically quite expensive quantity, since it involves the global substraction of two MPS. The proposition in Ref. [67] is:

$$P^\sigma_{\chi_{i-1}(a_i\chi_i)} = \alpha_F \sum_{a_{i-1},\chi'_{i-1}} \sum_{\sigma'} W^{\sigma\sigma'}_{a_{i-1}a_i} L^{a_{i-1}}_{\chi_{i-1}\chi'_{i-1}} A^{\sigma'}_{\chi'_{i-1}\chi^i} \tag{3.9}$$

This expansion works suprisingly well in a lot of applications, but it can not be proven rigorously that it provides suitable fluctuations. Certain is that fluctuations will not destroy an exactly converged state, since in this case all fluctuations will immediately disappear. The description above describes the expansion during the optimization from left to right (*direction = RIGHT* in Alg. 1). The procedure for the other direction follows readily. The control parameter α_F

can be chosen relatively large ($\alpha \sim 10 - 100$) as long as the exact groundstate can be reached with the available resources. Otherwise, the magnitude for the fluctuations needs to be scaled down to zero during the algorithm to reach a converged state for a given bond dimension χ. A scheme for the adjustment of α_F is given in Ref. [67].

3.1.2 Error estimations

For any algorithm which converges to the final result after multiple iteration steps, a reliable error estimation is necessary to evaluate the current accuracy of the result and to define adequate stopping criteria. An obvious criterion for Alg. 1 is the absolute difference between the variational energies at subsequent iteration steps. As discussed in the previous section (Sec. 3.1.1), the whole algorithm is not guaranteed to reach the global minimum. Furthermore, this stopping criterion is not able to distinguish between a local or a global minimum. For such an estimation, one needs a criterion for the whole state and not only for the energy. The simplest error estimation for the state is the overlap between the MPSs from adjacent iteration steps. This, however, would also vanish at a local minimum. A more involved measure also checks the quality of the state to be an eigenstate of the Hamiltonian by computing the energy variance $\Delta E = \langle H^2 \rangle - \langle H \rangle^2$. This measure provides a reliable stopping criterion since it will not be small if the algorithm is stuck somewhere in the variational landscape. However, it needs the computation of $\langle H^2 \rangle$ which is quite expensive; in particular when the auxiliary bond dimension χ_W of the MPO is large, e.g. for two-dimensional systems or long-range interactions. An approximation for the variance was recently suggested by C. HUBIG et al. [73] which is computationally feasible also in these cases. Although this method is not as reliable as the full variance, it is substantially better than the overlap and can be used for extrapolations [73]. It is also the preferred error estimation used for the computations in this thesis so I will present the essential ideas of the approximation.

The energy variance ΔE can be obtained as the squared norm of the residual $|\Phi\rangle = (H - E) |\Psi\rangle$:

$$\Delta E = \langle \Psi | H^2 | \Psi \rangle - \langle \Psi | H | \Psi \rangle^2 = \langle \Psi | (H - E)(H - E) | \Psi \rangle = \langle \Phi | \Phi \rangle \tag{3.10}$$

The idea is now to project this expression on the subspace of two-site variations of $|\Psi\rangle$ if $|\Psi\rangle = |\Psi[\{A\}]\rangle$ is the groundstate candidate from a 1sDMRG computation.

$$\Delta E_{2s} = \langle \Psi | (H - E)(\mathcal{P}_0 + \mathcal{P}_1 + \mathcal{P}_2)(H - E) | \Psi \rangle \tag{3.11}$$

The subspace of zero-site variations described by the projector $\mathcal{P}_0$ consists of multiples of $|\Psi[\{A\}]\rangle$, the subspace of single-site variations described by the projector $\mathcal{P}_1$ lies in the tangent space of the MPS manifold at the point $|\Psi[\{A\}]\rangle$ and the subspace of two-site variations described by the projector $\mathcal{P}_2$ lies formally in the double tangent space of the MPS manifold at the point $|\Psi[\{A\}]\rangle$. The projection of the full variance onto $\mathcal{P}_0$ vanishes per definition of E. The projection onto $\mathcal{P}_1$ vanishes at the variational optimum and can be added to the error measure to signal an insufficient number of iterations as well. The projection onto $\mathcal{P}_2$ then is a measure for the more global deviation from an eigenstate. The tangent elements forming $\mathcal{P}_1$ can be constructed similarly to the derivation of tangent elements for uMPS in the thermodynamic limit. Again, the nullspace N of the A-tensor is a significant quantity. A state in $\mathcal{P}_1$ can then

be written as:

$$|\Phi_i[\boldsymbol{X}_i,\{A\}]\rangle = \sum_{\boldsymbol{\sigma}} \boldsymbol{A}_L^{\sigma_1}(1)\cdots\boldsymbol{A}_L^{\sigma_{i-1}}(i-1)\boldsymbol{N}_L^{\sigma_i}(i)\boldsymbol{X}_i\boldsymbol{A}_R^{\sigma_{i+1}}(i+1)\cdots\boldsymbol{A}_R^{\sigma_L}(L)\,|\boldsymbol{\sigma}\rangle \qquad (3.12)$$

Here the tangent space is already properly parametrized by a $(d-1)\chi_i \times \chi_i$ matrix $\boldsymbol{X}_i$. The projector $\mathcal{P}_1$ can then be built from these states:

$$\mathcal{P}_1 = \sum_{i=1}^{L} |\Phi_i[\boldsymbol{X}_i,\{A\}]\rangle\,\langle\Phi_i[\boldsymbol{X}_i,\{A\}]| \qquad (3.13)$$

Similarly, the double tangent-space states span the projector $\mathcal{P}_2$:

$$\mathcal{P}_2 = \sum_{i=1}^{L-1} |\Xi_i[\boldsymbol{Y}_i,\{A\}]\rangle\,\langle\Xi_i[\boldsymbol{Y}_i,\{A\}]|\,, \qquad (3.14)$$

where each state is parametrized by a $(d-1)\chi_i \times (d-1)\chi_i$-matrix $\boldsymbol{Y}_i$ and defined as:

$$|\Xi_i[\boldsymbol{Y}_i,\{A\}]\rangle = \sum_{\boldsymbol{\sigma}} \boldsymbol{A}_L^{\sigma_1}(1)\cdots\boldsymbol{A}_L^{\sigma_{i-1}}(i-1)\boldsymbol{N}_L^{\sigma_i}(i)\boldsymbol{Y}_i\boldsymbol{N}_R^{\sigma_{i+1}}(i+1)\boldsymbol{A}_R^{\sigma_{i+2}}(i+2)\cdots\boldsymbol{A}_R^{\sigma_L}(L)\,|\boldsymbol{\sigma}\rangle \quad (3.15)$$

With these expressions, one can work out Eq. (3.11) and obtains explicit formulas for evaluating the approximated variance. These are presented in Ref. [73]. For a Hamiltonian which contains only nearest-neighbor terms, the approximation becomes exact. However, in this case, the full variance is usually also available. In the case of longer-ranged interactions, the approximation is not identical to the exact variance but still provides a non-local error measure which does not vanish at a local minimum.

3.2 VUMPS

Again, the starting point is the Ritz functional, in this case for uMPSs parametrized by a single A-tensor:

$$E(A^\dagger,A) = \frac{\langle\Psi[A^\dagger]\,|\,H\,|\,\Psi[A]\rangle}{\langle\Psi[A^\dagger]\,|\,\Psi[A]\rangle} \qquad (3.16)$$

However, the same idea as for the finite-system DMRG – dividing the global problem into a bunch of local problems – does not apply because there would be an infinite number of local problems and also the translational invariance would be destroyed immediately. Here, one rather has to tackle Eq. (3.16) directly. The derivative with respect to $A^\dagger$ leads to the optimization condition:

$$\left\langle \frac{\partial}{\partial A^\dagger}\Psi[A^\dagger] \,\middle|\, (H-E) \,\middle|\, \Psi[A] \right\rangle = 0 \qquad (3.17)$$

In Sec. 2.4, the states $\left\langle\frac{\partial}{\partial A^\dagger}\Psi[A^\dagger]\right|$ were identified with the tangent space of the MPS manifold $TM_{\langle\Psi[A^\dagger]|}$ so that there is a natural geometric interpretation of Eq. (3.17): The residual $(H-E)|\Psi[A]\rangle$ – which may do not vanish in the variational space exactly – should be
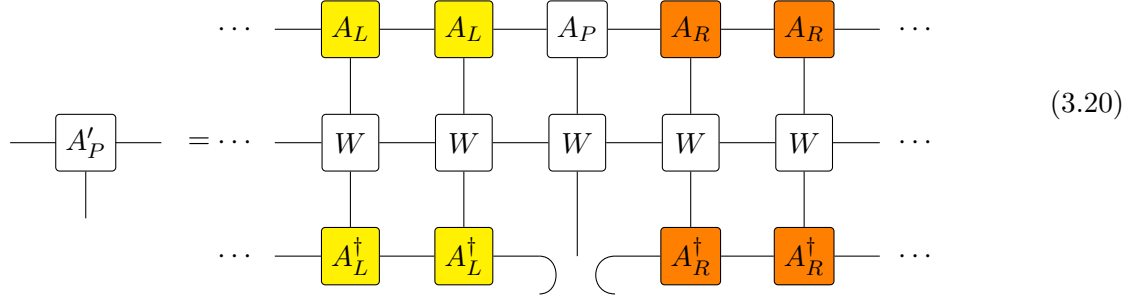
orthogonal to the tangent space at the point $|\Psi[A]\rangle$. Hence, one can use the tangent space projector $\mathcal{P}_{|\Psi[A]\rangle}$ (2.41 or 2.42) to rewrite Eq. (3.17):

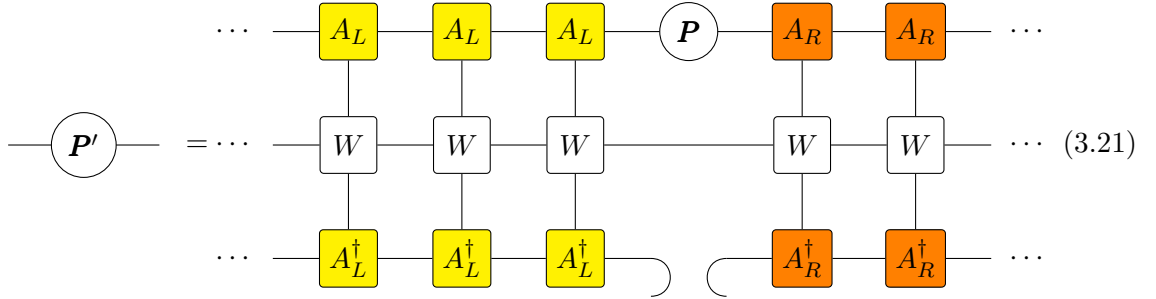$$\mathcal{P}_{|\Psi[A]\rangle}(H - E)|\Psi[A]\rangle = 0 \tag{3.18}$$

Note that the projector $\mathcal{P}_{|\Psi[A]\rangle}$ was constructed to project on the part of the tangent space orthogonal to $|\Psi[A]\rangle$. This is useful here because Eq. (3.18) is trivial for the MPS direction itself. The non-trivial part of Eq. (3.18) is hence the projection of the state $|\Phi\rangle = H|\Psi\rangle$. The action of the projector $\mathcal{P}_{|\Psi[A]\rangle}$ gives a tangent vector described by a tensor B which results in:

$$\boldsymbol{B}^\sigma = \boldsymbol{A}_P'^\sigma - \boldsymbol{A}_L^\sigma \boldsymbol{P}' \tag{3.19}$$

Here A_P' and $\boldsymbol{P}'$ are the actions of the two parts of $\mathcal{P}_{|\Psi[A]\rangle}$ onto A_P and $\boldsymbol{P}$, the pivot tensor and the center matrix of $|\Psi[A]\rangle$ in the *mixed gauge* representation, respectively:

$$\tag{3.20}$$

$$\tag{3.21}$$

With appropriately defined effective Hamiltonians, one can write the following equations:

$$A_P' = H_{A_P}^{\mathrm{eff}} A_P \tag{3.22}$$

$$\boldsymbol{P}' = H_{\boldsymbol{P}}^{\mathrm{eff}} \boldsymbol{P} \tag{3.23}$$

The form of the effective Hamiltonians follows directly from the expressions in Eq. (3.20) and (3.21). Note that they involve infinite contractions. The details are discussed in Sec. 3.2.1. The variational optimum is reached if $B = 0$ due to Eq. (3.18). This leads to the following condition:

$$\boldsymbol{A}_P'^\sigma = \boldsymbol{A}_L^\sigma \boldsymbol{P}' \tag{3.24}$$

By a gauge transformation for tangent vectors ($\boldsymbol{X} = \boldsymbol{P}'$, Eq. (2.34)), an equivalent condition reads as:

$$\boldsymbol{A}_P'^\sigma = \boldsymbol{P}' \boldsymbol{A}_R^\sigma \tag{3.25}$$

As an additional condition, one has the consistency equation (2.24) for the *mixed gauge* representation of the uMPS:

$$\boldsymbol{A}_P^\sigma = \boldsymbol{P} \boldsymbol{A}_R^\sigma = \boldsymbol{A}_L^\sigma \boldsymbol{P} \tag{3.26}$$

If both are fulfilled, $\boldsymbol{P}$ and $\boldsymbol{P}'$ have to be proportional so that Eq. (3.23) turns into an eigenvalue equation. This then transfers directly to A_P so that Eq. (3.22) is the second eigenvalue equation which enters the optimization procedure:

$$A_P' = H_{A_P}^{\text{eff}} A_P = E_{A_P} A_P \tag{3.27}$$

$$\boldsymbol{P}' = H_{\boldsymbol{P}}^{\text{eff}} \boldsymbol{P} = E_{\boldsymbol{P}} \boldsymbol{P} \tag{3.28}$$

Both E_{A_P} and $E_{\boldsymbol{P}}$ are proportional to the energy E, so that Eq. (3.27) and Eq. (3.28) are eigenvalue equations for the groundstate of the corresponding effective Hamiltonian and can be solved by Krylov-based methods. Due to the proportionality, E_{A_P} and $E_{\boldsymbol{P}}$ contain a divergent contribution, because the energy E is an extensive quantity. But by substracting the current energy expectation value, these divergent parts can be avoided. Note that the tensor B is finite even without subtracting the energy expectation value because it involves the difference between E_{A_P} and $E_{\boldsymbol{P}}$, which is finite in the thermodynamic limit. To summarize, Eq. (3.24), (3.25) and (3.26) are simultaneous conditions for an optimal uMPS – optimal in the sense that the uMPS minimizes the Ritz functional on the manifold of uMPS.

Algorithm 2 VUMPS algorithm

1: **procedure** GROUNDSTATE(Hamiltonian H,energyPrecision ϵ_E, variationalPrecision ϵ_V)
2:      $|\Psi[A_L,A_R,A_P,\boldsymbol{P}]\rangle \leftarrow$ INITIALIZE()
3:      $E_{old} \leftarrow 1000$
4:      **while** $\Delta E > \epsilon_E$ and $\epsilon > \epsilon_V$ **do**
5:          $H_{A_P}, H_{\boldsymbol{P}} \leftarrow$ CALCHEFF(A_L,A_R)   ▷ see Sec. 3.2.1
6:          $E_{A_P}, A_P' \leftarrow$ KRYLOVSOLVER(H_{A_P})
7:          $E_{\boldsymbol{P}}, \boldsymbol{P}' \leftarrow$ KRYLOVSOLVER($H_{\boldsymbol{P}}$)
8:          $A_L', A_R' \leftarrow$ POLARDECOMPOSE($A_p', \boldsymbol{P}'$)   ▷ see Sec. 3.2.2
9:          $\epsilon \leftarrow$ CALCERROR()   ▷ evaluate norm of tensor B (3.19)
10:         $A_L, A_R, A_P, \boldsymbol{P} \leftarrow A_L', A_R', A_P', \boldsymbol{P}'$
11:         $E_{curr} \leftarrow$ EXTRACTENERGY()   ▷ see Sec. 3.2.1
12:         $\Delta E \leftarrow |E_{curr} - E_{old}|$
13:         $E_{old} \leftarrow E_{curr}$
14:      **return** $E_{curr}, |\Psi[A_L,A_R,A_P,\boldsymbol{P}]\rangle$

To reach this optimum, an iterative algorithm – the VUMPS algorithm – is suggested in Ref. [47] which is presented in Alg. 2. The functions CALCHEFF() and POLARDECOMPOSE() are elaborated on some more detail in Sec. 3.2.1 and Sec. 3.2.2.

The measure of convergence (line 9 in Alg. 2) determines the variational quality of the state. If it is zero, the state is definitely the best variational state at bond dimension χ. However, this measure gives no global information as compared to the energy variance, for example. It is possible to compute the same approximation for the variance as in Sec. 3.1.2 (the *two-site* variance) also for the uMPS in the thermodynamic limit to get a global error measure. Note however, that the VUMPS algorithm works with global updates for the state, so that it is less likely to get stuck in a local minimum. But even if this were the case, the variational error measure would not be small. Nevertheless, the *two-site* variance also signals insufficient bond dimensions in the uMPS which can not be recognized with the other error measures.

The VUMPS algorithm is a single-site algorithm and therefore works at a fixed bond dimension χ. It is likely that the global state updates prevent the algorithm from remaining in a meta stable state without any fluctuations which are required for the finite size algorithm (Alg. 1). However, if the Schmidt spectrum contains degeneracies, it is important to keep all states in a multiplet. Otherwise, the convergence speed is highly suppressed. In Ref. [47], it was said that the convergence speed is only negatively influenced. In my personal experience, however, I found that in some cases, convergence is never reached at least for complicated problems. Fluctuations can then help to get closed multiplets in the Schmidt spectrum of the state. The fluctuations become absolutely necessary if symmetries are exploited, because otherwise it is impossible to find the relevant symmetry blocks for the uMPS. An efficient expansion scheme for the uMPS was already developed in [47] (see Appendix B therein). It works similarly to the scheme in 3.1.1, but the expansion tensor P is different.

3.2.1 Effective Hamiltonians

The effective Hamiltonians in Eq. (3.20) and (3.21) are determined by the tangent space projector $\mathcal{P}_{|\Psi[A_L, A_R, A_P, \boldsymbol{P}]\rangle}$ from Eq. (2.42). Their concrete evaluation, however, is not trivial since it involves infinite contractions. As the basic building block for these contractions, one has the MPO transfer matrix $T_W^{L,R}$, i.e. with the Hamiltonian (represented by an MPO) included:

$$(T_W^{L,R})_{ab} = \sum_{\sigma, \sigma'} W_{ab}^{\sigma\sigma'} \boldsymbol{A}_{L,R}^{\dagger\sigma} \otimes \boldsymbol{A}_{L,R}^{\sigma'} \tag{3.29}$$

To perform the relevant contractions, one has to find the left (L) and right (R) fixed point of $T^{L,R}$. However, it will turn out that $T^{L,R}$ has no fixed points and L and R are only quasi-fixed points. A general analysis of fixed points of triangular MPOs is done in Ref. [63]. Let us concentrate on the right fixed point, an analogous procedure will also work for the other one. The fixed point equation can be written as:

$$\boldsymbol{R}_a = \sum_b (T_W^R)_{ab} \boldsymbol{R}_b = (T_W^R)_{aa} \boldsymbol{R}_a + \sum_{b<a} (T_W^R)_{ab} \boldsymbol{R}_b := (T_W^R)_{aa} \boldsymbol{R}_a + \boldsymbol{\Lambda}_a \tag{3.30}$$

or in the graphical language as:

$$
\begin{array}{c}
\boxed{A_R} \\[4pt]
\boxed{W} \quad \boxed{R} \quad = \quad \boxed{R} \\[4pt]
\boxed{A_R^\dagger}
\end{array}
\tag{3.31}
$$

Note here that firstly, the transfer matrix $(T_W^R)_{ab}$ is a rank-4 object and hence a super-operator acting on the space of $\chi \times \chi$-matrices. Secondly, the decomposition into the term $b = a$ and $b \neq a$ can be restricted to the case $b < a$ since the $\boldsymbol{W}^{\sigma\sigma'}$-matrices are of lower triangular form. And thirdly, I have defined a partial contraction Λ for the terms with $b < a$. The idea then is that $\boldsymbol{\Lambda}_a$ contains only values from the transfer matrix for $b < a$ so that an iterative solution of Eq. (3.30) is possible, starting with $a = 1$. For $a = 1$, the equation is trivial, since $W_{11}^{\sigma\sigma'} = \delta_{\sigma\sigma'}$ and therefore $(T_W^R)_{aa} = \sum_\sigma \boldsymbol{A}_R^{\dagger\sigma} \otimes \boldsymbol{A}_R^\sigma$, so that the solution is $\boldsymbol{R}_1 = \mathbb{1}$. For $a > 1$, the solution is simple if $(T_W^R)_{aa} = 0$ ($W_{aa}^{\sigma\sigma'} = 0$), because then one can just set $\boldsymbol{R}_a = \boldsymbol{\Lambda}_a$. Note that for short-ranged Hamiltonians, one always has $W_{aa}^{\sigma\sigma'} = 0$ for $1 < a < \chi_W$, while the edge elements ($a = 1$ or $a = \chi_W$) are the identity operators in the physical space. For quasi-long-range interactions, other diagonal elements may also be proportional to the identity, but with a prefactor with magnitude strictly smaller than one. Ignoring this case, one can set all entries of the fixed point by the simple identification with $\boldsymbol{\Lambda}_a$ beside of the last element $a = \chi_W$. In this case Eq. (3.30) reads:

$$
\boldsymbol{R}_{\chi_W} = T^R \boldsymbol{R}_{\chi_W} + \boldsymbol{\Lambda}_{\chi_W}
\tag{3.32}
$$

Here, the MPO transfer matrix T_W^R is already substituted by the MPS transfer matrix T^R, because the operator acts as the identity. Eq. (3.32) can be rewritten:

$$
(\mathbb{1} - T^R)\boldsymbol{R}_{\chi_W} = \boldsymbol{\Lambda}_{\chi_W},
\tag{3.33}
$$

with $\mathbb{1}$ being an identity super-operator. To solve this equation for $\boldsymbol{R}_{\chi_W}$, one needs the inverse of $(\mathbb{1} - T^R)$. However, this inverse is not defined because the transfer matrix T^R has an eigenvalue $\lambda = 1$. The inverse of $(\mathbb{1} - T^R)$ can only be taken for the subspace orthogonal to the dominant eigenvector (the eigenvector to $\lambda = 1$), while the operator projected on the eigenspace of the dominant eigenvector needs to be discarded, since it has no inverse. Note that per definition of T^R, the right eigenvector belonging to $\lambda = 1$ is the $\chi \times \chi$ identity matrix. The projector onto the eigenspace of $\lambda = 1$ is readily computed as $\mathcal{P} = \mathbb{1}_{\chi\times\chi} \otimes \boldsymbol{l}$, where $\boldsymbol{l}$ is the left fixed point of T^R ($\mathbb{1}$ is the right fixed point). With this in hand, one can compute the projection $(\mathbb{1} - T^R)$ onto the complementary subspace $\mathcal{Q} = 1 - \mathcal{P}$:

$$
(\mathbb{1} - \mathcal{Q}T^R\mathcal{Q}) = \mathbb{1} - T^R + \mathcal{P} = \mathbb{1} - T^R + \mathbb{1}_{\chi\times\chi} \otimes \boldsymbol{l},
\tag{3.34}
$$

which can be inverted to give an equation for the quasi fixed point:

$$\boldsymbol{R}_{\chi W} = \left(\mathbb{1} - T^R + \mathbb{1}_{\chi \times \chi} \otimes \boldsymbol{l}\right)^{-1} \left(\boldsymbol{\Lambda}_{\chi W} - \mathbb{1}_{\chi \times \chi} \operatorname{tr}(\boldsymbol{l}\boldsymbol{\Lambda}_{\chi W})\right) \tag{3.35}$$
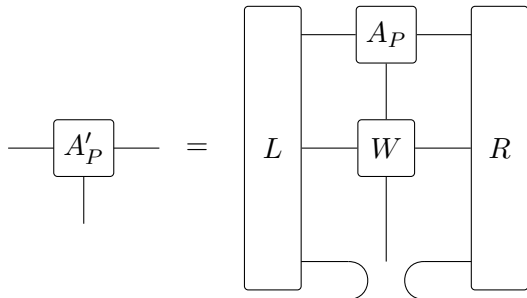
Here, also the right hand side of Eq. (3.33) is projected with $\mathcal{Q}$. The inverse $\left(\mathbb{1} - T^R + \mathbb{1}_{\chi \times \chi} \otimes \boldsymbol{l}\right)^{-1}$ is often called the pseudo-inverse of $(\mathbb{1} - T^R)$. It does not need to be computed directly but Eq. (3.35) can be solved as a system of linear equations of the form $\boldsymbol{A}x = y$, where $y = \boldsymbol{\Lambda}_{\chi W} - \mathbb{1}_{\chi \times \chi} \operatorname{tr}(\boldsymbol{l}\boldsymbol{\Lambda}_{\chi W})$ and $\boldsymbol{A}$ is the regularized operator from Eq. (3.34). For this task, standard routines can be used, e.g. the GEMRES algorithm.

As mentioned above, this solution discards the part in the eigenspace of the eigenvalue $\lambda = 1$ and it is of particular importance to figure out what exactly is discarded. The discarded part of T^R is $\mathcal{P}T^R = \mathcal{P} = \mathbb{1}_{\chi \times \chi} \otimes \boldsymbol{l}$ so that the fixed point equation (3.30) only holds up to an additive constant for $a = \chi_W$:

$$\sum_b (T_R^W)_{\chi W b} \boldsymbol{R}_b = T_R \boldsymbol{R}_{\chi W} + \boldsymbol{\Lambda}_{\chi W} = \boldsymbol{R}_{\chi W} + \mathbb{1}_{\chi \times \chi} \operatorname{tr}(\boldsymbol{l}\boldsymbol{\Lambda}_{\chi W}) \neq \boldsymbol{R}_{\chi W} \tag{3.36}$$
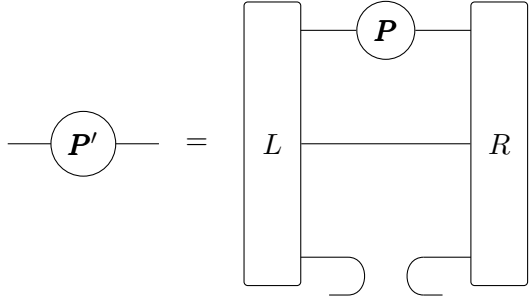
This constant would only shift the diagonal elements of $\boldsymbol{R}_{\chi W}$. Hence when using the quasi-fixed point R, one discards the term $\operatorname{tr}\boldsymbol{l}\boldsymbol{\Lambda}_{\chi W}$. This term turns out to be identical to the energy density e [63], so that discarding it corresponds only to a shift in the energy which does not change the eigenstates of the Hamiltonian. On the contrary, the discard of the energy density for each application of the MPO transfer matrix ensures that the eigenvalue equations (3.27) and (3.28) have finite eigenvalues. Hence it allows a numerical computation of these equations.

After the computation of the quasi-fixed points L and R, the effective Hamiltonians H_{A_P} and $H_{\boldsymbol{P}}$ take a simple form. Note that the effective Hamiltonians do not need to be calculated explicitly, but only the action on a corresponding state. For H_{A_P} this action corresponds exactly to Eq. (3.5), which can also be translated into the graphical notation:

$$\tag{3.37}$$

The action of $H_{\boldsymbol{P}}$ is similar and reads as:

(3.38)

or in the formula notation:

$$H_{\boldsymbol{P}}\boldsymbol{P} = \boldsymbol{P}' = \sum_{a=1}^{\chi_W} \boldsymbol{L}_a \boldsymbol{P} \boldsymbol{R}_a \tag{3.39}$$

With these considerations at hand, it is possible to obtain the action of the effective Hamiltonians when the environments L and R are precalculated with a function CALCHEFF() (line 5 in Alg. 2). Notice that also the energy expectation value can be extracted (line 11 in Alg. 2) from the above computations, namely as $e = \operatorname{tr} \boldsymbol{l} \boldsymbol{\Lambda}_{\chi_W}$ or from the part for the left fixed point as $e = \operatorname{tr} \tilde{\boldsymbol{\Lambda}}_1 \boldsymbol{r}$.

3.2.2 Obtaining A_L, A_R from A_P and $\boldsymbol{P}$

To complete the necessary steps for the VUMPS algorithm (Alg. 2), one needs to update the whole state after the eigensolver update of the current A_P and $\boldsymbol{P}$. Again it is mandatory to perform a global update, since local updates would destroy the translational symmetry. To perform this, one can use the consistency equations for the uMPS (3.26) to obtain the optimal A_L and A_R for given A_P and $\boldsymbol{P}$:

$$\min_{A_L} \left\| \sum_\sigma \boldsymbol{A}_P^\sigma - \boldsymbol{P}\boldsymbol{A}_L^\sigma \right\| \tag{3.40}$$

$$\min_{A_R} \left\| \sum_\sigma \boldsymbol{A}_P^\sigma - \boldsymbol{A}_R^\sigma \boldsymbol{P} \right\| \tag{3.41}$$

This minimization problem can be solved exactly without using an iterative procedure. The solution requires an SVD (Chap. A) of the properly reshaped tensors X and Y defined as $\boldsymbol{X}^\sigma = \boldsymbol{A}_P^\sigma \boldsymbol{P}^\dagger$ and $\boldsymbol{Y}^\sigma = \boldsymbol{P}^\dagger \boldsymbol{A}_P^\sigma$:

$$\tilde{X}_{(i,\sigma)j} = X_{ij}^\sigma = \sum_k U_{(i\sigma)k}^{(X)} \Sigma_{kk}^{(X)} V_{kj}^{\dagger(X)} \tag{3.42}$$

$$\tilde{Y}_{i(j,\sigma)} = Y_{ij}^\sigma = \sum_k U_{ik}^{(Y)} \Sigma_{kk}^{(Y)} V_{k(j,\sigma)}^{\dagger(Y)} \tag{3.43}$$

The isometries ($\boldsymbol{U}^{(X)}$ and $\boldsymbol{V}^{\dagger(X)}$) of the decomposition from X constitute the tensor A_L, while the isometries of Y constitute the tensor A_R:

$$A_{L(ij)}^\sigma = \sum_k U_{(i\sigma)k}^{(X)} V_{kj}^{\dagger(X)} \tag{3.44}$$

$$A_{R(ij)}^\sigma = \sum_k U_{ik}^{(Y)} V_{k(j,\sigma)}^{\dagger(Y)} \tag{3.45}$$

In Ref. [47], it is mentioned that this computation of A_L and A_R is numerically unstable, because of small singular values in the SVD, at least close to the variational optimum. Hence, they also suggested a different method which sets A_L and A_R only approximately, but with a numerically stable algorithm (see Sec. II C in Ref. [47]).

CHAPTER 4

Symmetric matrix product states

So far, matrix product states have turned out to be a flexible variational ansatz for the ground state of one-dimensional Hamiltonians both in finite and infinite systems. In this chapter, I will present how to improve the efficiency of the presented algorithms (Chap. 3 or Sec. 2.7) significantly. The incorporation of Abelian and non-Abelian symmetries leads to a substantial gain in both accuracy and computational speed. While Abelian symmetries was included to the algorithms from the beginning on [13], the use of non-Abelian symmetries was introduced about 10 years later by pioneering work from [74] for the traditional DMRG. The construction of symmetric MPS followed closely and now there exists several different construction schemes [75–78].

This chapter is organized as follows: in Sec. 4.1, I will introduce several concepts of group theory on a fundamental level. A special focus is on the Lie group $SU(2)$ for which I derive the representation theory and Clebsch-Gordan expansion in some detail. In Sec. 4.2, I will discuss the general role of symmetries for physical systems and discuss afterwards in Sec. 4.3, 4.4 and 4.5 the construction of symmetric MPSs, symmetric MPOs and symmetric algorithms, respectively.

4.1 Group theory

Group theory is one of the major topics in mathematics with impacts for several other fields. The relevant part for this thesis is the representation theory of groups. I will start, by giving the basic definitions (Subsec. 4.1.1) on a fundamental level. Afterwards, I will present the representation theory for general compact Lie groups in Subsec. 4.1.2 and give a particular example for the compact Lie group $SU(2)$ (4.1.3). Furthermore, I will develop the Clebsch-Gordan expansion for this group and also introduce the recoupling coefficients for $SU(2)$ in Subsec. 4.1.4. Finally, I will introduce tensor operators and their couplings in Subsec. 4.1.5.

4.1.1 Basic definitions

In this section, I will review the properties and definitions of groups which are necessary for the following chapters. It is not a complete introduction to group theory and the content is contained in various text books. See for example Ref. [79] or Ref. [80].

Definition 4.1. A group $(G,\circ)$ is a set G of elements g together with a group operation $\circ : G \times G \to G$ with the following properties:

1. For all $g,h \in G$ the product $g \circ h$ is also in G (closure)

2. For all $g,h,f \in G$ it holds $(g \circ h) \circ f = g \circ (h \circ f)$ (associativity)

3. There exists an element $e \in G$ so that for all $g \in G$ it holds $e \circ g = g \circ e = g$ (identity element)

4. For all $g \in G$ there exists an element g^{-1} so that $g \circ g^{-1} = g^{-1} \circ g = e$ (inverse element)

A group $(G, \circ)$ is called Abelian if the group operation is also commutative.

This definition describes a very general structure and groups appear in multiple mathematical subtopics as well as in different parts of physics. A large subclass of groups are groups $(G, \circ)$ where the set G is a *smooth* set. The corresponding mathematical structure is a Lie group:

Definition 4.2. A real *Lie group* is a group $(G, \circ)$ where the set G is additionally a finite-dimensional real smooth manifold and the group operation a smooth map from $G \times G \rightarrow G$. A Lie group is called *simple* if it contains no normal subgroups and it is called *connected* (*compact*) if the manifold G is connected (compact).

A real matrix Lie group is a closed subgroup of $GL(n, \mathbb{C})$, the general linear group of matrices acting on $\mathbb{C}^n$.

From this definition it follows that the group elements g depend smoothly on continuous parameters ϑ_i. To see this, on can choose a chart ϕ for G which is a smooth bijection from G into the Euclidean space $\mathbb{R}^D$. Its inverse ϕ^{-1} can be used to write:

$$g = g(\vartheta_1, \ldots, \vartheta_D), \tag{4.1}$$

with D being the dimension of the manifold, which is per definition also the dimension of the Lie group. The concrete dependence of g on ϑ_i depends of course on the chosen chart around the element g of the manifold. The most important aspect of Lie groups is that many of their properties follow from infinitesimal group operations around the identity element. The mathematical description of this aspect is the concept of Lie algebras:

Definition 4.3. For a Lie group G the *Lie algebra* $\mathfrak{g}$ is the tangent space at the identity element e of G:

$$\mathfrak{g} = TG_e \tag{4.2}$$

The Lie bracket is connected to the commutator of the corresponding vector fields but its precise definition is quite technical for general Lie groups. The Lie algebra is *simple* if the Lie group G is simple. The Lie algebra is *semisimple* if it is a direct sum of simple Lie algebras.

The Lie algebra forms a vector space (as any algebra) and therefore it is possible to choose basis elements. Consider some Lie algebra $\mathfrak{g}$ with dimension d. A basis is then a collection of d

linearly independent elements $\{X_i\}_{i=1,\ldots,d}$. The Lie algebra is then entirely determined by the commutation relations of these basis elements:

$$[X_i, X_j] = i \sum_{k=1}^{d} f_{ijk} X_k \tag{4.3}$$

Here, the commutator of two basis elements is expanded again in the basis and the expansion coefficients f_{ijk} are called the structure constants of the Lie algebra. The inserted imaginary unit i corresponds to the physicist's notation. Note that by definition, the structure constants are basis-dependent. Furthermore it is also possible to introduce a non-degenerate bilinear form $\langle \cdot, \cdot \rangle$ on $\mathfrak{g}$[1] which defines an inner product on $\mathfrak{g}$. With this inner product one can define the Casimir element Ω of a semisimple Lie algebra $\mathfrak{g}$ as:

$$\Omega = \sum_{i=1}^{d} \langle X_i, X_i \rangle \tag{4.4}$$

for any basis $\{X_i\}_{i=1,\ldots,d}$. The Casimir element is basis-independent due to the properties of the inner product, and lies in the center of $\mathfrak{g}$. Hence it commutes with all elements $X \in \mathfrak{g}$. It is important that $\mathfrak{g}$ is semisimple because otherwise the inner product is degenerate (and therefore not really an inner product).

The exponential map of the manifold becomes a map from the Lie algebra $\mathfrak{g}$ (the tangent space) into the Lie group G (the manifold) and therefore allows to transfer properties of the Lie algebra to the group:

$$\exp: \quad \mathfrak{g} \longrightarrow G$$
$$X \longmapsto \exp(X)$$

In particular, the exponential map allows to introduce the *Riemannian normal coordinates* for G which parametrize elements $g \in G$ close to the identity element e. This chart can be constructed as follows: Choose a basis $\{X_i\}_{i=1,\ldots,d}$ in $\mathfrak{g}$ and define the map ξ as:

$$\xi: \quad U \subset \mathbb{R}^d \longrightarrow G$$
$$(x^1, \ldots, x^d) \longmapsto \exp\left(i \sum_{i=1}^{d} x^i X_i \right), \tag{4.5}$$

where the imaginary unit i is inserted for consistency with the physicist's notation. The basis elements $X_i \in \mathfrak{g}$ are called *generators* because of their role in the parametrization in Eq. (4.5). It is remarkable that the Lie algebra determines many of the group properties, and it is an important result of the mathematics of the 20th century. This is summarized in three theorems, which constitute the Lie group–Lie algebra correspondence. For this thesis, only the homomorphism theorem is important. It states that any Lie algebra homomorphism between two Lie algebras $\mathfrak{g}$ and $\mathfrak{h}$ induces a unique Lie group homomorphism between the corresponding

---

[1] This form may be defined via the Killing form on G.

Lie groups G and H if G is simply connected. A useful corollary for physics is that Lie algebra representations induce unique group representations. The importance of this theorem will become clear in the next chapter.

Definition 4.4. A *linear representation* of a group G is a linear map $D : G \to GL(V)$ where V is a vector space and $GL(V)$ are the invertible linear maps in V or equivalently the general linear group from matrices in V, with the following property:

- For all $g, h \in G$ it holds $D(g \circ h) = D(g) \circ D(h)$

A linear representation is therefore a group homomorphism from G into the general linear group $GL(V)$ acting on V.

The vector space V is the carrier space of the representation and its dimension is the dimension of the representation. Note, there is no requirement for bijectivity, so that there is always the so-called trivial representation where every group element is mapped to the unit element of the vector space. If two representations D and D' are connected via a simple vector space isomorphism, the two representations are equivalent. An important classification of representations is the concept of irreducibility:

Definition 4.5. A linear representation $D : G \to GL(V)$ of a group G is called *reducible* if there exists a subset U of V and $U \neq \{0\}, V$ so that $D(g)U \subset U$ for all $g \in G$. Otherwise D is called *irreducible*.

A representation D is called *fully reducible* if it can be written as the direct sum of irreducible representations (irreps). In this case the representation is called *semisimple*. Assuming D is finite, the expansion into irreps is:

$$D = \bigoplus_I n_I D^{(I)}, \tag{4.6}$$

where n_I is the multiplicity from the irrep $D^{(I)}$ and the direct sum contains finitely many terms, since D was assumed to be finite. The decomposition can be achieved by a basis transformation in the carrier space of V. For finite and unitary representations, this can always be done, since the basis transformation corresponds to a (block)-diagonalization. Thus all finite and unitary representations are fully reducible.

In an analogue manner, one can also define Lie algebra representations:

Definition 4.6. A *linear representation* of a Lie algebra $\mathfrak{g}$ is a map $\pi : \mathfrak{g} \to \mathfrak{gl}(V)$ where V is a vector space and $\mathfrak{gl}(V)$ is the Lie algebra of endomorphisms in V with the following property:

- For all $X, Y \in \mathfrak{g}$ it holds $\pi([X,Y]) = [\pi(X), \pi(Y)] = \pi(X)\pi(Y) - \pi(Y)\pi(X)$

A linear representation is therefore a Lie algebra homomorphism from $\mathfrak{g}$ into $\mathfrak{gl}(V)$. Two linear representations are equivalent if they are connected via a vector space isomorphism.

The notion of irreducibility can be defined as in Def. 4.5. For Lie algebras, there exists a special representation of outstanding importance which I will mention here explicitly.

Definition 4.7. For a Lie algebra $\mathfrak{g}$ the *adjoint representation* ad is a representation from $\mathfrak{g}$ in itself (viewed as a vector space) defined by:

$$\text{ad}: \quad \mathfrak{g} \longrightarrow \text{End}(\mathfrak{g})$$
$$X \longmapsto \text{ad}_X$$

The action of ad_X on another element $Y \in \mathfrak{g}$ is:

$$\text{ad}_X(Y) = [X,Y]$$

For irreps, one can formulate the fundamental lemma by Schur (essentially the same for groups and Lie algebras):

Lemma 4.1 (Schur's lemma). *Consider two irreps D_1 and D_2 of a group G or a Lie algebra $\mathfrak{g}$ with carrier spaces V_1 and V_2 respectively. Let φ be a vector space isomorphism from V_1 into V_2 and the following diagram commute for all $g \in G$:*

$$
\begin{array}{ccc}
V_1 & \xrightarrow{\varphi} & V_2 \\
\downarrow{\scriptstyle D_1(g)} & & \downarrow{\scriptstyle D_2(g)} \\
V_1 & \xrightarrow{\varphi} & V_2
\end{array}
$$

Then either $\varphi = 0$ or D_1 and D_2 are equivalent. The vector space isomorphisms φ fulfilling this requirement are called an intertwiner.

Schur's lemma has several corollaries. The most important one for physics says that:

Corollary 4.1.1. *If D is an irrep of a group G or a Lie algebra $\mathfrak{g}$ with carrier space V and φ a linear intertwiner map on V, i.e.:*

$$\varphi D(g) = D(g)\varphi \Leftrightarrow [\varphi, D(g)] = 0, \quad \forall g \in G \tag{4.7}$$

then $\varphi = \lambda\mathbb{1}$ is a scalar multiple of the identity matrix with $\lambda \in \mathbb{C}$.

A further corollary says that irreps of Abelian groups are one-dimensional and another corollary of Schur's lemma is the orthogonality relation for irreps of finite groups:

$$\sum_{g \in G} D^{(I)}(g)_{mn} D^{(J)}(g)_{kl} = \delta_{IJ}\delta_{mk}\delta_{nl}\frac{|G|}{d_I} \tag{4.8}$$

A generalization of this relation for compact (Lie) groups is also possible:

$$\int_G D^{(I)}(g)_{mn} D^{(J)}(g)_{kl} \, dg = \delta_{IJ}\delta_{mk}\delta_{nl}\frac{1}{d_I} \tag{4.9}$$

In both equations, $D^{(I)}(g)_{mn}$ is a matrix element of the corresponding representation and the Kronecker δ_{IJ} is understood up to similarity transformations. Irreps of a group are determined

up to similarity transformations and it would be desirable to have basis independent quantities. This is achievable by defining the character of a representation:

Definition 4.8. The *character* χ of a representation D with carrier space V ($\mathbb{K}$-vector space) is the following function:

$$\chi: \quad G \longrightarrow \mathbb{K}$$
$$g \longmapsto \mathrm{tr}(D(g))$$

For a Lie algebra representation π, the character is defined as:

$$\chi: \quad \mathfrak{g} \longrightarrow \mathbb{K}$$
$$X \longmapsto \mathrm{tr}\left(e^{\pi(X)}\right)$$

From the definition, it follows directly that the characters are equal for equivalent representations, since the trace operation is cyclically invariant. Notice, if a representation is semisimple (fully reducible) the converse is also true: if the characters are the same, the representations are equivalent. When inserting the characters $\chi^{(I)}(g)$ and $\chi^{(J)}(g)$ of the irreps $D^{(I)}(g)$ and $D^{(J)}(g)$ into Eq. 4.8, one naturally obtains the orthogonality relations for the characters of irreps:

$$\sum_{g \in G} \chi^{(I)}(g)\chi^{(J)}(g) = \delta_{IJ}, \tag{4.10}$$

or for compact (Lie) groups:

$$\int_G \chi^{(I)}(g)\chi^{(J)}(g)dg = \delta_{IJ} \tag{4.11}$$

For two group representations D_1 and D_2 one can define the tensor product representation by taking the tensor product of $D_1(g)$ and $D_2(g)$ (the tensor product of linear maps on V_1 and V_2):

$$[D_1 \otimes D_2](g) = D_1(g) \otimes D_2(g), \qquad \forall g \in G \tag{4.12}$$

The resulting representation $D_1 \otimes D_2$ has the carrier space $V_1 \otimes V_2$. For Lie algebra representations, there is a subtle difference in the definition of the tensor product representation. If π_1 and π_2 are Lie algebra representations with carrier spaces V_1 and V_2, then the tensor product representation $\pi_1 \otimes \pi_2$ is defined as:

$$[\pi_1 \otimes \pi_2](X) = \pi_1(X) \otimes \mathbb{1}_{V_2} + \mathbb{1}_{V_1} \otimes \pi_2(X) \qquad \forall X \in \mathfrak{g} \tag{4.13}$$

This definition can be understood when considering the corresponding Lie group representations and the property of the exponential map, that a *product* of exponentials is the exponential of the *sum* of the arguments. Even if the tensor product is built from irreps D_1 (π_1) and D_2 (π_2), the tensor product representation $D_1 \otimes D_2$ ($\pi_1 \otimes \pi_2$) is in general reducible, but may be decomposed into a direct sum of irreps as in Eq. 4.6. The decomposition of the tensor product

representation (if it exists) is called Clebsch-Gordan expansion (completely analogous for Lie algebras):

Definition 4.9. The *Clebsch-Gordan expansion* (CGe) for a tensor product of two irreps $D^{(J)}$ and $D^{(K)}$ is the transformation from the canonical tensor product basis of $V_1 \otimes V_2$ into the basis where the tensor product representation takes the following form:

$$D^{(J)} \otimes D^{(K)} = \bigoplus_I n_I D^{(I)}, \tag{4.14}$$

where $D^{(I)}$ is an irrep and n_I is the multiplicity of the irrep $D^{(I)}$. If the tensor product representation is not fully reducible, the CGe is not defined.

To get an explicit form of the CGe one has to choose a basis in each space. Let $\{|J,j\rangle\}_{j=1,\dots,d_J}$ be a basis of V^J and $\{|K,k\rangle\}_{k=1,\dots,d_K}$ be a basis of V^K. To label the basis in the tensor product space in which the representation takes the form of Eq. 4.14, one can choose $|I,J,K,i,\alpha_I\rangle$. Here I runs over all irreps which appear after the full reduction, i runs over the dimension of the representation I and α_I over the multiple copies of the representation I. The indices J and K are fixed and included for convenience. Such a basis is called *properly sorted* basis with respect to the symmetry group G. With these conventions, the defining equation for the CGe becomes:

$$|I,J,K,i,\alpha_I\rangle = \sum_{j,k} \Gamma^{J,K\to I(\alpha_I)}_{j,k\to i} |J,j,K,k\rangle \tag{4.15}$$

Here $\Gamma^{J,K\to I(\alpha_I)}_{j,k\to i}$ is a Clebsch-Gordan coefficient (CGc). Its interpretation is that it couples basis states from the irreps $D^{(J)}$ and $D^{(K)}$ to basis states from the irrep $D^{(I)}$. The multiplicity index α_I is necessary to distinguish between the different copies of $D^{(I)}$. Since the CGc define a unitary transformation, they obey orthonormality conditions. These are the known conditions for a unitary matrix, if one combines the indices j and k to a combined column index $C = (j,k)$ and I, i and α_I to a combined row index $R = (I,i,\alpha_1)$ to obtain a $d_I \cdot d_J \times d_I \cdot d_J$ dimensional unitary matrix with elements U_{CR}. Notice that the CGc are by far not unique. In the case without multiplicity, the only freedom is a phase factor $\alpha \in U(1)$ but if the multiplicity is greater than one, the CGc are only determined up to unitary transformations $U \in U(n^I)$ in the multiplicity spaces.

At the end of this section, I want to introduce tensor operators. Tensor operators have a significant role in physics, e.g. by the derivation of selection rules in atomic physics. In the definition of Schur's lemma (4.1), the intertwiner map φ is actually an example of a tensor operator of rank 0. Hence, a map which commutes with the group action is a *scalar* map or a *scalar* operator. A basis independent general definition for a tensor operator can be given as follows (see e.g. chapter 6 in Ref. [80]).

Definition 4.10. Consider a Hilbert space $\mathcal{H}$ with a representation D of a group G and a finite-dimensional representation D_0 with carrier space V_0 of G. Then the map O

$$O: \quad \mathcal{H} \times V_0 \to \mathcal{H}$$
$$|\Psi\rangle \otimes x \mapsto O(|\Psi\rangle \otimes x)$$

is called *tensor operator* if it is invariant under the action of G represented as $\tilde{D} = D \otimes D_0$ and D:

$$O\left(\tilde{D}[|\Psi\rangle \otimes x]\right) = O\left((D\,|\Psi\rangle) \otimes (D_0 x)\right) = DO(|\Psi\rangle \otimes x) \tag{4.16}$$

If D_0 is an irrep, O is called *irreducible tensor operator*. A tensor operator is also sometimes called *representation operator* in literature.

By choosing a basis in V_0, one can introduce the components of the tensor operator by:

$$\begin{aligned} O_i: \quad & \mathcal{H} \to \mathcal{H} \\ & |\Psi\rangle \mapsto O(|\Psi\rangle \otimes e_i) \end{aligned}$$

Eq. (4.16) can than be written as:

$$D^\dagger O_i D = \sum_j (D_0)_i{}^j O_j \tag{4.17}$$

If D_0 is chosen as the trivial (one-dimensional) representation, Eq. (4.17) is equivalent to a vanishing commutator of O_1 and $D(g)$ for all $g \in G$ so that the map φ from the definition of Schur's lemma indeed satisfies the above definition. Note that $(D_0)_i{}^j$ are the matrix elements of D_0 in the chosen basis. If D and D_0 are irreducible, one gets similar constraints as for the map φ in Schur's lemma but the situation is slightly more complicated since even if D and D_0 are irreducible, in general their tensor product $D \otimes D_0$ is not. For this reason tensor operators are only useful if one is able to decompose the tensor product representation. If one assumes that it is possible to decompose the tensor product into irreps by the CGe, one can formulate the Wigner-Eckart theorem which is basically a corollary of Schur's lemma:

Theorem 4.2 (Wigner-Eckart Theorem)**.** *Let $\mathcal{H}$ be a Hilbert space, $D^{(J)}$, $D^{(K)}$ and $D^{(L)}$ be irreps of a group G. Furthermore, let O be an irreducible tensor operator from $D^{(J)} \times D^{(K)}$ onto $D^{(L)}$ and $D^{(J)} \times D^{(K)} = \bigoplus_I n_I D^{(I)}$ be the known CGe (Def. 4.9) of the tensor product representation with CGc $\Gamma_{j,k\to i}^{J,K\to I(\alpha_I)}$. Then one makes the following conclusions for O:*

1. *$O = 0$ if the irrep $D^{(L)}$ is not contained in the CGe ($D^{(L)} \neq D^{(I)}$ for all I in the CGe)*

2. *If the irrep $D^{(L)}$ is contained in the decomposition, O is precisely given by a scalar multiple of the CGc $\Gamma_{j,k\to i}^{J,K\to I(\alpha_I)}$ with $D^{(I)} = D^{(L)}$.*

The first proposition follows directly from Schur's lemma because in this case the irreps of the domain and of the codomain are not equivalent. The second proposition is also a consequence of Schur's lemma. In this case the lemma predicts that the map is a scalar multiple of the identity. Notice, that this is only valid after the unitary transformation via the CGc so that the map O needs to be proportional to the CGc.

4.1.2 Representation theory for compact and connected Lie groups

The representation theory for a group G is the classification of all inequivalent irreps of the group G. The classification is the basis for the CGe and the CGc. At the beginning, I mention

some general facts about the representation theory of arbitrary Lie groups, where some are also valid for arbitrary finite groups.

A fundamental theorem of the representation theory for groups is the Peter-Weyl theorem, which holds for compact groups[1]. The theorem has several parts and requires a complex notation. However, the important proposition for the following can be summarized as:

Theorem 4.3 (Peter-Weyl Theorem)**.** *The irreps of G are finite-dimensional and discrete in the sense that they are countable and can therefore be labeled by an integer value (or if more convenient, by a set of integer values).*

A second basis is the Lie algebra – Lie group correspondence mentioned in Sec. 4.1.1. It states that there is a one-to-one correspondence between Lie algebra and Lie group representations. Thus, one can shift the task of finding irreps from the Lie group to the Lie algebra. This simplifies the problem in the sense that one is now searching for representations of a linear space (the Lie algebra) in contrast to the non-linear manifold of a Lie group.

Consider from now on a Lie algebra $\mathfrak{g}$ over the field of complex numbers $\mathbb{C}$, which corresponds uniquely to a connected Lie group G. Notice, that it is important that $\mathfrak{g}$ is a complex Lie algebra. For real Lie algebras, one can analyse their complexification instead, since both have the same irreps. The irreps of $\mathfrak{g}$ can then be found by the *theory of the highest weight*. This a straightforward procedure to classify all irreps of the Lie algebra. If desired, these can be transferred to the Lie Group G afterwards via the exponential map. I will sketch this procedure following chapter 9 of Ref. [79] and present the important quantities step by step and give an example for the Lie algebra $\mathfrak{sl}(2,\mathbb{C})$ in the next Section (Sec. 4.1.3).

1. The first step is to construct a Lie subalgebra $\mathfrak{h}$ (a Cartan subalgebra) which is spanned by basis elements $\{H_i\}_{i=1,\ldots,h}$ which form a maximally commuting subsystem. This means, there does not exist a subset $\tilde{\mathfrak{h}}$ of linearly independent elements in $\mathfrak{g}$ so that all elements in $\tilde{\mathfrak{h}}$ commute and that $\dim\tilde{\mathfrak{h}} > h$. For a Cartan subalgebra one additionally requires that the adjoint representation ad_H is diagonalizable for each $H \in \mathfrak{h}$. Since $\mathfrak{h}$ is a subalgebra it is also a linear sub subspace of $\mathfrak{g}$ so that one can decompose $\mathfrak{g}$ as $\mathfrak{g} = \mathfrak{h} \oplus \mathfrak{h}^\perp$. It is then convenient to name basis elements in $\mathfrak{h}$ by $\{H_i\}_{i=1,\ldots,h}$ and basis elements in the complement by $\{X_i\}_{i=h+1,\ldots,d}$.

2. The second step is to assume that there exists some finite-dimensional irrep π of $\mathfrak{g}$ with carrier space V. The commutation relations as in Eq. (4.3) stay the same for the images of the basis elements $\{\pi(H_i) \in \mathfrak{h}\}_{i=1,\ldots,h}$ and $\{\pi(X_i) \in \mathfrak{h}^\perp\}_{i=h+1,\ldots,d}$. For this irrep π one can then introduce *weights* and *weight vectors*. $\Lambda = (\lambda_1,\ldots,\lambda_h) \in \mathbb{C}^h$ is called a *weight*, if there exists a nonzero $v \in V$ such that $\pi(H_i)v = \lambda_i v$, i.e. v is a simultaneous eigenvector of all $\pi(H_i)$ with eigenvalue λ_i. The nonzero vector v is called a *weight vector* and the set of all nonzero vectors satisfying this condition is called the *weight space* for the *weight* Λ. The dimension of the weight spaces is also called the *inner multiplicity* of a weight Λ. One then readily recognizes that every representation has at least one *weight*, because $\pi(H_i)$ will have at least one simultaneous eigenvector because V is a $\mathbb{C}$-vector space. Here, it becomes clear that it is important to have an algebraically closed field.

---

3. The third step is to introduce the *roots*. In short, *roots* are nonzero weights of the adjoint representation of $\mathfrak{g}$ (Def. 4.7). That means that $A = (\alpha_1, \ldots, \alpha_h) \in \mathbb{C}^h$ is a root if there exists a nonzero vector $X \in \mathfrak{g}$ such that $\mathrm{ad}_{H_i} X = [H_i, X] = \alpha_i X$ for at least one $\alpha_i \neq 0$. And in analogy to the *weight vectors*, *root vectors* are elements $X \in \mathfrak{g}$ obeying this relation. All roots A can be collected into a set R of $\mathbb{C}^h$-vectors. The vectors in the collection span the vector space $\mathbb{C}^h$ and one can choose an inner product in $\mathbb{C}^h$. A subset Δ of R which forms a basis of $\mathbb{C}^h$ is called a collection of simple roots. The roots allow the definition of *integral* and *dominant* weights. A weight Λ is called *integral* if for all $A \in R$:

$$n = 2 \cdot \frac{\langle \Lambda, A \rangle}{\langle A, A \rangle} \tag{4.18}$$

is an integer. A weight Λ is called *dominant* with respect to simple roots Δ if for all $A \in \Delta$:

$$\langle A, \Lambda \rangle \geq 0 \tag{4.19}$$

It is called *strictly dominant* if the strict inequality holds.

One of the crucial steps is now that roots are raising and lowering operators for the weights: if A is a root, X the corresponding root vector and Λ a weight of π with weight vector v the following equation follows readily from the above definitions:

$$\pi(H)\,(\pi(X)v) = (\Lambda + A)\,\pi(X)v \tag{4.20}$$

That is to say $\pi(X)v$ is either another weight vector with weight $\lambda_i' = \lambda_i + \alpha_i$ for all $i = 1, \ldots, h$ or $\pi(X)v$ is the zero vector. Another implication is that one can explore the weight space of π with the roots.

4. The fourth step is to examine the weights of π by the action of the roots. In particular, one introduces a partial order for weights. The definition of the partial order involves the roots A and is as follows: if Λ_1 and Λ_2 are two weights of π then Λ_1 is greater than Λ_2 if:

$$(\Lambda_1 - \Lambda_2)_i = a_i \cdot \alpha_i, \qquad a_i \geq 0, \qquad i = 1, \ldots, h \tag{4.21}$$

A weight Λ is called a *highest weight* if $\Lambda > M$ for all other weights M.

With these considerations and definitions one can formulate the basic theorem for representations of Lie algebras:

Theorem 4.4 (Theorem of the highest weight)**.** *For a d-dimensional representation π with carrier space V of a complex Lie algebra $\mathfrak{g}$ the following holds:*

(i) V is the direct sum of the weight spaces of π.

(ii) π has a unique *highest weight.*

(iii) Two irreps with the same highest weight are equivalent.

(iv) The highest weight Λ of π is always dominant and integral.

(v) For every *dominant and integral weight there is a finite-dimensional irrep π of $\mathfrak{g}$.*

The proof of this theorem can be found in many text books, e.g. in Ref. [79]. Instead of analysing it here, I will present a concrete example in the upcoming section.

4.1.3 Representation theory for $SU(2)$

In this section, I will apply the theory of the highest weight to a concrete example. In this case, it is not hard to prove all parts of the theorem of the highest weight. As the example case, I choose the Lie group $SU(2)$ since its irreps are important for this thesis. Since $SU(2)$ is simply connected, its irreps are in one-to-one correspondence with the irreps of its Lie algebra $\mathfrak{su}(2)$

The group $SU(2)$ is defined as the set of complex 2×2 matrices U with the property $\det(U) = 1$. Its underlying manifold has dimension three and the group is non-Abelian. It is a connected, compact and semisimple real Lie group and as argued above, one can search for the irreps of its real Lie algebra $\mathfrak{su}(2)$. The Lie algebra $\mathfrak{su}(2)$ can be computed as:

$$\mathfrak{su}(2) = \left\{ M \in \mathrm{Mat}(2,\mathbb{C}) \mid \mathrm{tr}\, M = 0 \wedge M^\dagger = -M \right\} \tag{4.22}$$

Note that this is a real Lie algebra since for $X \in \mathfrak{su}(2)$, iX is not in the algebra. The Lie bracket is the commutator for matrices and Eq. 4.22 forms the defining representation of $\mathfrak{su}(2)$. The common basis $\{X_i\}_{i=1,2,3}$ is given by the Pauli matrices:

$$2X_1 = \sigma_x = \begin{pmatrix} 0 & 1 \\ 1 & 0 \end{pmatrix}, \quad 2X_2 = \sigma_y = \begin{pmatrix} 0 & -i \\ i & 0 \end{pmatrix}, \quad 2X_3 = \sigma_z = \begin{pmatrix} 1 & 0 \\ 0 & -1 \end{pmatrix}, \tag{4.23}$$

whose structure constants (see Eq. (4.3)) are the entries of the totally antisymmetric tensor ε_{ijk}. Note that the factor of 2 in Eq. (4.23) corresponds to the physics convention. The corresponding Casimir element (Def. 4.4) $\Omega = X_1^2 + X_2^2 + X_3^2 = 0.75 \cdot \sigma_0$ is proportional to the identity which is a direct consequence from Schur's lemma since the Casimir element commutes with all elements in $\mathfrak{su}(2)$. Since $\mathfrak{su}(2)$ is a real Lie algebra, one has to switch to its complexification to apply the *theorem of the highest weight*. The complexification of $\mathfrak{su}(2)$ is isomorphic to $\mathfrak{sl}(2,\mathbb{C})$, the vector space of all traceless matrices. In $\mathfrak{sl}(2,\mathbb{C})$, the convenient basis is (again the physics convention):

$$X_1 = \sigma_+ = \begin{pmatrix} 0 & 1 \\ 0 & 0 \end{pmatrix}, \quad X_2 = \sigma_- = \begin{pmatrix} 0 & 0 \\ 1 & 0 \end{pmatrix}, \quad 2X_3 = \sigma_z = \begin{pmatrix} 1 & 0 \\ 0 & -1 \end{pmatrix}, \tag{4.24}$$

which is not available in $\mathfrak{su}(2)$ The basis elements obey the following fundamental Lie brackets:

$$\left[S^+,S^-\right] = 2S^z \tag{4.25}$$
$$\left[S^z,S^\pm\right] = \pm S^\pm \tag{4.26}$$

For the case of $\mathfrak{sl}(2,\mathbb{C})$ the Cartan subalgebra $\mathfrak{h}$ is one-dimensional and spanned by $H_1 = X_3$. Now assume that there exists some finite dimensional irrep π of $\mathfrak{sl}(2,\mathbb{C})$ with carrier space V. In this representation the images $\pi(X_1)$, $\pi(X_2)$ and $\pi(X_3) = \pi(H)$ fulfil the same commutation

relations as in Eq. (4.25) and (4.26). $\lambda \in \mathbb{C}$ is called a weight, if there exists a nonzero $v \in V$ such that $\pi(H_1)v = \lambda v$. From the commutation relation in Eq. (4.26), one can conclude that X_1 and X_2 are root vectors for the roots $\alpha_1 = +1$ and $\alpha_2 = -1$ respectively. Notice, that $[H,H] = 0 \cdot H$ does not define a root, since the eigenvalue is zero. The collection R of the roots is therefore $R = \{\alpha_1 = +1, \alpha_2 = -1\}$ and they span the (complex) vector space $\mathbb{C}$ of all complex numbers. A subset $\Delta \subset R$ which forms a basis of $\mathbb{C}$ is then $\Delta = \{\alpha_1 = +1\}$ while the other choice $\Delta = \{\alpha_2 = -1\}$ would work properly, too. Eq. (4.18) simplifies for the root system of $\mathfrak{sl}(2,\mathbb{C})$. A weight λ is integral if $n = \pm 2\lambda$ is an integer. Hence weights are integral if they are integers or half integers. A dominant weight as defined in Eq. (4.19) fulfils $\lambda > 0$ for the above choice of Δ. Notice that the other choice would lead to the condition $\lambda < 0$. The theorem of the highest weight tells now that for every dominant integral weight – positive integer or half-integer – there exists a unique irrep for $\mathfrak{sl}(2,\mathbb{C})$. The proof is not hard in this special case:

Eq. (4.20) reads in this case

$$\pi(H)\left(\pi(X_1)v\right) = (\lambda + 1)\,\pi(X_1)v \tag{4.27}$$

Since the carrier space V is finite, $\pi(H)$ can only have finitely many eigenvectors. From this it follows immediately that there exists a $\lambda^{\max}$ together with the corresponding eigenvector $v^{\max}$ with $\pi(X_1)v^{\max} = 0$. $v^{\max}$ is then a maximum weight state, as will become clear later. Setting $v_0 = v^{\max}$, one can define a chain of vectors by $v_k = (\pi(X_2))^k\,v_o$. Because of Eq. 4.27 (but for $\pi(X_2)$), it follows that $\pi(H)v_k = (\lambda - k)\,v_k$. By induction one sees additionally that:

$$\pi(X_1)v_k = \left(2k\left(\lambda^{\max} - \frac{k-1}{2}\right)\right)v_{k-1} \tag{4.28}$$

The finiteness of the vector space implies again the existence of a largest value m for k, so that $v_m \neq 0$ but $v_{m+1} = 0$. Plugging this into Eq. 4.28, one obtains:

$$0 = \pi(X_1)v_{m+1} = \left(2(m+1)\left(\lambda^{\max} - \frac{m}{2}\right)\right)v_m \tag{4.29}$$

And since trivially $m + 1 \neq 0$, it follows $\lambda^{\max} - \frac{m}{2} = 0$. To fulfill this equation, $\lambda^{\max}$ must be a half integer if m is odd or an integer if m is even. One also has $\lambda^{\max} > 0$ since $m > 0$ by definition so that $\lambda^{\max}$ is indeed dominant and integral. This proves (iv) from the theorem of the highest weight for this case.

All the nonzero vectors v_k are eigenvectors of $\pi(H)$ with different eigenvalues, so that they are linearly independent. The v_k therefore build a basis of the $m + 1$-dimensional vector space so that the carrier space V is a direct sum of the weight spaces (part (i)). The partial order defined in Eq. (4.21) reduces to the convenient order for real numbers in this case, so that $\lambda^{\max}$ is indeed the highest weight. It is unique because $\pi(H)$ has no degenerate eigenvalue (part (ii)). Furthermore, since all weights are different, the weight spaces are all one-dimensional for the case of $\mathfrak{sl}(2,\mathbb{C})$. Hence, there is no inner multiplicity in this case.

The remaining parts ((iii) and (v)) follow since the above construction can be performed for any $\lambda^{\max}$ being dominant and integral (part (v)) and the procedure leads to a unique matrix form (up to isomorphisms) of $\pi(H)$ and also $\pi(X_{1,2})$ (part (iii)).

From this, one concludes that for every integer m, there exists an irrep of dimension $m+1$ with highest weight $\frac{m}{2}$. The convenient label of this representation in physics is $l = \frac{m}{2}$ which is then either a half integer or an integer value and has dimension $2l+1$. The representation with label l is called the spin-l representation of $\mathfrak{sl}(2,\mathbb{C})$. All $2l+1$ different states for a given l form the spin l multiplet. These irreps are in one-to-one correspondence with the irreps of $SU(2)$ since $SU(2)$ is simply connected and $\mathfrak{sl}(2,\mathbb{C})$ is the complexification of $\mathfrak{su}(2)$, the Lie algebra of $SU(2)$. For completeness, I list the matrix elements of the generators and also for the Casimir element S^2 in the spin-l irrep of $\mathfrak{sl}(2,\mathbb{C})$. These are the common matrix elements for angular-momentum operators and they follow directly from Eq. (4.28) after a proper normalization of the states v_k. The convenient label for the multiplet is $|l,m\rangle$ where l is the label from the irrep and m the weight (eigenvalue of $\pi(H) = S^z$).

$$S^z \, |l,m\rangle = m \, |l,m\rangle \tag{4.30}$$

$$S^\pm \, |l,m\rangle = \sqrt{l(l+1) - m(m \pm 1)} \, |l,m \pm 1\rangle \tag{4.31}$$

$$S^2 \, |l,m\rangle = l(l+1) \, |l,m\rangle \tag{4.32}$$

The Casimir element is independent of the weight m as required by Schur's lemma (4.1).

Having classified the irreps of $\mathfrak{sl}(2,\mathbb{C})$, one can also compute the character (Def. 4.8) for later use. As the character is the same for equivalent representations[1], it is sufficient to calculate the character on the Cartan subalgebra $\mathfrak{h} \subset \mathfrak{sl}(2,\mathbb{C})$. An element $X \in \mathfrak{h}$ represented by the irrep $\pi^{(l)}$ can be parameterized by a single parameter ϑ when choosing the basis element $H = X_3 \in \mathfrak{h}$:

$$\pi^{(l)}(X(\vartheta)) = \vartheta \cdot \pi^{(l)}(H) = \vartheta \cdot \begin{bmatrix} l & & & \\ & l-1 & & \\ & & \ddots & \\ & & & -l \end{bmatrix} \tag{4.33}$$

so that also the character $\chi_{(l)}$ can be evaluated as $\chi_{(l)}(X(\vartheta)) = \mathrm{tr}\left[\pi^{(l)}(e^{iX(\vartheta)})\right]$ (Def. 4.8):

$$\chi_{(l)}(X(\vartheta)) = \frac{\sin\left((2l+1)\frac{\vartheta}{2}\right)}{\sin\left(\frac{\vartheta}{2}\right)} \tag{4.34}$$

This compact result is a special case of the Weyl character formula. In the case of $\mathfrak{sl}(2,\mathbb{C})$, it can also be derived directly using the known results for the geometric progression.

4.1.4 Clebsch-Gordan expansion and recoupling coefficients for $SU(2)$

After the classification of the irreps for a group G one can construct the CGe as defined in Def. 4.9. The orthogonality relations between irreps (Eq. (4.8)) or the equivalent relation between the characters (Eq. (4.10)) can in principle be used to obtain the CGe and the CGc. Since $SU(2)$ is a simply connected Lie group, it is however more convenient to obtain the CGe for its Lie algebra $\mathfrak{su}(2)$. Furthermore, since the irreps of $\mathfrak{su}(2)$ are in one-to-one correspondence with the irreps of $\mathfrak{sl}(2,\mathbb{C})$, I will derive the CGe for this Lie algebra in this section.

---

1   The character is a class function.

Consider two irreps $\pi^{(j_1)}$ and $\pi^{(j_2)}$ (with highest weight j_1 and j_2 respectively) of $\mathfrak{sl}(2,\mathbb{C})$ as derived in Sec. 4.1.3. Both can be combined to another (reducible) representation of $\mathfrak{sl}(2,\mathbb{C})$ via the tensor product (Eq. (4.13)):

$$\pi^{(j_1)} \otimes \pi^{(j_2)} = \pi^{(j_1)} \otimes \mathbb{1}_{j_2} + \mathbb{1}_{j_1} \otimes \pi^{(j_2)} \tag{4.35}$$

The goal is then to find a decomposition of $\pi^{(j_1)} \otimes \pi^{(j_2)}$ as in Def. 4.9 to write:

$$\pi^{(j_1)} \otimes \pi^{(j_2)} = \bigoplus_J n_J \pi^{(J)}, \tag{4.36}$$

where $\pi^{(J)}$ is the irrep with highest weight J. The first step is to find out which irreps appear in this decomposition and how often. For $SU(2)$, an irrep appears at most once and every irrep J fulfils $|j_1 - j_2| \leq J \leq j_1 + j_2$:

$$\pi^{(j_1)} \otimes \pi^{(j_2)} = \bigoplus_{J=|j_1-j_2|}^{j_1+j_2} \pi^{(J)}, \tag{4.37}$$

This can be proved by calculating the character (Def. 4.8) of both sites. For the character on the left side one computes:

$$\chi_{(j_1 \otimes j_2)}(X(\vartheta)) = \chi_{(j_1)}(X(\vartheta)) \cdot \chi_{(j_2)}(X(\vartheta)) = \frac{\sin\left((2j_1+1)\frac{\vartheta}{2}\right)}{\sin\left(\frac{\vartheta}{2}\right)} \cdot \frac{\sin\left((2j_2+1)\frac{\vartheta}{2}\right)}{\sin\left(\frac{\vartheta}{2}\right)} \tag{4.38}$$

For the right hand side one obtains:

$$\chi_{(\bigoplus_J J)}(X(\vartheta)) = \sum_{J=j_1-j_2}^{j_1+j_2} \chi_{(J)}(X(\vartheta)) \tag{4.39}$$

$$= \sum_{J=j_1-j_2}^{j_1+j_2} \frac{\sin\left((2J+1)\frac{\vartheta}{2}\right)}{\sin\left(\frac{\vartheta}{2}\right)} \tag{4.40}$$

$$= \frac{1}{\sin^2\left(\frac{\vartheta}{2}\right)} \sum_{J=j_1-j_2}^{j_1+j_2} \frac{1}{2}\left(\cos\left(J\vartheta\right) - \cos\left(J\vartheta + \vartheta\right)\right) \tag{4.41}$$

$$= \frac{\sin\left((2j_1+1)\frac{\vartheta}{2}\right)}{\sin\left(\frac{\vartheta}{2}\right)} \cdot \frac{\sin\left((2j_2+1)\frac{\vartheta}{2}\right)}{\sin\left(\frac{\vartheta}{2}\right)}, \tag{4.42}$$

where Eq. (4.34) was used and the sum in Eq. (4.40) is transformed into a telescope sum (Eq. (4.41)) by using the trigonometric identity $\sin(A)\sin(B) = \frac{1}{2}\cos(A-B) - \frac{1}{2}\cos(A+B)$ with the choice $A = i\vartheta + \frac{\vartheta}{2}$ and $B = \frac{\vartheta}{2}$. Since both sides have the same character, they must be isomorphic and Eq. (4.37) is the correct expansion into irreps. The CGe for $SU(2)$ is therefore free of any multiplicity which facilitates several algorithms and irreps in the tensor product fulfil the *triangle rule* triad(j_1,j_2,J): $|j_1 - j_2| \leq J \leq j_1 + j_2$. For the computation of the concrete CGc one can use:

1. Recursion relations generated by the roots (for $SU(2)$ the operators S^+ and S^-).

2. Diagonalization of the Casimir operators for every irrep satisfying the triangle rule. For numerical purposes, the unitary matrix for the diagonalization has to be uniquely chosen. For $SU(2)$, this is a simple phase convention whereas in the case of inner- and outer-multiplicity it is nontrivial to obtain a unique choice.

3. Evaluation of explicit formulas.

For $SU(2)$, one explicit formula reads as:

$$
\begin{aligned}
\Gamma^{j_1,j_2\to J}_{m_1,m_2\to M} = {} & \delta_{M,m_1+m_2} \sqrt{\frac{(2J+1)(J+j_1-j_2)!(J-j_1+j_2)!(j_1+j_2-J)!}{(j_1+j_2+J+1)!}} \times \\
& \sqrt{(J+M)!(J-M)!(j_1+m_1)!(j_1-m_1)!(j_2+m_2)!(j_2-m_2)!} \times \\
& \sum_k \frac{(-1)^k}{k!(j_1+j_2-J-k)!(j_1-m_1-k)!(j_2+m_2-k)!(J-j_2+m_1+k)!(J-j_1-m_2+k)!}
\end{aligned}
\tag{4.43}
$$

The summation is done for all k for which the factorials are taken from non-negative numbers and the exact evaluation of Eq. (4.43) leads to a square root of a rational number; notably the CGc can be chosen as real numbers. The complete symmetry relations for the CGc are rather complicated and were fully discovered by REGGE [81] as a group of order 72. However, some symmetries are evident, e.g. the flip operation of all z-quantum numbers:

$$
\Gamma^{j_1,j_2\to J}_{m_1,m_2\to M} = (-1)^{j_1+j_2-J}\Gamma^{j_1,j_2\to J}_{-m_1,-m_2\to -M}
\tag{4.44}
$$

Note that for more complicated Lie groups, the evaluation of the CGc is much more involved, especially for numerical algorithms. An explicit formula is not available in most cases and the diagonalization of the Casimir operators is not optimal either. This is due to inner- and outer-multiplicity in general semisimple Lie algebras which prohibit a *unique* calculation of the CGc. A stable algorithm for the evaluation of the CGc for general semisimple Lie algebras was, however, suggested by WEICHSELBAUM [76] (see Appendix B therein) which essentially uses the recursion relations obtained through the roots.

The CGe decomposes the tensor product of *two* irreps but in later algorithms also three or four irreps will appear which need to be combined. In the case of three irreps $\pi^{(j_1)}$, $\pi^{(j_2)}$ and $\pi^{(j_3)}$ one might first combine $\pi^{(j_1)}$ and $\pi^{(j_2)}$ into $\bigoplus_{J_{12}}\pi^{(J_{12})}$ and afterwards every representation $\pi^{(J_{12})}$ is combined with $\pi^{(j_3)}$. However, one could also combine $\pi^{(j_2)}$ and $\pi^{(j_3)}$ first into $\bigoplus_{J_{23}}\pi^{(J_{23})}$ and $\pi^{(j_1)}$ afterwards with the result. The two procedures give bases for $\left(\pi^{(j_1)}\otimes\pi^{(j_2)}\right)\otimes\pi^{(j_3)}$ and $\pi^{(j_1)}\otimes\left(\pi^{(j_2)}\otimes\pi^{(j_3)}\right)$, respectively and both spaces are isomorphic because of the properties of the tensor product. The isomorphism is given by a contraction of four CGc and is called a *recoupling coefficient*:

$$
\begin{aligned}
\left\langle J'M'j_1 J_{23}(j_2,j_3)\,\middle|\,JMJ_{12}(j_1,j_2)j_3\right\rangle = {} & \delta_{JJ'}\delta_{MM'} \\
& \sum_{\boldsymbol{m}} \Gamma^{j_2,j_3\to J_{23}}_{m_2,m_3\to m_{23}}\Gamma^{j_1,J_{23}\to J'}_{m_1,m_{23}\to M'}\Gamma^{j_1,j_2\to J_{12}}_{m_1,m_2\to m_{12}}\Gamma^{J_{12}j_3\to J}_{m_{12}m_3\to M}
\end{aligned}
\tag{4.45}
$$

A related object of higher symmetry is the $6j$-symbol defined as:

$$\begin{Bmatrix} j_1 & j_2 & J_{12} \\ j_3 & J & J_{23} \end{Bmatrix} = (-1)^{j_1+j_2+j_3+J} \frac{1}{\sqrt{(2J_{12}+1)(2J_{23}+1)}} \langle JM j_1 J_{23}(j_2,j_3) \,|\, JM J_{12}(j_1,j_2)j_3 \rangle$$

$$(4.46)$$

The $6j$-symbol will appear in many calculations later and many of its properties are discussed in Ref. [82, 83]. Its evaluation can be performed by an explicit formula which was discovered by RACAH [84, 85]. For my application, I used the implementation in the GNU SCIENTIFIC LIBRARY (GSL). The $6j$-symbol is zero unless triad(j_1,J_2,J_{12}), triad(j_1,J,J_{23}), triad(j_2,j_3,J_{23}) and triad(j_3,J,J_{12}) are fulfilled. The $6j$-symbol is symmetric under the transposition of the columns and under a swap of two elements from the first row with to elements from the second row (from pairwise equal columns). There are also additional symmetry operations which go beyond simple permutations which lead to a symmetry group of order 144 (see e.g. Ref. [86]).

With similar considerations, one can also analyse the coupling of four irreps $\pi^{(j_1)}$, $\pi^{(j_2)}$, $\pi^{(j_3)}$ and $\pi^{(j_4)}$. The recoupling coefficient is conveniently written as:

$$\langle M'J'(J_{13}(j_1,j_3)J_{24}(j_2,j_4)) \,|\, MJ(J_{12}(j_1,j_2),J_{34}(j_3,j_4)) \rangle = \delta_{JJ'}\delta_{MM'} \begin{bmatrix} j_1 & j_2 & J_{12} \\ j_3 & j_4 & J_{34} \\ J_{13} & J_{24} & J \end{bmatrix}, \quad (4.47)$$

and directly related to the $9j$-symbol:

$$\begin{Bmatrix} j_1 & j_2 & J_{12} \\ j_3 & j_4 & J_{34} \\ J_{13} & J_{24} & J \end{Bmatrix} = \frac{1}{\sqrt{(2J_{12}+1)(2J_{34}+1)(2J_{13}+1)(2J_{24}+1)}} \begin{bmatrix} j_1 & j_2 & J_{12} \\ j_3 & j_4 & J_{34} \\ J_{13} & J_{24} & J \end{bmatrix} \quad (4.48)$$

The $9j$-symbol is zero unless the triangle rule is fulfilled for every column and for every row. It is symmetric under *even* permutations of its rows or columns as well as a reflection on the diagonals. For *odd* permutations of its rows or columns, the symbol picks up a phase $(-1)^{\sum j}$ from the sum all involved quantum numbers. The computation of the $9j$-symbol can be performed by a contraction of three $6j$-symbols:

$$\begin{Bmatrix} j_1 & j_2 & J_{12} \\ j_3 & j_4 & J_{34} \\ J_{13} & J_{24} & J \end{Bmatrix} = \sum_x (-1)^{2x}(2x+1) \begin{Bmatrix} j_1 & j_3 & J_{13} \\ J_{24} & J & x \end{Bmatrix} \begin{Bmatrix} j_2 & j_4 & J_{24} \\ j_3 & x & J_{34} \end{Bmatrix} \begin{Bmatrix} J_{12} & J_{34} & J \\ x & j_1 & j_2 \end{Bmatrix} \quad (4.49)$$

For my implementation, I use again the GNU SCIENTIFIC LIBRARY (GSL). Since the $6j$-symbol can be represented by the CGc, one can also determine the $9j$-symbol directly from the CGc:

$$\begin{Bmatrix} j_1 & j_2 & J_{12} \\ j_3 & j_4 & J_{34} \\ J_{13} & J_{24} & J \end{Bmatrix} = \frac{1}{\sqrt{(2J_{12}+1)(2J_{34}+1)(2J_{13}+1)(2J_{24}+1)}} \sum_{m_i, M_{ik}}$$

$$\Gamma^{j_1,j_2 \to J_{12}}_{m_1,m_2 \to M_{12}} \Gamma^{j_3,j_4 \to J_{34}}_{m_3,m_4 \to M_{34}} \Gamma^{J_{12},J_{34} \to J}_{M_{12},M_{34} \to M}$$

$$\Gamma^{j_1,j_3 \to J_{13}}_{m_1,m_3 \to M_{13}} \Gamma^{j_2,j_4 \to J_{24}}_{m_2,m_4 \to M_{24}} \Gamma^{J_{13},J_{24} \to J}_{M_{13},M_{24} \to M}$$

$$(4.50)$$

The sum over the six CGc is therefore identical with the recoupling coefficient from Eq. (4.47).

4.1.5 Tensor operators and the Wigner-Eckart theorem for $SU(2)$

Tensor operators are of particular importance for the exploitation of symmetries in numerical algorithms. From a physical perspective, tensor operators are intensively studied in Ref. [82, 83].

The general definition Def. 4.10 is quite abstract, so I will start by giving some examples for tensor operators. The common tensor operators in quantum mechanics are also called vector operators and the corresponding group is $SO(3)$, i.e. the proper rotations in three-dimensional Euclidian space. The representation D_0 in Def. 4.10 is typically the defining representation of $SO(3)$, which is irreducible. The irreps of $SO(3)$ are the integer spin representations of $SU(2)$ derived in Sec. 4.1.3 and the defining representation has the label $l = 1$ so that it is $2l + 1 = 3$-dimensional. A vector operator therefore has three components – one for each basis state of $\mathbb{R}^3$ – which are operators on a Hilbert space $\mathcal{H}$. The rotation group $SO(3)$ is also represented on $\mathcal{H}$ and the condition in Eq. (4.17) is then that the induced representation on the operators has the same action as the irrep with $l = 1$ acting on the set of three operators. A common example is the position operator $\boldsymbol{r} = (x,y,z)$. There are also examples for tensor operators with higher rank, e.g. the electrical quadrupole tensor. Notice that these are usually reducible tensor operators. For the quadrupole tensor for example, D_0 from Def. 4.10 is the tensor product of the $l = 1$ irrep from $SO(3)$ with itself which is reducible. In this case, it is possible to decompose the operator into irreducible tensor operators. In this thesis, tensor operators with respect to the group $SU(2)$ are relevant but since any irrep of $SO(3)$ is also an irrep of $SU(2)$[1] one can define an analogue tensor operator for $SU(2)$.

Since $SU(2)$ is a Lie group, one can expand the group elements $D(g)$ with the Riemannian normal coordinates (Eq. 4.5) around the identity element $D(e)$:

$$D(g) = \exp\left(i\sum_{j=1}^{3} x^j \pi(X_j)\right) \tag{4.51}$$

For an irreducible tensor operator O with respect to $SU(2)$ with D_0 being the spin k representation of $SU(2)$ the components can be labeled by the standard basis elements of the irrep k, namely $m = -k, \ldots, +k$. The condition for the components $O_m^{[k]}$ from Eq. (4.17) can then be transferred to the elements of the Lie algebra with Eq. (4.51):

$$\left[\pi(X_1), O_m^{[k]}\right] = \sqrt{k(k+1) - m(m+1)} O_{m+1}^{[k]} \tag{4.52}$$

$$\left[\pi(X_2), O_m^{[k]}\right] = \sqrt{k(k+1) - m(m-1)} O_{m-1}^{[k]} \tag{4.53}$$

$$\left[\pi(X_3), O_m^{[k]}\right] = m O_m^{[k]} \tag{4.54}$$

---

[1] The converse is not true, since $SU(2)$ also has half-integer irreps.

The generators X_i of $SU(2)$ are defined as in Eq. (4.24) and π is the corresponding Lie algebra representation to D. These equations can be compared with Eq. (4.30) and Eq. (4.31), so that the behaviour of irreducible tensor operators is quite similar to that of the basis states from a irrep.

The Wigner-Eckart theorem (Def. 4.2) reads in the case of $SU(2)$:

$$\left\langle j_1 m_1 \left| O_m^{[k]} \right| j_2 m_2 \right\rangle = \left\langle j_1 \left\| O^{[k]} \right\| j_2 \right\rangle \Gamma_{m_2, m \to m_1}^{j_2, k \to j_1}, \tag{4.55}$$

where the scalar constant is now conveniently written as the *reduced matrix element* indicated by the double lines and I also used the convenient labels for the $SU(2)$ irreps. The CGc have no multiplicity label, since there is no multiplicity for $SU(2)$ (see Sec. 4.1.4). If the bra and ket spaces are a direct sum of irreps, i.e. *properly sorted* bases, Eq. (4.55) reads:

$$\left\langle \alpha_{j_1} j_1 m_1 \left| O_m^{[k]} \right| \alpha_{j_2} j_2 m_2 \right\rangle = \left\langle \alpha_{j_1} j_1 \left\| O^{[k]} \right\| \alpha_{j_2} j_2 \right\rangle \Gamma_{m_2, m \to m_1}^{j_2, k \to j_1}, \tag{4.56}$$

This equation is obtained by applying the Wigner-Eckart theorem block wise. Eq. (4.56) is the reason, why irreducible tensor operators are numerically useful. The internal degrees of the representation factor out and are solely determined by the symmetry group G. In the case of $SU(2)$ it is particularly useful, since several contractions over the CGc can be carried out analytically. Algebraic operations on irreducible tensor operators can therewith be performed on the level of the reduced matrix elements. The easiest operations – the sum of two operators and a scalar multiplication – can be performed readily for the reduced matrix elements while the CGc stay the same. Note that a sum can only be taken between operators having the same rank. The product operation is more complex though. Consider two irreducible tensor operators $O_{m_1}^{[k_1]}$ and $S_{m_2}^{[k_2]}$. Their product can be performed to give another irreducible tensor operator $\left(O^{[k_1]} \times S^{[k_2]} \right)^{[K]}$ with several possibilities for the rank K[1]:

$$\left(O^{[k_1]} \times S^{[k_2]} \right)_M^{[K]} = \sum_{m_1, m_2} \Gamma_{m_1, m_2 \to M}^{k_1, k_2 \to K} O_{m_1}^{[k_1]} S_{m_2}^{[k_2]} \tag{4.57}$$

The reason for this formula is that the product of two irreducible tensor operators will generally give a reducible tensor operator. This can be decomposed into several irreducible tensor operators. For $SU(2)$ it was derived in Sec. 4.1.4 that one has an irreducible tensor operator for $K = |k_1 - k_2|, \ldots, k_1 + k_2$. A quite useful result is that one can obtain the reduced matrix elements from $\left(O^{[k_1]} \times S^{[k_2]} \right)^{[K]}$ directly from the reduced matrix elements of $O^{[k_1]}$ and $S^{[k_2]}$

---

1   The multiplication of two operators defined in this way does not form an algebra because of the several possibilities for the total quantum number. A different definition leads to the *Racah-Wigner* algebra as discussed in [87]

while the product of the CGc can be efficiently shifted into a $6j$-symbol (Eq. (4.46)):

$$\left\langle \alpha_{j_1}j_1 \left| \left(O^{[k_1]} \times S^{[k_2]} \right)^{[K]} \right| \alpha_{j_2}j_2 \right\rangle = (-1)^{(j_1+j_2+K)} \sum_J \sqrt{(2K+1)(2J+1)} \begin{Bmatrix} j_1 & k_1 & J \\ k_2 & j_2 & K \end{Bmatrix}$$
$$\sum_{\alpha_J} \left\langle \alpha_{j_1}j_1 \left\| O^{[k_1]} \right\| \alpha_J J \right\rangle \left\langle \alpha_J J \left\| S^{[k_2]} \right\| \alpha_{j_2}j_2 \right\rangle$$

$$(4.58)$$

This is essentially an ordinary product of the reduced operators (second line in Eq. (4.58)) with an additional factor (the $6j$-symbol). It is somewhat tedious to derive this equation but it follows straight forwardly from the definition in Eq. (4.57) and the Wigner-Eckart theorem in Eq. (4.56). If the product $\left(O^{[k_1]} \times S^{[k_2]} \right)^{[K]}$ is essentially a tensor product because $O^{[k_1]} = O_1^{[k_1]} \otimes \mathbb{1}_2$ and $S^{[k_2]} = \mathbb{1}_1 \otimes S_2^{[k_2]}$ the coupling law in Eq. (4.58) can be rewritten as:

$$\left\langle \alpha_J J(\alpha_{j_1}j_1\alpha_{j_2}j_2) \left| \left(O^{[k_1]} \otimes S^{[k_2]} \right)^{[K]} \right| \alpha_{J'}J'(\alpha_{j_1'}j_1'\alpha_{j_2'}j_2') \right\rangle =$$
$$= \begin{bmatrix} j_1' & j_2' & J' \\ k_1 & k_2 & K \\ j_1 & j_2 & J \end{bmatrix} \left\langle \alpha_{j_1}j_1 \left\| O^{[k_1]} \right\| \alpha_{j_1'}j_1' \right\rangle \left\langle \alpha_{j_2}j_2 \left\| S^{[k_2]} \right\| \alpha_{j_2'}j_2' \right\rangle$$

$$(4.59)$$

Here the symbol in square brackets is a recoupling coefficient for four irreps (Eq. (4.47)) which is closely related to the $9j$-symbol in Eq. (4.48). The states $|\alpha_J J\rangle$ are obtained by coupling the states $|\alpha_{j_1}j_1\rangle$ and $|\alpha_{j_2}j_2\rangle$. In an implementation, it is crucial to find a consistent algorithm for this coupling.

The coupling law in Eq. (4.57) can be used to introduce an inner product for irreducible tensor operators of rank k. This inner product maps the two rank-k tensors onto a scalar operator:

$$\langle O^{[k]}, S^{[k]} \rangle = \left(O^{[k]} \times S^{[k]} \right)_0^{[0]} = \sum_{m_1,m_2} \Gamma_{m_1,m_2 \to 0}^{k,k \to 0} O_{m_1}^{[k_1]} S_{m_2}^{[k_2]} \qquad (4.60)$$

The bilinear form for this inner product is given by the CGc $\Gamma_{m_1,m_2 \to 0}^{k,k \to 0} = \delta_{m_1,-m_2} \frac{(-1)^{k-m_1}}{\sqrt{2k+1}}$. One may then define a Hermitian conjugate (adjoint) tensor with respect to this inner product by:

$$\left(O^\dagger \right)_m^{[k]} = (-1)^{k-m} \left(O_{-m}^{[k]} \right)^\dagger \qquad (4.61)$$

The reduced matrix elements of the Hermitian conjugate tensors can again be calculated from the reduced matrix elements of the primary operator:

$$\left\langle \alpha_{j_1}j_1 \left\| O^{\dagger[k]} \right\| \alpha_{j_2}j_2 \right\rangle = (-1)^{k+j_2-j_1} \sqrt{\frac{2j_2+1}{2j_1+1}} \left\langle \alpha_{j_2}j_2 \left\| O^{[k]} \right\| \alpha_{j_1}j_1 \right\rangle^* \qquad (4.62)$$

The reduced matrix elements have the property that $\left\langle \left\| O^{\dagger[k]} \right\| \right\rangle = (-1)^{2k} \left\langle \left\| O^{[k]} \right\| \right\rangle$ which

needs to be taken into account, if algorithms work only with the reduced matrix elements.

At the end of this section, I want to give a concrete example for an $SU(2)$ irreducible tensor operator, namely the generators $\pi(X_i)$ themselves. The generators have the known relation to the angular momentum operators: $\pi(X_1) = S^+$, $\pi(X_2) = S^-$ and $\pi(X_3) = S^z$. It is easy to compute that the definitions in Eq. (4.52), (4.53) and (4.54) are fulfilled by the irreducible tensor operator $S_m^{[1]}$ with $S_1^{[1]} = -\frac{1}{\sqrt{2}}S^+$, $S_0^{[1]} = S^z$ and $S_{-1}^{[1]} = \frac{1}{\sqrt{2}}S^-$. The reduced matrix elements for $S^{[1]}$ follow from Eq. (4.30) and (4.31) and are given by:

$$\left\langle \alpha_{j_1} j_1 \left\| S^{[1]} \right\| \alpha_{j_2} j_2 \right\rangle = \sqrt{j_1(j_1+1)}\delta_{\alpha_1 \alpha_2}\delta_{j_1 j_2} \tag{4.63}$$

The reduced matrix elements of the Hermitian adjoint of $S^{[1]}$ are given by $\left\langle \left\| S^{\dagger[1]} \right\| \right\rangle = (-1)\left\langle \left\| S^{[1]} \right\| \right\rangle$.

4.2 Symmetries in physics

In physical systems, symmetry operations play an essential role in many different aspects.

1. Fundamental symmetries are symmetry operations which are expected to leave any physical system invariant by causality. For example, a linear translation in real space of a system should not affect any physics, because otherwise experiments can not be reproduced in other places. Hence any fundamental theory needs to be invariant under linear translations in real space. The whole group of fundamental symmetries is believed to be the Poincare group.

2. Internal symmetries of a physical theory are decisive for their properties. In particular, they determine which interactions are possible.

3. In general, symmetries can help to find a solution for physical systems since they often enforce constants of motion due to Noether's theorem [88]. These can be used to find a much simpler solution than solving the general equations of motions. Also from a numerical perspective, symmetries can help to achieve the solution more efficiently, because sometimes the problem divides into smaller problems because of a symmetry.

Symmetry operations are a natural way to group operations as they can be concatenated and have inverse elements. The identity operation is also present in a canonical way by simply doing nothing. As a basis of every symmetry in a physical system, one therefore has a group G. A physical system is invariant under a symmetry described by the group G if the fundamental equations do not change by the action of any element $g \in G$.

In quantum mechanics, the central quantity is the wave function which is a vector in a Hilbert space $\mathcal{H}$. To describe symmetry transformations of wavefunctions, a representation D of the

group G in this Hilbert space $\mathcal{H}$ is necessary[1]:

$$D : \quad G \to GL(\mathcal{H}) \tag{4.64}$$
$$g \mapsto D(g)$$

Where $GL(\mathcal{H})$ is the set of invertible operators acting on the Hilbert space $\mathcal{H}$. I assume here that D is a unitary representation, which is a small constraint due to Wigner's theorem [89] from which it is known that physical representations are either unitary or anti-unitary. The anti-unitary case is only present if time-reversal symmetry transformations are involved. It is easy to see that a representation D in the Hilbert space can be canonically transferred to a group action Γ on the space $\text{End}(\mathcal{H})$ of linear operators acting on $\mathcal{H}$:

$$\Gamma : \quad G \times GL(\mathcal{H}) \to GL(\mathcal{H}) \tag{4.65}$$
$$(g,O) \mapsto D(g)^{\dagger}OD(g)$$

Furthermore this group action might be identified with a representation of G on $\text{End}(\mathcal{H})$. The fundamental equation is the Schrödinger (SG) equation:

$$-i\hbar\frac{\partial}{\partial t}\ket{\Psi} = H\ket{\Psi} \tag{4.66}$$

which is entirely determined by the Hamilton operator H of the system. The SG equation might then be invariant under the action of the group represented as in Eq. (4.64) on the states or Eq. (4.65) on the Hamilton operator. Notice that a transformation of a physical system is described by the transformation of the operators *only* (or equivalently the states only) and not both. Transforming both states *and* operators leaves the system invariant trivially. After Eq. (4.65), the Hamilton operator is invariant if it commutes with the group representation $D(g)$ for any $g \in G$:

$$D^{\dagger}(g)HD(g) = H \iff [H,D(g)] = 0, \quad \forall g \in G \tag{4.67}$$

This condition is exactly the same condition as in Schur's lemma (4.1) for φ (but D was assumed to be irreducible in Schur's lemma). From another point of view, the Hamilton operator is a linear function acting on a vector and a dual vector (it is actually a (1,1)-tensor). Then the invariance demonstrates in the fact that the image of H acting on a transformed vector and dual vector is the same as if H acts on the original vectors. Here, it is important that tranformations on the dual vector space are performed with the adjoint ($D^{\dagger}$) of the representation in the vector space (D).

The invariance of the Hamilton operator has consequences which can facilitate numerical computations. Especially the block diagonal form allows a more efficient diagonalization of the Hamilton operator. To derive these consequences, one has to study the representation D. In general, the representation D in the Hilbert space is reducible but it may be possible to

---

[1] To be more precise, a projective representation of the symmetry is sufficient since wavefunctions are only determined up to a constant.

decompose the representation into a direct sum of irreps.

$$D = n_1 D^{(1)} \oplus n_2 D^{(2)} \oplus \cdots \oplus n_k D^{(k)} \tag{4.68}$$

The corresponding unitary transformation which decomposes the representation into this block-diagonal form also leads to a *properly sorted* basis with respect to the symmetry G. In this basis, one can attach to every state:

- A label I from the irrep it belongs to. This label is called the *quantum number* of the state.

- A label i to which the internal state from the irrep belongs to. This label is often called the *z-quantum number*.

- A label α_I to distinguish different states in the same irrep. This label is often called *degeneracy index*.

The basis states are then labeled as $|I,i,\alpha_I\rangle$ and the decomposed representation is diagonal within this basis. One can then evaluate Eq. (4.67) for each two blocks; one from $D^\dagger$ and one from D. Each block of D comprises an irrep of G labeled by (I,α_I) and (J,α_J), respectively, so that one can apply Schur's lemma (4.1) which says: if the two irreps are not equivalent $(I \neq J)$, H must vanish. If the two irreps are equivalent $(I = J)$, H must be a scalar multiple of the identity. This scalar might depend on the irrep I and on the degeneracy indices α_I, α_J of both irreps. Hence, one obtains the following matrix representation of H in the *properly sorted* basis:

$$H^{(IJ)(ij)}_{\alpha_I \beta_J} = C^I_{\alpha_I \beta_I} \delta_{IJ} \delta_{ij} \tag{4.69}$$

Eq. (4.69) shows that the Hamilton operator

1. has a block-diagonal form in the different irreps $D^{(I)}$ – the term δ_{IJ},

2. is independent of the internal structure of the representation – the term δ_{ij} and $C^I_{\alpha_I \beta_J}$ is independent of i and j,

3. has for any irrep a degenerate eigenspace of dimension d^I, the degree of the irrep. Since the degree of irreps is 1 for Abelian symmetries, it directly follows that symmetry-induced degeneracy is only possible for non-Abelian symmetries.

The main difficulty here is to find the irreps in the representation D and to construct the unitary transformation to obtain the form of Eq. (4.68) and the *properly sorted* basis with respect to a given symmetry G. In the next section, I will discuss how to achieve a *properly sorted* basis in a MPS representation.

4.3 Construction of symmetric MPSs

Global symmetries of a physical system lead to a block-diagonal Hamiltonian for each irrep as discussed in Sec. 4.2. From a numerical perspective, this is quite useful because the problem can be divided into a bunch of smaller problems. For example the diagonalization of the Hamilton matrix can be performed in each block instead of diagonalizing the full Hamiltonian.

A requirement for this simplification is that the basis is a *properly sorted* basis with respect to the symmetry. Or in other words the states in which the Hamilton matrix is evaluated have to transform as irreps of the symmetry group G.

Consider a Hilbert space as in Eq. (2.1) and a MPS representation of a state as in Eq. (2.3). Additionally, consider a symmetry described by a group G, which is represented locally in the Hibert spaces of each site. A representation in the total Hilbert space is then readily obtained by taking the tensor product of all local representations. Now the task is to obtain an MPS that transforms as some irrep of this global representation. Or in other words, one tries to find an MPS which lies in the subspace of a given irrep after the decomposition of the representation into the form of Eq. (4.6). For the group $G = SU(2)$, such a procedure was first presented by MCCULLOCH [75] and for general compact Lie groups G by WEICHSELBAUM [76].

The crucial step in obtaining such a MPS is to consider the basic building block of the MPS which is the site-tensor A. As explained in Sec. 2.2, one can interpret this tensor as a map from two vectors onto another vector (hence A is a (2,1)-tensor).

$$A: \quad \mathcal{I}_{p-1} \times \mathcal{H}_{\text{loc},p} \to \mathcal{I}_p$$

$$|I,i,\alpha_I\rangle \otimes |\Sigma,\sigma,\alpha_\Sigma\rangle \mapsto \sum_{J,j,\alpha_J} A^{\Sigma,\sigma,\alpha_\sigma}_{I,i,\alpha_i;J,j,\alpha_J} |J,j,\alpha_J\rangle \tag{4.70}$$

It is clear from this equation that the left auxiliary and the physical index are contravariant while the right auxiliary index is covariant. However, I do not use the standard convention for indices. With contravariant indices as lower and covariant as upper indices, but rather use the position to distinguish between physical (upper) and auxiliary indices (lower). This map is invariant under the action of the symmetry G, when it is the same map after transforming the input and output vectors. This is essentially the same condition as in Sec. 4.2 for the Hamiltonian but generalized to a higher-rank tensor. And in analogy to the block-diagonal form of the Hamiltonian, conditions for the A-tensor also arise. Assume for the beginning that each individual Hilbert space has exactly one irreducible representation of the group G, so that one can label the basis in each space as $|I,i\rangle$, $|\Sigma,\sigma\rangle$ and $|J,j\rangle$. The conditions for the A-tensor can then be obtained by the following steps:

1. Combine the incoming auxiliary Hilbert space and the physical Hilbert space into a composite space by taking their tensor product. This also implies the tensor product of both irreps.

2. Decompose the tensor-product representation into irreps $\bigoplus_K n_K D^{(K)}$ by the CGe (4.9). Also find the CGc which perform the unitary transformation.

3. Now the A-tensor is reshaped to a matrix and has to be block-diagonal in the irreps and independent of the internal structure of the irreps due to Schur's lemma (4.1). This strictly enforces that the A-tensor is zero unless the irrep J is contained in the tensor-product from I and Σ. If this is the case, the A-tensor has to exactly map the matching irreps.

From this consideration, it follows that the A-tensor has to behave exactly as the CGe and is therefore given by the CGc $\Gamma^{I,\Sigma \to J}_{i,\sigma \to j}(\alpha_J)$. One might also recognize that the A-tensor for a single irrep on each leg is actually an irreducible tensor operator (Def. 4.10) which would lead

to the same result after applying the Wigner-Eckart theorem (Theo. 4.2). Because of potential outer-multiplicity, the A-tensor is not completely fixed by this condition, but is already largely compressed compared to the non-symmetric case. Three examples for $U(1)$, $SU(2)$ and $SU(3)$ may make this more concrete:

U(1)

$\quad$ $U(1)$ is an Abelian symmetry and hence all irreps are one-dimensional. Therefore the considerations above become rather trivial. Consider three irreps for each space as follows: $|I = +5, i = 1\rangle$, $|\Sigma = -3, \sigma = 1\rangle$ and $|J = +2, j = 1\rangle$. The A-tensor only has a single entry, since each Hilbert space is one-dimensional. The element might be non-zero since the irrep $|J = +2, j = 1\rangle$ is exactly the tensor-product representation $|I = +5, 1\rangle \otimes |\Sigma = -3, \sigma = 1\rangle$. The value for the single element in the A-tensor is in principle arbitrary but any normalization condition would fix the A-tensor completely.

SU(2)

$\quad$ $SU(2)$ is a non-Abelian group but without outer-multiplicity. Consider the following irreps in the three spaces: $|I = 0.5, i = 0.5\rangle$, $|I = 0.5, i = -0.5\rangle$, $|\Sigma = 0.5, \sigma = 0.5\rangle$, $|\Sigma = 0.5, \sigma = -0.5\rangle$ and $|J = 0, j = 0\rangle$. These are two doublets and one singlet. First of all, $|J = 0, j = 0\rangle$ lies in the tensor product of the two others so that the A-tensor can be non-zero. But the $2 \cdot 2 \cdot 1 = 4$ components are not allowed to be arbitrary. They have to couple the four states from the incoming Hilbert spaces into a singlet state by the CGc $\Gamma_{i,\sigma \to 0}^{0.5, 0.5 \to 0}$ which in this case is the common 2×2 matrix which couples to doublets onto a singlet. The resulting freedom again is a single factor which would be fixed by a normalization condition. From this example it becomes clear that non-Abelian symmetries create a lot more constraints in comparison to Abelian symmetries.

SU(3)

$\quad$ $SU(3)$ is a non-Abelian group with outer-multiplicity. Consider the same irrep in each space which is given by the *octet*-representation of $SU(3)$ and is labeled as $I = (1,1)$. It has 8 internal states and the *octet* lies within the tensor product of two *octets* so that the A-tensor is allowed to be non-zero. The A-tensor has $8 \cdot 8 \cdot 8 = 512$ elements. Now an additional complexity arises because the *octet* appears two times in the tensor product decomposition which means that there exist two different possibilities to couple the 64 states in the tensor product onto the *octet* representation, which is marked by the outer-multiplicity index α_J in the CGc. The A-tensor can then perform an arbitrary combination of the two different *octets* arising in the decomposition. This originates already from the freedom in the CGc if outer-multiplicity is present. Overall, this is a remarkable compression from the original 512 components of the A-tensor.

Now consider the general case, where in each Hilbert space there is a collection of irreps and a *properly sorted* basis with respect to the symmetry G labeled as $|I, i, \alpha_I\rangle$, $|\Sigma, \sigma, \alpha_\Sigma\rangle$ and $|J, j, \alpha_J\rangle$. Then the A-tensors split in the same manner as the Hamiltonian into a part, which is determined by the symmetry and a part which maps the degeneracy indices. It can be written as:

$$A_{I,i,\alpha_i;J,j,\alpha_J}^{\Sigma,\sigma,\alpha_\sigma} = \Gamma_{i,\sigma \to j}^{I,\Sigma \to J(\alpha_J)} \tilde{A}_{I,\alpha_I;J\alpha_J}^{\Sigma,\alpha_\Sigma} \tag{4.71}$$

When writing the A-tensors in this form, they are automatically invariant under the symmetry G. $\tilde{A}$ is called the *reduced A-tensor* and its elements are referred to as *reduced matrix elements*. Note again the outer-multiplicity index in the CGc in the general case, which complicates the situation, because it arises in both parts. Since the degeneracy part of the A-tensor can reorder the multiple copies of an irrep, a unique convention for the CGc is absolutely mandatory, since otherwise the ordering of the copies becomes confused. In this thesis however, I focus on the groups $U(1)$ and $SU(2)$ which are free of any multiplicity.

Now if the A-tensors are constructed in a symmetric form, it is easy to show that the resulting MPS as an element of the full lattice Hilbert space $\mathcal{H}$ transforms exactly as an irrep of the representation in $\mathcal{H}$. To see this, it is again useful to interpret the MPS as an RG process as in Sec. 2.2. In this picture, the last A-tensor $A(L)$ maps states from $\mathcal{I}_{L-1}$ and $\mathcal{H}_L$ onto an element of the full Hilbert space $\mathcal{H}$ since then every sum in the definition of the MPS (2.3) is passed. Per construction, the spaces $\mathcal{I}_{L-1}$ and $\mathcal{H}_L$ have *properly sorted* bases and also $A(L)$ maps them to a *properly sorted* basis in $\mathcal{I}_L \subset \mathcal{H}$. One can then even controls under which irrep the full MPS transforms by demanding $\mathcal{I}_L = \{|T,t\rangle\}$. This is the irrep labeled by T (which has quantum number T) and with internal state label (z-quantum number) t. For completeness, it is also necessary to choose the incoming auxiliary space of the first A-tensor to be $\mathcal{I}_0 = \{|0,0\rangle\}$. Where 0 is the label for the trivial representation (*singlet*), which is unique for any group G.

This splitting of the A-tensor can be performed for any group G as long as the CGe and the CGc can be determined. For all compact Lie groups in particular, this is a straightforward task, however, caution has to be paid in the case of outer-multiplicity. For the compact Lie group $SU(2)$, the CGc can be evaluated efficiently and furthermore even contractions and recoupling coefficients can be obtained by efficient formulas which make the algorithm especially useful for $SU(2)$ as it will be discussed in Sec. 4.5. In this case, the algorithms can be formulated with the reduced A-tensors only while the CGc are solely in mind. The reduced A-tensors has less elements which is one of the crucial numerical advantages of incorporating symmetries. The bond dimension χ_{red} of the reduced A-tensors describes not the full bond dimension χ as soon as the symmetry is non-Abelian. For a *properly sorted* basis $|I,i,\alpha_I\rangle$, the individual symmetry blocks for the quantum number I has dimension n_I. The reduced bond dimension χ_{red} is then computed as:

$$\chi_{\text{red}} = \sum_I n_I \tag{4.72}$$

and the full bond dimension χ might be larger for non-Abelian symmetries:

$$\chi = \sum_I d^I n_I \tag{4.73}$$

Here, d^I is the dimension of the irrep I.

4.4 Construction of symmetric MPOs

When the A-tensors are constructed symmetrically, one obviously also needs to build the MPO in the same basis to calculate expectation values from operators. This can be achieved in two steps:

1. Construct the local operators as irreducible tensor operators so that they already operate on the *properly sorted* basis and calculate their decomposition from the Wigner-Eckart theorem (Eq. (4.56)) into the reduced matrix elements and CGc.

2. Couple these irreducible tensor operators in an analogous manner to the MPS to an operator in the full Hilbert space via the auxiliary spaces from the MPO.

First, I want to introduce in some detail the standard local operators of quantum lattice models and how to build them in a symmetric form. Then, I will describe the symmetric structure of the whole MPO.

4.4.1 Local operators for quantum lattice models

The most common lattice models consist of spin-, fermionic and bosonic degrees of freedom. Since bosonic models are not part of this thesis, I will omit further considerations regarding bosons. Fermions are restricted to a set of orbitals: in the easiest case to a single s-orbital. Since there is no intrinsic spin in one dimension, the fermions become an explicit spin one-half degree of freedom.

A quantum-mechanical spin of magnitude s is per definition the irrep with highest weight s of the group $SU(2)$ which was derived in Sec. 4.1.3. The observables which describe the spin degree of freedom are the Casimir operator (Def. 4.4) S^2 and the generators of $\mathfrak{su}(2)$, namely S^x, S^y and S^z. They are all Hermitian operators in the vector space of the irrep which is at the same time the $2s + 1$-dimensional Hilbert space of a lattice site containing one spin. The generators can be combined into an irreducible tensor operator as already discussed in Sec. 4.1.5. Note that they need to be transformed to the generators of $\mathfrak{sl}(2,\mathbb{C})$ beforehand. The result for the reduced matrix elements of this operator can be obtained directly from Eq. (4.63). This gives the single reduced matrix element of a spin operator $S^{[1]}$ for a lattice site which consists of the spin s irrep of $SU(2)$:

$$\left\langle s \, \middle\| \, S^{[1]} \, \middle\| \, s \right\rangle = \sqrt{s(s+1)} \tag{4.74}$$

A spin one-half fermion in an s-orbital builds a 4-dimensional Hilbert space spanned by the states $|0\rangle$, $|\uparrow\rangle$, $|\downarrow\rangle$ and $|\uparrow\downarrow\rangle$. The creation $c_\sigma^\dagger$ and annihilation c_σ operators for the fermion with spin projection $\sigma = \uparrow, \downarrow$ are 4×4-matrices on this Hilbert space. E.g. the annihilation operators for both spin projections with respect to the order in which I listed the basis states above take the following form:

$$c_\uparrow = \begin{pmatrix} 0 & 1 & 0 & 0 \\ 0 & 0 & 0 & 0 \\ 0 & 0 & 0 & 1 \\ 0 & 0 & 0 & 0 \end{pmatrix} \qquad c_\downarrow = \begin{pmatrix} 0 & 0 & 1 & 0 \\ 0 & 0 & 0 & -1 \\ 0 & 0 & 0 & 0 \\ 0 & 0 & 0 & 0 \end{pmatrix} \tag{4.75}$$

The fermionic operators obey the standard fermionic anticommutation relations $\{c_\sigma^\dagger, c_\tau\} = \delta_{\sigma\tau}$.

One might recognize that the operators

$$s_x = \frac{1}{2}(c_\uparrow^\dagger c_\downarrow + c_\downarrow^\dagger c_\uparrow) \tag{4.76}$$

$$s_y = \frac{1}{2i}(c_\uparrow^\dagger c_\downarrow - c_\downarrow^\dagger c_\uparrow) \tag{4.77}$$

$$s_z = \frac{1}{2}(c_\uparrow^\dagger c_\uparrow - c_\downarrow^\dagger c_\downarrow) \tag{4.78}$$

fulfill the same commutation relations as the generators of $SU(2)$ in Eq. (4.23) and therefore constitute a representation of the Lie algebra of $\mathfrak{su}(2)$ which might be extended to a group representation via the exponential map. This group representation is referred to as the *spin-$SU(2)$* symmetry for fermions. Notice that this representation is reducible. However, one is not faced with the problem of finding a unitary transformation which diagonalizes the Casimir and one of the generators, because the standard basis is already a *properly sorted* basis. It is easy to compute that the states $|\uparrow\rangle$ and $|\downarrow\rangle$ transform as the doublet (spin one-half) irrep of $\mathfrak{su}(2)$ with weights (eigenvalue of s_z) $+\frac{1}{2}$ and $-\frac{1}{2}$ respectively. The states $|0\rangle$ and $|\uparrow\downarrow\rangle$ both transform under the trivial irrep so that one needs to introduce a degeneracy index to distinguish them. With the convenient basis label $|s,s_z,\alpha_s\rangle$ the basis elements can be written as

$$|0\rangle := |s = 0, s_z = 0, \alpha_0 = 1\rangle \tag{4.79}$$

$$|\uparrow\rangle := |s = 1/2, s_z = 1/2\rangle \quad |\downarrow\rangle := |s = 1/2, s_z = -1/2\rangle \tag{4.80}$$

$$|\uparrow\downarrow\rangle := |s = 0, s_z = 0, \alpha_0 = 2\rangle \tag{4.81}$$

The reduced matrix elements of the generators of the spin-$SU(2)$ symmetry can be obtained readily by the same argument as for the quantum spins by Eq. (4.63). The creation and annihilation operators themselves, however, might also form an irreducible tensor operator for $SU(2)$, so that they can also be compressed through the Wigner-Eckart theorem. Indeed, the operators $c_{1/2}^{[1/2]} = -c_\downarrow$ and $c_{-1/2}^{[1/2]} = c_\uparrow$ fulfill the requirements for a irreducible tensor operator in Eq. (4.52), (4.53) and (4.54) for $k = \frac{1}{2}$. Half-integer irreducible tensor operators are usually referred to as *spinors*. It is therefore possible to calculate the reduced matrix elements for the annihilation spinor to factor out the symmetry part of these operators. Through the application of the Wigner-Eckart theorem from Eq. (4.56), one readily obtains the following reduced matrix representation in the basis from Eq. (4.79), (4.80) and (4.81):

$$c^{[1/2]} = \begin{pmatrix} 0 & \sqrt{2} & 0 \\ 0 & 0 & 1 \\ 0 & 0 & 0 \end{pmatrix} \tag{4.82}$$

The Hermitian adjoint corresponds to the spinor $c^{\dagger[1/2]}$ if one defines $c_{1/2}^{\dagger[1/2]} = c_\uparrow^\dagger$ and $c_{-1/2}^{\dagger[1/2]} = c_\downarrow^\dagger$. Its matrix elements may then be computed by Eq. (4.62):

$$c^{\dagger[1/2]} = \begin{pmatrix} 0 & 0 & 0 \\ 1 & 0 & 0 \\ 0 & -\sqrt{2} & 0 \end{pmatrix} \tag{4.83}$$

Note that both spinors fulfill the requirements for irreducible tensor operators (Eq. (4.52), (4.53) and (4.54)) but this choice is not unique. Each spinor can be multiplied by -1 and still obeys the requirements. However, one has to be careful that the actual choice respects the condition $c^{\dagger[1/2]} = \left(c^{[1/2]}\right)^{\dagger}$. It is useful to recognize that the anticommutation relations for the reduced matrix elements of the spinors are unfamiliar. This is a consequence of the symmetry relations of the CGc and needs to be taken care of in numerical implementations. E.g. one finds for the commutator of two annihilation spinors $\left[c_i^{[1/2]}, c_j^{[1/2]}\right] = 0$:

$$\left(c_i^{[1/2]} \times c_j^{[1/2]}\right)_0^{[0]} = \sum_{m_1,m_2} \Gamma_{m_1,m_2,0}^{1/2,1/2,0} c_{i,m_1}^{[1/2]} c_{j,m_2}^{[1/2]} \tag{4.84}$$

$$= (-1)(-1)^{1/2+1/2-0} \sum_{m_1,m_2} \Gamma_{m_2,m_1,0}^{1/2,1/2,0} c_{j,m_2}^{[1/2]} c_{i,m_1}^{[1/2]} \tag{4.85}$$

$$= \left(c_j^{[1/2]} \times c_i^{[1/2]}\right)_0^{[0]} \tag{4.86}$$

Where the first minus sign results from the anticommutation of $c_{i,\sigma}$ and $c_{j,\tau}$ and the phase factor from the symmetries of the CGc $\Gamma_{...}^{...}$.

One might further recognize that the operators

$$t_x = \frac{1}{2}(c_\uparrow c_\downarrow + c_\downarrow^\dagger c_\uparrow^\dagger) \tag{4.87}$$

$$t_y = \frac{1}{2i}(c_\uparrow c_\downarrow - c_\downarrow^\dagger c_\uparrow^\dagger) \tag{4.88}$$

$$t_z = \frac{1}{2}(1 - (c_\uparrow^\dagger c_\uparrow + c_\downarrow^\dagger c_\downarrow)) \tag{4.89}$$

obey the same commutation relations as the generators of $SU(2)$ in Eq. $(4.23)^1$. Since additionally $[t_i, s_j] = 0$, these operators form a second independent representation of $\mathfrak{su}(2)$. This additional $SU(2)$ symmetry is referred to as the *charge-$SU(2)$* [91, 92]. In fact s_i and t_i together form a representation of the 6-dimensional Lie algebra $\mathfrak{so}(4)$. The Lie algebra $\mathfrak{so}(4)$ is not semisimple as it decomposes into the direct product of Lie subalgebras. Namely $\mathfrak{so}(4) \sim \mathfrak{su}(2) \times \mathfrak{su}(2)$ so that its representation theory is basically the same as for $\mathfrak{su}(2)$. An irrep can therefore be labeled by two spin labels. The fermionic basis is then given by:

$$|0\rangle := |s = (0,1/2), s_z = (0,1/2)\rangle \quad |\uparrow\downarrow\rangle := |s = (0,1/2), s_z = (0,-1/2)\rangle \tag{4.90}$$

$$|\uparrow\rangle := |s = (1/2,0), s_z = (1/2,0)\rangle \quad |\downarrow\rangle := |s = (1/2,0), s_z = (-1/2,0)\rangle \tag{4.91}$$

The two spinors $c^{\dagger[1/2]}$ and $c^{[1/2]}$ can be combined into a four-component spinor $\psi^{[1/2,1/2]}$ which forms an irreducible tensor operator with respect to $\mathfrak{so}(4)$ with the irrep $(1/2,1/2)$. Its reduced

---

1   The operators t_x and t_y might be multiplied by a sign (-1) and still obey the required commutation relations. In a lattice model one has to define a site-dependent sign $(-1)^i$ for t_x and t_y so that the Hamiltonian is invariant under the represented $SU(2)$ symmetry. Actually, this is only possible if the lattice is bipartite and the sign needs to switch between the sublattices. The operators t_i correspond in this case to the action of an asymmetric particle-hole transformation acting on the s_i [90].

matrix elements can be computed with respect to the basis in Eq. (4.90) and (4.91):

$$\psi^{[1/2,1/2]} = \begin{pmatrix} 0 & \sigma\sqrt{2} \\ \sqrt{2} & 0 \end{pmatrix}, \tag{4.92}$$

where σ is a possible extra sign in the definition of t_x and t_y in Eq. (4.87) and (4.88) respectively.

I have introduced the basic ingredients for lattice models, namely the system of a quantum spin and a fermion in a *s*-orbital. The obtained representations in these local quantum systems can always be extended to representations on the full Hilbert space via the tensor product operation. It is important to clarify that the symmetries can only be used in the numerical solution if the Hamiltonian is an intertwiner, i.e. if it commutes with the representation of all group elements or equivalently with the representation of the generators. As will become clear later, in the central model system for this thesis only the spin-$SU(2)$ can be exploited while the Hamiltonian breaks the charge-$SU(2)$.

4.4.2 Symmetric MPO

The construction of the local operators in the form of reduced matrix elements times the CGc according to the Wigner-Eckart theorem is only the first step in constructing the full MPO. According to the definition in Eq. (2.53), the full MPO is obtained by the matrix products of the site matrices $\boldsymbol{W}^{\sigma\sigma'}(i)$. In the case that the local basis $|\sigma\rangle$ is transformed into a *properly sorted* basis $|\Sigma,\sigma,\alpha_\sigma\rangle$ each site matrix $\boldsymbol{W}^{\sigma\sigma'}$ can be decomposed into irreducible matrix elements times the CGc:

$$\boldsymbol{W}^{\Sigma_1\sigma_1\alpha_{\Sigma_1};\Sigma_2\sigma_2\alpha_{\Sigma_2}} = \boldsymbol{W}^{[k]\Sigma_1\alpha_{\Sigma_1};\Sigma_2\alpha_{\Sigma_2}} \Gamma^{\Sigma_2,k\to\Sigma_1}_{\sigma_2,m\to\sigma_1} \tag{4.93}$$

This procedure was discussed in Sec. 4.4.1 for the common local operators of quantum lattice models. The auxiliary matrix structure of $\boldsymbol{W}^{[k]\Sigma_1\alpha_{\Sigma_1};\Sigma_2\alpha_{\Sigma_2}}$ can now be interpreted as the following map:

$$W: \quad \mathcal{I}_{p-1} \otimes \mathcal{V}_k \to \mathcal{I}_p$$

$$|A,a,\alpha_A\rangle \otimes |k,m\rangle \mapsto \sum_{B,b,\alpha_B} \left(W^{[k]}_m\right)^{\Sigma_1\alpha_{\Sigma_1}:\Sigma_2\alpha_{\Sigma_2}}_{A,a,\alpha_A;B,b,\alpha_B} |B,b,\alpha_B\rangle, \tag{4.94}$$

where $\mathcal{V}_k$ is the carrier space of the irrep with label k. Eq. (4.94) is an equation for an irreducible tensor operator for each value of the quantum numbers $\Sigma\alpha_\Sigma$ and $\Sigma'\alpha_{\Sigma'}$ according to the Definition in Def. 4.10. The form is also in analogue to Eq. (4.70) and it follows that $\left(W^{[k]}_m\right)^{\Sigma_1\alpha_{\Sigma_1}:\Sigma_2\alpha_{\Sigma_2}}_{A,a,\alpha_A;B,b,\alpha_B}$ again decomposes in a reduced part and a CGc. In total, one obtains two CGc for the MPO site tensors $W(i)$:

$$W^{\Sigma_1\sigma_1\alpha_{\Sigma_1};\Sigma_2\sigma_2\alpha_{\Sigma_2}}_{Aa\alpha_A;Bb\alpha_B} = \sum_{k,m} W^{[k]\Sigma_1\alpha_{\Sigma_1};\Sigma_2\alpha_{\Sigma_2}}_{A\alpha_A;B\alpha_B} \Gamma^{\Sigma_2,k\to\Sigma_1}_{\sigma_2,m\to\sigma_1} \Gamma^{A,k\to B}_{a,m\to b} \tag{4.95}$$

The sum goes over all values of k for which the product of the two CGc is none-zero. Note that the quantum number k plays the role of an outgoing quantum number for the first CGc while

it is an incoming quantum number in the second CGc. This is consistent, since Eq. (4.95) is essentially a contraction of the two CGc. In fact, this contraction builds a *yoga fusion tree* as described in Ref. [78].

4.5 Construction of symmetric algorithms

The decomposition of both the A-tensors and the W-tensors into a reduced part and the CGc can be exploited to decompose contractions of several of those basic building blocks. The one part is the contraction of the reduced matrix elements and the other part contains the contraction of the CGc. A key step is that the CGc part can be cast analytically into the evaluation of recoupling coefficients similar to the case of the product of irreducible matrix elements (Eq. (4.58)) as was first introduced by McCulloch [75] in his description of the non-Abelian DMRG algorithm. In Sec. 2.7, I will describe several basic operations on MPSs for which all of them can be performed on the level of the reduced matrix elements while the CGc part enters only via some effective coefficients. These coefficients can be calculated efficiently so that the overhead is very small. As examples, I want to present the sweepstep (Eq. (2.57) and (2.59)), the update of the environments (Eq. (2.65)) and the action of the effective Hamiltonian for the local optimization of a single A-tensor (Eq. (3.5)). Other operations – like the product of two MPS or MPO site-tensors – can also be evaluated by similar expressions. They are presented in the appendix in Chap. B.

4.5.1 MPS sweeping

The basic operation for the sweepstep consists of bringing the A-tensor at site p into the left- or right-canonical form and shifting the rest of the transformation to the next or previous site tensor as discussed in Sec. 2.7.1. For the right sweepstep, one therefore needs to reshape the A-tensor by combining the incoming auxiliary index i with the physical index σ as in Eq. (2.57). Notice that the combination of both indices essentially corresponds to a bijective unitary mapping Π of the states from the sets $\mathcal{I}$ and $\mathcal{H}_{\mathrm{loc}}$ into the tensor product $\mathcal{K} := \mathcal{I} \otimes \mathcal{H}_{\mathrm{loc}}$. In this case, Π should map the states into the *properly sorted* basis so that it has to behave like the CGc because that is the case they were defined for[1]. The states that transform under the same irrep have to be mapped after some canonical bijection for tensor product states. One can obtain the reshaped tensor $\tilde{A}$ with the help of the inverse of Π:

$$
\tilde{A}: \quad \mathcal{K} \otimes \mathcal{J}^* \to \mathbb{C}
$$
$$
|K,k,\alpha_K\rangle \otimes \langle J,j,\alpha_J| \mapsto \sum_{Ii\alpha_I;\Sigma\sigma\alpha_\Sigma} \left(\Pi^{-1}\right)^{\Sigma\sigma\alpha_\sigma}_{Ii\alpha_i;Kk\alpha_K} A^{\Sigma\sigma\alpha_\sigma}_{Ii\alpha_i;Jj\alpha_J}
\tag{4.96}
$$

After the decomposition of both tensors Π^{-1} and A, the CGc part reads as follows:

$$
\sum_{i\sigma} \Gamma^{K\to I,\Sigma}_{k\to i,\sigma} \Gamma^{I,\Sigma\to J}_{i,\sigma\to j} = \delta_{JK}\delta_{jk}
\tag{4.97}
$$

---

1 Π actually has the same structure as the A-tensor itself.

Here, the first CGc is actually the inverse of the standard CGc but the CGc form a unitary matrix and for $SU(2)$ they are all real so that the inverse is identical with the standard CGc. Eq. (4.97) is therefore a standard orthonormality condition for the CGc. Note that an analogous equation to Eq. (4.97) also ensures that Π is unitary if it is decomposed into the standard CGc. The Kronecker deltas imply that $\tilde{A}$ behaves as a scalar operator with respect to the symmetry as required by Schur's lemma. In the convenient notation for a reshaping process which omits the concrete form of Π^{-1} one therefore obtains for the reduced matrix elements of the reshaped tensor:

$$\tilde{A}^{J(I;\Sigma),(\alpha_I \alpha_\Sigma)}_{J\alpha_J} = A^{\Sigma\alpha_\Sigma}_{I\alpha_I;J\alpha_J} \tag{4.98}$$

This equation should be understood that for a fixed value of the outgoing quantum number J one has to couple the irreps with quantum number I and Σ to J and afterwards reshape the degeneracy indices α_I and α_Σ into a composite index $(\alpha_I \alpha_\Sigma)$. The resulting tensor is then a rectangular matrix for which one can apply either the QR or the SVD decomposition (Chap. A) as discussed in Sec. 2.7.1. The back transformation is performed with Π which has the same symmetry structure as A so that Eq. (4.98) can be read backwards.

These considerations can be transferred to the other direction, namely the left sweepstep. In this case, the bijection Π maps the states from the sets $\mathcal{J}^*$ and $\mathcal{H}_{\text{loc}}$ onto the tensor product $\mathcal{K}^* := \mathcal{J}^* \otimes \mathcal{H}_{\text{loc}}$. The CGc part of Π consists then of $\Gamma^{K,\Sigma\to J}_{k,\sigma\to j}$ for which one needs an additional factor of $\sqrt{\frac{2K+1}{2J+1}}$ to ensure that Π is unitary. The CGc part of the analogue of Eq. (4.96) is then slightly different:

$$\sqrt{\frac{2K+1}{2J+1}} \sum_{\sigma j} \Gamma^{J\to K,\Sigma}_{j\to k,\sigma} \Gamma^{I,\Sigma\to J}_{i,\sigma\to j} = \sqrt{\frac{2K+1}{2J+1}} \sum_{\sigma j} \Gamma^{K,\Sigma\to J}_{k,\sigma\to j} \Gamma^{I,\Sigma\to J}_{i,\sigma\to j}$$
$$= \sqrt{\frac{2K+1}{2J+1}} \frac{2J+1}{\sqrt{(2I+1)(2K+1)}} \delta_{IK}\delta_{ik} = \sqrt{\frac{2J+1}{2I+1}} \delta_{IK}\delta_{ik}, \tag{4.99}$$

where again the inverse CGc is substituted with its standard CGc and the second equality follows readily when using a symmetry relation of the CGc. Because of the Kronecker deltas, the reshaped tensor transforms again as a scalar but the additional factor in Eq. (4.99) needs to be taken into account when reshaping for a left sweepstep:

$$\tilde{A}^{I\alpha_I}_{I(J;\Sigma),(\alpha_J \alpha_\Sigma)} = A^{I\alpha_I;\Sigma\alpha_\Sigma}_{J\alpha_J} \sqrt{\frac{2J+1}{2I+1}} \tag{4.100}$$

For the back transformation one has to use the bijection Π which has the normalization factor $\sqrt{\frac{2I+1}{2J+1}}$ so that Eq. (4.100) can be read backwards, but with the inverse factor.

4.5.2 Environment updates and effective Hamiltonian

Important contractions for any DMRG-related method are the updates of the environments as described in Eq. (2.65) for the left environment L. The environment tensors L and R are rank 3 tensors and structurally similar to the A-tensors. More precisely, in my convention, the right environment R is structurally identical to the A-tensor while the left environment L is

identical to the adjoint of an A-tensor. The decomposition of all the tensors can be exploited to obtain two parts for Eq. (2.65). As usual one part for the reduced matrix elements and one for the CGc. The CGc part reads as:

$$\Gamma^{J'\to I'A'}_{j'\to i',a'} = \sum_{\sigma_1,\sigma_2,i,a,j,m} \Gamma^{J'\to J,\Sigma_1}_{j'\to j,\sigma_1} \Gamma^{J\to IA}_{j\to i,a} \Gamma^{I,\Sigma_2\to I'}_{i,\sigma_2\to i'} \Gamma^{\Sigma_2,k\to\Sigma_1}_{\sigma_2,m\to\sigma_1} \Gamma^{A,k\to A'}_{a,m\to a'} \tag{4.101}$$

For clearness, I used the split coefficients here but as discussed previously they are identical to the standard CGc. Hence, one substitutes them and multiplies Eq. (4.101) by $\Gamma^{I'A'\to N'}_{i',a'\to n'}$ and sums over i' and and a'. The left hand side is then $\delta_{N'J'}\delta_{n'j'}$ due to the orthogonality conditions for the CGc and the right hand side turns out to be a recoupling coefficient for four angular momenta as defined in Eq. (4.47) by using Eq. (4.50):

$$\delta_{N'J'}\delta_{n'j'} = \begin{bmatrix} I & \Sigma_2 & I' \\ A & k & A' \\ J & \Sigma_1 & J' \end{bmatrix} \delta_{N'J'}\delta_{n'j'} \tag{4.102}$$

The $[\ldots]$-symbol can be shifted into the reduced part of the equation so that one obtains the correct CGc for the updated L automatically. The reduced matrix elements can be contracted ordinarily but with the coupling coefficient included:

$$L_{I',\alpha_{I'};A',\alpha_{A'};J'\alpha_{J'}}(l+1) = \sum \begin{bmatrix} I & \Sigma_2 & I' \\ A & k & A' \\ J & \Sigma_1 & J' \end{bmatrix}$$
$$B^{\dagger\Sigma_1,\alpha_{\Sigma_1}}_{J,\alpha_J;J'\alpha_{J'}}(l) L_{I,\alpha_I;A,\alpha_A;J\alpha_J}(l) A^{\Sigma_2,\alpha_{\Sigma_2}}_{I,\alpha_I;I'\alpha_{I'}}(l) W^{[k]\Sigma_1\alpha_{\Sigma_1};\Sigma_2\alpha_{\Sigma_2}}_{A\alpha_A;A'\alpha_{A'}}(l) \tag{4.103}$$

The action of the effective Hamiltonian as in Eq. (3.5) shares exactly the same CGc structure so that one can immediately deduce that the same coupling coefficient applies. When performing the update of the right environment, however, there is a subtle difference as compared to Eq. (4.101). The difference has a similar reason as for the two different sweepsteps (Sec. 4.5.1). A careful evaluation of the CGc leads to the following coupling coefficient[1]:

$$R_{I,\alpha_I;A,\alpha_A;J\alpha_J}(l-1) = \sum \frac{2J'+1}{2J+1} \begin{bmatrix} I & \Sigma_2 & I' \\ A & k & A' \\ J & \Sigma_1 & J' \end{bmatrix}$$
$$A^{\Sigma_2,\alpha_{\Sigma_2}}_{I,\alpha_I;I'\alpha_{I'}}(l) R_{I',\alpha_{I'};A',\alpha_{A'};J'\alpha_{J'}}(l) B^{\dagger\Sigma_1,\alpha_{\Sigma_1}}_{J,\alpha_J;J'\alpha_{J'}}(l) W^{[k]\Sigma_1\alpha_{\Sigma_1};\Sigma_2\alpha_{\Sigma_2}}_{A\alpha_A;A'\alpha_{A'}}(l) \tag{4.104}$$

Beside the additional coupling coefficients, the algorithm can be performed identically by manipulating the reduced matrix elements only.

---

1   It might be more convenient to evaluate the formula for an identity MPO tensor and an identity environment. Then one can directly deduce the difference between the left and the right environment updates.

The Kondo lattice model

The Kondo lattice model (KLM) is the central many-body model system for this thesis. The model has its name from the famous Kondo impurity model introduced by KONDO [93] to explain the resistance minimum of metals like Au or Cu slightly doped with Fe or Ni. The Fe or Ni atoms build magnetic impurities in these systems which can be well described by the Kondo impurity model. In the lattice version of the model, the impurities are equally distributed at every lattice site with the same point group symmetry.

In this chapter, I will introduce the Hamiltonian and give an overview over experimental and theoretical studies in Sec. 5.1. Afterwards, I will present perturbative approximations for the KLM in Sec. 5.2 and finally discuss the Doniach phase diagram in Sec. 5.3.

5.1 Introduction

The class of materials with incomplete $4f$ or $5f$ shells shows a large variety of anomalous properties. In particular, heavy quasi-particles develop in these materials wherefore they are also called *heavy-fermion* systems. The basic ingredient for this effect is the presence of two distinct electronic orbitals per lattice site so that a simple one-band model, e.g. the Hubbard model, is not appropriate for their description.

A model candidate for the description of some properties of the heavy-fermion systems is the KLM. I will introduce therefore the Hamiltonian and its symmetries in some detail in the upcoming subsection and give afterwards an experimental and theoretical overview.

5.1.1 Hamiltonian and symmetries

The Hamiltonian for the KLM can be written in standard notation as:

$$H = -\sum_{i,j,\sigma} t_{ij} c_{i\sigma}^{\dagger} c_{j\sigma} + J \sum_{i} \boldsymbol{S}_i \cdot \boldsymbol{s}_i \tag{5.1}$$

The lattice indices i and j count the sites of a d-dimensional lattice $\mathcal{L}$, i.e. $i = (i_1, \ldots, i_d) = i_1 \boldsymbol{a}_1 + \cdots + i_d \boldsymbol{a}_d$ where $\boldsymbol{a}_i$ are primitive lattice vectors. $c_{i\sigma}^{\dagger}$ ($c_{i\sigma}$) is the creation (annihilation) operator for an electron with spin projection $\sigma = \uparrow, \downarrow$ at lattice site i and $\boldsymbol{s}_i = \sum_{\tau,\tau'} c_{i\tau}^{\dagger} \boldsymbol{\sigma}_{\tau\tau'} c_{i\tau'}$ is the orbital spin of the electrons at site i. Here $\boldsymbol{\sigma}$ is the vector of Pauli matrices which is the defining representation of $SU(2)$ (see Eq. (4.22)). $\boldsymbol{S}_i$ is a quantum-spin with quantum number S and adds an additional degree of freedom. The quantum-spins are called *localized*

moments throughout this thesis. The KLM therefore has a local Hilbert space $\mathcal{H}_{\text{loc}}$ at each site which consists of the tensor product of the Hilbert space of a single electronic orbital and a quantum-spin S. The local dimension d is therefore $d = 4 \cdot (2S + 1) \stackrel{S=1/2}{=} 8$. The first term in Eq. (5.1) describes the kinetic part of the electronic system, i.e. t_{ij} are hopping amplitudes for the tunneling of an electron from lattice site i to lattice site j. For a translationally invariant system, t_{ij} can be diagonalized by a Fourier transformation which leads to a single band $\varepsilon(\boldsymbol{k})$ with band width W. The second term describe the interaction between the orbital spin and the localized moments at the same lattice site i. The interaction energy J is taken to be positive ($J > 0$) in this thesis. For this choice, the coupling of the two spins is antiferromagnetic. The less studied ferromagnetic KLM has a negative exchange interaction $J < 0$.

The two distinct parts, namely the electronic operator $c_{i\sigma}^{\dagger}$ and the localized moments $\boldsymbol{S}_i$, can be assigned to the s-like orbital and the f orbital in the heavy-fermion systems respectively. Since the s-like orbitals in these materials are weakly correlated, they form a noninteracting electron band. On the contrary, the f orbitals are strongly correlated and under specific circumstances their valence is frozen out and there remains only an effective spin-degree of freedom. For this to happen, the f-shell needs to be half-filled and the energetic width of the f-levels needs to be small as compared to their distance to the band energies from the s-orbitals. This defines actually a specific limit of the more general periodic Anderson model (PAM) [8]:

$$H = -\sum_{i,j,\sigma} t_{ij} c_{i\sigma}^{\dagger} c_{j\sigma} + V \sum_{i\sigma} \left(c_{i\sigma}^{\dagger} f_{i\sigma} + f_{i\sigma}^{\dagger} c_{i\sigma} \right) + \varepsilon_f \sum_{i\sigma} f_{i\sigma}^{\dagger} f_{i\sigma} + \frac{U}{2} \sum_{i\sigma} f_{i\sigma}^{\dagger} f_{i\sigma} f_{i-\sigma}^{\dagger} f_{i-\sigma} \quad (5.2)$$

The limit corresponds to $V \ll U$ and at half-filling one can map the low energy part of the PAM by a Schrieffer Wolff transformation [94] onto the KLM with (antiferromagnetic) Kondo coupling $J = \frac{8V^2}{U}$. Beside the role of the low-energy model of the PAM for which the KLM is in the weak coupling regime, the KLM with arbitrary exchange coupling J defines an independent quantum lattice model.

The Hamiltonian of the KLM in Eq. (5.1) has several symmetries. First, H commutes with representations of the generators of the spin-$SU(2)$ symmetry. The representations arise from the multiple tensor products of the elementary representations in the Hilbert space of an electronic orbital and of a quantum-spin as described in Sec. 4.4.1. This implies that the total spin $\boldsymbol{S}_{\text{tot}} = \sum_i \boldsymbol{S}_i + \boldsymbol{s}_i$ is a conserved quantity. That the Hamiltonian commutes with these generators can be verified by direct computation. Another route is to show that the two terms in the Hamiltonian are actually products of irreducible tensor operators with target quantum number $k = 0$. As introduced in Eq. (4.74) the operator $\boldsymbol{S}$ of the localized moments is a spin-1 operator $S^{[1]}$ which is also true for the electronic spin $s^{[1]}$ (see Eq. (4.76), (4.77) and (4.78)). The second term is then the product of both irreducible tensor operators as introduced in Eq. (4.57) with $K = 0$. The creation and annihilation operators build spinors with $k = 1/2$ (Eq. (4.82) and (4.83)) and the hopping term in Eq. (5.1) is the product of both spinors again to a singlet operator ($K = 0$). This allows to rewrite the Hamiltonian in a manifestly $SU(2)$ invariant form:

$$H^{[0]} = -\sqrt{2} \sum_{i,j,\sigma} t_{ij} \left(c_i^{\dagger[1/2]} \times c_j^{[1/2]} \right)^{[0]} + \sqrt{3} J \sum_i \left(S_i^{\dagger[1]} \times s_i^{[1]} \right)^{[0]} \quad (5.3)$$

Here I adapt the notation according to the notation in Sec. 4.1.5. The square roots balance the CGc in the definition of the product of irreducible tensor operators (Eq. (4.57)).

Beside the spin-$SU(2)$ symmetry, the KLM Hamiltonian also has a $U(1)$-particle symmetry, i.e. the total electron number $N = \sum_{i\sigma} c^\dagger_{i\sigma} c_{i\sigma}$ is conserved. In the special case of a bipartite hopping matrix, this symmetry can be extended to a $SU(2)$-charge symmetry. Since this will not be the case for the model studied in this thesis, the corresponding charge-$SU(2)$ symmetric formulation of the Hamiltonian will be omitted. Finally the KLM can have discrete spatial symmetries which are determined by the point group of the lattice.

5.1.2 Experimental overview

The heavy-fermion materials are characterized by incomplete $4f$ or $5f$ shells. Prototypical examples are compounds which contain cerium (Ce) or uranium (U). The $4f$ or $5f$ electrons can form local moments, i.e. their charge degree of freedom is projected out by a large coulomb repulsion U. The resulting local moments interact then with conduction electrons which originate from less localized orbitals. A good overview over the basic physical properties and the different materials is written by Coleman [95].

Standard heavy-fermion systems, i.e. materials which does not exhibit an ordered state, can be assigned into two different classes [95].

Fermi liquid
> This is the phase which is responsible for the name *heavy-fermion*. In this phase, the materials can be described by Landau-Fermi liquid theory [96], i.e. by a Fermi gas with renormalized parameters. However as compared to ordinary metals, the renormalization of the parameters is surprisingly large. In some systems, the renormalized mass is two or three magnitudes larger than the free electron mass. This is attributed to the formation of singlets between the conduction electrons and the local moments resulting from the incomplete f-shell. This singlet formation decreases the mobility of the conduction electrons and leads to a large effective mass. A prototypical example for this category is $CeCu_6$ [97]. A quasi one-dimensional heavy-fermion system is realized in $CeCo_2Ga_8$ [98, 99]

Kondo insulator
> In these materials, the chemical potential lies in the hybridization gap of the two different electronic orbitals which leads to a completely filled heavy electron band. In literature, they are often called *renomalized band insulators*, but this name is somewhat confusing. In fact, these materials are correlated insulators and lots of their properties cannot be described within band theory. The first material in this class, namely SmB_6, was discovered early by Menth et al. [100]. Another prominent example is $Ce_3Bi_4Pt_3$ [101].

Additionally, there have been detected a large variety of ordered phases in heavy-fermion systems. This includes antiferromagnetism [102] and unconventional superconductivity [103]. In particular, one was able to tune materials between two different phases by either doping [104, 105], applying pressure [106] or external magnetic fields [107]. Consequently, one can shift materials to a quantum critical point at which non Fermi liquid behaviour [108] or unconventional superconductivity emerges [109, 110]. E.g. the Fermi liquid $CeCu_6$ can be

doped with gold to obtain $CeCu_{6-x}Au_x$ and can therewith be tuned to a long-range ordered antiferromagnetic ground state. A quantum phase transition is observed at $x_c = 0.1$ [104]. In the vicinity of this quantum critical point, this compound shows non Fermi liquid behaviour [108]. Another example is the Kondo insulator SmB_6. Under a critical pressure of $p_c = 6\,GPa$, the system undergoes a quantum phase transition again to an antiferromagnetic ground state [106]. Interestingly, the system becomes metallic at the same point [106]. The quasi one-dimensional compound is expected to be close to a quantum critical point under normal conditions [98].

Recently, materials were detected which exhibit *partial* order, i.e. a fraction of the localized moments order antiferromagnetically while the other fraction is in a Kondo singlet. In CePdAl e.g., two-thirds of the localized moments are in an ordered state, while the remaining one-third remains unordered even at the lowest accessible temperatures [26, 27]. These materials cannot be classified by the usual categories as they are at the border between different classes. In fact in the above material CePdAl, the driving force for this unconventional state is geometrical frustration.

5.1.3 Theoretical overview

As the KLM is believed to describe some of the above mentioned properties of heavy-fermion systems, the model was studied intensively over the last decades. One of the key properties of heavy-fermion systems is the quantum phase transition between a nonmagnetic and an antiferromagnetic phase. It was pointed out early by DONIACH [25] that this quantum phase transition is also included in the KLM. The corresponding famous Doniach phase diagram will be explained in more detail in Sec. 5.3.

The Hamiltonian of the KLM (Eq. (5.1)) defines a strongly interacting quantum many body problem. Hence its exact solution is restricted to special cases. Because of that, a lot of approximations were suggested to obtain the fundamental physics of the KLM. A mean-field like approximation is the large-N expansion [111–113] where the spin one-half is substituted by an object with N degrees of freedom and the coupling to the conduction electrons is written in an $SU(N)$ symmetric form. This requires also N flavours for the conduction electrons. In this form, the limit $N \to \infty$ can be treated exactly.

In the special case of one-dimensional systems, a variety of tools are available to treat the KLM exactly. First and foremost the density-matrix renormalization group (DMRG, see Sec. 3.1) is a powerful tool to study one-dimensional lattice models. The key results for the one-dimensional Kondo lattice model are collected in the review of TSUNETSUGU et al. [114] which contain in addition to DMRG results also exact-diagonalization calculations and perturbative approximations:

- At half-filling, the KLM is a Kondo insulator for any $J > 0$ with gapped excitations.

- At finite doping, the KLM is ferromagnetic for sufficiently large J.

- In the paramagnetic region at finite doping, the KLM is a metal with large Fermi surface at least for strong J.

More recently, several aspects were discovered that were missing in Ref. [114]. The one-dimensional KLM has an additional ferromagnetic phase at finite doping for intermediate values of J. This phase was first discovered in Ref. [115, 116] and characterized as a spin-selective Kondo insulator by PETERS et al. [117]. A recent DMRG study confirms that the paramagnetic metal has a large Fermi surface [118] but the situation is still controversial [119]. Another special phase is found at quarter-filling, where the KLM has a dimerized and insulating ground state [120]. An extensive bosonization study can be found in Ref. [121–123]. In these works, the ferromagnetic phase transition is accurately determined and a nonperturbative indirect effective spin-spin interaction is derived.

In higher dimensions, exact results are rare. A milestone was the discovering of a quantum phase transition of the two-dimensional KLM at half-filling by a quantum Monte-Carlo study by ASSAAD [124]. It was found that at $J_c \approx 1.45t$, the ground state changes from a nonmagnetic Kondo insulator to an antiferromagnetically ordered insulator.

The study of the KLM with geometrical frustration is even harder. Variational Monte-Carlo results suggest a partially ordered state, named *partial Kondo screening* (PKS) [29]. The PKS ground state was also obtained on the static mean-field level [125, 126]. On the dynamical mean-field level, the PKS ground state was only observed off half-filling in the periodic Anderson model [127]. Recently, exact quantum Monte-Carlo simulations were performed for a geometrically frustrated KLM that also confirm a PKS ground state in a specific parameter regime [128]. However, it should be pointed out that the geometrical frustration is introduced by a direct spin-spin interaction instead of a non-bipartite lattice for the conduction electrons. In the latter case, the quantum Monte-Carlo calculations would suffer from the sign problem.

5.2 Perturbation theory

The KLM has two different energy scales. First, the hopping amplitudes t_{ij} or equivalently the bandwidth W of the free band structure $\varepsilon(\boldsymbol{k})$ and second the interaction energy J. If one of the two energy scales dominates the other, one might develop perturbative approximations. Strong-coupling perturbation theory applies in the regime $J \gg t,W$ while weak-coupling perturbation theory applies if $J \ll t,W$. Here, I will discuss both perturbations for the case of half-filling ($n = 1$).

5.2.1 Strong-coupling perturbation theory

Strong-couling perturbation theory is an expansion about the atomic limit $t_{ij} = 0$. In the atomic limit, the eigenstates are determined by the eigenstates of a single atom of the Kondo lattice. Each atom has eight internal states, which can be brought into a *proper sorted* basis with respect to the spin-$SU(2)$ and the charge-$U(1)$ symmetry:

Table 5.1: Atomic basis of the Kondo lattice. The canonical basis is made from the tensor product of the standard basis for a spin-1/2 and a Hubbard site. The localized moments are denoted with a thick arrow. See Fig. 5.1 for a pictorial representation of these states. The dashed lines seperate different $SU(2)$-multiplets.

Number	*Proper sorted* basis	Expansion into canonical basis	Energy $J\boldsymbol{S}\boldsymbol{s}$
1	$\lvert S=0, m_0=0, N=1 \rangle$	$\frac{1}{\sqrt{2}}\left(\lvert\Uparrow\otimes\downarrow\rangle - \lvert\Downarrow\otimes\uparrow\rangle\right)$	$-0.75J$
2	$\lvert S=1/2, m_{1/2}=+1/2, N=0 \rangle$	$\lvert\Uparrow\otimes 0\rangle$	0
3	$\lvert S=1/2, m_{1/2}=-1/2, N=0 \rangle$	$\lvert\Downarrow\otimes 0\rangle$	0
4	$\lvert S=1/2, m_{1/2}=+1/2, N=2 \rangle$	$\lvert\Uparrow\otimes\uparrow\downarrow\rangle$	0
5	$\lvert S=1/2, m_{1/2}=-1/2, N=2 \rangle$	$\lvert\Downarrow\otimes\uparrow\downarrow\rangle$	0
6	$\lvert S=1, m_1=+1, N=1 \rangle$	$\lvert\Uparrow\otimes\uparrow\rangle$	$0.25J$
7	$\lvert S=1, m_1=0, N=1 \rangle$	$\frac{1}{\sqrt{2}}\left(\lvert\Uparrow\otimes\downarrow\rangle + \lvert\Downarrow\otimes\uparrow\rangle\right)$	$0.25J$
8	$\lvert S=1, m_1=-1, N=1 \rangle$	$\lvert\Downarrow\otimes\downarrow\rangle$	$0.25J$

These states are already eigenstates of the local interaction $H_{\text{int}} = J\boldsymbol{S}\boldsymbol{s}$ with eigenenergies as depicted in the last column of Tab. 5.1 and a pictorial representation is displayed in Fig. 5.1. An eigenstate of the lattice model consists of a L-times tensor product of these local eigenstates. The ground state $\lvert G\rangle$ for positive J has one electron per site (half-filling) and spin $S=0$, i.e. it is the L-fold tensor product of state number 1 in Tab. 5.1. The ground state energy is $E_G/L = -0.75J$ and $\lvert G\rangle$ is nondegenerate. This is actually remarkable since it is a unique feature of the antiferromagnetic KLM with spin-1/2 moments because the ferromagnetic ground state would be 3^L-fold degenerate and for $S > 1/2$, the moments cannot be completely screened by the conduction electron system. It is also a unique property of quantum mechanics, that the singlet state (number 1 in Tab. 5.1) is non degenerate. This state has no classical analogue which is actually the reason why the classical KLM has a highly degenerate ground state in the atomic limit.

To obtain the corrections to the ground state $\lvert G\rangle$ and the ground state energy E_G in powers of
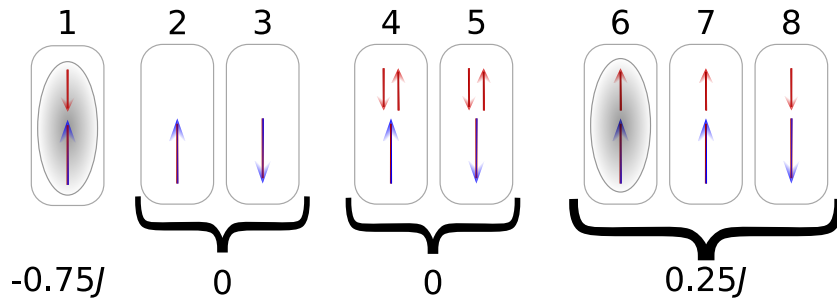
Figure 5.1: Pictorial representation of the eight eigenstates for one atom of the Kondo lattice. Blue arrows display localized moments and red arrows display conduction electron moments. The state numbers are the same as in Tab. 5.1 and the braces group the states belonging to the same $SU(2)$-multiplet. The numbers below the pictograms are the eigenenergies of the local interaction $H_{\text{int}} = J\boldsymbol{S}\boldsymbol{s}$. The grey shaded states 1 and 6 are entangled states instead of simple product states.

$\frac{t}{J}$, one can work out standard nondegenerate perturbation theory around the atomic limit for the Hamiltonian:

$$H = H_0 - tV, \tag{5.4}$$

where H_0 is the interaction and V the hopping part (see Eq. (5.1)). The hopping amplitude t is assumed to be small as compared to the energy scale J of H_0. Note that I assume that the hopping energies t_{ij} decompose as $t_{i\sigma,j\tau} = t f_{i\sigma,j\tau}$ where t sets the energy scale and $f_{i\sigma,j\tau}$ is dimensionless and maximally of the order $f_{i\sigma,j\tau} \sim 1$. The first order energy correction $E_G^{(1)}$ is then given by:

$$E_G^{(1)} = t \langle G | V | G \rangle \tag{5.5}$$

It is easy to calculate, that the correction vanishes as long as $f_{i\sigma,i\tau} \equiv 0$. The second order term is:

$$E_G^{(2)} = t^2 \sum_k \frac{|\langle k | V | G \rangle|^2}{E_G - E_k}, \tag{5.6}$$

where k is an index labeling the excited states of the atomic limit. It is worthwhile to evaluate the action of V on the ground state $|G\rangle$ separately:

$$V |G\rangle = \frac{1}{2} \sum_{i \neq j \sigma \tau} f_{i\sigma,j\tau} \Sigma_{i\sigma,j\tau} |i, -\sigma; j,\tau\rangle \tag{5.7}$$

Here, $\Sigma_{i\sigma,j\tau} = \pm 1$ is a sign coming from the fermionic commutation relations which is not important for the following results. The excited states $|i,\sigma; j,\tau\rangle$ are states in which at site i the electronic orbital is empty and the localized moment has spin-projection σ (state number 2 and 3 in Tab. 5.1) and at site j the electronic orbital is doubly occupied and the localized moment has spin-projection τ (state number 4 and 5 in Tab. 5.1). In Eq. (5.7) I have again assumed that there are no onsite energies ($f_{i\sigma,i\tau} \equiv 0$). With the result in Eq. (5.7), one can restrict the summation over k in Eq. (5.6) to excited states in the form $|i,\sigma; j,\tau\rangle$. The denominator in Eq. (5.7) is $E_G - E_{i\sigma,j\tau} = -1.5J$ because $E_{i\sigma,j\tau} = -(L-2)0.75J$. In summary, one obtains for the second order energy correction:

$$E_G^{(2)} = -\frac{t^2}{6J} \sum_{i \neq j \sigma \tau} |f_{i\sigma,j\tau}|^2 \tag{5.8}$$

This can be evaluated e.g. for the hopping of a zigzag ladder with hopping amplitude $t f_1$ along the rungs and $t f_2$ along the legs:

$$E_G^{(2)}/L = -\frac{2t^2}{3J} \left(|f_1|^2 + |f_2|^2\right) \tag{5.9}$$

More interesting than this energy shift is the state correction, or more specific: expectation values of observables in the state correction. Of particular interest are the spin correlations $\langle \boldsymbol{S}_i \boldsymbol{S}_j \rangle$ of the local moments. Since the KLM is spin-$SU(2)$ symmetric, one can calculate the longitudinal correlations $\langle S_i^z S_j^z \rangle$ instead of the full spin correlations. To zeroth order, one has

$\langle S_i^z S_j^z \rangle = 0.25\delta_{ij}$. To first order, there is no contribution so that the first non-trivial correction is at second order. To second order, one has the overlap $\left\langle G^{(0)} \middle| S_i^z S_j^z \middle| G^{(2)} \right\rangle$ which involves the second order state correction and the expectation value in the first order state correction $\left| G^{(1)} \right\rangle$:

$$\langle S_i^z S_j^z \rangle^{(2)} = \left\langle G^{(1)} \middle| S_i^z S_j^z \middle| G^{(1)} \right\rangle + \left\langle G^{(0)} \middle| S_i^z S_j^z \middle| G^{(2)} \right\rangle + \left\langle G^{(2)} \middle| S_i^z S_j^z \middle| G^{(0)} \right\rangle \tag{5.10}$$

The first order state correction is given by:

$$\left| G^{(1)} \right\rangle = t \sum_k \frac{\langle k \mid V \mid G \rangle}{E_k - E_G} \left| k \right\rangle = \frac{t}{2J} \sum_{n \neq m\sigma\tau} f_{n(-\sigma),m\tau} \Sigma_{n(-\sigma),m\tau} \left| n,\sigma; m,\tau \right\rangle \tag{5.11}$$

Plugging this into Eq. (5.10) gives the first contribution to the spin correlations in second order in $\frac{t}{J}$. For $i \neq j$, one obtains:

$$\langle S_i^z S_j^z \rangle^{(2)} = \frac{t^2}{2J^2} \sum_{\sigma\tau} |f_{i(-\sigma),j\tau}|^2 \sigma\tau \tag{5.12}$$

The contribution from the overlap matrix element $\left\langle G^{(0)} \middle| S_i^z S_j^z \middle| G^{(2)} \right\rangle$ vanishes. For the onsite term, one gets:

$$\langle S_i^z S_i^z \rangle^{(2)} = 0, \tag{5.13}$$

since both contributions cancel each other. This is a direct consequence of the normalization condition $2\left\langle G^{(0)} \middle| G^{(2)} \right\rangle + \left\langle G^{(1)} \middle| G^{(1)} \right\rangle = 0$ for the state corrections. Eq. (5.12) shows that the spin correlations in second order are only between sites which are directly connected by a hopping term. Furthermore, the nonlocal correlations are always *negative* (antiferromagnetic) as long as the hopping does not produce a spin flip ($f_{i\uparrow,j\downarrow} = 0$). One can evaluate the formulas e.g. for the zigzag ladder with hopping amplitude tf_1 along the rungs and tf_2 along the legs:

$$\langle S_i^z S_j^z \rangle^{(2)} = \frac{t^2}{4J^2} \left(-f_1^2 \delta_{i,j+1} - f_2^2 \delta_{i,j+2} \right) \tag{5.14}$$

The spin-structure factor $S(Q) = \frac{1}{L} \sum_{ij} e^{iQ(R_i - R_j)} \langle \boldsymbol{S}_i \boldsymbol{S}_j \rangle$ up to second order follows after a Fourier transformation and by using $\langle \boldsymbol{S}_i \boldsymbol{S}_j \rangle = 3\langle S_i^z S_j^z \rangle$ in the $SU(2)$ symmetric case:

$$S(Q) = \frac{3}{4} - \frac{3t^2}{4J^2} \left(2f_1^2 \cos(Q) + 2f_2^2 \cos(2Q) \right) \tag{5.15}$$

The dominant spin correlations have the wave-vector Q^* for which $S(Q^*) = \max$. An easy calculation shows that:

$$Q^* = \begin{cases} \pi & \text{for } f_1 > 2f_2 \\ \arccos\left(-\frac{f_1^2}{4f_2^2}\right) & \text{for } f_1 \leq 2f_2 \end{cases} \tag{5.16}$$

5.2.2 Weak-coupling perturbation theory

The other limit of the KLM is substantially more complicated. In the case $J = 0$, the ground state $|G\rangle$ is the Fermi sea but in that case, the ground state is highly degenerate since the localized moments are completely decoupled from the conduction electrons. The exact degeneracy is $(2S + 1)^L \overset{S=1/2}{=} 2^L$.

In the original works [9, 22, 23], the authors derived an approximate Hamiltonian for the case of only two localized moments coupled locally to the conduction electrons. This effective Hamiltonian was later called the *RKKY* Hamiltonian named by the authors of the original publications. The extension to a lattice of localized moments is straight-forward. The derivation by KASUYA [9], RUDERMAN et al. [22], and YOSIDA [23] is not very thorough and an alternative approach to obtain the same results was given in Ref. [129, 130].

Here, I derive the effective Hamiltonian by using linear response theory as described by ZIENER et al. [131].

Let $|G\rangle$ be the ground state of a noninteracting electron system, i.e. the Fermi sea. The interaction of the conduction electrons with a magnetic field $\{\boldsymbol{B}_i(t)\}_{i=1,\dots,L}$ leads to a Zeeman term:

$$H_{\text{int}} = -\sum_i \boldsymbol{s}_i \cdot \boldsymbol{B}_i(t) \tag{5.17}$$

The linear response of the magnetization $\Delta \langle \boldsymbol{s}_j \rangle (\omega)$ at site j on the magnetic fields can be evaluated by Kubo's formula:

$$\Delta \left\langle s_j^\beta \right\rangle (\omega) = \sum_{i\alpha} \chi_{ij}^{\alpha\beta}(\omega) B_i^\alpha(\omega), \tag{5.18}$$

where I have switched to frequency space and $\chi_{ij}^{\alpha\beta}(\omega)$ is the magnetic susceptibility of the conduction electron system:

$$\chi_{ij}^{\alpha\beta}(\omega) = \int_0^\infty dt e^{i\omega t} \left\langle s_i^\alpha(t) s_j^\beta(0) \right\rangle \tag{5.19}$$

This magnetization at site j leads to an energy change of the field energy caused by the field $\boldsymbol{B}_j$ at site j according to Eq. (5.17). The sum of all energy changes becomes for static fields ($\omega = 0$):

$$\Delta E = -\frac{1}{2} \sum_{ij} \sum_{\alpha\beta} B_i^\alpha \chi_{ij}^{\alpha\beta}(\omega = 0) B_j^\beta \tag{5.20}$$

The factor $1/2$ balances the double counting in the sum. One can now identify $J\boldsymbol{S}_i$ as the magnetic fields $\boldsymbol{B}_i$ and assume an isotropic susceptibility so that one arrives at the RKKY Hamiltonian:

$$H_{\text{RKKY}} = -\frac{J^2}{2} \sum_{ij} \chi_{ij}(\omega = 0) \boldsymbol{S}_i \cdot \boldsymbol{S}_j = \sum_{ij} J_{ij} \boldsymbol{S}_i \cdot \boldsymbol{S}_j, \tag{5.21}$$

which is an effective spin-model with coupling $J_{ij} = -\frac{J^2}{2}\chi_{ij}(\omega = 0)$.

In contrast to the strong coupling case, the weak coupling limit is described by an effective Hamiltonian. This Hamiltonian defines a complex spin model with long-range interactions and its solution is a nontrivial problem. However for bipartite lattices, one can show that the static susceptibility oscillates between the two sub lattices and is antiferromagnetic between the A- and B-lattice. From this one can conclude that the spin model is not frustrated and therefore has a magnetically ordered ground state[1]. On the contrary, for nonbipartite lattices, one has to solve the effective model explicitly.

5.3 Doniach picture

The perturbative considerations in the last section motivate a central competition in the KLM. This competition was firstly suggested by DONIACH [25].

The strong-coupling perturbation theory predicts a spin-liquid ground state with gapped excitations and exponentially decaying two-point correlations. In this state, the localized moments are screened mutually by their conduction electron partner. In this sense, the situation is reminiscent to the Kondo effect which is present for a single localized moment only. A single localized moment is screened by a conduction electron cloud (the *Kondo cloud*). This explains that the resistivity of the conduction electrons *increases* for low temperature which was the first signal of the Kondo effect [93, 133]. The characteristic energy scale of the Kondo effect is:

$$E_{\mathrm{Kondo}} \sim W e^{-\frac{1}{2J\rho(\varepsilon_F)}} \tag{5.22}$$
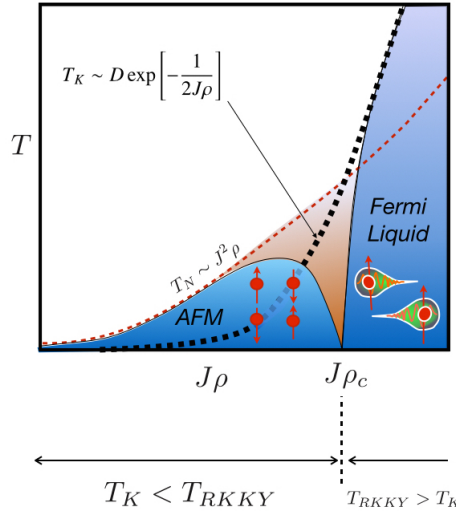
Figure 5.2: Doniach phase diagram for the Kondo lattice. Taken from COLEMAN [132] (Fig. 5).

---

1   For one-dimensional systems the ground state is quasi-long-range ordered only.

Here, W is the band width of the noninteracting electron dispersion $\varepsilon(\boldsymbol{k})$ and $\rho(\varepsilon_F)$ is the noninteracting density of states at the Fermi energy.

On the other hand the weak-coupling perturbation predicts a magnetically ordered ground state, at least for bipartite lattices. The characteristic energy scale is in this case given by:

$$E_{\text{Kondo}} \sim J^2 \rho(\varepsilon_F) \tag{5.23}$$

Both predictions contradict each other. This defines the competition which is at the heart of Kondo lattice systems: The screening of the localized moments through the conduction electrons competes with an ordering mechanism caused by the conduction electrons. By comparing the energy scales in Eq. (5.22) and Eq. (5.23), one gets the famous Doniach phase diagram which is sketched in Fig. 5.2. For weak J, the screening is exponentially small and the RKKY coupling dominates, which leads to an antiferromagnetic ground state. For strong J, the screening dominates and the system is a spin-liquid. In between those two regimes, one expects a quantum-phase transition at a critical coupling J_c.

CHAPTER 6

The half-filled frustrated Kondo ladder

In this chapter, I will present extensive DMRG calculations for the one-dimensional frustrated Kondo ladder on a zigzag ladder. In Sec. 6.1, I will introduce the specific model and parameters and discuss preliminary works. In Sec. 6.2, I will present the numerical results as well as the interpretations and conclusions. As a simplified picture, I will finally discuss the phase diagram of the classical frustrated Kondo ladder in Sec. 6.3.

6.1 Introduction

The frustrated Kondo ladder is obtained when choosing the hopping elements t_{ij} in Eq. (5.1) to the topology of a zigzag ladder as sketched in Fig. 6.1 B. This system is equivalent to an ordinary one-dimensional Kondo chain with nearest-neighbor (nn) hopping t_1 and next-nearest-neighbor hopping (nnn) t_2 (see Fig. 6.1 A). The Hamiltonian from Eq. (5.1) takes the following form with these definitions:

$$H = -t_1 \sum_{i,\sigma} \left(c_{i\sigma}^\dagger c_{i+1\sigma} + \text{h.c.} \right) - t_2 \sum_{i,\sigma} \left(c_{i\sigma}^\dagger c_{i+2\sigma} + \text{h.c.} \right) + J \sum_i \boldsymbol{S}_i \cdot \boldsymbol{s}_i \tag{6.1}$$
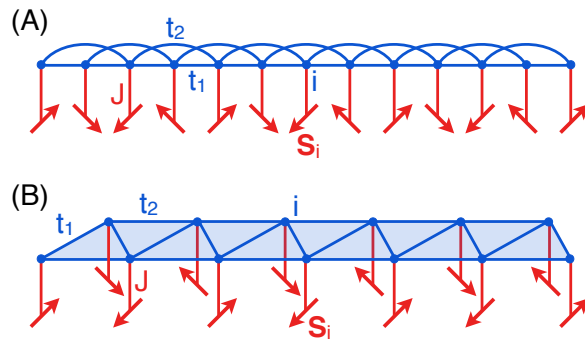
Figure 6.1: (A) Sketch of the one-dimensional Kondo-lattice model with nearest-neighbor hopping $-t_1$ and next-nearest-neighbor hopping $-t_2$, parameterized as $t_1 = t\cos\varphi$ and $t_2 = t\sin\varphi$ with $t > 0$ and $0 \leq \varphi \leq \pi/2$. Local antiferromagnetic exchange $J > 0$, see Eq. (6.1). (B) Equivalent representation of the model as a zigzag ladder. The rungs of the ladder correspond to t_1 and the legs are linked by t_2. For $\varphi = 0$, i.e., $t_1 = t$ and $t_2 = 0$, the model reduces to the Kondo lattice on the one-dimensional chain. At $\varphi = \pi/4$, one has $t_1 = t_2$, and for $\varphi = \pi/2$, i.e., $t_1 = 0$ and $t_2 = t$, the model is given by two decoupled one-dimensional chains.

The parameters are chosen so that $t_1 > 0$, $t_2 > 0$ and $J > 0$ in this convention. It is suitable to parametrize the two hoppings as $t_1 = t \cos \varphi$ and $t_2 = t \sin \varphi$ to obtain $t_1/t_2 = \tan \varphi$. φ runs then between 0 and $\frac{\pi}{2}$ and the edge case $\varphi = 0$ corresponds to $t_2 = 0$ (the ordinary Kondo chain) while $\varphi = \frac{\pi}{2}$ corresponds to $t_1 = 0$ (two decoupled ordinary Kondo chains). The case $t_1 = t_2$ is reached for $\varphi = \frac{\pi}{4}$. The Hamiltonian in Eq. (6.1) has a $SU(2)$-spin symmetry generated by the total spin $\boldsymbol{S}_{\text{tot}} = \sum_i \boldsymbol{S}_i + \boldsymbol{s}_i$ as discussed in Sec. 5.1.1. The $SU(2)$-charge symmetry is not obeyed by this Hamiltonian since the hopping is not bipartite. But the Hamiltonian is invariant under a $U(1)$-charge symmetry generated by the total number of electrons $N = \sum_{i\sigma} n_{i\sigma}$. Beside these continous symmetries, the Hamiltonian in Eq. (6.1) has a discrete translational symmetry $\langle a \rangle = \{\text{id}, \pm a, \pm 2a, \ldots\}$ generated by a primitive translation by one lattice site in the chain geometry (Fig. 6.1A). This Abelian symmetry is a subgroup of the dihedral group D_L consisting of the L rotations and L reflections of a regular polygon with L edges. Since the Hamiltonian is also invariant under reflections, it respects the full dihedral group. For later purposes, only the translational symmetry is important.

The non-interacting part of H can be diagonalized with a Fourier transformation due to the translational symmetry. One obtains a single band $\varepsilon(k)$:

$$\varepsilon(k) = -2t_1 \cos(k) - 2t_2 \cos(2k) \tag{6.2}$$

This band structure has a Lifshitz point at which the number of Fermi-points (FP) change from two FP to four FP. The Lifshitz transition can be seen in Fig. 6.2 for the case of a half-filled band. For values $\varphi < \varphi_0$ ($t_2 < 0.5t_1$) there are two FP and a single nesting vector $Q = \pi$. For values $\varphi > \varphi_0$ ($t_2 > 0.5t_1$) there are four FP but interestingly two φ-independent nesting vectors with $Q = \frac{\pi}{2}$. The other nesting vectors are φ-dependent in this case.

The ordinary Kondo chain ($t_2 = \varphi = 0$) has undergone extensive studies in the last decades. The key results are summarized in the review of TSUNETSUGU et al. [114]. It is remarkable that the Doniach competition (see Sec. 5.3) is never decided towards a magnetically ordered ground
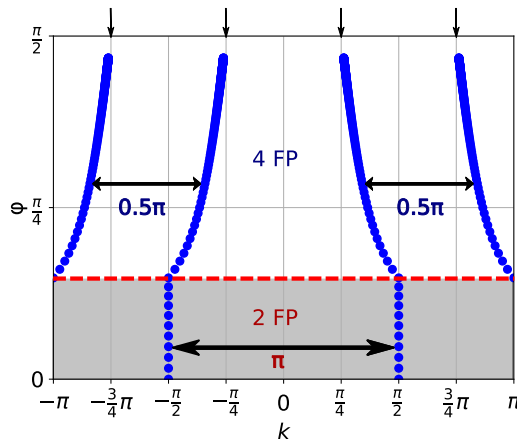
Figure 6.2: Location of the Fermi points in k-space as a function of φ. The Lifshitz transition between a state with two (2 FP) and with four Fermi points (4 FP) takes place at $\varphi = \varphi_0 = \arctan\left(\frac{1}{2}\right) \approx 0.148\pi$, i.e., at $t_1 = 2t_2$ (dashed red line). Horizontal arrows: nesting vectors. Vertical arrows mark the decoupled-chains limit $\varphi = \pi/2$.

state, or – more precise for a one-dimensional quantum system – towards a quasi ordered ground state. The Kondo chain has a spin gap $\Delta E_S > 0$ for any $J > 0$ and furthermore it was shown that the weak J limit is dominated by a Kondo-like energy scale:

$$\Delta E_S \sim e^{-\frac{1}{\nu J \rho}}, \tag{6.3}$$

for which the coupling J is renormalized by ν as compared to the impurity case. DMRG results suggest the value $\nu = 1.41$ [134]. Hence, this model has no quantum phase transition and is a featureless Kondo insulator. From this result, one can draw constraints for the phase diagram of the frustrated ladder as depicted in Fig. 6.3. The strong coupling regime is adiabatically connected to the atomic limit as it is the case for any Kondo lattice. This is indicated by the paths $\mathcal{C}$ in Fig. 6.3. Furthermore, the ordinary chain limits $t_2 = 0$ (single chain) and $t_1 = 0$ (two decoupled chains) can be reached from the atomic limit for each value $J > 0$ (paths $\mathcal{C}'$). Since the ground state of the chain limit has a finite spectral gap, one can also connect the regions with small t_2 or small t_1 to the two limits $t_2 = 0$ and $t_1 = 0$ respectively (paths $\mathcal{C}''$). Nevertheless, one needs to keep in mind that the spectral gap gets exponentially small for $J \to 0$, so that also the perturbatively accessible regions shrink exponentially when reaching the weak coupling regime. The blue line in Fig. 6.3 indicates the path with $t_1 = t_2$ which leaves the perturbatively accessible regime at some J. The further development of the ground state along this line is a major topic of this thesis.

Beside the usual Doniach competition along this line towards smaller J, the geometrical frustration enters the competition as a third entrant. For decreasing J, antiferromagnetic
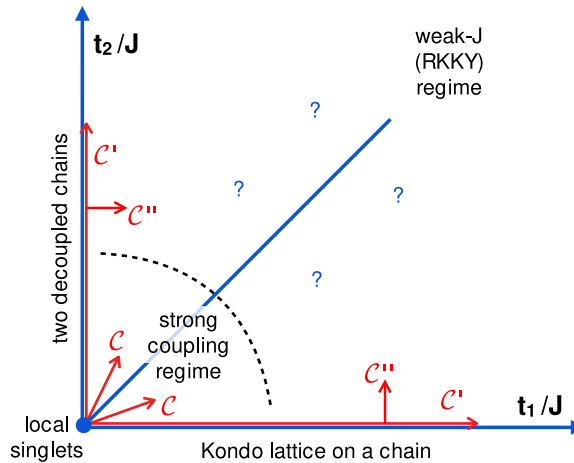
Figure 6.3: Sketch of the phase diagram for the frustrated Kondo ladder with several paths which adiabatically connect different regions to the atomic limit ($t_1 = t_2 = 0$). The paths $\mathcal{C}$ connect regions with $t_1, t_2 \ll J$ by non-degenerate strong coupling perturbation theory. The paths $\mathcal{C}'$ indicate that the ordinary chain is adiabatically connected to the atomic limit for all $J > 0$ and the paths $\mathcal{C}''$ adiabatically connect the regions with $t_2 \ll t_1$ ($t_1 \ll t_2$) to the ordinary chain $t_2 = 0$ (decoupled chain $t_1 = 0$) again with non-degenerate perturbation theory in the spectral gap. Notice however, that the gap for the ordinary chain vanishes exponentially as $J \to 0$. The blue line indicate the path at $t_1 = t_2$ which leaves the perturbative regime at some J and may undergo a quantum phase transition. The RKKY regime might become relevant for weak J.

correlations increase which are frustrated on the triangles from the zigzag ladder. It turns out, that the frustration has a large impact on the ground state and leads to at least two quantum phase transitions along the blue line in Fig. 6.3 as presented in the next section.

6.2 Ground state phase diagram

In this section, I present the numerical results and describe the ground state phase diagram for the frustrated Kondo ladder at half-filling. I will present a condensed overview by discussing briefly the obtained phases. Afterwards, I will analyse the different regimes in detail and provide the necessary data for obtaining the phase boundaries. Fig. 6.4 shows the $J - \varphi$ phase diagram in the thermodynamic limit as obtained by extensive DMRG and VUMPS calculations.

For strong J, the frustrated Kondo ladder develops two different types of short-range order. Firstly, an antiferromagnetic spin alignment for short distances (AF-SRO) which has dominant spin correlations at $Q = \pi$ and secondly, an incommensurate spiral short-range order (IC-SRO) with dominant spin correlations at wave-vectors $\frac{\pi}{2} < Q < \pi$. Both phases are separated by the green line in Fig. 6.4 and the green arrow indicates the phase boundary for $J \to \infty$. The phase boundary is defined by a kink in the function $Q(\varphi)$ where Q is the wave-vector of the dominating spin correlations. For weaker exchange couplings $J \sim 0.9t$, the correlations are no longer dominated by a single wave-vector so that the transition becomes less well defined. A detailed description can be found in Sec. 6.2.1.

At intermediate values for J, there is an extended region in which the translational symmetry is spontaneously broken by the ground state. The spin-correlations along the rungs of the ladder show an alternating pattern of ferro- and antiferromagnetic alignment. It is called the spin-dimerized phase (DIM) and the transition is marked by the blue line in Fig. 6.4. As will be argued in detail in Sec. 6.2.2, the spin-dimerization alleviates the magnetic frustration and is actually a precursor of a gapless ground state with quasi-long-range spiral magnetic order at wave-vector $Q = \frac{\pi}{2}$. This phase is denoted as SP-QLRO and the phase boundary is marked by the red line in Fig. 6.4.

For weak J, the phase boundary for the transition into the spin-dimerized phase is found to end at the Lifshitz-transition of the non-interacting Fermi sea, namely at $\varphi_c(J \to 0) = \arctan\left(\frac{1}{2}\right) \approx 0.148\pi$. This accidentally coincides with transition point at $J \to \infty$ between AF-SRO and IC-SRO as indicated by the lower dotted line in Fig. 6.4.

6.2.1 Strong-J regime

In the limit $J \to \infty$, the unique ground state consists of completely local Kondo singlets between the localized moments and the electronic spin at site i. All excitations are gapped by J and consequently the two-point correlations decay exponentially with increasing distance. The short-range correlations develop in perturbation theory at order $\frac{t^2}{J}$ and for bipartite lattices the spin-structure factor

$$S(Q) = \frac{1}{L} \sum_{ij} e^{i\boldsymbol{Q}(\boldsymbol{R}_i - \boldsymbol{R}_j)} \langle \boldsymbol{S}_i \cdot \boldsymbol{S}_j \rangle \tag{6.4}$$
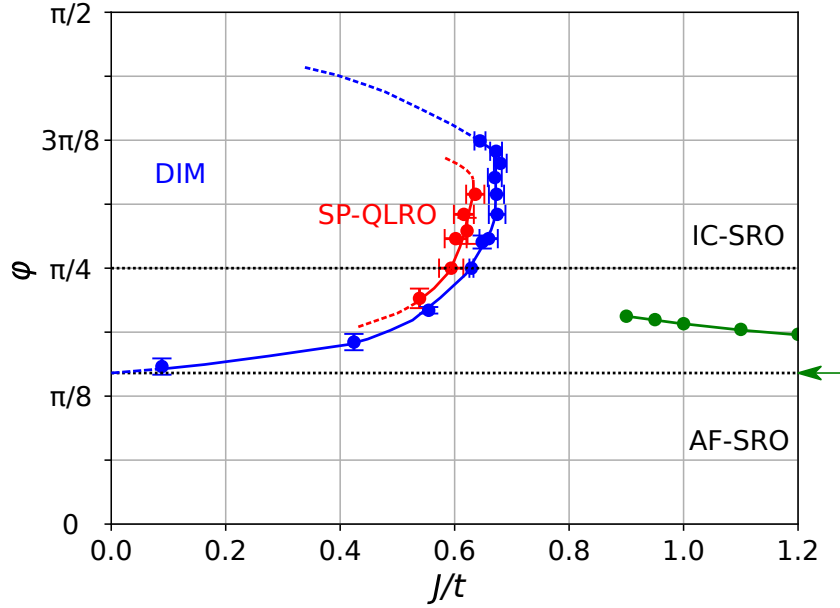
Figure 6.4: Ground state phase diagram in the $J - \varphi$ plane for the half-filled quantum-spin Kondo model on the zigzag ladder, as obtained by DMRG calculations for systems of up to $L = 52$ sites (and extrapolated to $L = \infty$) as well as by VUMPS calculations working directly in the thermodynamical limit (with bond dimensions extrapolated to $m = \infty$ where necessary). AF-SRO: antiferromagnetic short-range order with wave vector $Q = \pi$. IC-SRO: incommensurate spiral short-range order with $\pi/2 \leq Q < \pi$. DIM: spin-dimerized phase. SP-QLRO: spiral quasi-long-range order with $Q = \pi/2$. Points with error bars locate the various transitions. Black dashed lines: $t_2 = t_1$ (upper) and $t_2 = t_1/2$ (lower). Blue and red dashed lines: see text.

is peaked at the antiferromagnetic wave-vector $\boldsymbol{Q} = (\pi, \ldots, \pi)$ as already discussed in Sec. 5.3. For the ordinary Kondo chain, this corresponds to $Q = \pi$ and one may study the evolution $Q(\varphi)$ of this peak as a function of φ, the level of frustration. In Fig. 6.5 the evolution of the peak is presented for several values of J. For φ varying from $0 \to \frac{\pi}{2}$, the peak position evolves continuously from $\pi \to \frac{\pi}{2}$. However, at a critical value φ_c, the function $Q(\varphi)$ has a kink exactly at the point where the peak position shifts away from the antiferromagnetic value $Q = \pi$ towards incommensurate values $Q < \pi$. In the strong-J regime captured in Fig. 6.5 the transition is weakly J-dependent and matches the result from strong coupling perturbation theory (see black line in Fig. 6.5, which is the prediction of Eq. (5.16)). This transition can be traced down to $J \sim 0.9t$ as indicated by the green line in the phase diagram 6.4. It is observed that the critical value φ_c increases for decreasing J. For values $J < 0.9t$ the transition fades away and the spin-structure factor is not dominated by a single peak only. For that to become clear, I plotted the spin-structure factor in Fig. 6.6 for $J = t$ and $J = 0.85t$ and various values of φ. For $J = t$ the spin-structure factor has a broad maximum located at $Q = \pi$ for $\varphi = 0.61$ and this maximum is shifted away from $Q = \pi$ for $\varphi = 0.62$ (see the arrows in Fig. 6.6(a)). Hence the transition point can be located to $0.61 < \varphi_c < 0.62$ for $J = t$. Increasing φ further shifts the maximum towards $Q = \frac{\pi}{2}$. The speed of the shift is rather high for values φ slightly above φ_c while the convergence to $Q = \frac{\pi}{2}$ for $\varphi = \frac{\pi}{2}$ becomes slower and slower. This behaviour can also be seen in Fig. 6.5 for the strong-coupling limit.
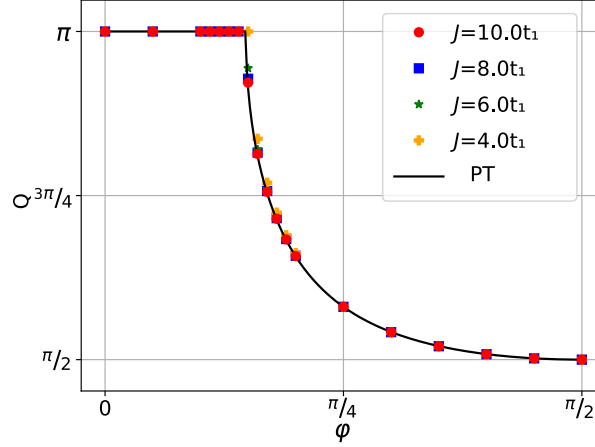
Figure 6.5: Position Q of the peak maximum in the reciprocal unit cell of the spin-structure factor $S(Q)$, see Eq. (6.4), as a function of φ. The kink defines $\varphi_c(J)$, i.e., the transition from short-range AF to IC magnetic order. The symbols denote results of VUMPS calculations in the thermodynamic limit for various interaction strengths J. For strong J, the peak position matches with the prediction of strong-coupling perturbation theory (PT) , i.e., with Eq. (5.16), see the solid line.

(a) $J = t$
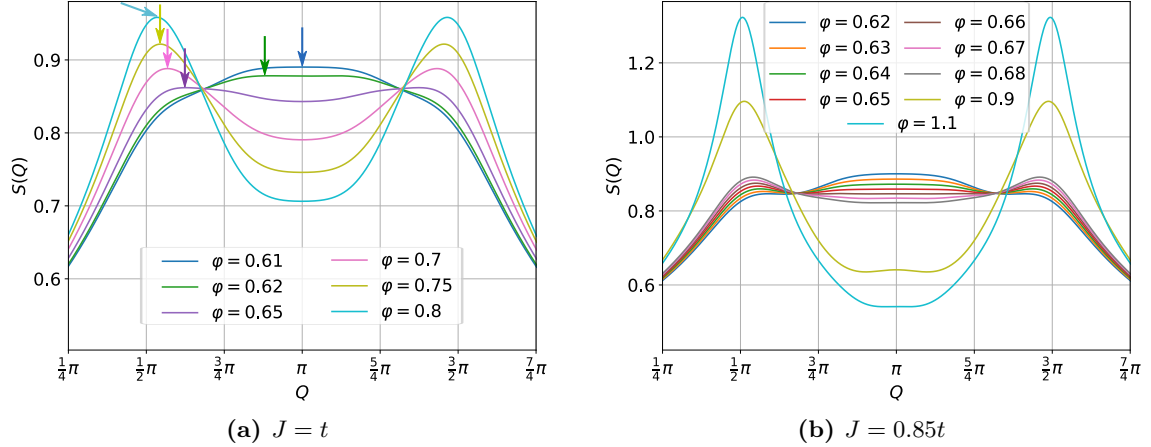
(b) $J = 0.85t$

Figure 6.6: The spin-structure factor $S(Q)$ for a) $J = t$ and b) $J = 0.85t$ and several values of φ as indicated.

For $J = 0.85t$, the situation is different. Still for $\varphi = 0.62$ for example, the spin-structure factor has a broad maximum at $Q = \pi$ but simultaneously the spin-structure factor has a shoulder in the vicinity of $Q = \frac{\pi}{2}$. This shoulder develops into a peak for increasing φ, while the maximum at $Q = \pi$ remains. Even at $\varphi = 0.9$, a small local maximum at $Q = \pi$ is present but the dominating order is already at incommensurate wave-vectors Q slightly above $\frac{\pi}{2}$. Finally, for a large value of $\varphi = 1.1$ the small local maximum disappears and one obtains a qualitative similar spin-structure factor as for $J = t$ in the large-φ limit (compare to $\varphi = 0.8$ in Fig. 6.6(a)).

In summary, the strong-J regime consists of two different kinds of short-range order which are well seperated by a kink in the function $Q(\varphi)$, where Q is the peak position in the spin-structure factor. The first short-range order is antiferromagnetic with $Q = \pi$ and the second consists of

incommensurate correlations with $\frac{\pi}{2} < Q < \pi$. The two different types of short-range order do not have different symmetries and both do not break any symmetries of the Hamiltonian H from Eq. (6.1). When leaving the strong-coupling regime, the transition fades away, because the short-range order is already influenced by a precursor of the quasi-ordered magentic spiral phase with wave-vector $Q = \frac{\pi}{2}$ (see Sec. 6.2.3). One might compare this situation to the phase diagram of water: the liquid and steam phase have the same symmetries and under normal conditions there is a phase transition separating both phases, but the transition line ends in a critical point[1]. Beyond the critical point, there is no transition (discontinuity in a equation of state) anymore and one cannot distinguish between two different phases anymore.

6.2.2 Translational symmetry breaking

The Hamiltonian for the Kondo zigzag ladder (Eq. (6.1)) is invariant under the translation group $\langle a \rangle$ as discussed in Sec. 6.1. This discrete symmetry might be spontaneously broken by the ground state even in a one-dimensional system since the Mermin-Wagner theorem only applies to continuous symmetries. A simple form of a symmetry-broken ground state is a dimerized state in which the expectation value $\langle A_i A_j \rangle$ of a correlation from a local observable A_i is not translationally invariant anymore:

$$O_{\mathrm{D}} := \langle A_{i-1} A_i \rangle - \langle A_i A_{i+1} \rangle = \mathrm{const.} \times (-1)^i, \tag{6.5}$$

while the local expectation value $\langle A_i \rangle$ is still translationally invariant ($\langle A_i \rangle \equiv \langle A \rangle$). Eq. (6.5) defines the order parameter for dimerization, since the difference of the two correlations would be identically zero for a translational invariant state. In the following, I will analyse spin-dimerization for which the order parameter becomes:

$$O_{\mathrm{D}} := \langle \boldsymbol{S}_{i-1} \boldsymbol{S}_i \rangle - \langle \boldsymbol{S}_i \boldsymbol{S}_{i+1} \rangle \tag{6.6}$$

In the upcoming subsection, I will analyse the evolution of the nearest-neighbor spin-correlations which determines the order parameter O_{D} as a function of both J and t_2. Afterwards, I will discuss in detail how one can obtain the precise transition point into the spin-dimerized phase.

Nearest-neighbor spin-correlations

For the beginning, I concentrate on the case $t_2 = t_1$ (blue line in Fig. 6.3) and elaborate on the evolution of the spin-correlations $\langle \boldsymbol{S}_i \boldsymbol{S}_j \rangle$ as a function of J/t_1 for nearest-neighbors of the frustrated ladder geometry (Fig. 6.1B). In Fig. 6.7, these correlations can be viewed in a color code for various values of J. The color code maps the values for the spin-correlations $-0.75 \leq \langle \boldsymbol{S}_i \boldsymbol{S}_j \rangle \leq 0.25$ onto colors with blue for $\langle \boldsymbol{S}_i \boldsymbol{S}_j \rangle < 0$ (AF) and red for $\langle \boldsymbol{S}_i \boldsymbol{S}_j \rangle > 0$ (FM). For strong interactions ($J = 3.0t_1$ in 6.7) the correlations are weak and antiferromagnetic. The dominant correlations are the Kondo correlations $\langle \boldsymbol{S}_i \boldsymbol{s}_i \rangle$ (not shown) which are close to their maximum value $\langle \boldsymbol{S}_i \boldsymbol{s}_i \rangle = -0.75$. Both can be understood in strong-coupling perturbation theory (see Sec. 5.3) and the local nature of the state is also reflected by the complete absence of boundary effects even though the lattice is cut at sites $i = 1$ and $i = L$. The throughout

---

1   See for example https://en.wikipedia.org/wiki/Properties_of_water (last accessed 18 February 2019)
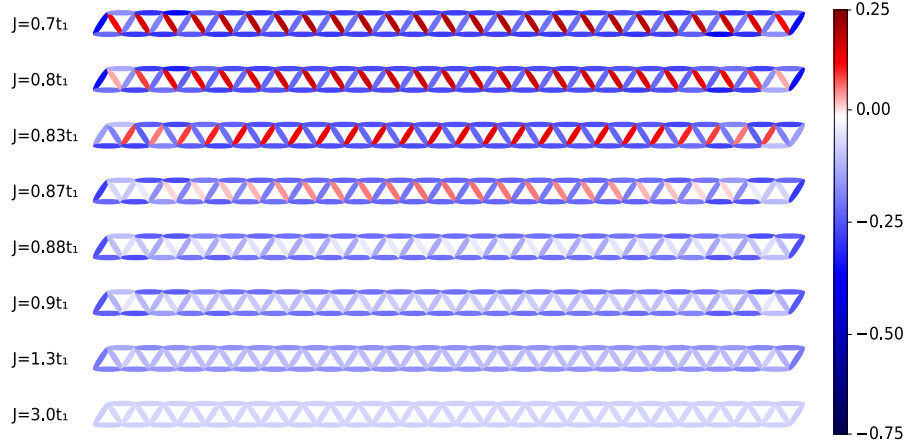
Figure 6.7: Ground state spin-correlations $\langle \boldsymbol{S}_i \boldsymbol{S}_j \rangle$ (see color code) for nearest neighbors i, j on the zigzag ladder for an isotropic ladder ($t_1 = t_2$) ladder with $L = 52$ sites at half-filling and for various coupling strengths J/t_1.

antiferromagnetic correlations already show the geometrical frustration on the zigzag geometry which is, however, not important in the case of large J.

The complete homogeneity of the correlations disappears if J decreases. Already for $J = 1.3t_1$, two different inhomogeneities emerge:

1. Boundary effects become visible. The correlations at the two edge-bonds ([1,2] and [$L-1,L$]) are significantly stronger than in the bulk which is easily traced back to the weaker frustration of these bonds. The boundary effects get stronger and extend further in the bulk for decreasing J. Nevertheless, Fig. 6.7 shows that the boundary effects are well controlled and the center region of the chain is free of any boundary effects.

2. The correlations on the legs of the ladder start to differ from the correlations along the rungs. Already for $J = 1.3t_1$ it is visible that the leg-correlations are stronger as compared to the rung-correlations. This is a bulk effect, caused by the special ladder geometry and can be understood when analysing carefully the competing interactions for a bond on a leg and a bond on a rung respectively. For the bond [$i-1,i$] on a rung, *two* competing correlations exist due to the paths: 1) $i-1 \rightarrow i-2 \rightarrow i$ and 2) $i-1 \rightarrow i+1 \rightarrow i$. For the bond [$i-2,i$] on a leg, only *one* such path exists: $i-2 \rightarrow i-1 \rightarrow i$. Therefore, the correlations along the legs are less frustrated and develop stronger values in magnitude for $\langle \boldsymbol{S}_i \boldsymbol{S}_j \rangle$ than the correlations along the rungs. For a two-dimensional triangular lattice, the legs and the rungs would be equivalent.

In general, the non-local correlations grow if J decreases, which make the frustration more and more important.

For even weaker J, there is a third inhomogeneity in the correlations which can be seen at first for $J = 0.88t_1$. The correlations along the rungs have an alternating behaviour reflecting a break of the translational symmetry in form of spin-dimerization. The translational symmetry group $\langle a \rangle$ is reduced to the group $\langle 2a \rangle$, generated by translations $2a$. It is clearly visible that this is a bulk effect and with further decreasing J, the dimerization becomes stronger. For

$J = 0.8t_1$, the correlations already show an oscillating behaviour because they switch periodically from ferro- to antiferromagnetic. The spin-dimerized state has to be interpreted as a direct consequence to the geometrical frustration because the resultant dimerized structure alleviates the frustration. This is best seen in Fig. 6.7 for $J = 0.7t_1$ (top panel) for which the remaining antiferromagnetic bonds form a bipartite nonfrustrated sub-lattice. In a finite system, even discrete symmetries cannot be spontaneously broken but for the finite-size DMRG calculations producing the data in Fig. 6.7, the open boundary conditions act as a weak perturbation which break the translational symmetry of the system. Because of this small perturbation the two different dimerized states ([ferro-anti-ferro-anti-...] and [anti-ferro-anti-ferro-...]) are not exactly degenerate for a system with open boundary conditions while they are degenerate for an infinite system (or a system with periodic boundary conditions). For L even a state as depicted in Fig. 6.7 for $J = 0.7t_1$ has a slightly lower energy as a state like the one for $J = 0.83t_1$. This is because in a configuration as for $J = 0.7t_1$ there is one additional antiferromagnetic bond as compared to a configuration as for $J = 0.83t_1$. Because of the small energy difference $\frac{\Delta E}{E}$, the DMRG calculations converge sometimes to the *wrong* state dependent on the randomly chosen initial state.

Before analysing the transition to the dimerized ground state in more detail, I will view the evolution of the correlations along another path in the $J - \varphi$ phase diagram. The above considerations are done as a function of J and now I will turn to the evolution of the correlations from the ordinary Kondo chain ($t_2 = \varphi = 0$) towards the frustrated ladder as a function of t_2. Fig. 6.8 shows the same quantities as Fig. 6.7 but now for a fixed value of $J = 0.7t_1$ and various values of t_2. In the limit $t_2 \to 0$, the lattice is bipartite and it is known ([114]) that nearest-neighbors of the ordinary chain (rung correlations) are antiferromagnetically correlated while next-nearest-neighbors (leg correlations) are ferromagnetically correlated. These correlations are free of any frustration and in Fig. 6.8 it is visible that the ground state correlations are stable against a finite but small t_2 (see $t_2 = 0.1t_1$ in Fig. 6.8). This is the expected behaviour, since the ground state of the ordinary chain has a finite spectral gap so that non-degenerate perturbation theory is applicable as long as the gap stays finite. The
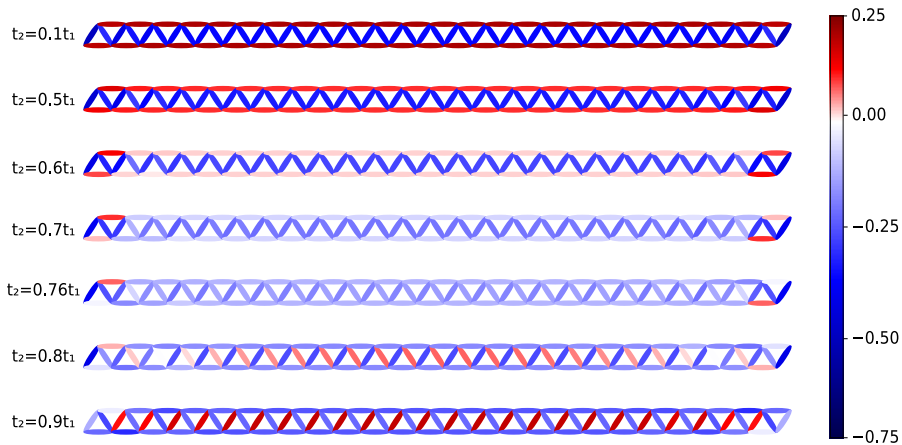
Figure 6.8: Nearest-neighbor spin correlations $\langle \mathbf{S}_i \mathbf{S}_j \rangle$ (color code) as obtained from DMRG for a ladder with $L = 52$ sites at $J = 0.7t_1$ and for various values of the next-nearest neighbor hopping t_2 as indicated.

effect of increasing t_2 is that the ferromagnetic correlations along the legs decrease because of the geometrical frustration introduced by the hopping t_2 along the legs. Still, at $t_2 = 0.5t_1$[1] the qualitative picture did not change but the leg correlations decreased to $\langle \boldsymbol{S}_i \boldsymbol{S}_{i+2} \rangle \approx 0.1$ from the initial value $\langle \boldsymbol{S}_i \boldsymbol{S}_{i+2} \rangle \approx 0.2$ for $t_2 = 0.1t_1$. The further increase of t_2 leads to a sign change in the correlations along the legs as is visible for $t_2 = 0.7t_1$ in Fig. 6.8. Now the magnetic frustration is obvious since the localized spins $\boldsymbol{S}_i$ try to align antiferromagnetically on the triangles from the zigzag ladder. The response to the frustration is already slightly visible for $t_2 = 0.76t_1$: spin-dimerization along the rungs of the ladder because the correlations differ on the $\diagdown$-bonds as compared to the $\diagup$-bonds. The dimerization is already strongly apparent for $t_2 = 0.8t_1$. There, also the oscillation from ferro- to antiferromagnetic correlations is visible. The closeness to the transition point leads to comparably large boundary effects for $t_2 = 0.8t_1$, but nevertheless the bulk region is well observable. Finally for $t_2 = 0.9t_1$, one obtains qualitative similar ground state correlations as compared to $J = 0.7t_1, t_2 = t_1$ in Fig. 6.7. However, the evolution of the correlations from the weakly frustrated limit (strong J in Fig. 6.7 and weak t_2 in Fig. 6.8) towards the strongly frustrated regime is qualitatively different.

All results so far are shown for lattices with $L = 52$ sites. Fig. 6.9 shows data for fixed $t_2 = t_1$ and fixed $J = 0.7t_1$ and various system sizes from $L = 20$ up to $L = 60$. Finite size effects are nearly absent. In addition, the values of the correlations in the center region of the chain coincide with results from VUMPS correlations for a two-site unit cell.

Phase boundary

The results from the last subsection imply that the frustrated Kondo zigzag ladder has an extended region in the $J - \varphi$ phase diagram in which the ground state spontaneously breaks the translational symmetry of the Hamiltonian. To locate the phase boundary precisely, the order parameter O_D from Eq. (6.6) can be calculated. Fig. 6.11 shows the order parameter O_D as a function of J/t_1 (Fig. 6.11(a)) and as a function of t_2/t_1 (Fig. 6.11(b)). In finite-size calculations the transition is smeared out and no exact transition point can be located for finite L. But still, the data for several system sizes L can determine the transition point accurately.
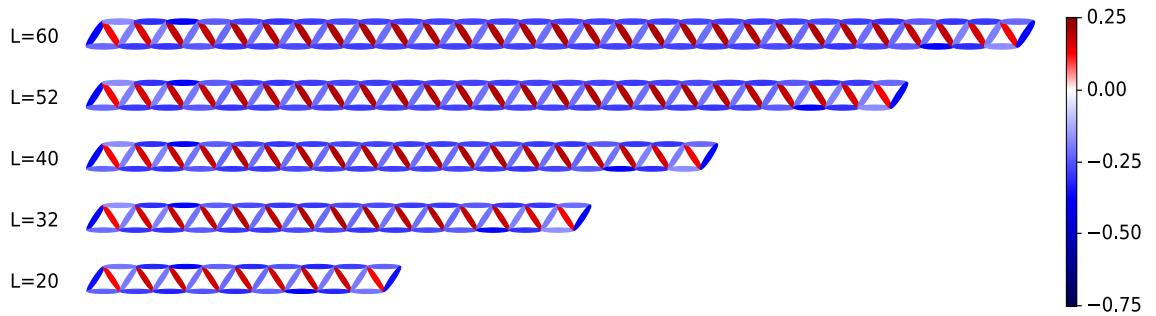
Figure 6.9: Nearest-neighbor spin correlations as in Fig. 6.7 but for different L at fixed $J = 0.7t_1$ and fixed $t_2 = t_1$.

---

1   The Lifshitz-transition point from the free band structure.

In Fig. 6.11(a) the order parameter has its *lowest* value for the largest system ($L = 52$) for all $J \geq 0.9t_1$ while it has its *highest* value for the largest system ($L = 52$) for $J \leq 0.88t_1$. Hence, one might expect that the order parameter scale to $O_D = 0$ for $J \geq 0.9t_1$ and to $O_D > 0$ for $J \leq 0.88t_1$ for $L \to \infty$. This determines the critical value $(J/t_1)_c^{(\text{dim})}$ to the region $0.88 < (J/t_1)_c^{(\text{dim})} < 0.9$. Additional VUMPS calculations (see the curve $L = \infty$ in Fig. 6.11(a)) support this proposition and provide an even more accurate determination of the transition point. Therefore, one has to scale the order parameter obtained by a VUMPS calculation at finite bond dimension χ to the infinite bond dimension limit. An example can be seen in Fig. 6.10. For $J = 0.9t_1$, the order parameter O_D apparently scales to zero. On the contrary, for $J = 0.89t_1$ one needs bond dimensions $\chi \sim 50{,}000$ to observe that the order parameter will vanish in the infinite χ limit. For $J = 0.88t_1$, I have performed the computations for bond dimensions up to $\chi \sim 100{,}000$ and still the extrapolation to $\chi = \infty$ is not trivial. But taking into account the finite-size calculations, one concludes that the order parameter stays finite. To conclude, both scalings (finite-size and finite-entanglement) in combination, deliver reliable and accurate results and the critical interaction is obtained at $(J/t_1)_c^{(\text{dim})} \approx 0.885 \pm 0.005$. In the parametrization used in the phase diagram in Fig. 6.4 this corresponds to $(J/t)_c^{(\text{dim})} \approx 0.63 \pm 0.01$.

Fig. 6.11(b) provides the same analysis but as a function of t_2/t_1. In this case, the finite-size calculations predict that the order parameter is $O_D = 0$ for $t_2 \leq 0.76t_1$ and $O_D > 0$ for $t_2 \geq 0.8t_1$. The calculations for $t_2 = 0.78t_1$ suggest a vanishing order parameter, but they would be also consistent with a small but finite value of O_D. The VUMPS results, however, clearly show a vanishing order parameter for $t_2 = 0.78t_1$ so that one can conclude: $(t_2/t_1)_c^{(\text{dim})} \approx 0.785 \pm 0.005$. In the parametrization used in the phase diagram in Fig. 6.4 this
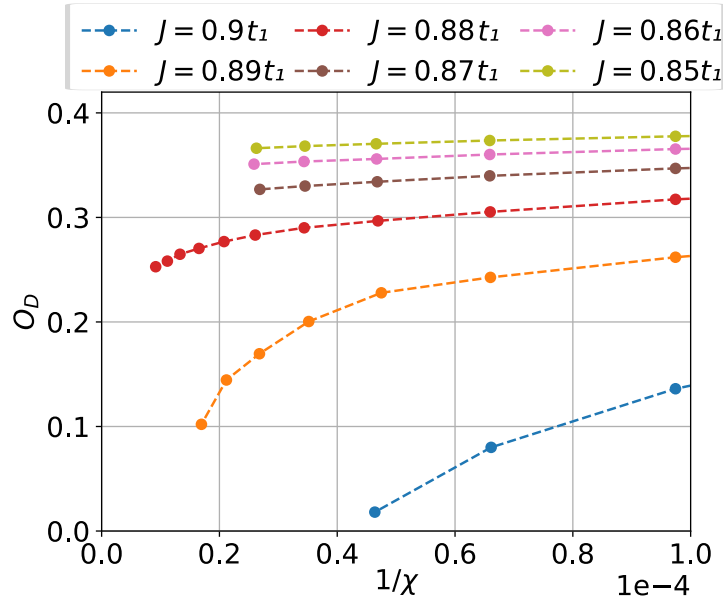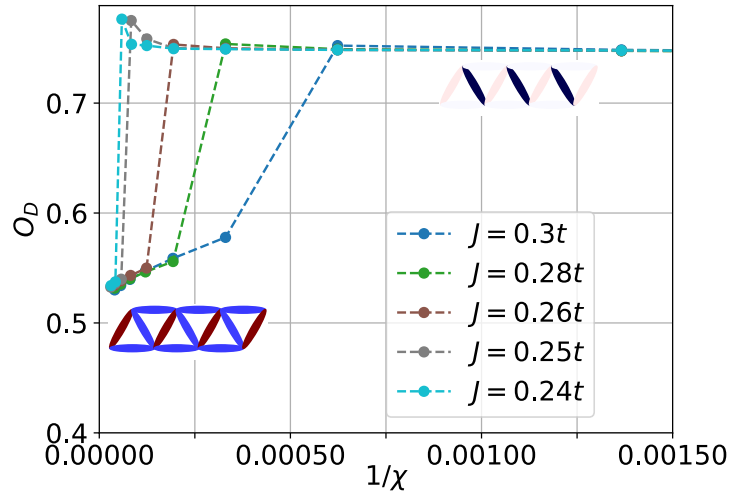

Figure 6.10: The order parameter O_D for dimerization as a function of $1/\chi$ for several J and fixed $t_2 = t_1$ as obtained by VUMPS calculations in the thermodynamic limit. The bond dimension χ refers to the total bond dimension (see Eq. (4.73)).

corresponds to $\varphi_c^{(\mathrm{dim})} \approx 0.67 \approx 0.21\pi$ for $J \approx 0.55t$. The trend of the order parameter O_D does not reveal the order of the phase transition unambiguously. In Fig 6.11(a), the data is consistent with a second order or weakly first order phase transition. On the contrary, the data in Fig. 6.11(b) suggests a first order or a weakly first order phase transition. It would not be excluded, that the order of the phase transition changes along the boundary but this would imply another critical point. For a refined determination of the order of the transition, one might study the fidelity $\langle \Psi_0(t_2) | \Psi_0(t_2') \rangle$ but its evaluation is technically difficult because of the two degenerate dimerized ground states. One would also need to increase the resolution in the parameter space which would require large computational resources.

I have performed extensive calculations for various values of the parameters J and t_2 (φ) to obtain the phase boundary in the $J - \varphi$ plane for the transition into the dimerized ground state (see blue line Fig. 6.4). Starting from $\varphi = \frac{\pi}{4}$, the phase boundary decreases with decreasing J. For $J \to 0$, my calculations support that the critical line ends at $\varphi_c(J \to 0) = \arctan\left(\frac{1}{2}\right) \approx 0.148\pi$. This corresponds to $t_2 = 0.5t_1$ and is exactly the point of the Lifshitz transition of the free band structure (see Fig. 6.2). Calculations in the weak-J regime are generally more involved but the determination of the transition at $J \approx 0.1t$ is still possible. However, the state within the symmetry broken phase ($t_2 > 0.5t_1$) cannot be determined as accurately as for larger values of J. It is therefore not excluded, that the ground state has an even more complex structure as compared to the spin-dimerization (see Subsec. 6.2.2 for further discussion of this regime).

Starting again at $\varphi = \frac{\pi}{4}$ but now following the other direction (increasing J), the phase boundary increases only until it reaches a maximum at $J \approx 0.68t$. Afterwards the transition line bends back and $(J/t)_c^{(\mathrm{dim})}$ starts to decrease. This is the expected behaviour in fact, since it is impossible that the transition line ends in a critical point $J \neq 0$ for $\varphi = \frac{\pi}{2}$. As indicated

(a) $O_{\mathrm{D}}\left(\frac{J}{t_1}\right)$ **(b)** $O_{\mathrm{D}}\left(\frac{t_2}{t_1}\right)$
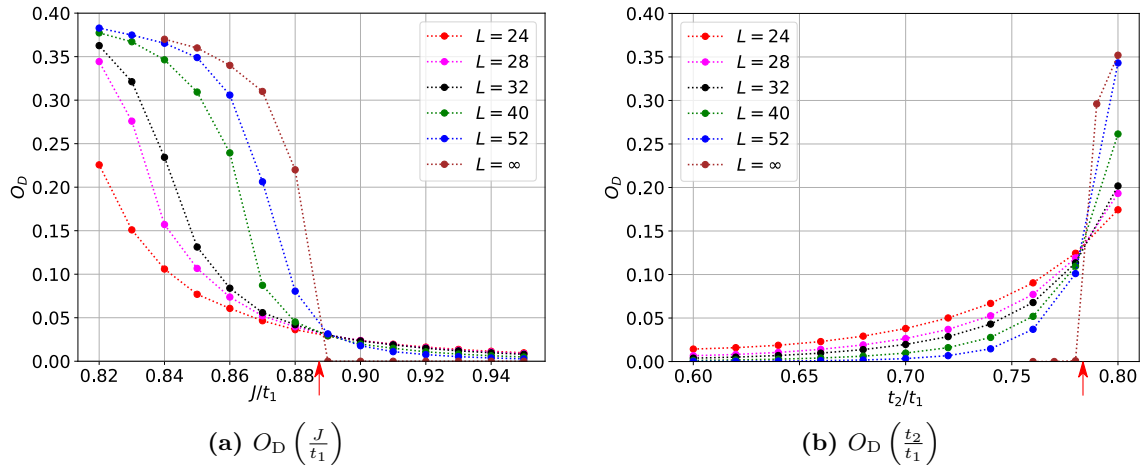
Figure 6.11: Order parameter for spin dimerization O_{dim}, Eq. (6.6), as a function of a) J/t_1 and b) t_2/t_1 for different system sizes L, as obtained by DMRG. The $L = \infty$ values are obtained by the VUMPS algorithm after scaling to the infinite bond-dimension limit. In a), t_2 is fixed to $t_2 = t_1$ while b) is for fixed $J = 0.7t_1$. The red arrows mark the transition: a) $(J/t_1)_c^{(\mathrm{dim})} \approx 0.885 \pm 0.005$. b) $(t_2/t_1)_c^{(\mathrm{dim})} \approx 0.785 \pm 0.005$. This corresponds to a) $(J/t)_c^{(\mathrm{dim})} \approx 0.63 \pm 0.01$ and b) $\varphi_c^{(\mathrm{dim})} \approx 0.67 \approx 0.21\pi$ at $J \approx 0.55t$, see the phase diagram in Fig. 6.4.

by the paths $\mathcal{C}''$ in Fig. 6.3, non-degenerate perturbation theory applies for the decoupled chain limit ($\varphi = \frac{\pi}{2}$) since the ground state is unique and has a finite spectral gap in this case. The dotted blue line in Fig. 6.4 suggests a possible further trend of the transition line towards the $J = 0$ axis where the line is expected to end. It is tempting that the critical line ends in the point $\varphi = \frac{\pi}{2}$ and $J = 0$ since there is no further exceptional point in the noninteracting band structure beside the Lifshitz transition at $\varphi = \arctan\left(\frac{1}{2}\right)$.

Transition at weak J

Finally, I will present some data for the weak-J regime ($J \sim 0.1t$) in which the computations become particularly difficult. VUMPS as well as DMRG calculations suggest a ground state for $J \sim 0.1t$ which is close to a valence-bond solid (VBS), i.e. $\langle \boldsymbol{S}_{i-1}\boldsymbol{S}_i \rangle = -0.75$ and $\langle \boldsymbol{S}_i\boldsymbol{S}_{i+1} \rangle = 0$[1]. Note, however, that an exact VBS can never be the ground state since in that case the localized spins $\boldsymbol{S}_i$ decouple completely from the conduction electron system. This is due to the monogamy theorem of entanglement [135] which predicts, that if a subsystem is maximally entangled with another one, it cannot be entangled with a third system. A spin-1/2 which is one part of a singlet with another spin-1/2 is, however, maximally entangled. The entanglement entropy is $S_{\mathrm{vN}} = \ln 2$ which is the highest value for a system with two degrees of freedom (spin-↑ and spin-↓). This consideration demonstrates that the ground state cannot be an exact VBS, however, it might be very close to a VBS.

Fig. 6.12 shows VUMPS calculations for $\varphi = \frac{\pi}{4}$ ($t_2 = t_1$) and several values of J for the order parameter O_{D} as a function of $1/\chi$. For small bond dimensions χ, the ground state is close to a VBS (see upper-right inset) with the order parameter $O_{\mathrm{D}} \approx 0.75$. But when increasing the bond dimension, the ground state changes over suddenly into the standard spin-dimerized

Figure 6.12: The order parameter for dimerization as a function of $1/\chi$ for several J and fixed $\varphi = \frac{\pi}{4}$ as obtained by VUMPS calculations in the thermodynamic limit. The bond dimension χ refers to the total bond dimension (see Eq. (4.73)). The insets show the short-range spin correlations in the corresponding ground states.

---

1 See upper-right inset of Fig. 6.12 for a color plot of the nearest-neighbor spin-correlations.

ground state (see lower-left inset in Fig. 6.12). For weaker J, the change happens at higher bond dimensions. This suggests that the calculations at even lower J ($J = 0.1t$) are not well converged and that the spin-dimerized phase extends to $J \to 0$ without qualitative changes.

6.2.3 Quasi-long-range order

The general Doniach picture predicts that the indirect magentic interactions between the localized moments mediated by the conduction electron system increase in the weak-J regime. The development of magnetic order, however, is not realized for the ordinary Kondo chain in one dimension and the ground state is a featureless spin-liquid for any $J > 0$. In the case of the frustrated ladder, the usual increase of indirect magnetic interactions leads to a spontaneous break of the translational symmetry (see last Sec. 6.2.2). This a direct consequence of the geometrical frustration, whose increase goes along with the increase of indirect magnetic interactions. It is an interesting question if the alleviation of the frustration paves the way for a magnetically ordered ground state. In one dimension, the ground state cannot be long-range ordered because of the Mermin-Wagner theorem. But still, a quasi-long-range ordered critical ground state is possible. Such a state stands out by gapless spin-excitations and algebraically decaying spin-correlations. The algebraic decay of the spin-correlations implicates that the spin-structure factor $S(q)$ (Eq. 6.4) diverges at a specific wave-vector $q = Q$ and likewise the correlations length for the localized moments diverges.

I will demonstrate in the next two subsections that the spin-dimerized phase is indeed a precursor for a quasi-long-range magnetically ordered phase with spiral spin-correlations at wave-vector $Q = \frac{\pi}{2}$. First, I will present results for the spin-structure factor $S(q)$ and second, I will analyse the spin gap ΔE_S.

Divergence of the spin-structure factor at $Q = \frac{\pi}{2}$

During this subsection, I will focus on the case $t_2 = t_1$ and analyse the spin-structure factor as a function of J/t_1. The distance dependence of the spin-correlations $\langle \boldsymbol{S}_i \boldsymbol{S}_{i+\Delta_i} \rangle$ gives insights to the amount of indirect magnetic interactions. Fig. 6.13 displays $\langle \boldsymbol{S}_i \boldsymbol{S}_{i+\Delta_i} \rangle$ in the upper panel for a system with $L = 60$ sites together with $i = 10$ to ensure that boundary effects are negligible. The analogue $\langle \boldsymbol{s}_i \boldsymbol{s}_{i+\Delta_i} \rangle$ for the conduction electron spins is plotted in the lower panel. In the strong J-regime, the correlations are known to decay exponentially and for $J = 3.0t_1$ this is also well visible in Fig. 6.13. This behaviour persists down to $J = 0.9t_1$ but for $J = 0.7t_1$, the correlations suddenly extend over the entire system. The conduction electron spins undergo a similar behaviour but the absolute magnitude of $\langle \boldsymbol{s}_i \boldsymbol{s}_{i+\Delta_i} \rangle$ is much smaller as compared to the localized moments. This can be traced back to the weak local moment $\langle \boldsymbol{s}_i^2 \rangle$ of the conduction electrons which is e.g. $\langle \boldsymbol{s}_i^2 \rangle \approx 0.4$ for $J = 0.7t_1$. This value is only slightly larger than the value $\langle \boldsymbol{s}_i^2 \rangle = \frac{3}{8}$ for the noninteracting Fermi gas.

Furthermore, the correlations develop a characteristic period $\Delta i = 4$, which is already slightly visible for $J = 0.9t_1$. This characteristic wave-length can be observed more clearly in momentum space when considering the Fourier transformation of the spin-correlations, i.e. the spin-structure factor from Eq. (6.4). Fig. 6.14 shows the spin-structure factor $S(q)$ as a function of J/t_1 in a color plot and provides an overview over the development of $S(q)$ from the strong-J
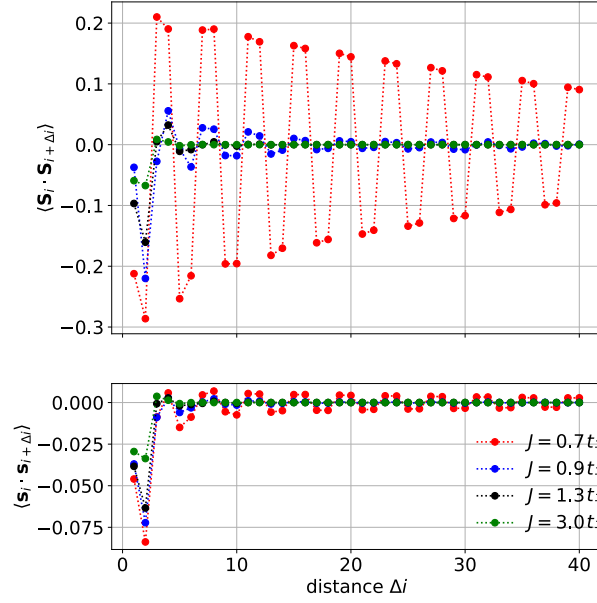
Figure 6.13: Top: Distance dependence of the spin correlation function $\langle \boldsymbol{S}_i \boldsymbol{S}_{i+\Delta_i} \rangle$ for $i = 10$, obtained by finite-size DMRG for $L = 60$ sites, $t_1 = t_2$ and for various coupling strengths J/t_1. Bottom: the same but for the conduction-electron spin correlations $\langle \boldsymbol{s}_i \boldsymbol{s}_{i+\Delta i} \rangle$.
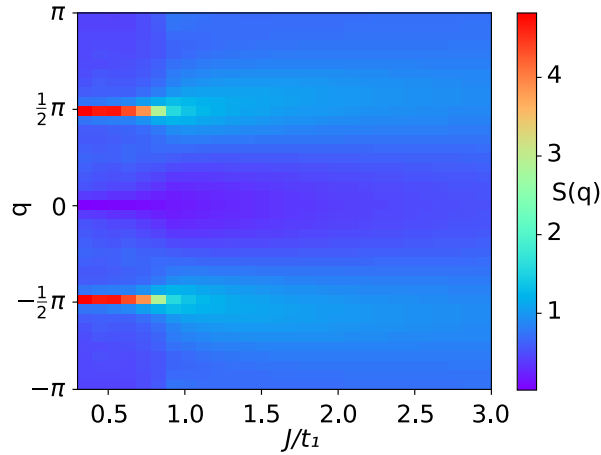
Figure 6.14: J-dependence of the spin-structure factor $S(q) = L^{-1} \sum_{i,j}^{L} e^{iq(R_i - R_j)} \langle \boldsymbol{S}_i \boldsymbol{S}_j \rangle$ (color code on the right) for $L = 40$ sites and $t_2 = t_1$.

regime ($J \sim 3.0t_1$) towards the intermediate-J regime ($J \sim 0.5t_1$). For $J > 0.84t_1$, the spin-structure factor is featureless and has a broad maximum located at $Q > \frac{\pi}{2}$. On the contrary, for $J < 0.84t_1$ one observes a sharp peak of $S(q)$ at $Q = \frac{\pi}{2}$ which might be a feature of a quasi-long range magnetic ground state if the peak height diverges in the thermodynamic limit $L \to \infty$. The peak formation is also displayed in Fig. 6.15 for four different values of J/t_1. For $J = 3.0t_1$, the location of the broad maximum is found at $Q \approx 1.82$ which fits exactly the position predicted by strong-coupling perturbation theory (Eq. (5.16)): $Q = \arccos\left(-\frac{t_1^2}{4t_2^2}\right) \approx 1.82 \; \widehat{=} \; 104°$ as indicated by the green arrow in Fig. 6.15.

The L-dependence of the peak height for $J < 0.84t_1$ is of particular importance for the question whether the ground state exhibits quasi-long-range order or not. I have therefore displayed $S\left(Q = \frac{\pi}{2}\right)$ as a function of L in Fig. 6.16 with a logarithmic L-axis. While for $J > 0.84t_1$, $S\left(\frac{\pi}{2}\right)$ converges to a finite value for $L \to \infty$, the data for $J = 0.7t_1$ propose a logarithmic divergence of $S\left(\frac{\pi}{2}\right)$ when reaching the thermodynamic limit. This is consistent with spin-correlations in real space in the form:

$$\langle \boldsymbol{S}_i \boldsymbol{S}_{i+\Delta_i} \rangle \sim \frac{e^{-iQ\Delta_i} \ln^\sigma (\Delta_i)}{\Delta_i}, \tag{6.7}$$

i.e. with an algebraic decay for increasing distance. Indeed, an easy calculation shows that if the real-space correlations have the form as in Eq. (6.7), the Fourier transformation becomes:

$$S(Q) \sim \ln^{1+\sigma} L \tag{6.8}$$

The data in Fig. 6.16 is not sufficient to determine the possible logarithmic corrections σ to the power law behaviour from Eq. (6.7) but it is nevertheless a clear sign for quasi-long-range spiral magnetic order in the ground state at wave-vector $Q = \frac{\pi}{2}$.

To corroborate this proposition and to find the critical interaction $J_c^{(\mathrm{mag})}$, a refined finite-size scaling analysis is helpful. Since the specific finite-size dependence of $S\left(\frac{\pi}{2}\right)$ is not known for
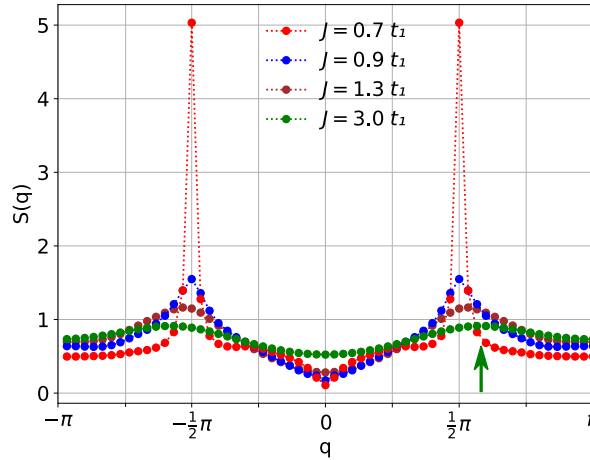
Figure 6.15: Spin-structure factor $S(q)$ for different J/t_1 as indicated and for $L = 60$ sites.
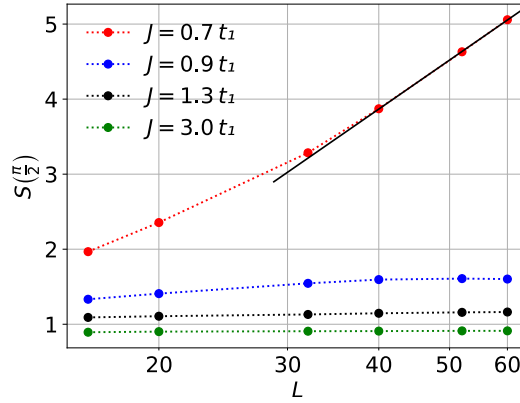
Figure 6.16: Spin-structure factor $S(Q)$ at $Q = \pi/2$ for different J/t_1 as functions of L on a logarithmic scale.

couplings $J > J_c^{(\text{mag})}$, the data collapse method [136–138] is appropriate. Here, the general idea is to absorb the finite-size dependence in a scaling function $f(x)$ for the dimensionless parameter $x = \frac{L}{\xi}$ where ξ is the correlation length (see App. C for a detailed description). The correlation length is readily obtained from the DMRG data for couplings $J > J_c^{(\text{mag})}$ from a fit of the distance dependence of the spin-correlations:

$$\langle \boldsymbol{S}_i \boldsymbol{S}_{i+\Delta_i} \rangle = \text{const} \times e^{-\frac{\Delta_i}{\xi}}, \tag{6.9}$$

and is expected to diverge at $J_c^{(\text{mag})}$ as $\xi \propto \left(J - J_c^{(\text{mag})} \right)^{-\nu}$. For a *fixed* system size, the correlation length ξ is displayed in Fig. 6.17(a) as a function of J/t_1. The data is well described by a power law fit for a critical interaction $(J/t_1)_c^{(\text{mag})} \approx 0.84$. The only deviations from the
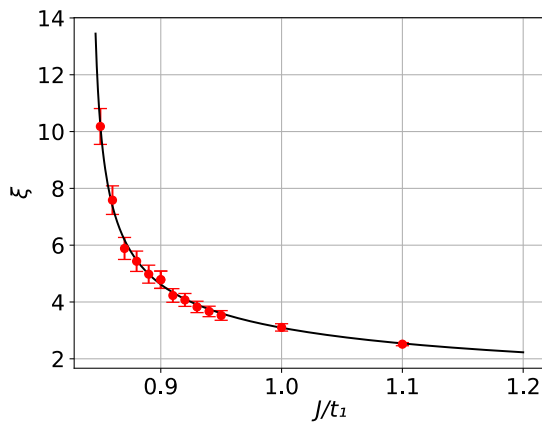
(a) Fit parameters: $(J/t_1)_c^{(\text{mag})} = 0.84$, $\nu = 0.4$ **(b)** Fit parameters: $(J/t_1)_c^{(\text{mag})} = 0.84$, $\gamma = 0.2$
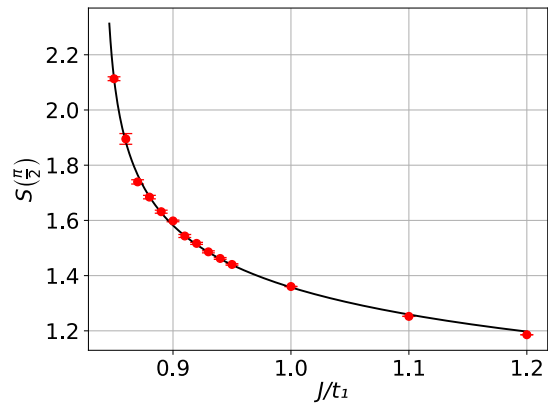
Figure 6.17: The correlation length $\xi_{L=40}$ and the spin-structure factor $S(Q)_{L=40}$ at $Q = \frac{\pi}{2}$ as a function of J/t_1. Both are fitted with a power law $\left(J - J_c^{(\text{mag})} \right)^{-X}$ with $X = \{\nu, \gamma\}$.

power law behaviour is visible for $J \approx J_c^{(\mathrm{dim})} = 0.89t_1$, which is traced back to the influence of the phase transition into the spin-dimerized phase.

Eq. (C.7) describes the data collapse for the static magnetic susceptibility $\chi_L \left(\omega = 0, Q = \frac{\pi}{2}\right)$ for a system of size L. The static magnetic susceptibility is defined as:

$$\chi_L(\omega = 0, Q) = \lim_{\beta \to 0} \frac{1}{L} \sum_{ij} e^{-iQ(i-j)} \int_0^\beta d\tau \langle \boldsymbol{S}_i(\tau) \boldsymbol{S}_j(0) \rangle \tag{6.10}$$

For a continuous phase transition, the susceptibility $\chi_{L \to \infty}$ is expected to diverge with a power law behaviour $\chi \propto \left(J - J_c^{(\mathrm{mag})}\right)^{-\gamma}$ (see Eq. (C.2)). However, the static susceptibility is a numerically expensive quantity as compared to the spin-structure factor from Eq. (6.4). The spin-structure factor is the equal-time susceptibility and one may expect that these two quantities share a similar divergent behaviour. Hence, I will evaluate Eq. (C.7) for the spin-structure factor instead of the static susceptibility. For a *fixed* size $L = 40$ the divergent behaviour of $S\left(\frac{\pi}{2}\right)$ is well visible in Fig. 6.17(b) where the critical interaction $J_c^{(\mathrm{mag})}$ is again found to be $(J/t_1)_c^{(\mathrm{mag})} \approx 0.84$. Similar to Fig. 6.17(a), the only deviations are found in the vicinity of the dimerization phase transition at $J_c^{(\mathrm{dim})}$.

The data in Fig. 6.17 is calculated for $t_1 = t_2$ at *fixed* system size $L = 40$. It provides therefore only a hint to the divergent behaviour of both quantities while truly divergent behaviour can only occur in the thermodynamic limit $L \to \infty$. The data collapse condition (Eq. C.7) for $S\left(\frac{\pi}{2}\right)$, however, is a reliable check for divergent behaviour for $L \to \infty$. I find, that the curves collapse for system sizes $L = 20, 24, 28, 32, 40$ when choosing $(J/t_1)_c^{(\mathrm{mag})} = 0.84$, $\nu = 0.4$ and $\gamma = 0.2$ as is showed in Fig. 6.18. While the critical interaction $J_c^{(\mathrm{mag})}$ can be determined
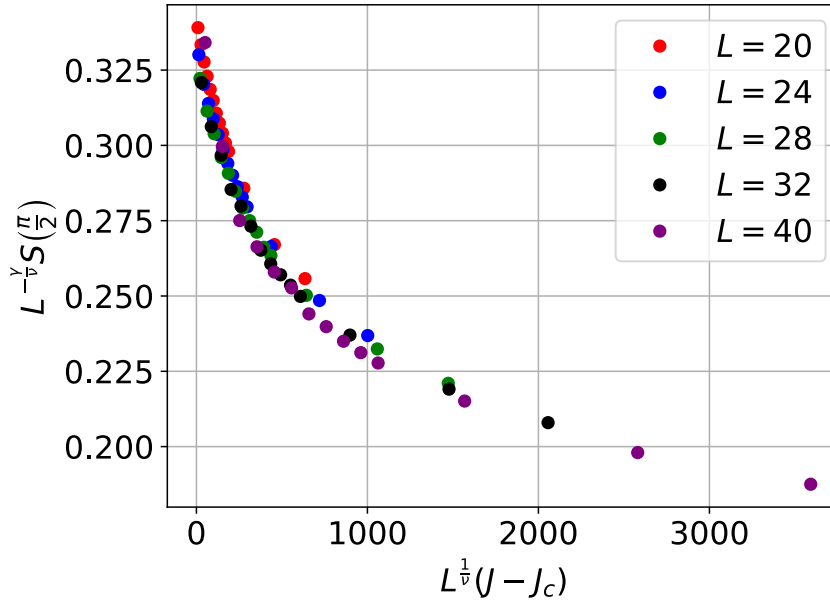
Figure 6.18: Finite-size scaling for $S\left(\frac{\pi}{2}\right)$ (see text). The data for different L as indicated and for $J/t_1 = 0.85, 0.86, \ldots, 0.95$ collapse to a single line at $(J/t_1)_c^{(\mathrm{mag})} \approx 0.845$, $\nu \approx 0.4$ and $\gamma \approx 0.2$.

rather precisely, up to a few percent, the critical exponents ν and γ have a much larger error. This is caused by the nearby phase transition into the spin-dimerized ground state.

In summary, the analysis of the spin-structure factor and the correlation length unveils a second quantum phase-transition in the Kondo zigzag ladder at a critical interaction $(J/t_1)_c^{(\mathrm{mag})} \approx$ 0.84 and $t_2 = t_1$. The transition is in the direct vicinity of the dimerization transition at $(J/t_1)_c^{(\mathrm{dim})} \approx 0.89$ but the data clearly propose $J_c^{(\mathrm{mag})} <_c^{(\mathrm{dim})}$. This is consistent with the intuitive picture, that the dimerization paves the way for a magnetically ordered ground state since it alleviates the geometrical frustration.

Spin gap ΔE_S

An independent possibility for the determination of the magnetic phase boundary is the spin gap ΔE_S because it vanishes at the transition point $J_c^{(\mathrm{mag})}$. The spin gap is defined as the following energy difference:

$$\Delta E_S = E(S = 1) - E(S = 0), \tag{6.11}$$

where $E(S)$ describes the ground state energy in the sector of the Hilbert space which transforms under the spin-S representation of $SU(2)$. With the help of the $SU(2)$-symmetric implementation, one is able to target states with fixed S directly, so that the spin gap can be computed to high precision. A gapless ground state can only occur in the thermodynamic limit since for finite L the complete spectrum of the Hamiltonian is discrete. Hence, the spin gap for finite systems $\Delta E_S(L)$ needs to be scaled to the limit $L \to \infty$. If one assumes quasi-particle gapless low-energy excitations with a dispersion $\omega(k) = ck$, the functional dependence $\Delta E_S(L)$ follows from the discretization of k-space:

$$\Delta E_S(L) \propto \frac{1}{L}, \tag{6.12}$$

at least in the gapless case. Notice that this would be different, if the dispersion of the low-energy excitations would be quadratic. In the right panel of Fig. 6.19(a) (Fig. 6.19(b)), one can see numerical DMRG data for the spin gap $\Delta E_S(L)$ for several values of J/t_1 (t_2/t_1) as a function of L^{-1}. The data is extrapolated to $L \to \infty$ with the ansatz $\Delta E_S(L) - \Delta E_S(\infty) \propto \frac{1}{L}$, where $\Delta E_S(\infty)$ is the spin gap in the thermodynamic limit. The extrapolated values are displayed in the left panel of Fig. 6.19(a) (Fig. 6.19(b)) as a function of J/t_1 (t_2/t_1). The error bars display the uncertainty from the linear extrapolation in L^{-1}. The data is consistent with a linear closure of the spin gap both as a function of J and as a function of t_2:

$$\Delta E_S \propto J - J_c^{(\mathrm{mag})} \quad \text{and} \quad \Delta E_S \propto t_2 - t_{2c}^{(\mathrm{mag})} \tag{6.13}$$

The data in Fig. 6.19(a) is calculated for fixed $t_2 = t_1$ and the spin gap vanishes at $(J/t_1)_c^{(\mathrm{mag})} \approx 0.84 \pm 0.03$ (see horizontal red bar in the left panel of Fig. 6.19(a)). This value is in excellent agreement with the critical value determined in the last subsection by examining the divergence of the spin-structure factor. Fig. 6.19(b) yields a critical value $(t_2/t_1)_c^{(\mathrm{mag})} \approx 1.26 \pm 0.03$ for the transition as a function of t_2 for fixed $J = t_1$.

An overview of the evolution of the spin gap in the whole parameter space is also interesting.
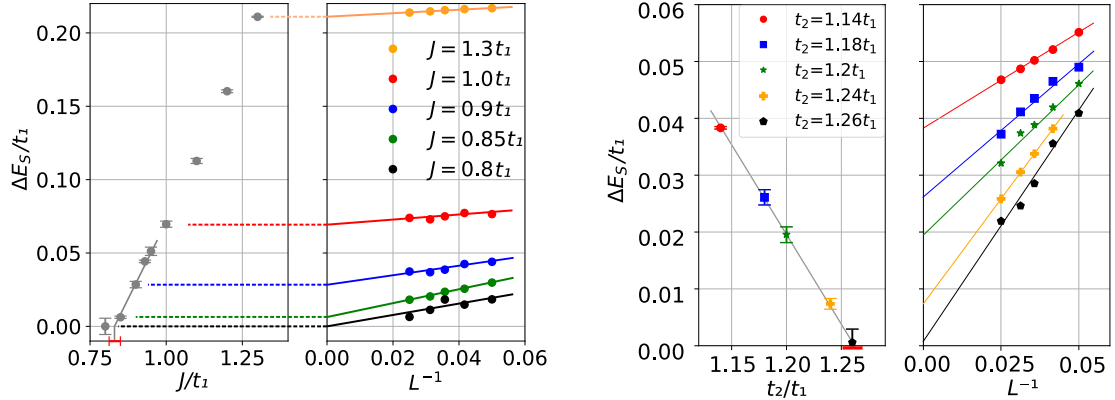
(a) Linear fit (grey line) yields: $J_c^{\mathrm{mag}} = 0.84t_1 \pm 0.03t_1$ ($J_c^{\mathrm{mag}}(\varphi) \approx 0.90t$ at $\varphi = \frac{\pi}{4}$) (see red horizontal bar) for $t_2 = t_1$.

(b) Linear fit (grey line) yields: $t_{2,c}^{\mathrm{mag}} = 1.26t_1 \pm 0.03t_1$ ($\varphi_c^{\mathrm{mag}}(J) \approx 0.90 \approx 0.29\pi$ at $J \approx 0.62t$) (see red horizontal bar) for $J = t_1$.

Figure 6.19: Right panels: L-dependence of the spin gap. Lines: linear fits $\Delta E_{\mathrm{S}}(L) - \Delta E_{\mathrm{S}}(\infty) \propto 1/L$. Left panels: $\Delta E_{\mathrm{S}}(\infty)$, obtained by extrapolation to the $1/L \to 0$ limit, as a function of a) J/t_1 and b) t_2/t_1. Bars: extrapolation errors
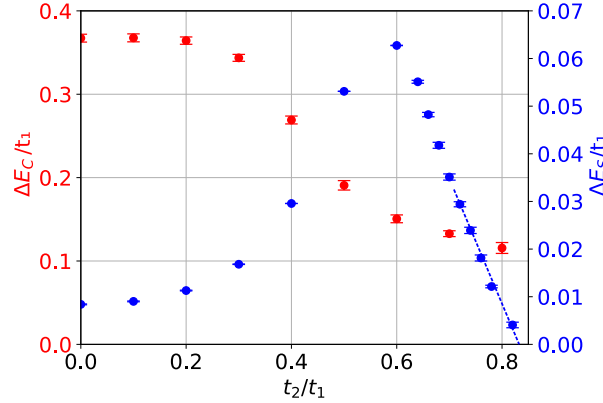
Figure 6.20: The evolution of the spin gap ΔE_{S} [see Eq. (6.11)] and the charge gap ΔE_{C} [see Eq. (6.14)] as functions of next-nearest-neighbor hopping t_2/t_1 at $J = 0.7t_1$ from the ordinary chain limit ($t_2 = 0$) to the frustrated zigzag ladder ($t_2 \approx t_1$). All values are obtained by extrapolation to the thermodynamic limit. Bars: errors of the fit. Blue dotted line: linear fit $\Delta E_{\mathrm{S}} \propto (t_2 - t_{2,c}^{\mathrm{mag}})$. The spin gap closes at $t_{2,c}^{\mathrm{mag}} \approx 0.83t_1 \pm 0.03t_1$. This corresponds to $\varphi_c^{\mathrm{mag}}(J) \approx 0.69 \approx 0.22\pi$ at $J \approx 0.54t$, see the phase diagram in Fig. 6.4.

Strong-coupling perturbation theory proves that the spin gap is of order J for $J \gg t_1, t_2$. The gap then decreases monotonically with decreasing J and this trend is already visible in the left panel of Fig. 6.19(a). On the contrary, the situation is different for the evolution of the gap as a function of t_2. The evolution of the gap from the ordinary chain limit ($t_2 = 0$) towards the frustrated Kondo zigzag ladder ($t_2 \approx t_1$) is displayed by the blue curve in Fig. 6.20. In the limit of the ordinary Kondo chain ($t_2 = 0$), the spin gap is already very small but clearly finite ($\Delta E_S/t_1 \approx 0.01$). When increasing t_2, the spin gap undergoes the expected behaviour: it *increases* because the next-nearest neighbor hopping introduces geometrical frustration. At a maximally frustrated point t_2^*, the spin gap has a maximum and starts to decrease for even larger t_2. Surprisingly, the decrease is clearly different from the increase and in Fig. 6.20, the

gap vanishes at $t_{2,c}^{\mathrm{mag}} \approx 0.83t_1 \pm 0.03t_1$ $(J = 0.7t_1)$.

Fig. 6.20 displays additionally the evolution of the charge gap ΔE_C (red line) defined as:

$$\Delta E_C = \frac{E(L+2,0) + E(L-2,0) - 2E(L)}{2}. \tag{6.14}$$

It is well visible that the charge gap is considerably larger than the spin gap and stays finite in the whole t_2 regime. The effect of t_2 is a decrease of ΔE_C which can be traced back to the enhanced freedom of the conduction electrons due to the next-nearest neighbor hopping. I have also checked that the gap is finite in the whole J regime for $t_2 = t_1$ so that the zigzag Kondo ladder at half-filling is an insulator in the whole $J - t_1 - t_2$ parameter space if $J > 0$.

The criterion of a vanishing spin gap has turned out to be more suitable for the determination of the phase boundary for the transition into the SP-QLRO phase. I have performed analogue computations for various parameters as indicated by the red points in the global phase diagram (Fig. 6.4). In all cases, the magnetic transition is close to the dimerization transition but the magnetic phase is clearly surrounded by the dimerized phase. The latter is expected to extend down to the $J \to 0$ limit as discussed in Subsec. 6.2.2. Whether the magnetic phase also extends to the weak coupling limit, is an interesting question. However, DMRG computations become quite exhausting in the weak coupling regime since the entanglement grows dramatically due the increase of non-local effective interactions. Therefore, I could not make a conclusive statement in the weak-J regime but I will present several scenarios in the upcoming subsection.

Transition at weak J

The weak-J regime is dominated by strong nonlocal effective interactions between the localized moments. One route to tackle the problem in this regime is to apply weak coupling perturbation theory but I will start here by presenting calculations for the spin gap at $J = 0.1t_1$ for the full Kondo lattice. Fig. 6.21 displays results for the spin gap in the weak coupling regime $(J = 0.1t_1)$. Calculations for the ordinary chain limit $(t_2 = 0)$ are well controlled even in the weak-J regime. The red curve $\Delta E_S(L)$ in the left panel of Fig. 6.21 is a perfect linear function of $1/L$ and extrapolations to $L \to \infty$ lead to a very small but finite spin gap $\Delta E_S/t_1 \approx 1.97 \times 10^{-5}$. For small t_2, the spin gap is almost unchanged. It slightly increases to $\Delta E_S/t_1 \approx 2.00 \times 10^{-5}$ which cannot be seen on the scale of the figure. The increase constitutes the same behaviour as in Fig. 6.19(b) and continues for $t_2 = 0.2t_1$. However, already at $t_2 = 0.3t_1$, the spin gap has decreased slightly to $\Delta E_S/t_1 \approx 1.97 \times 10^{-5}$ so that the maximally frustrated point t_2^* satisfies $0.2t_1 < t_2^* < 0.3t_1$. The computations for $t_2 = 0.3t_1$ are still well controlled and the extrapolation error is of the order of the symbol size. For even stronger $t_2 = 0.4t_1$, the spin gap drops significantly $(\Delta E_S/t_1 \approx 1.27 \times 10^{-5})$ and the extrapolation becomes less clear. One might actually guess that the curve for $t_2 = 0.4t_1$ in the right panel of Fig. 6.21 obeys a quadratic scaling $\Delta E_S \propto L^{-2}$ but it is also possible that the calculations for $L = 40$ $(L^{-1} = 0.025)$ are not fully converged and the true gap for $L = 40$ is slightly smaller. For $t_2 = 0.5t_1 \approx t_{2,c}^{\mathrm{dim}}$, it was not possible to reach converged results even with the $SU(2)$-symmetric DMRG implementation. Hence, there is no conclusive answer, if the spin gap closes at some $t_{2,c}^{\mathrm{mag}}$. But one can clearly say that first, the spin gap remains finite
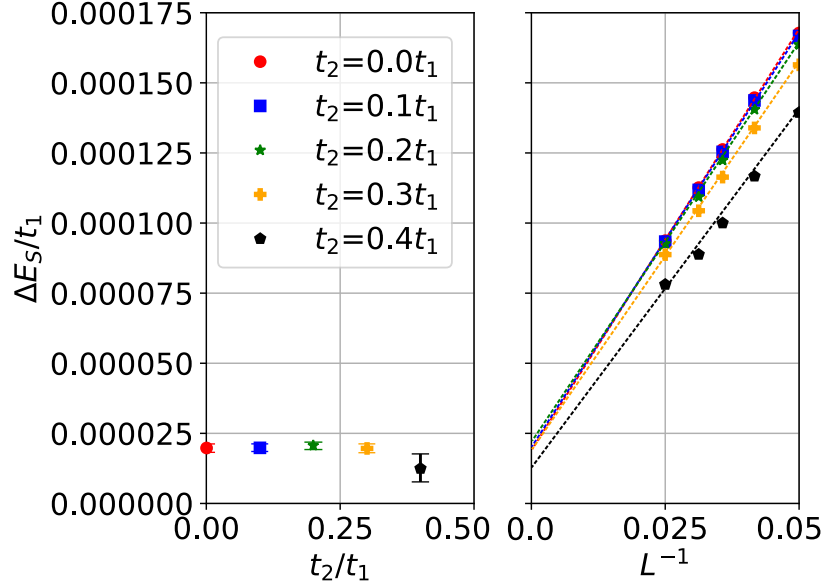
Figure 6.21: Right: The spin gap $\Delta E_S(L)$ as a function of L^{-1}. Dashed lines are extrapolations to $L^{-1} \to 0$ with a linear ansatz: $\Delta E_S(L) - \Delta E_S(\infty) \propto L^{-1}$. Left: The spin gap ΔE_S in the weak coupling regime $J = 0.1 t_1$ for several values of t_2/t_1 as obtained by extrapolations to $L \to \infty$.

when including a small t_2 and second the spin gap is asymmetric with respect to the maximal frustrated point t_2^* (the location of the maximum of $\Delta E_S(t_2)$).

Since direct computations are beyond the numerical capabilities, one may tackle the problem perturbatively in the Kondo interaction J. Because of the high degeneracy of the ground state for $J = 0$, the perturbation theory is much more involved as compared to the strong-J limit. One can derive an effective low-energy Hamiltonian for the localized moments by standard RKKY theory (see Sec. 5.2.2). Before calculating the parameters J_{ij} of the effective Hamiltonian, one may discuss the conclusions from the existence of a spin-only effective model at weak J. For pure spin-models, one can express the Lieb-Schultz-Matthis (LSM) theorem [139, 140] which states:

Theorem 6.1 (Lieb-Schultz-Matthis Theorem)**.** *If the ground state of a half-integer spin model is nondegenerate, the excitation spectrum is gapless in the thermodynamic limit.*

The contrary proposition for degenerate ground states is not true in general. Note also, that the theorem does not make any propositions for integer spin models. The ground state of the ordinary Kondo chain ($t_2 = 0$) is known to be nondegenerate for all $J > 0$. Furthermore, the ordinary Kondo chain has a finite spin gap. Both together is in contradiction to the LSM theorem so that one can conclude that the RKKY theory does not apply to the case $t_2 = 0$. As demonstrated above, the finite spin gap and the unique ground state is stable against a weak t_2 so that this regime cannot be described by RKKY theory either. However for $t_2 > t_{2,c}^{\mathrm{dim}}$, the ground state is twofold degenerate so that the LSM theorem is not applicable and the system might be described by an effective low-energy theory for the localized moments.

The spin-only Hamiltonian (Eq. (5.21)) has interactions J_{ij} determined by the static susceptibility $\chi_{ij}(\omega = 0)$ of the noninteracting conduction electrons:

$$\chi_{ij}(\omega = 0) = \lim_{\beta \to \infty} \int_{\tau=0}^{\beta} d\tau \, \langle \boldsymbol{s}_i(\tau) \boldsymbol{s}_j(0) \rangle \tag{6.15}$$

Because of the absence of interactions, this can be easily evaluated by using Wick's theorem. For a non-degenerate Fermi sea, one obtains:

$$\chi_{ij}(\omega = 0) = \sum_{k > k_F, q \le k_F} \frac{U_{ik} U_{jk}^* U_{jq} U_{iq}^*}{\varepsilon(k) - \varepsilon(q)}, \tag{6.16}$$

where U_{ik} describes the unitary diagonalization of the hopping matrix t_{ij}. Eq. (6.16) can be evaluated numerically. Fig. 6.22(a) displays the distance dependence of the suceptibility χ_{ij} for a chain with $L = 80$ and open boundary conditions. For $t_2 = 0$ (the ordinary chain), one observes the expected regular pattern: χ_{ij} oscillates with a period $(-1)^i$. This oscillation expresses itself in a sharp peak of the Fourier transformation $\chi(Q)$ at the antiferromagnetic wave-vector $Q = \pi$ (see Fig. 6.22(b)). Furthermore, χ_{ij} decays rather slowly which is a typical behaviour for one-dimensional systems. In fact, the susceptibilty behaves as:

$$\chi_{i,i+\Delta_i} \propto \frac{(-1)^{\Delta_i}}{\Delta_i^d}, \tag{6.17}$$

for d-dimensional bipartite lattices [141, 142]. The $1/\Delta_i$ behaviour will lead to a divergence of $\chi(Q = \pi)$ in the thermodynamic limit $L \to \infty$.

On the contrary for $t_2 = t_1$ (the frustrated ladder), the pattern is rather disordered and several periodicities are present. This results in several peaks of the Fourier transformation $\chi(Q)$. The dominating peak is found at $Q = \frac{\pi}{2}$. Again, the decay seems to obey a power law behaviour.

To prove this, I have plotted the L-dependence of the maximum of $\chi(Q)$ in Fig. 6.23. In this

(a) Distance dependence: $\chi_{i,i+\Delta_i}$ ($i = 20$).

(b) Fourier transformation of χ_{ij}.
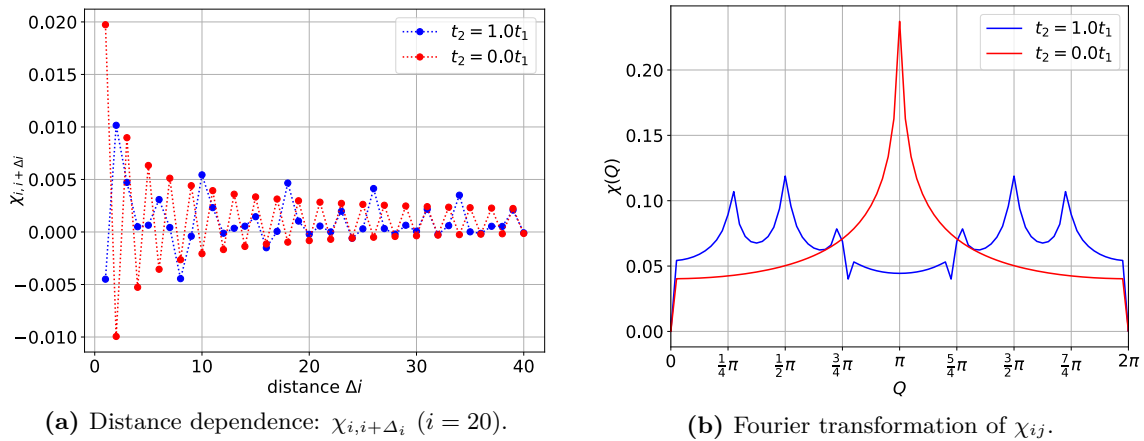
Figure 6.22: The static susceptibility χ of the conduction electrons for a chain with $L = 80$ sites and open boundary conditions. Data is calculated for the ordinary chain ($t_2 = 0$) and the frustrated ladder ($t_2 = t_1$).

case, the calculations are done for periodic systems, for which one can perform the Fourier transformation analytically:

$$\chi(Q) = \frac{1}{2L} \sum_k \frac{n_{Q+k,\uparrow} - n_{k,\downarrow}}{\varepsilon(k) - \varepsilon(Q+k)} \tag{6.18}$$

Fig. 6.23 shows that the peak height of $\chi(Q)$ indeed diverges logarithmically with the system size for both $t_2 = 0$ and $t_2 = t_1$. However, the finite-size effects of $\chi(Q = \frac{\pi}{2})$ are remarkable for $t_2 = t_1$ and indicate the complexity of the effective Hamiltonian. Note that the divergence could also be derived from Eq. (6.18), when expanding the denominator in k around $k = k_F$. This leads to a logarithmic divergence for all nesting vectors Q. The ordinary chain has only a single nesting vector $Q = \pi$, while the frustrated ladder ($t_2 = t_1$) has several nesting vectors, amongst others $Q = \frac{\pi}{2}$ (see Fig. 6.2).

A solution of the effective low energy Hamiltonian (Eq. (5.21)) is difficult for several reasons. First, the Hamiltonian has power law interactions so that it is not suited for the DMRG method. Second, the effective couplings J_{ij} have strong finite size effects, so that the model needs to be solved for large systems to eliminate the finite size effects. Nevertheless, I have studied the effective model briefly with DMRG and exact diagonalization. I have observed the following:

- For open boundary conditions, the short-range spin correlations are dimerized in the center of chains up to $L = 32$. However, strong finite-size effects are present. In particular, it is found that for some system sizes the ground state is not in the $S = 0$ sector of the Hilbert space but has a small spin $S = 2$.

- For periodic boundary conditions, the spin-correlations are translational invariant. This is
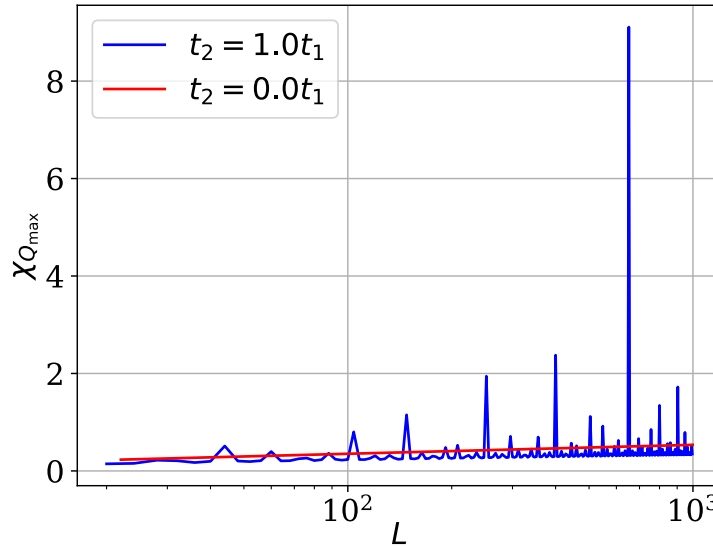
Figure 6.23: The maximum value of χ_Q as a function of L on a logarithmic scale. For $t_2 = t_1$, the maximum is at $Q_{\max} = \frac{\pi}{2}$ and for $t_2 = 0$ at $Q_{\max} = \pi$.

the expected behaviour in fact, since the translational symmetry cannot be spontaneously broken for finite periodic systems. Exact diagonalization calculations show, that the ground state is non-degenerate for systems up to $L = 20$. The first excited state is in the triplet sector, so that a closure of the spin gap could also induce a symmetry broken state. It was not possible to scale the gap to the $L = \infty$ limit because the finite size effects are too strong. Beside the spin gap, also the excitation gap in the $S = 0$ sector might scale to 0 and produce a symmetry broken state.

In summary, I cannot exclude that the RKKY theory applies in the weak-J limit for $t_2 > t_{2,c}^{\text{dim}}$. If the RKKY Hamiltonian would describe the physics correctly, it is tempting that the magnetic phase extends to the limit $J \to 0$. In the other case, one would expect that the magnetic phase forms an *island* in the $J - \varphi$ phase diagram.

6.3 Comparison with the classical frustrated Kondo ladder

At the end of this chapter, I will compare the obtained results for the $J - \varphi$ phase diagram to the classical spin variant of the Kondo lattice. The Kondo lattice with classical spins is a quantum-classical hybrid model which contains both quantum mechanical degrees (conduction electrons) and classical degrees of freedom (localized moments). The Hamiltonian for this system looks the same as compared to the quantum-mechanical case:

$$H = -t_1 \sum_{i,\sigma} \left(c_{i\sigma}^\dagger c_{i+1\sigma} + \text{h.c.} \right) - t_2 \sum_{i,\sigma} \left(c_{i\sigma}^\dagger c_{i+2\sigma} + \text{h.c.} \right) + J \sum_i \boldsymbol{S}_i \cdot \boldsymbol{s}_i \tag{6.19}$$

But in this case, the localized moments $\boldsymbol{S}_i$ are classical vectors with $|\boldsymbol{S}_i| = 1/2$ while the electronic quantities are unchanged. The ground state for this model can be obtained by minimizing the following energy functional of the spin configuration $\{\boldsymbol{S}\} = (\boldsymbol{S}_1, \ldots, \boldsymbol{S}_L)$:

$$E\left(\{\boldsymbol{S}\}\right) = \sum_{ii'\sigma\sigma'} \left(t_{ii'}\delta_{\sigma\sigma'} + \frac{J}{2}(\boldsymbol{\tau} \cdot \boldsymbol{S}_i)_{\sigma\sigma'}\delta_{ii'} \right) \langle c_{i\sigma}^\dagger c_{i'\sigma'} \rangle_{\{\boldsymbol{S}\}}, \tag{6.20}$$

where $\boldsymbol{\tau}$ is the vector of Pauli matrices and the expression within the brackets defines an effective hopping matrix $\boldsymbol{t}^{(\text{eff})}$. The expectation value $\langle c_{i\sigma}^\dagger c_{i'\sigma'} \rangle_{\{\boldsymbol{S}\}}$ is the one-particle reduced density matrix $\rho_{ii'\sigma\sigma'}$. For a fixed spin configuration, it can be obtained by diagonalization of
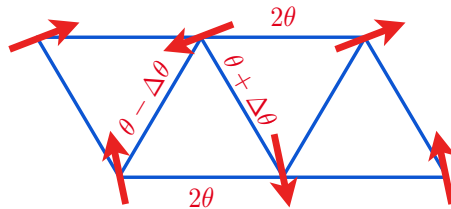
Figure 6.24: Parameterization of possible classical spin configurations. 2θ: angle between neighboring spins along the legs of the zigzag ladder. $\theta + \Delta\theta$ and $\theta - \Delta\theta$: alternating angles between neighboring spins along the rungs. $\Delta\theta \neq 0$ indicates a dimerized state. Incommensurate spiral states with pitch angle θ are described with $\Delta\theta = 0$. For the given example spin configuration, $\theta = \pi/2$, $\Delta\theta > 0$. It is sufficient to consider the parameter ranges $0 \leq \theta \leq \pi$ and $0 \leq \Delta\theta \leq \pi/2$.

the effective hopping matrix:

$$\boldsymbol{\rho} = \Theta(-\boldsymbol{t}^{(\text{eff})}) = \boldsymbol{U}\Theta(-\boldsymbol{\varepsilon})\boldsymbol{U}^{\dagger}, \tag{6.21}$$

where $\boldsymbol{U}$ is a unitary matrix which diagonalizes the (Hermitian) effective hopping matrix and Θ denotes the Heaviside step function. The variational set is already considerably large for systems with $L \sim 100$ so that one might choose a particular parametrization for the spin configuration which covers the physically significant sector. Ferromagnetic, antiferromagnetic, spiral and dimerized configurations can be parametrized by two parameters $(\vartheta, \Delta\vartheta)$ as sketched in Fig. 6.24. The parameter space consists in this case of $0 \leq \vartheta \leq \pi$ and $0 \leq \Delta\vartheta \leq \pi/2$ since $\vartheta \rightarrow \pi - \vartheta$ and $\Delta\vartheta \rightarrow \pi - \Delta\vartheta$ is a symmetry. Furthermore for periodic boundary conditions, the allowed pitch angles ϑ fulfill $\vartheta = n2\pi/L$ with integer n. The minimization process can the be performed by numerical diagonalization of the effective hopping matrix $\boldsymbol{t}^{(\text{eff})}$.

In the case of $\Delta\vartheta = 0$, one can apply a Fourier transformation to simplify this procedure. In this case, the classical spin at site i can be described by:

$$\boldsymbol{S}_i = S \begin{pmatrix} \cos(qR_i) \\ \sin(qR_i) \\ 0 \end{pmatrix}, \tag{6.22}$$

where q describes the wave vector of this spin wave configuration which corresponds to the angle ϑ between neighboring spins. Inserting this into Eq. (6.19) and performing a Fourier transformation $c_{i\sigma}^{\dagger} = \frac{1}{\sqrt{L}} \sum_k e^{ikR_i} c_{k\sigma}^{\dagger}$, one can transform the Hamiltonian into a 2×2 matrix for each value of k:

$$H = \sum_k \begin{pmatrix} c_{k\uparrow}^{\dagger} & c_{k\oplus q\downarrow}^{\dagger} \end{pmatrix} \begin{pmatrix} \varepsilon(k) & \Delta \\ \Delta & \varepsilon(k \oplus q) \end{pmatrix} \begin{pmatrix} c_{k\uparrow} \\ c_{k\oplus q\downarrow} \end{pmatrix}, \tag{6.23}$$

with $\Delta = \frac{JS}{2}$ and $k \oplus q$ denotes the summation of wave vectors with backfolding into the first Brillouin zone if necessary. The 2×2-matrix can be diagonalized for each k leading to two bands:

$$E_{\pm}(k,q) = \frac{\varepsilon(k) + \varepsilon(k \oplus q)}{2} \pm \sqrt{\left(\frac{\varepsilon(k) - \varepsilon(k \oplus q)}{2}\right)^2 + \Delta^2} \tag{6.24}$$

Note that there is not always a gap between both bands so that the filling of the bands is nontrivial for particular values of q. However, the remaining part of the minimization can be performed numerically for systems up to $L = 100{,}000$ sites without difficulty.

A similar procedure can be applied to the case of a dimerized spin configuration $\uparrow\uparrow\downarrow\downarrow\uparrow\uparrow \cdots$. in this case, one has a two-site unit cell and the spin configuration is realized by choosing:

$$\boldsymbol{S}_{I\alpha} = (-1)^I S\boldsymbol{e}_z, \tag{6.25}$$

where I denotes the unit cell and $\alpha = 0,1$ labels the site within each unit cell. Plugging this expression into Eq. (6.19) and working out the Fourier transformation for the unit cells, one

obtains a 4×4 Hamilton matrix for each value of K^1:

$$H = \sum_{\sigma} \sum_{K} \begin{pmatrix} c^{\dagger}_{K0,\sigma} & c^{\dagger}_{K1,\sigma} & c^{\dagger}_{K \oplus \pi 0,\sigma} & c^{\dagger}_{K \oplus \pi 1,\sigma} \end{pmatrix}$$

$$\begin{pmatrix} \varepsilon_2(K) & \varepsilon_1(K) & \Delta & 0 \\ \varepsilon_1(K)^{\star} & \varepsilon_2(K) & 0 & \Delta \\ \Delta & 0 & -\varepsilon_2(K) & \varepsilon_1(K \oplus \pi) \\ 0 & \Delta & \varepsilon_1(K \oplus \pi)^{\star} & -\varepsilon_2(K) \end{pmatrix} \begin{pmatrix} c_{K0,\sigma} \\ c_{K1,\sigma} \\ c_{K \oplus \pi 0,\sigma} \\ c_{K \oplus \pi 1,\sigma} \end{pmatrix}, \qquad (6.26)$$

with dispersions $\varepsilon_2(K) = 2t_2 \cos(K)$ and $\varepsilon_1(K) = t_1(1 + e^{-iK})$. This matrix cannot be diagonalized analytically but straight-forwardly with a computer. Note that in the case of Eq. (6.26) there is no variational parameter anymore but Eq. (6.26) describes the energy of the dimerized collinear spin configuration.

With this at hand, one can explore the phase diagram of the classical Kondo zigzag ladder in the $J - \varphi$ plane. Fig. 6.25 displays the calculations performed by Lena-Marie Woelk. The data can be compared with the phase diagram of the quantum model (Fig. 6.4):

1. The magnetic patterns found for the classical model are the same as for the quantum case; namely the antiferromagnetic (AF), the incommensurate (IC) and the spiral (SP) pattern. A crucial difference is however, that all of these magnetic patterns are long-range ordered. This is due to the absence of the Kondo effect and the quantum fluctuations.

2. The classical model shows also a large region in which the translational symmetry of the Hamiltonian is spontaneously broken. This is remarkable and serves as a simple explanation of the spin-dimerization. The dimerization is definitely a direct consequence of the geometrical frustration and shows up already in the case of classical spins.

3. The critical line $J_c^{(\text{dim})}(\varphi)$ is about one order of magnitude above the line for the quantum case. E.g.: $J_c^{(\text{dim})}(\varphi = \pi/4) \approx 6.4t$ in the classical case and $J_c^{(\text{dim})}(\varphi = \pi/4) \approx 0.62t$ in the quantum case. This can be traced back to the mean-field character of the classical spin theory since these approximations tends to overestimate the ordering as compared to the full quantum case where quantum fluctuations always act against the order.

4. The classical phase diagram has a triple-point at $(\varphi = 0.188\pi, J = 4.1t)$ which is absent in the quantum case. As presented in Sec. 6.2.1 for the quantum case, the critical line separating AF-SRO and IC-SRO ends in a critical point before reaching the transition line for the dimerization. It was argued that this is caused by a precursor of the SP-QLRO phase, namely a peak in the spin-structure factor at $Q = \frac{\pi}{2}$. The spiral magnetic order in the quantum model competes with the Kondo screening which is absent in the classical approximation. Hence, there is no *development* of magnetic order in the classical model[2] so that the critical line reaches the 'triple point'.

5. The critical line $\varphi_c^{(\text{dim})}(J)$ does not bend back but terminates at a critical point $(\varphi = 0.5\pi, J = J_{\text{crit}})$. This is another major difference as compared to the quantum case, where

---

1   Since the unit cell contains two sites, there are only $L/2$ k-points in the first Brillouin zone.
2   The whole $J - \varphi$ plane is magnetically ordered in the classical case.
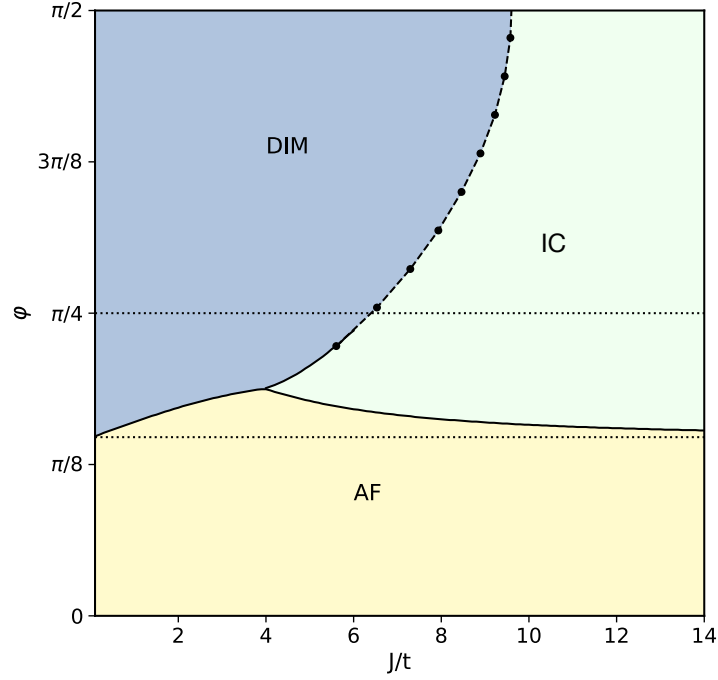
Figure 6.25: $J - \varphi$ magnetic phase diagram of the classical-spin variant of the Kondo lattice with an antiferromagnetic phase (AF, $\theta = \pi$, $\Delta\theta = 0$), an incommensurate spiral phase (IC, $\pi/2 < \theta < \pi$, $\Delta\theta = 0$), and a dimerized phase (DIM, $\theta = \pi/2$, $\Delta\theta = \pi/2$). The dashed line indicates $t_1 = t_2$ ($\varphi = \pi/4$). Calculations have been performed for $L = 200$. This is sufficient for convergence, except for the regime $\varphi \gtrsim \pi/4$ where much larger systems with up to $L = 100,000$ sites are necessary (see text for discussion). The dotted line interpolates between the data points.

  this scenario is excluded. In the classical case, it is not because the limits $\varphi = \pi/2$ (two decoupled chains) and $\varphi = 0$ (single chain) have highly degenerate ground states as opposed to the quantum case where the corresponding ground states are non-degenerate.

Finally, I want to emphasize that the spin-dimerized phase is also non-perturbative in the classical case. Strong J perturbation theory as well as perturbation theory in t_1 (valid for arbitrary t_2 and J) and t_2 (valid for arbitrary t_1 and J) does not reproduce a spin-dimerized phase. Even the weak-J RKKY theory does not capture the spin-dimerization [143].

CHAPTER 7

The doped frustrated Kondo ladder

In most common quantum lattice models, half-filling represents a very special case with very distinct properties as compared to the doped regime. This is due to the enhanced charge degrees of freedom which are present in the doped regime. Half-filling corresponds to $n := \frac{N}{L} = 1$ and the hole doped regime is obtained for $n < 1$ while the electron doped regime corresponds to $n > 1$. For a bipartite lattice, a particle-hole transformation maps the physics for $n > 1$ onto the case $n < 1$ and the phase diagram is symmetric with respect to half-filling. This is not true for the frustrated Kondo ladder since the next-nearest neighbor hopping t_2 breaks the particle-hole symmetry. However, a particle-hole transformation maps the phase diagram for $+t_2$ and $n > 1$ to $-t_2$ and $n < 1$. Hence, it would be sufficient to study the frustrated Kondo ladder only in the hole doped regime but for both signs of t_2. Since the DMRG method can handle hole and electron doping with equal computational cost, I will analyse the model for a fixed sign of t_2[1] and all fillings $0 < n < 2$.

As already discussed in Sec. 5.1.2 and 5.1.3, one expects a metallic ground state in the doped regime. The metallic phases can often be described by Fermi liquid theory for dimensions $d \geq 2$ but with highly renormalized parameters. In particular, the large effective mass motivated the label *heavy fermion* systems. In the heavy fermion materials, one has also found non Fermi-liquid behaviour including unconventional superconductivity [103] for example. In the one-dimensional case, Fermi liquid theory fails in general and the ground state might be described by Tomonaga-Luttinger liquid (TLL) theory [144] instead.

In this chapter, I will start with collecting the results for the doped regime of the ordinary Kondo chain ($t_2 = 0$) in Sec. 7.1. Afterwards, I will present an overview over the ground state phase as obtained by my DMRG calculations in Sec. 7.2. This includes a detailed discussion of the infinite-J limit, the ferromagnetic regions and the short-range spin correlations.

7.1 Summary for the ordinary Kondo chain

The ordinary Kondo chain was extensively studied over the last decades. Major results were collected in the review of TSUNETSUGU et al. [114]. The doped regime $n < 1$ contains a ferromagnetic phase above a critical line $J_c^{\mathrm{FM}}(n)$ and a paramagnetic phase below this line. However, it was missed at the beginning that an additional ferromagnetic phase occurs in the intermediate J region for fillings $\frac{1}{2} < n < 1$ (see Fig. 7.1). This phase was detected in

---

1   I choose $t_2 > 0$ for the Hamiltonian as in Eq. (6.1)
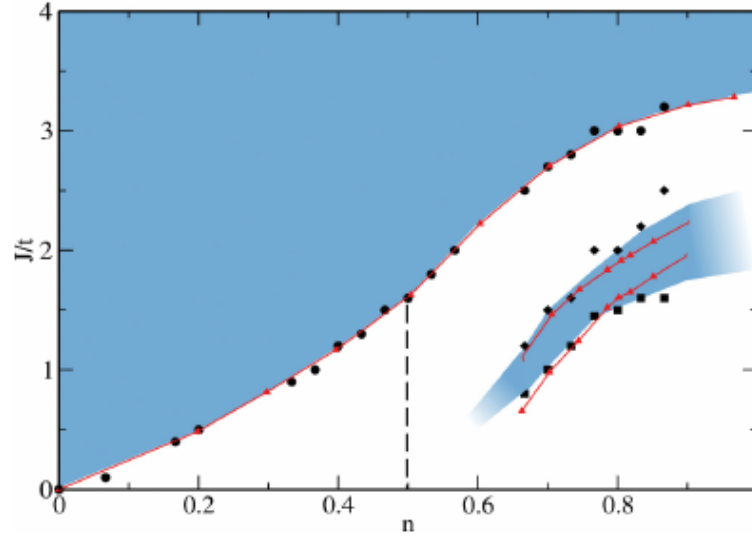
Figure 7.1: $J - n$ phase diagram of the ordinary Kondo chain taken from Ref. [117] (Fig. 1 therein, black dots are obtained from the authors of Ref. [117], red dots are obtained from the authors in Ref. [116]).

Ref. [115]. The extreme case of only one conduction electron is known to be ferromagnetic for a long time [145] and this ferromagnetic phase is also stable in the low density limit [146] and generated by a double-exchange mechanism [147]. As a mechanism for the ferromagnetic state at high densities, PETERS et al. [117] propose the notion of the spin-selective Kondo insulator. Here the idea is that in the polarized ferromagnetic state ($m_{\text{tot}} = S_{\text{tot}} = \frac{1}{2}(L - N)$) the minority conduction electrons are Kondo screened by the minority spin projection of the localized moments while the majority conduction electrons generates the metallic state. This leads to an emergent commensurability condition:

$$\frac{1}{2} = n_{i\downarrow} - S_i^z, \tag{7.1}$$

if the minority spin projection is $\downarrow$. In Ref. [117] it was argued that this emergent commensurability is found also in the second ferromagnetic phase of the Kondo chain and is even present at low densities.

The nature of the paramagnetic region has been more unclear though. The physics in this case can be described by TLL theory but a central question is if the local moments contribute to Luttinger's sum rule or not. This question is often formulated as: is the Fermi surface large (local moments do contribute) or small (local moments do not contribute)? Numerical studies proposed a large Fermi surface for intermediate and strong J below the ferromagnetic phase [116, 148–150]. In the review [114], the authors show that the Fermi surface is large in the infinite-J limit when the ferromagnetic phase is destroyed by a small t_2 with the correct sign. A recent DMRG study confirms that the Fermi surface is large in between the two ferromagnetic phases [118]. If the large Fermi surface extends to the weak J regime is not entirely understood. Some authors propose a *RKKY liquid* below the second ferromagnetic phase with a small Fermi surface [116, 150]. That would mean that the second ferromagnetic region would be the

separation between the large Fermi surface above and the small Fermi surface below for fillings $\frac{1}{2} < n < 1$. A small Fermi surface was also suggested for fillings below quarter filling but the situation is not clear in the weak J regime [116]. The transition at quarter filling from a large Fermi surface to a small Fermi surface is conceivable since exactly at quarter filling the ground state is found to be insulating [120, 151], i.e. there is no Fermi surface. The study at quarter filling unveils also a spin-dimerized ground state driven by the RKKY interactions [120]. Very recently, another DMRG study unveils a charge-density wave ground state of the Kondo chain at three-eighth filling ($n = \frac{3}{4}$) below the second ferromagnetic phase [152].

The above summary demonstrates that also the ordinary Kondo chain has a very rich phase diagram in the doped regime. In my present study, I will focus therefore on particular aspects only. Firstly, I will discuss the infinite-J limit which can be mapped to the $U = \infty$ Hubbard model. Afterwards, I will analyse the development of the ferromagnetic phases as a function of t_2 and analyse the short-range correlations at quarter and three-quarter filling respectively. Let me finally note, that the question of the size of the Fermi surface is much more difficult as compared to the ordinary chain since the topology of the Fermi surface may change for a sufficiently large t_2. In this case, one would have more than two Fermi points and the simple relation $k_F = \frac{1}{2} n^{\mathrm{CE}}$ ($k_F = \frac{1}{2}(n^{\mathrm{CE}} + 1)$) for the small (large) Fermi surface is not valid anymore. Here, n^{CE} denotes the filling of the conduction electrons.

7.2 Ground state phase diagram

In this section I will present a condensed summary of the ground state phase diagram for the frustrated Kondo zigzag ladder as a function of doping n, Kondo coupling J and next-nearest neighbor hopping t_2. A detailed discussion of the infinite-J limit follows subsequently in Sec. 7.2.1. Afterwards, I will analyse the ferromagnetic regimes in more detail in Sec. 7.2.2 and finally discuss two specific cases from the paramagnetic region in Sec. 7.2.3.

The ground state phase diagram for the frustrated zigzag ladder off half-filling has as a third axis the concentration n of conduction electrons. The electron concentration n is defined as:

$$n = \frac{N}{L}, \tag{7.2}$$

where L is the number of lattice sites and N the number of electrons. Fig. 7.2 displays the schematic $J - n$ phase diagram for the case $t_2 = t_1$. As expected, the phase diagram has a strong asymmetry with respect to half-filling, i.e. hole-doping ($n < 1$) is different from electron-doping ($n > 1$).

At half-filling, the phase diagram was intensively discussed in Chap. 6: at strong J the ground state is a Kondo insulator with gapped excitations (green area). A first critical point then marks the transition into a spin-dimerized phase (yellow area) and a second critical point separates a quasi-long-range ordered spiral phase.

At hole-doping, the ground state is ferromagnetic (red area) in a large region for sufficiently large J. The shape of the critical line $J_c^{\mathrm{FM}}(n)$ is qualitatively different as compared to the case $t_2 = 0$ (see Fig. 7.1). This is attributed to an additional van Hove singularity in the density of states. In the paramagnetic region at quarter filling, there is a second dimerized phase at weak coupling.
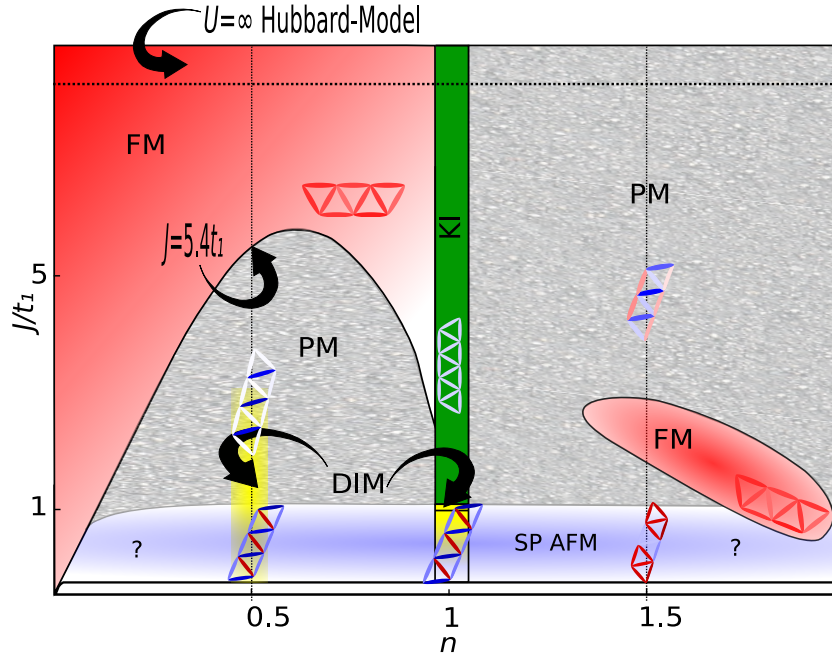
Figure 7.2: Schematic $J - n$ phase diagram of the Kondo zigzag ladder for fixed $t_2 = t_1$. Indicated phases are: 1) FM: ferromagnetism, 2) PM: paramagnetism, 3) KI: Kondo insulator, 4) DIM: spin-dimerized and 5) SP AFM: spiral antiferromagnetic order. Small pictograms display short-range correlations of the corresponding ground states.

For electron doping, most parts of the phase diagram are paramagnetic. In the limit $J \to \infty$, this is understood since the next-nearest neighbor hopping t_2 leads to a paramagnetic state just as in the $U = \infty$ Hubbard model [153]. However at intermediate coupling strength and strong electron-doping there is a small ferromagnetic island. At three-quarter filling and weak J, the ground state develops ferromagnetic clusters of size $L_C = 4$ which constitutes another form of translational symmetry breaking. This is indicated in Fig. 7.2 by a sketch of the emerging clusters at $n = 1.5$.

7.2.1 Infinite-J limit

In the limit $J = \infty$, the Kondo lattice simplifies considerably but still, the remaining degrees of freedom build a non-trivial lattice model for fillings off half-filling. Lets recap the atomic eigenstates of the KLM as introduced in Tab. 5.1. In the case of $N < L$ (hole doped regime), N sites are in the Kondo singlet state (state number 1 in Tab. 5.1) while $L - N$ sites are in the states number 2 or 3. On these sites, the unpaired local moment has a spin-projection σ. In total, there are three remaining states while the other five states are projected out through the constraint $J = \infty$ (see Fig. 7.3 for a pictorial representation). Note that at half-filling the model would become trivial since only a single state would remain. In the other case ($N > L$, electron doped regime), the situation is similar but in this case the $N - L$ excessive electrons build local states 4 and 5. Still the corresponding local moments deliver a spin degree of freedom via their spin-projection σ.

After the determination of the relevant local basis states, the next task is to find the Hamilton
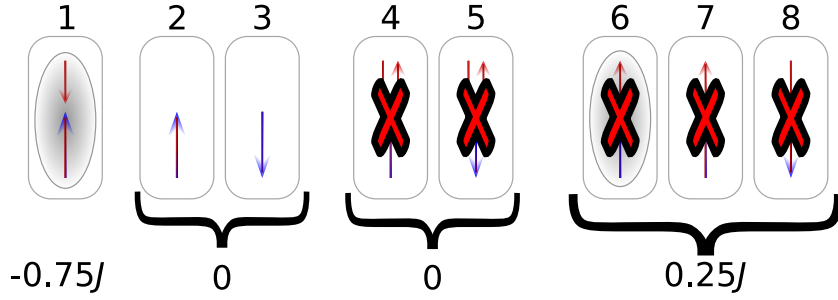
Figure 7.3: From originally eight local states for each atom of the KLM, only three states remain in the $J = \infty$ limit while the other five are projected out. This figure displays the three remaining states for the hole doped regime ($N < L$). For electron doping ($N > L$), states 1, 4 and 5 would remain.

operator restricted to these basis states. LACROIX [154] found an exact mapping to the $U = \infty$ Hubbard model via identifying the Kondo singlet as the empty state of the Hubbard model and the states 2 and 3 as the singly occupied states of the Hubbard model with spin-projection σ. This means that the unpaired localized moments have the role of mobile electrons with the constraint of no double occupancy. Note that the filling $\tilde{n}$ of the unpaired localized moments is given by $\tilde{n} = 1 - n$, when n is filling of the conduction electrons. For a pictorial representation of this mapping see Fig. 7.4.

When performing the transformation, one ends up with a Hamiltonian which is the same as for the $U = \infty$ Hubbard Hamiltonian but with a reversed sign of the hopping amplitude and the half bandwidth:

$$H_\infty = + \sum_{ij\sigma} \frac{1}{2} t_{ij} \tilde{f}^\dagger_{i\sigma} \tilde{f}_{j\sigma}, \tag{7.3}$$

where $\tilde{f}^\dagger_{i\sigma}$ ($\tilde{f}_{i\sigma}$) is the creation (annihilation) operator for the unpaired local moments with spin-projection σ at site i. These operators satisfy additionally the constraint of no doubly occupied sites.

The phase diagram for the Kondo zigzag ladder at $J = \infty$ can therefore be deduced from
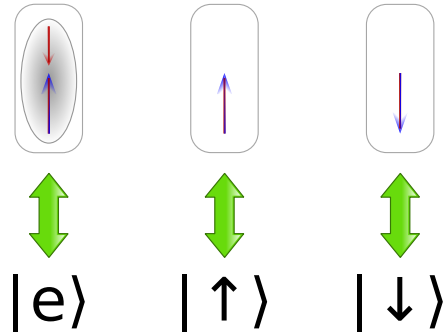
Figure 7.4: Pictorial representation of the mapping between the $J = \infty$ Kondo model and the $U = \infty$ Hubbard model as introduced by LACROIX [154].

the phase diagram for the Hubbard model on the zigzag ladder at $U = \infty$. A detailed study was done by DAUL et al. [153]. Their result is displayed in Fig. 7.5 for fillings $n < 1$ and negative t_2[1]. They found ferromagnetism for any $t_2 < 0$ for small densities and high densities. For intermediate densities there is a nonmagnetic region for sufficiently large t_2. This phase diagram can be directly shifted to the Kondo zigzag ladder at $J = \infty$ but one has to keep in mind the subtleties of the mapping: the sign of t_2 needs to be reversed and the filling needs to be adapted as $\tilde{n} = 1 - n$ so that low densities correspond to fillings close to half-filling and vice versa. Since t_2 is measured in units of t_1 in Fig. 7.5, one does not have to rescale t_2 by $\frac{1}{2}$. That means, that the Kondo zigzag ladder is ferromagnetic for $t_2 > 0$ and $n < 1$. For $n > 1$, there is no ferromagnetism for the same sign of t_2. The phase diagram in Fig. 7.2 is for the case $t_2 = t_1$ for which there is ferromagnetism for all densities $n < 1$ referred to the calculations of DAUL et al. [153].

The precise nature of the nonmagnetic state for $n > 1$ is unclear for $t_2 \sim t_1$ even in the $U = \infty$ Hubbard model[2]. For $t_2 \ll t_1$ however, it is known that the $U = \infty$ Hubbard model is a Tomonaga-Luttinger liquid (TLL) [155]. This TLL phase again translates to the $J = \infty$ Kondo model in the weak-t_2 regime. It was pointed out by TSUNETSUGU et al. [114] that this TLL phase for the Kondo lattice has a large Fermi surface. This is consistent because the localized moments directly contribute to the physics as they effectively hop through the lattice. Whether this phase extends to arbitrary t_2 is an open question.
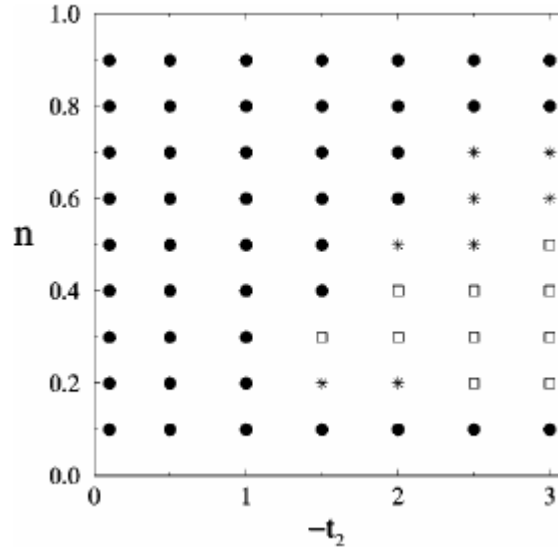
Figure 7.5: Ground state phase diagram of the $U = \infty$ Hubbard model as obtained by DAUL et al. [153]. The figure is taken from this publication (Fig. 17 in [153]). The filled dots denote a ferromagnetic ground state, the empty squares a paramagnetic ground state and the stars denote a partially polarized ground state.

---

1   DAUL et al. [153] use the same convention as me in that the hopping part of the Hamiltonian is defined as $H = -\sum_{ij} t_{ij\sigma} c_{i\sigma}^\dagger c_{j\sigma}$. Therefore, a *negative* t_2 corresponds to a *positive* hopping amplitude in front of the term $c^\dagger c$.

2   At least to the best of my knowledge.

Let me finally emphasize that although the extreme case $J = \infty$ is equivalent to the $U = \infty$ Hubbard model, the perturbation in $\frac{t^2}{J}$ is not equivalent to the perturbation in $\frac{t^2}{U}$.

7.2.2 Ferromagnetism

The extreme limit $J \to \infty$ already shows that ferromagnetism is only present for hole doping while it is destroyed for electron doping by an arbitrary weak but finite t_2. Indeed in Ref. [156] it was pointed out, that in the limit $J \to \infty$ a weak t_2 leads to an effective spin-spin interaction for the local moments with coupling constant:

$$J_{\text{eff}}^{(1)} = -\frac{t_2}{2\pi} \left(\frac{2}{\pi\tilde{n}} \sin^2 \pi\tilde{n} - \sin 2\pi\tilde{n} \right), \tag{7.4}$$

were $\tilde{n} = 1 - n$ denotes the density of $\tilde{f}$ particles. The term within the brackets is positive for hole-doping ($1 > \tilde{n} > 0$) and negative for electron-doping $0 > \tilde{n} > -1$. Hence for positive t_2, the effective interaction is ferromagnetic for hole-doping and antiferromagnetic for electron-doping. This is consistent with the results discussed in the last section. Ref. [156] is one of the rare publications which presents calculations for the one-dimensional Kondo chain with next-nearest neighbor hopping t_2. However, they studied only the limit of weak t_2 ($t_2 = -0.1t_1$) and calculated the phase diagram with exact diagonalization for systems with $L = 4$ up to $L = 9$ sites. They found that the ferromagnetic phase vanishes at strong J as predicted by Eq. (7.4). At intermediate values for J, there is still a ferromagnetic region which was attributed to the second order term in the perturbation theory [157]:

$$J_{\text{eff}}^{(2)} = -\frac{t_1^2}{\pi J} \left(\frac{2}{\pi\tilde{n}} \sin^2 \pi\tilde{n} - \sin 2\pi\tilde{n} \right), \tag{7.5}$$

which is always ferromagnetic.

Here, I will present systematic computations for $0 \leq t_2 \leq 1$ and unveil the impact of a large t_2 on the ferromagnetism in the frustrated Kondo ladder. Fig. 7.6 shows calculations for a system with $L = 20$ sites obtained by finite-size 1sDMRG. Each subfigure displays the energy difference between the polarized ground state with $S = \frac{1}{2}(L - N)$ and the singlet ground state with $S = 0$ on a logarithmic color scale. The respective ground state energies can be directly targeted with the $SU(2)$-symmetric DMRG implementation which is a very efficient procedure for determining the ferromagnetic phases. The calculations were performed for $J/t_1 = 1.0, 2.0, \ldots, 10.0$ and $n = \frac{1}{10}, \frac{2}{10}, \ldots, \frac{18}{10}$.

For $t_2 = 0$, the results are consistent with previous calculations and the phase diagram shows the expected particle-hole symmetry. In Fig. 7.6(a), the point ($n = 0.8, J = 2t_1$) belongs to the second ferromagnetic phase of the ordinary Kondo chain. A higher J-resolution would uncover more points in this phase.

For $t_2 = 0.2t_1$ (Fig. 7.6(b)), the situation on the hole-doped site is only slightly changed. The second ferromagnetic phase is still present but shifted slightly to larger values of J. The same happened for the other ferromagnetic region. On the contrary, the electron-doping regime changed significantly. The ferromagnetism disappears for strong J as expected by perturbation theory. It is also observed that the suppression of the ferromagnetic phase is particularly
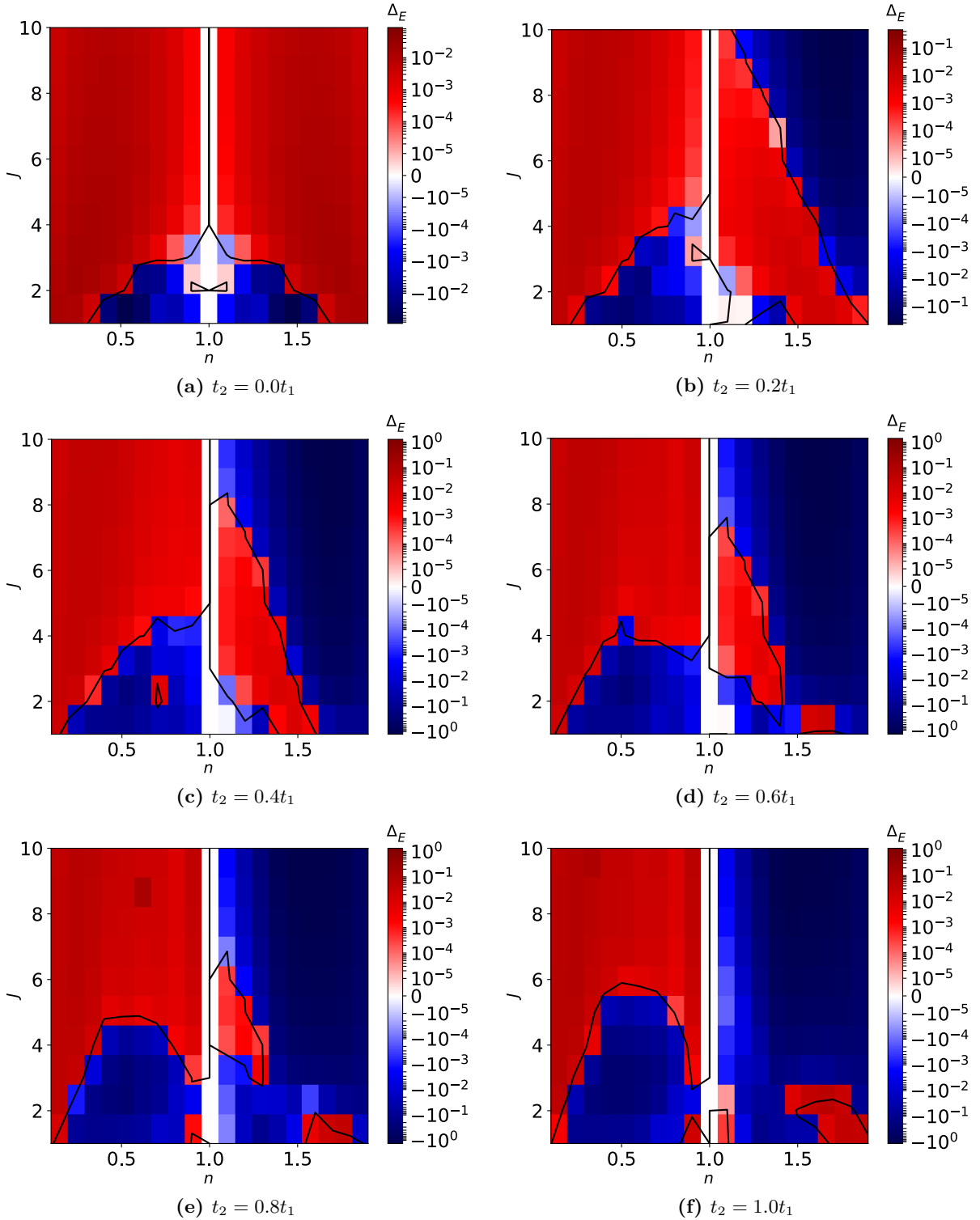
Figure 7.6: The energy difference Δ_E between the ground state with $S = 0$ and $S = \frac{1}{2}(L - N)$ in the $J - n$ plane for various values of t_2. Calculations are done for a system with $L = 20$ sites. Red colors denote a ferromagnetic ground state, blue colors denote a ground state with $S = 0$. Black lines are interpolations for the line $\Delta_E = 0$ and marks the phase boundary between the para- and ferromagnetic phase.

strong in the vicinity of the full band ($n = 2$) while close to half-filling, it survives even for $J = 10t_1$. This behaviour is consistent with the results in Ref. [156] for the case $t_2 = 0.1t_1$[1]. Extremely small energy differences were found for slight electron doping ($n = 1.1$ and $n = 1.2$) and $J = 1.0t_1$. For example $\Delta_E \approx 2 \times 10^{-6}$ for $n = 1.1$ and $J = 1.0t_1$. In this regime, it is therefore very difficult to distinguish the para- and the ferromagnetic phase and the dependence on the system size should be taken into account.

For $t_2 > 0.25t_1$, the non-interacting band structure changes qualitatively and there are densities with 4 Fermi points (FP) instead of 2 FP. This happens for densities $n <\approx 2$ close to the full band for $t_2 >\approx 0.25t_1$. Fig. 7.6(c) shows calculations for $t_2 = 0.4t_1$ and an even stronger suppression of the ferromagnetic phase in the electron-doped regime is observed. For $n > 1.6$, the ferromagnetism completely disappears in the considered J-region. The hole-doped regime is still qualitative similar to the case $t_2 = 0$ so that one may argue that the Fermi surface is unchanged in this regime. At least for the Fermi surface of the non-interacting system, this is indeed the case.

For $t_2 = 0.6t_1$ (Fig. 7.6(d)) there are two qualitative changes for hole-doping: firstly, the critical line $J_c^{\mathrm{FM}}(n)$ for the first ferromagnetic region has a clear maximum for $n < 1$ and secondly the ferromagnetic island disappears at least in the considered J-region. The first effect might be attributed to the density of states (DOS) $\rho(\varepsilon_F)$ at the Fermi level. Arguing with the Stoner criterion, a high DOS at the Fermi level is beneficial for ferromagnetism in itinerant electron systems. Albeit the mechanism for ferromagnetism in the Kondo lattice model is different, the DOS seems to play a significant role either. For example for $t_2 = 0$, the non-interacting DOS has a van Hove singularity at the Fermi level for $n = 0$ and $n = 2$ and for low and high electron concentrations the FM phase is indeed mostly expanded. The next-nearest neighbor hopping t_2 introduces an additional van Hove singularity if $t_2 > 0.25t_1$. The DOS $\rho(\varepsilon_F)$ at the Fermi level is displayed in Fig. 7.7 for several values of t_2 as a function of n: the van Hove singularity at the Fermi level shifts quickly to intermediate densities. For $t_2 = 0.6t_1$, it appears already at $n \approx 0.9$ which might be the reason for that the FM region is more extended close to half-filling and that the critical line has a maximum at $n \approx 0.5$. The disappearance of the ferromagnetic island might also be explained by a qualitative change of the Fermi surface for densities $n \approx 0.8$ when t_2 changes from $t_2 = 0.4t_1$ to $t_2 = 0.6t_1$. With this argument, one can suppose that the two ferromagnetic regions observed in the ordinary Kondo chain are caused by different mechanisms since the ferromagnetic island disappears while the other ferromagnetic phase does not. In the electron-doped regime, one also observes a qualitative change at $t_2 = 0.6t_1$: a new ferromagnetic island develops at densities $n \approx 1.5$. The other ferromagnetic region shrinks further.

For $t_2 = 0.8t_1$ (Fig. 7.6(e)) this evolution continues. A clear maximum around $n \approx 0.5$ of $J_c^{\mathrm{FM}}(n)$ develops in the hole-doped regime while the main ferromagnetic phase for electron doping is only present close to half-filling for intermediate Kondo couplings J. On the contrary, the new ferromagnetic phase for fillings $n \approx 1.5$ extends slightly.

Finally for $t_2 = t_1$ (Fig. 7.6(f)), the main ferromagnetic phase has disappeared completely in

---

1   In fact in Ref. [156], the authors took $t_2 = -0.1t_1$ and calculated the phase diagram in the hole-doped regime. However this is equivalent to $t_2 = 0.1t_1$ and electron doping.
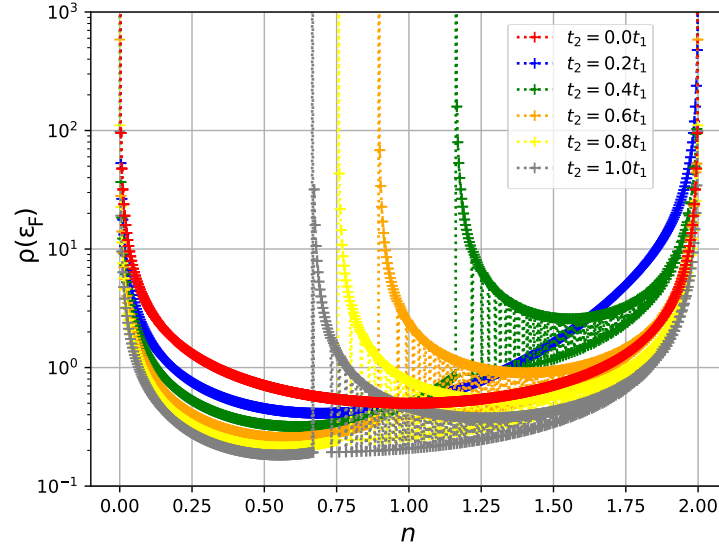
Figure 7.7: The non-interacting DOS at the Fermi energy ε_F for various values of t_2 as indicated.

electron-doped regime while the new island is now clearly visible. The small ferromagnetic points close to half-filling ($n = 0.9$ and $n = 1.1$) at $J = t_1$ may indicate additional ferromagnetic phases, but a careful finite-size scaling is necessary for a conclusive answer. A clear dome structure is visible in the hole-doped regime for the phase boundary between the ferro- and paramagnetic phase. Fig. 7.6(f) might be compared to the schematic phase diagram in Fig. 7.2. The determination of the character of the ferromagnetic phases would require more detailed calculations and constitutes an open task.

7.2.3 Paramagnetic phase at commensurate fillings

The short-range spin correlations are featureless in the ferromagnetic regions of the phase diagram. However, in the paramagnetic regions, the situation is much more complicated and different short-range patterns emerge. To give an impression of the complexity, I will present calculations for quarter ($n = \frac{1}{2}$) and three-quarter ($n = \frac{3}{2}$) filling in the upcoming subsections. Computations at other (also incommensurate) fillings would be highly interesting but are postponed for future work.

Quarter filling

The ground state at quarter filling is ferromagnetic for strong J. This can also be seen in the short-range spin-correlations in the top row of Fig. 7.8 ($J = 5.4t_1$). In the paramagnetic region right below the ferromagnetic phase, the short-range spin correlations do not break the translational symmetry and are antiferromagnetic along the rungs and ferromagnetic along the legs of the ladder. This pattern leads to a peak of the spin-structure factor at the wave-number $Q = \pi$. For decreasing J, the peak at $Q = \pi$ shrinks and the short-range spin-correlations get slightly different on the $\diagdown$- and $\diagup$ bonds, i.e. the ground state gets slightly dimerized (see $J = 3.2t_1$ in Fig. 7.8). This evolution goes in hand with a growth of the spin-structure factor at $Q = \frac{\pi}{2}$. The two peaks of the spin-structure factor at $Q = \pi$ and $Q = \frac{\pi}{2}$ are approximately equal at $J \approx 2.2t_1$. The short-range spin-correlations show in this case a pattern which is
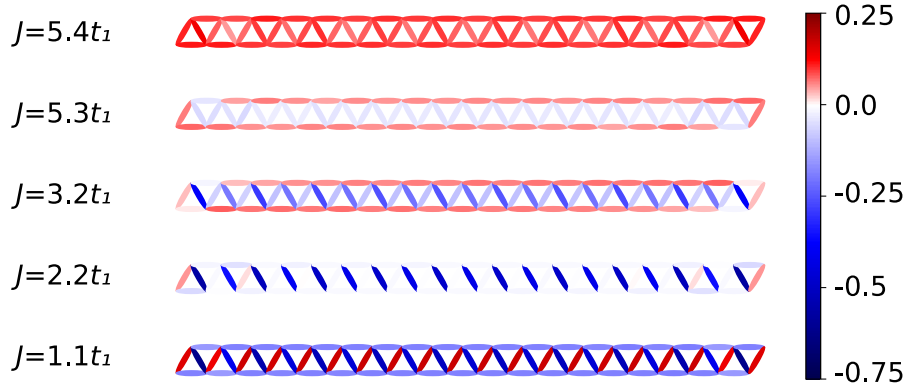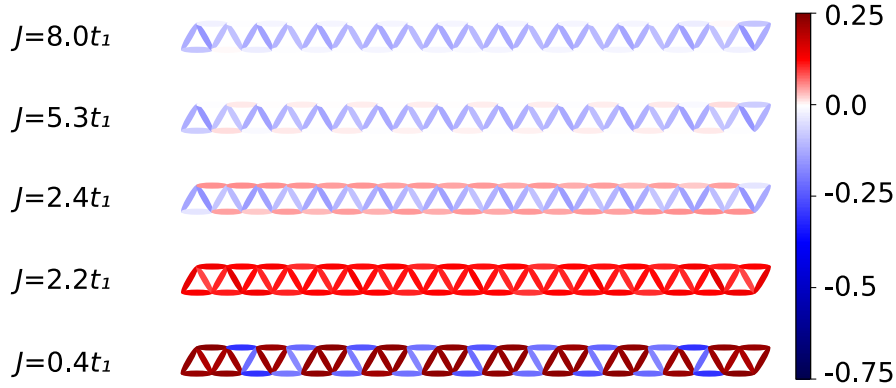
Figure 7.8: Ground state spin-correlation function $\langle \boldsymbol{S}_i \boldsymbol{S}_j \rangle$ (see color code) for nearest neighbors i, j on the zigzag ladder for $t_2 = t_1$ and $n = \frac{1}{2}$ for various values of J.

reminiscent to a valence bond solid, i.e. $\langle \boldsymbol{S}_i \boldsymbol{S}_{i+1} \rangle = -0.75$ and $\langle \boldsymbol{S}_{i-1} \boldsymbol{S}_i \rangle = 0$. However, in Fig. 7.8 ($J = 2.2t_1$) the values for the spin-correlations are $\langle \boldsymbol{S}_i \boldsymbol{S}_{i+1} \rangle \approx -0.42$ and $\langle \boldsymbol{S}_{i-1} \boldsymbol{S}_i \rangle \approx -0.008$ and the *rest* of the correlations appear in correlations of higher distance. For even weaker J, the trend goes further, i.e. the peak at $Q = \pi$ shrinks and the peak at $Q = \frac{\pi}{2}$ grows. The continuous development of the peak from $Q = \pi$ to $Q = \frac{\pi}{2}$ is also displayed in Fig. 7.9.

At $J = 1.1t_1$, the short-range spin correlations of the ground state are very similar to the correlations at half-filling. The spin-dimerization is strongly developed and the correlations alternate on the rungs between ferro- and antiferromagnetic. This can also be compared to the case $t_2 = 0$ where the short-range spin-correlations are also very similar to the case observed
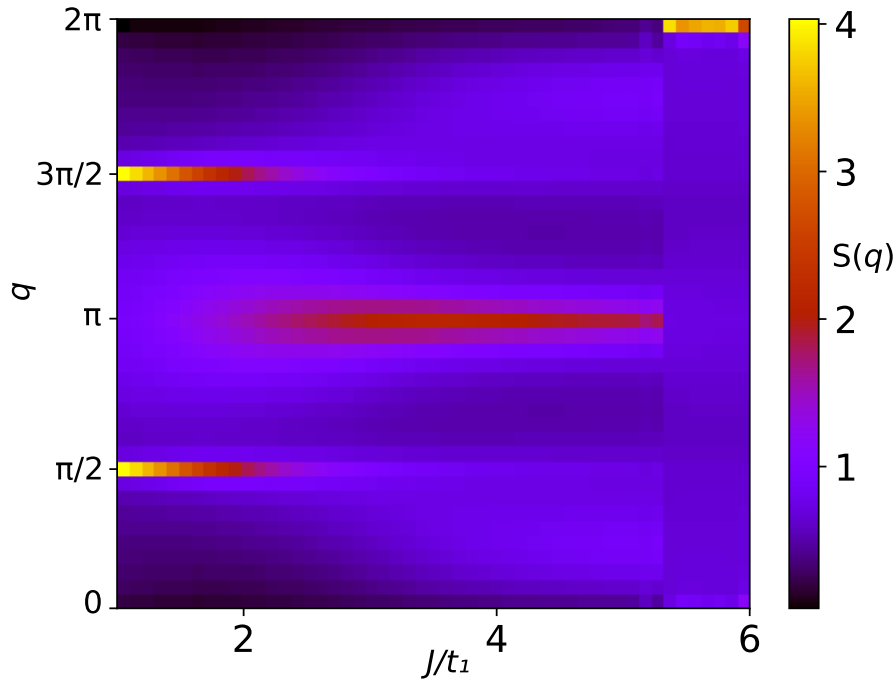
Figure 7.9: J-dependence of the spin-structure factor $S(q) = L^{-1} \sum_{i,j}^{L} e^{iq(R_i - R_j)} \langle \boldsymbol{S}_i \boldsymbol{S}_j \rangle$ (color code on the right) for $L = 40$ sites, $t_2 = t_1$ and quarter filling ($N = 20$).
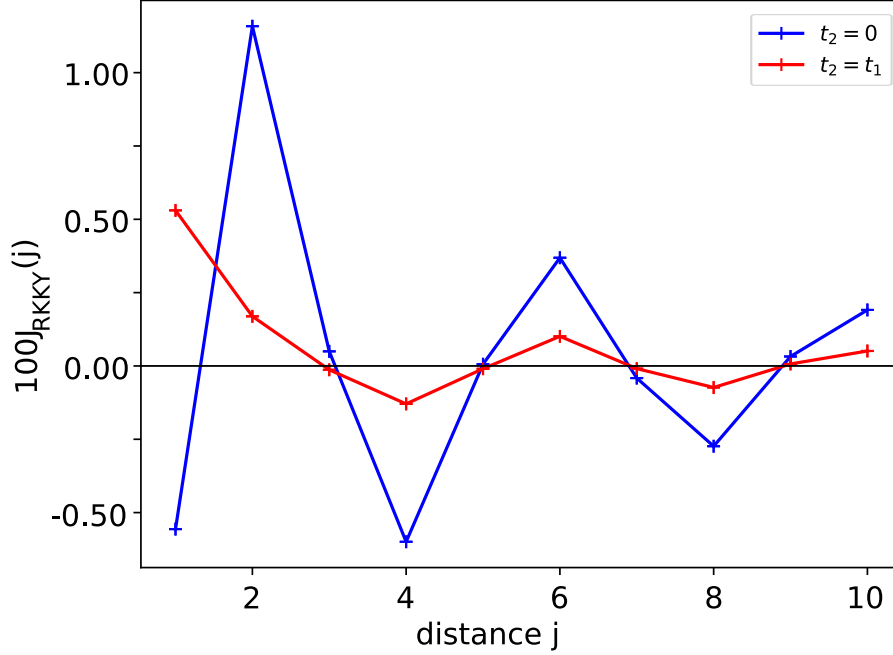
Figure 7.10: The first ten RKKY couplings for a system with open boundaries, $L = 100$ and quarter filling ($N = 50$). Data is shown for the ordinary Kondo chain ($t_2 = 0$) and the frustrated zigzag ladder ($t_2 = t_1$). Note, the RKKY couplings are scaled to be consistent with Fig. 4 in Ref. [120].

here [120]. In Ref. [120], the authors argue that the spin-dimerization can be traced back to the effective RKKY interactions because the nearest (J_1) and next-nearest (J_2) RKKY coupling correspond to a $J_1 - J_2$ Heisenberg model with dimerized spin-correlations. The first ten RKKY couplings are displayed in Fig. 7.10. In fact for $t_2 = 0$, one has $J_1 < 0$ and $J_2 > 0$, i.e. a ferromagnetic next-nearest neighbor interaction on top of an antiferromagnetic Heisenberg chain. This leads to a spin-dimerized ground state if $-4J_2 < J_1 < 0$ [158]. For $t_2 = t_1$ however, one has $J_1 > 0$ and $J_2 > 0$, i.e. a purely ferromagnetic Heisenberg model when considering only the first two couplings. In this case, the spin-correlations are obviously not dimerized so that this simple explanation does not work. On the contrary, the behaviour of the RKKY couplings is qualitatively similar for distances $j \geq 3$. In particular one has $J_{\mathrm{RKKY}}(j) \approx 0$ for $j = 3, 5, 7, \ldots$. Hence it is tempting to argue that this feature is responsible for the dimerization. But since $J \sim t_1$, it is questionable if the RKKY theory applies in general.

Three-quarter filling

At three-quarter filling, the ground state is non-magnetic in the limit $J \to \infty$. Fig. 7.11 provides a summary over the short-range spin-correlations for various values of J for the isotropic ladder $t_2 = t_1$. At strong coupling $J = 8.0t_1$ the correlations on the rungs dominate the correlations along the legs. Both are antiferromagnetic and differ by one order of magnitude. The rung correlations around the center of the chain are found to be $\langle \boldsymbol{S}_i \boldsymbol{S}_{i+1} \rangle \approx 0.1$ while the leg correlations are considerably weaker ($\langle \boldsymbol{S}_i \boldsymbol{S}_{i+2} \rangle \approx 0.01$). For decreasing J, the leg correlations become ferromagnetic and at $J = 2.4t_1$ the state is nearly homogeneous with

Figure 7.11: Ground state spin-correlation function $\langle \boldsymbol{S}_i \boldsymbol{S}_j \rangle$ (see color code) for nearest neighbors i, j on the zigzag ladder for $t_2 = t_1$ and $n = \frac{3}{2}$ for various values of J.

antiferromagnetic correlations on the rungs and ferromagnetic correlations on the legs. The spin-structure factor evolves featureless in this case and has peaks at $Q = \pi$ and $Q = \frac{\pi}{2}$. When J is decreased, the peaks become sharper but there is no qualitative change visible. At $J \approx 2.3t_1$, the ground state becomes ferromagnetic which is also clearly visible in Fig. 7.11 for $J = 2.2t_1$. However, this phase is only present for intermediate J and the weak-coupling regime is again not ferromagnetic. The transition takes place at $J \approx 1.6t_1$ but is hard to determine because the ground state tends to develop large ferromagnetic domains. Well below the ferromagnetic phase at $J = 0.4t_1$, the ground state chooses another interesting trade-off as the response to the geometrical frustration. In the bottom row of Fig. 7.11, it is visible that the system forms clusters of size $L_C = 4$ which are coupled antiferromagnetically with each other. Within each cluster, the correlations are ferromagnetic which indicates a polarized cluster-spin $S = 2$. Potentially, the state can therefore be described by an effective spin-2 model. The spin-structure factor peaks at $Q = \frac{\pi}{4}$ which corresponds to a wavelength of $\lambda = 8$ lattice sites for this structure. It is interesting to realize that this state is similar to the spin-dimerized state observed at half-filling. In fact the spin-dimerized state can also be interpreted as ferromagnetic clusters coupled antiferromagnetically with each other. In this case however, the cluster size is $L_C = 2$.

CHAPTER 8

Summary and perspectives

8.1 Summary of the work

The present work provides the first detailed study of the one-dimensional Kondo lattice model with a next-nearest neighbour hopping t_2. The geometry is equivalent to a zigzag ladder with hoppings t_1 along the rungs and t_2 along the legs.

Half-filling

At half-filling and homogeneous couplings $t_1 = t_2$, the KLM on a zigzag chain has at least two quantum critical points: at $J_c^{\dim} \approx 0.89t_2$ the spin correlations $\langle \boldsymbol{S}_i \boldsymbol{S}_j \rangle$ of the localized moments spontaneously break the translational symmetry leading to a twofold degenerate ground state. In this way, the system copes with the geometrical frustration. In the symmetry-broken state the remaining antiferromagnetic correlations form a bipartite sublattice and therewith alleviate the frustration. This is interpreted as a precursor for a second quantum phase transition to a quasi-long-range ordered quantum spin spiral with wave-vector $Q = \frac{\pi}{2}$ at $J_c^{\mathrm{mag}} \approx 0.84t_2$. This phase transition constitutes the general Doniach competition between a Kondo-screened nonmagnetic ground state and a magnetically ordered ground state. This is in contrast to the KLM on the ordinary chain for which no quantum phase transition was observed in previous studies [114] and the ground state is in a spin liquid state with gapped charge and spin excitations. It is remarkable that the geometrical frustration introduced by t_2 triggers a *magnetic* phase transition which is not present in the nonfrustrated model ($t_2 = 0$). The observed state eludes a perturbative explanation as it is well above the RKKY regime. The phase boundaries of both the dimerization and the magnetic transition are systematically traced out in the whole $J - \varphi$ plane. It is found that the two transitions follow each other closely while the dimerization transition is always located at higher J and smaller φ. This confirms that the dimerization is the precursor for the magnetic quantum critical point. It was shown that the dimerization transition begins at $(J = 0, \varphi = \arctan \frac{1}{2})$ which coincides with the Lifshitz point of the noninteracting band structure $\varepsilon(k)$. From there on, the transition line $\varphi_c^{\dim}(J)$ increases monotonically only up to a specific value of J and afterwards bends back. It is tempting to suppose that the transition line finally ends in the point $(J = 0, \varphi = \frac{\pi}{2})$. It was argued by perturbative arguments that the transition line can not end at $\varphi = \frac{\pi}{2}$ and $J \neq 0$ so that the only alternatives to the point $(J = 0, \varphi = \frac{\pi}{2})$ have a different value of φ. But since there is no special point other than the Lifshitz point, the expected trend of the transition line ends in the upper left corner of the phase diagram. The trend of the magnetic phase transition could not be determined in the limit $J \to 0$ because of a heavy growth of the

ground state entanglement in this case. Nevertheless, it was shown that the magnetic phase is surrounded by the dimerization and that the phase boundary of the magnetic transition bends back at the same value of J, too. Two scenarios for the weak-J regime were analysed: firstly, the magnetic phase can constitute island so that at sufficiently weak J the magnetic phase entirely disappears. Secondly, the transition can extend to the Lifshitz point, i.e. $J = 0$ and $\varphi = \arctan \frac{1}{2}$. Both scenarios are compatible with the Lieb-Schultz-Matthis theorem since the ground state is twofold degenerate because of the spin dimerization.

Doped

The KLM on a zigzag chain off half-filling shows the expected asymmetry with respect to half-filling because the underlying lattice is not bipartite. For hole doping, the phase diagram has a large region with a spin-polarized ground state with $S = \frac{1}{2}(L - N)$. This phase is present for sufficiently strong J and the separation line $J_c^{\mathrm{FM}}(n)$ has a dome structure with the maximum located at $n \approx 0.5$. This is in contrast to the ordinary Kondo chain ($t_2 = 0$) where the transition line $J_c^{\mathrm{FM}}(n)$ increases monotonically. This fact is supposed to be attributed to an additional van Hove singularity in the density of states at the Fermi level which is present only for a sufficiently large t_2. The ferromagnetic island of the ordinary Kondo chain disappears for strong enough t_2. The paramagnetic phase at quarter-filling ($n = 0.5$) shows an interesting behaviour of the spin-structure factor. At strong J, there is a well-defined peak at $Q = \pi$ while at weak J the peak is located at $Q = \frac{\pi}{2}$. In between, there is a smooth crossover and at the point where both peaks are of equal height, the ground state has short-range correlations similar to a valence bond solid.

For electron doping, the main ferromagnetic phase is destroyed by t_2. This was already explained perturbatively in the strong-J limit some time ago. Surprisingly, a new ferromagnetic phase develops for electron doping at $n \approx 1.5$ and strong $t_2 \approx t_1$. This phase is potentially qualitatively different as compared to the other magnetic phases of the one-dimensional Kondo lattice as it is driven by t_2. The paramagnetic phase at three-quarter filling *above* the new ferromagnetic phase is mainly J-independent and characterized by broad peaks of the spin-structure factor at $Q = \pi$ and $Q = \frac{\pi}{2}$. The paramagnetic phase at three-quarter filling *below* the new ferromagnetic phase is characterized by a sharp peak of the spin-structure factor at $Q = \frac{\pi}{4}$. The corresponding short-range correlations show that the ground state is built of clusters of size $L_C = 4$.

8.2 Perspectives

The complete phase diagram of the Kondo zigzag ladder exceeds the scope of this thesis. Several questions could not be paid attention to, so that there are interesting perspectives for future work.

Bosonization

At half-filling, the most challenging regime is the weak-J limit. Here, the matrix product state approaches suffer from a very high entanglement in the ground state. As an alternative method, one may study the system using the bosonization approach. With the bosonization mapping one can apply renormalization group techniques to study the weak-coupling limit. This was

quite successful for the one-dimensional Hubbard model with next-nearest neighbour hopping t_2 [159–161]. But the bosonization approach is tedious at half-filling because of additional umklapp processes. For that reason, a simpler task is to study the doped Kondo lattice model by bosonization. Here, previous works could shine light on the ferromagnetic phases of the one-dimensional Kondo chain [121, 122].

Dynamic quantities

In the present work, I focused solely on static correlation functions. A more detailed characterization of the different phases can be achieved by the analysis of dynamical correlation functions. A central quantity is the dynamical spin-structure factor $S(q,\omega)$:

$$S(q,\omega) = \frac{1}{L} \sum_{ij} e^{iq(R_i - R_j)} \int_0^\infty dt\, e^{i\omega t} \langle \boldsymbol{S}_i(t) \boldsymbol{S}_j(0) \rangle \tag{8.1}$$

$$= \frac{2\pi}{L} \sum_{ij} e^{iq(R_i - R_j)} \sum_n \langle 0 \,|\, \boldsymbol{S}_i \,|\, n \rangle \langle n \,|\, \boldsymbol{S}_j \,|\, 0 \rangle\, \delta\left(\omega - (E_n - E_0)\right) \tag{8.2}$$

The dynamical properties provide information not only for the ground state but also for elementary excitations on top of the ground state. The dynamical spin-structure factor, in particular, is the key quantity for spin-excitations. Fig. 8.1 shows a DMRG calculation[1] of
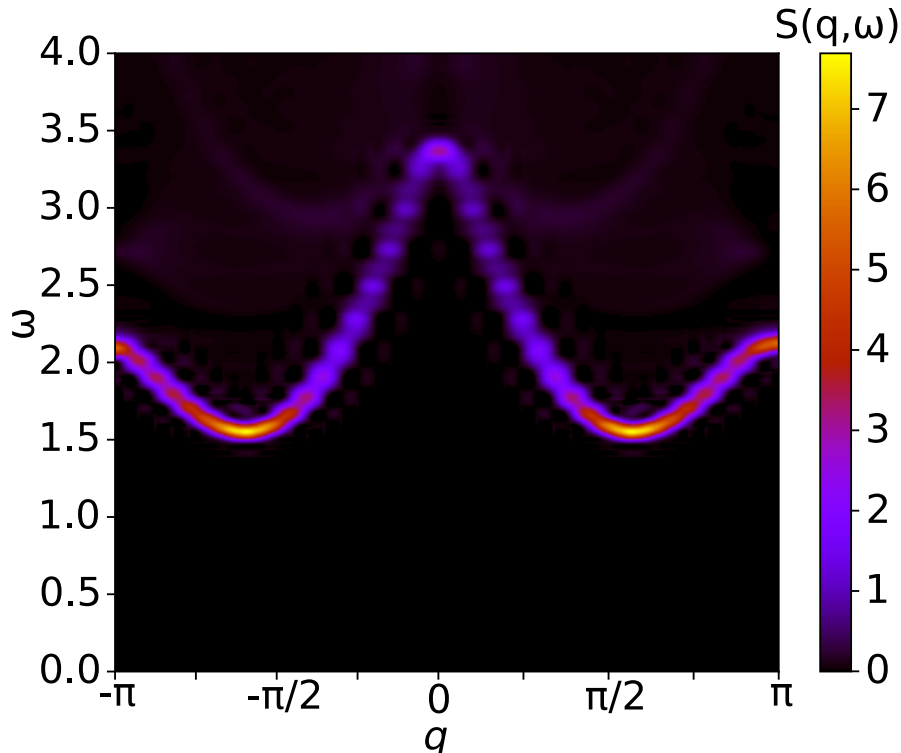
Figure 8.1: Dynamical spin-structure factor $S(q,\omega)$ for $t_2 = t_1$, $J = 3.0t_1$, $L = 40$ sites and half-filling ($n = 1$).

$S(q,\omega)$ for a system with $L = 40$ sites and half-filling in the strong coupling regime ($J = 3.0t_1$). It can be seen that there is a sharp massive magnon band. The band minimum lies at $Q \approx 104°$ which is consistent with the peak location of the static spin-structure factor. The spin gap $\Delta E_S \approx 1.5t_1$ can be directly deduced from Fig. 8.1. It is now very interesting to study the development of $S(q,\omega)$ for decreasing J. The present work has showed that the spin gap closes at $J_c^{\text{mag}} \approx 0.84t_1$ but the nature of the gapless excitations is completely unclear. They could consists of a sharp magnon band but also of a spinon continuum.

Another interesting quantity is the spin-resolved one-particle spectral function $A_\sigma(q,\omega)$:

$$A_\sigma(q,\omega) = \frac{1}{L} \sum_{ij} e^{iq(R_i - R_j)} \int_0^\infty dt e^{i\omega t} \langle c_{i\sigma}^\dagger(t) c_{j\sigma}(0) \rangle \tag{8.3}$$

This quantity can characterize the spin-selective Kondo insulator introduced in Ref. [117] which was suggested to be the general mechanism for ferromagnetism in the KLM.

Superconductivity

The heavy-fermion compounds have rich phase diagrams containing also unconventional superconductivity [109]. Unconventional superconductivity in general is believed to be connected with magnetic ordering as it appears often in the vicinity of a magnetically ordered phase [163]. Since the present work uncovers a (quasi-)magnetically ordered phase at half-filling, one can search for superconductivity for hole- or electron doping. Such studies need to analyse quantities which were not addressed in this thesis. A key correlation function is the static pairing function $\Delta(q)$:

$$\Delta(q) = \frac{1}{L} \sum_{ij} e^{iq(R_i - R_j)} \langle c_{i\uparrow}^\dagger c_{i\downarrow}^\dagger c_{j\downarrow} c_{j\uparrow} \rangle \tag{8.4}$$

This pairing function would signal singlet superconductivity with onsite pairing. However, also the study of triplet superconductivity is interesting since there are examples of heavy-fermion systems with a triplet superconducting ground state [164].

---

1   Calculation is done with the Chebyshev expansion techniques [162].

Bibliography

1. Van Leeuwen, H.-J.: 'Problèmes de la théorie électronique du magnétisme'. *J. Phys. Radium* (1921), vol. 2(12): pp. 361–377. DOI: 10.1051/jphysrad:01921002012036100 (cit. on p. 1).

2. Bardeen, J., L. N. Cooper, and J. R. Schrieffer: 'Theory of Superconductivity'. *Phys. Rev.* (1957), vol. 108: pp. 1175–1204. DOI: 10.1103/PhysRev.108.1175 (cit. on p. 1).

3. Bednorz, J. G. and K. A. Müller: 'Possible high T_c superconductivity in the BaLaCuO system'. *Zeitschrift für Physik B Condensed Matter* (1986), vol. 64(2): pp. 189–193. ISSN: 1431-584X. DOI: 10.1007/BF01303701 (cit. on p. 1).

4. Boer, J. H. de and E. J. W. Verwey: 'Semi-conductors with partially and with completely filled3d-lattice bands'. *Proceedings of the Physical Society* (1937), vol. 49(4S): pp. 59–71. DOI: 10.1088/0959-5309/49/4s/307 (cit. on p. 1).

5. Mott, N. F. and R. Peierls: 'Discussion of the paper by de Boer and Verwey'. *Proceedings of the Physical Society* (1937), vol. 49(4S): pp. 72–73. DOI: 10.1088/0959-5309/49/4s/308 (cit. on p. 1).

6. Mott, N. F.: 'The Basis of the Electron Theory of Metals, with Special Reference to the Transition Metals'. *Proceedings of the Physical Society. Section A* (1949), vol. 62(7): pp. 416–422. DOI: 10.1088/0370-1298/62/7/303 (cit. on p. 1).

7. Hubbard, John: 'Electron correlations in narrow energy bands'. *Proceedings of the Royal Society of London. Series A. Mathematical and Physical Sciences* (1963), vol. 276(1365): pp. 238–257. DOI: 10.1098/rspa.1963.0204 (cit. on p. 1).

8. Anderson, P. W.: 'Localized Magnetic States in Metals'. *Phys. Rev.* (1961), vol. 124: pp. 41–53. DOI: 10.1103/PhysRev.124.41 (cit. on pp. 1, 76).

9. Kasuya, Tadao: 'A Theory of Metallic Ferro- and Antiferromagnetism on Zener's Model'. *Progress of Theoretical Physics* (1956), vol. 16(1): pp. 45–57. ISSN: 0033-068X. DOI: 10.1143/PTP.16.45 (cit. on pp. 1, 2, 83).

10. Anderson, P. W.: 'Resonating valence bonds: A new kind of insulator?' *Materials Research Bulletin* (1973), vol. 8(2): pp. 153–160. ISSN: 0025-5408. DOI: https://doi.org/10.1016/0025-5408(73)90167-0 (cit. on p. 2).

11. Balents, Leon: 'Spin liquids in frustrated magnets'. *Nature* (2010), vol. 464: p. 199. DOI: 10.1038/nature08917 (cit. on p. 2).

12. Anderson, P. W.: 'The Resonating Valence Bond State in La2CuO4 and Superconductivity'. *Science* (1987), vol. 235(4793): pp. 1196–1198. ISSN: 0036-8075. DOI: 10.1126/science.235.4793.1196 (cit. on p. 2).

13. WHITE, STEVEN R.: 'Density matrix formulation for quantum renormalization groups'. *Phys. Rev. Lett.* (1992), vol. 69: pp. 2863–2866. DOI: 10.1103/PhysRevLett.69.2863 (cit. on pp. 2, 5, 29, 43).

14. SCHOLLWÖCK, ULRICH: 'The density-matrix renormalization group in the age of matrix product states'. *Annals of Physics* (2011), vol. 326(1). January 2011 Special Issue: pp. 96–192. ISSN: 0003-4916. DOI: https://doi.org/10.1016/j.aop.2010.09.012 (cit. on pp. 2, 4, 7, 22, 29).

15. JANI, V.: 'A new construction of thermodynamic mean-field theories of itinerant fermions: application to the Falicov-Kimball model'. *Zeitschrift für Physik B Condensed Matter* (1991), vol. 83(2): pp. 227–235. ISSN: 1431-584X. DOI: 10.1007/BF01309423 (cit. on p. 2).

16. GEORGES, ANTOINE, GABRIEL KOTLIAR, WERNER KRAUTH, and MARCELO J. ROZENBERG: 'Dynamical mean-field theory of strongly correlated fermion systems and the limit of infinite dimensions'. *Rev. Mod. Phys.* (1996), vol. 68: pp. 13–125. DOI: 10.1103/RevModPhys.68.13 (cit. on p. 2).

17. METZNER, WALTER and DIETER VOLLHARDT: 'Correlated Lattice Fermions in $d = \infty$ Dimensions'. *Phys. Rev. Lett.* (1989), vol. 62: pp. 324–327. DOI: 10.1103/PhysRevLett.62.324 (cit. on p. 2).

18. BLANKENBECLER, R., D. J. SCALAPINO, and R. L. SUGAR: 'Monte Carlo calculations of coupled boson-fermion systems. I'. *Phys. Rev. D* (1981), vol. 24: pp. 2278–2286. DOI: 10.1103/PhysRevD.24.2278 (cit. on p. 2).

19. HIRSCH, J. E. and R. M. FYE: 'Monte Carlo Method for Magnetic Impurities in Metals'. *Phys. Rev. Lett.* (1986), vol. 56: pp. 2521–2524. DOI: 10.1103/PhysRevLett.56.2521 (cit. on p. 2).

20. GULL, EMANUEL, ANDREW J. MILLIS, ALEXANDER I. LICHTENSTEIN, ALEXEY N. RUBTSOV, MATTHIAS TROYER, and PHILIPP WERNER: 'Continuous-time Monte Carlo methods for quantum impurity models'. *Rev. Mod. Phys.* (2011), vol. 83: pp. 349–404. DOI: 10.1103/RevModPhys.83.349 (cit. on p. 2).

21. LOH, E. Y., J. E. GUBERNATIS, R. T. SCALETTAR, S. R. WHITE, D. J. SCALAPINO, and R. L. SUGAR: 'Sign problem in the numerical simulation of many-electron systems'. *Phys. Rev. B* (1990), vol. 41: pp. 9301–9307. DOI: 10.1103/PhysRevB.41.9301 (cit. on p. 2).

22. RUDERMAN, M. A. and C. KITTEL: 'Indirect Exchange Coupling of Nuclear Magnetic Moments by Conduction Electrons'. *Phys. Rev.* (1954), vol. 96: pp. 99–102. DOI: 10.1103/PhysRev.96.99 (cit. on pp. 2, 83).

23. YOSIDA, KEI: 'Magnetic Properties of Cu-Mn Alloys'. *Phys. Rev.* (1957), vol. 106: pp. 893–898. DOI: 10.1103/PhysRev.106.893 (cit. on pp. 2, 83).

24. HEISENBERG, W.: 'Zur Theorie des Ferromagnetismus'. *Zeitschrift für Physik* (1928), vol. 49(9): pp. 619–636. ISSN: 0044-3328. DOI: 10.1007/BF01328601 (cit. on p. 2).

25. DONIACH, S.: 'The Kondo lattice and weak antiferromagnetism'. *Physica B+C* (1977), vol. 91: p. 231. ISSN: 0378-4363. DOI: http://dx.doi.org/10.1016/0378-4363(77)90190-5 (cit. on pp. 3, 78, 84).

26. OYAMADA, AKIRA, SATORU MAEGAWA, MASAHIDE NISHIYAMA, HIDEAKI KITAZAWA, and YOSIKAZU ISIKAWA: 'Ordering mechanism and spin fluctuations in a geometrically frustrated heavy-fermion antiferromagnet on the Kagome-like lattice CePdAl: A ^{27}Al NMR study'. *Phys. Rev. B* (2008), vol. 77: p. 064432. DOI: 10.1103/PhysRevB.77.064432 (cit. on pp. 3, 78).

27. FRITSCH, VERONIKA, STEFAN LUCAS, ZITA HUESGES, AKITO SAKAI, WOLFRAM KITTLER, CHRISTIAN TAUBENHEIM, SARAH WOITSCHACH, KAI PEDERSEN Bjørnand Grube, BURKHARD SCHMIDT, PHILIPP GEGENWART, OLIVER STOCKERT, and HILBERT V. LÖHNEYSEN: 'CePdAl - a Kondo lattice with partial frustration'. *Journal of Physics: Conference Series* (2017), vol. 807: p. 032003. DOI: 10.1088/1742-6596/807/3/032003 (cit. on pp. 3, 78).

28. CAPRIOTTI, LUCA, ADOLFO E. TRUMPER, and SANDRO SORELLA: 'Long-Range Néel Order in the Triangular Heisenberg Model'. *Phys. Rev. Lett.* (1999), vol. 82: pp. 3899–3902. DOI: 10.1103/PhysRevLett.82.3899 (cit. on p. 3).

29. MOTOME, YUKITOSHI, KYOYA NAKAMIKAWA, YOUHEI YAMAJI, and MASAFUMI UDAGAWA: 'Partial Kondo Screening in Frustrated Kondo Lattice Systems'. *Phys. Rev. Lett.* (2010), vol. 105: p. 036403. DOI: 10.1103/PhysRevLett.105.036403 (cit. on pp. 3, 79).

30. HASTINGS, M B: 'An area law for one-dimensional quantum systems'. *Journal of Statistical Mechanics: Theory and Experiment* (2007), vol. 2007(08): P08024–P08024. DOI: 10.1088/1742-5468/2007/08/p08024 (cit. on pp. 4, 21).

31. AMICO, LUIGI, ROSARIO FAZIO, ANDREAS OSTERLOH, and VLATKO VEDRAL: 'Entanglement in many-body systems'. *Rev. Mod. Phys.* (2008), vol. 80: pp. 517–576. DOI: 10.1103/RevModPhys.80.517 (cit. on p. 4).

32. EISERT, J., M. CRAMER, and M. B. PLENIO: 'Colloquium: Area laws for the entanglement entropy'. *Rev. Mod. Phys.* (2010), vol. 82: pp. 277–306. DOI: 10.1103/RevModPhys.82.277 (cit. on p. 4).

33. HOLZHEY, CHRISTOPH, FINN LARSEN, and FRANK WILCZEK: 'Geometric and renormalized entropy in conformal field theory'. *Nuclear Physics B* (1994), vol. 424(3): pp. 443–467. ISSN: 0550-3213. DOI: https://doi.org/10.1016/0550-3213(94)90402-2 (cit. on p. 4).

34. VIDAL, G., J. I. LATORRE, E. RICO, and A. KITAEV: 'Entanglement in Quantum Critical Phenomena'. *Phys. Rev. Lett.* (2003), vol. 90: p. 227902. DOI: 10.1103/PhysRevLett.90.227902 (cit. on p. 4).

35. CALABRESE, PASQUALE and JOHN CARDY: 'Entanglement entropy and quantum field theory'. *Journal of Statistical Mechanics: Theory and Experiment* (2004), vol. 2004(06): P06002. DOI: 10.1088/1742-5468/2004/06/p06002 (cit. on p. 4).

36. CALABRESE, PASQUALE and ALEXANDRE LEFEVRE: 'Entanglement spectrum in one-dimensional systems'. *Phys. Rev. A* (2008), vol. 78: p. 032329. DOI: 10.1103/PhysRevA.78.032329 (cit. on p. 4).

37. EVENBLY, G. and G. VIDAL: 'Tensor Network States and Geometry'. *Journal of Statistical Physics* (2011), vol. 145(4): pp. 891–918. ISSN: 1572-9613. DOI: 10.1007/s10955-011-0237-4 (cit. on pp. 4, 21).

38. Orús, Román: 'A practical introduction to tensor networks: Matrix product states and projected entangled pair states'. *Annals of Physics* (2014), vol. 349: pp. 117–158. ISSN: 0003-4916. DOI: https://doi.org/10.1016/j.aop.2014.06.013 (cit. on p. 4).

39. Fannes, M., B. Nachtergaele, and R. F. Werner: 'Finitely correlated states on quantum spin chains'. *Communications in Mathematical Physics* (1992), vol. 144(3): pp. 443–490. ISSN: 1432-0916. DOI: 10.1007/BF02099178 (cit. on pp. 4, 7).

40. Östlund, Stellan and Stefan Rommer: 'Thermodynamic Limit of Density Matrix Renormalization'. *Phys. Rev. Lett.* (1995), vol. 75: pp. 3537–3540. DOI: 10.1103/PhysRevLett.75.3537 (cit. on pp. 4, 7).

41. Vidal, G.: 'Entanglement Renormalization'. *Phys. Rev. Lett.* (2007), vol. 99: p. 220405. DOI: 10.1103/PhysRevLett.99.220405 (cit. on p. 4).

42. Vidal, G.: 'Class of Quantum Many-Body States That Can Be Efficiently Simulated'. *Phys. Rev. Lett.* (2008), vol. 101: p. 110501. DOI: 10.1103/PhysRevLett.101.110501 (cit. on p. 4).

43. Sierra, G. and M. A. Martin-Delgado: *The Density Matrix Renormalization Group, Quantum Groups and Conformal Field Theory.* arXiv preprint. 1998. eprint: arXiv:cond-mat/9811170 (cit. on pp. 4, 21).

44. Verstraete, F. and J. I. Cirac: *Renormalization algorithms for Quantum-Many Body Systems in two and higher dimensions.* arXiv preprint. 2004. eprint: arXiv:cond-mat/0407066 (cit. on pp. 4, 21).

45. Jordan, J., R. Orús, G. Vidal, F. Verstraete, and J. I. Cirac: 'Classical Simulation of Infinite-Size Quantum Lattice Systems in Two Spatial Dimensions'. *Phys. Rev. Lett.* (2008), vol. 101: p. 250602. DOI: 10.1103/PhysRevLett.101.250602 (cit. on pp. 4, 21).

46. Schollwöck, U.: 'The density-matrix renormalization group'. *Rev. Mod. Phys.* (2005), vol. 77: pp. 259–315. DOI: 10.1103/RevModPhys.77.259 (cit. on pp. 5, 29).

47. Zauner-Stauber, V., L. Vanderstraeten, M. T. Fishman, F. Verstraete, and J. Haegeman: 'Variational optimization algorithms for uniform matrix product states'. *Phys. Rev. B* (2018), vol. 97: p. 045145. DOI: 10.1103/PhysRevB.97.045145 (cit. on pp. 5, 30, 37, 38, 42).

48. Corboz, Philippe, Román Orús, Bela Bauer, and Guifré Vidal: 'Simulation of strongly correlated fermions in two spatial dimensions with fermionic projected entangled-pair states'. *Phys. Rev. B* (2010), vol. 81: p. 165104. DOI: 10.1103/PhysRevB.81.165104 (cit. on p. 5).

49. Corboz, Philippe, Jacob Jordan, and Guifré Vidal: 'Simulation of fermionic lattice models in two dimensions with projected entangled-pair states: Next-nearest neighbor Hamiltonians'. *Phys. Rev. B* (2010), vol. 82: p. 245119. DOI: 10.1103/PhysRevB.82.245119 (cit. on p. 5).

50. Vanderstraeten, Laurens, Michaël Mariën, Frank Verstraete, and Jutho Haegeman: 'Excitations and the tangent space of projected entangled-pair states'. *Phys. Rev. B* (2015), vol. 92: p. 201111. DOI: 10.1103/PhysRevB.92.201111 (cit. on p. 5).

51. VANDERSTRAETEN, LAURENS, JUTHO HAEGEMAN, PHILIPPE CORBOZ, and FRANK VERSTRAETE: 'Gradient methods for variational optimization of projected entangled-pair states'. *Phys. Rev. B* (2016), vol. 94: p. 155123. DOI: `10.1103/PhysRevB.94.155123` (cit. on p. 5).

52. CZARNIK, PIOTR and JACEK DZIARMAGA: 'Time evolution of an infinite projected entangled pair state: An algorithm from first principles'. *Phys. Rev. B* (2018), vol. 98: p. 045110. DOI: `10.1103/PhysRevB.98.045110` (cit. on p. 5).

53. CZARNIK, PIOTR, JACEK DZIARMAGA, and PHILIPPE CORBOZ: 'Time evolution of an infinite projected entangled pair state: An efficient algorithm'. *Phys. Rev. B* (2019), vol. 99: p. 035115. DOI: `10.1103/PhysRevB.99.035115` (cit. on p. 5).

54. HAEGEMAN, JUTHO, TOBIAS J. OSBORNE, and FRANK VERSTRAETE: 'Post-matrix product state methods: To tangent space and beyond'. *Phys. Rev. B* (2013), vol. 88: p. 075133. DOI: `10.1103/PhysRevB.88.075133` (cit. on pp. 13, 14).

55. HAEGEMAN, JUTHO, MICHAËL MARIËN, TOBIAS J. OSBORNE, and FRANK VERSTRAETE: 'Geometry of matrix product states: Metric, parallel transport, and curvature'. *Journal of Mathematical Physics* (2014), vol. 55(2): p. 021902. DOI: `10.1063/1.4862851` (cit. on pp. 13, 14, 17).

56. VANDERSTRAETEN, LAURENS, JUTHO HAEGEMAN, and FRANK VERSTRAETE: *Tangent-space methods for uniform matrix product states*. arXiv preprint. 2018. eprint: `arXiv:1810.07006[cond-mat.str-el]` (cit. on pp. 14, 27).

57. PLENIO, MARTIN B. and S. VIRMANI: 'An introduction to entanglement measures'. *Quant. Inf. Comput.* (2007), vol. 7: pp. 1–51. DOI: `10.26421/QIC7.1-2` (cit. on p. 19).

58. HORODECKI, RYSZARD, PAWE HORODECKI, MICHA HORODECKI, and KAROL HORODECKI: 'Quantum entanglement'. *Rev. Mod. Phys.* (2009), vol. 81: pp. 865–942. DOI: `10.1103/RevModPhys.81.865` (cit. on p. 19).

59. RÉNYI, ALFRÉD: 'On Measures of Entropy and Information'. *Proceedings of the Fourth Berkeley Symposium on Mathematical Statistics and Probability, Volume 1: Contributions to the Theory of Statistics.* Berkeley, Calif.: University of California Press, 1961: pp. 547–561 (cit. on p. 19).

60. CHEN, BIN-BIN, LEI CHEN, ZIYU CHEN, WEI LI, and ANDREAS WEICHSELBAUM: 'Exponential Thermal Tensor Network Approach for Quantum Lattice Models'. *Phys. Rev. X* (2018), vol. 8: p. 031082. DOI: `10.1103/PhysRevX.8.031082` (cit. on p. 21).

61. CROSSWHITE, GREGORY M., A. C. DOHERTY, and GUIFRÉ VIDAL: 'Applying matrix product operators to model systems with long-range interactions'. *Phys. Rev. B* (2008), vol. 78: p. 035116. DOI: `10.1103/PhysRevB.78.035116` (cit. on p. 21).

62. FRÖWIS, F., V. NEBENDAHL, and W. DÜR: 'Tensor operators: Constructions and applications for long-range interaction systems'. *Phys. Rev. A* (2010), vol. 81: p. 062337. DOI: `10.1103/PhysRevA.81.062337` (cit. on p. 21).

63. MICHEL, L. and I. P. MCCULLOCH: *Schur Forms of Matrix Product Operators in the Infinite Limit*. arXiv preprint. 2010. eprint: `arXiv:1008.4667[cond-mat.stat-mech]` (cit. on pp. 21, 38, 40).

64.   ANDERSON, P. W.: 'Infrared Catastrophe in Fermi Gases with Local Scattering Potentials'. *Phys. Rev. Lett.* (1967), vol. 18: pp. 1049–1051. DOI: `10.1103/PhysRevLett.18.1049` (cit. on p. 24).

65.   WHITE, STEVEN R.: 'Density matrix renormalization group algorithms with a single center site'. *Phys. Rev. B* (2005), vol. 72: p. 180403. DOI: `10.1103/PhysRevB.72.180403` (cit. on pp. 29, 33).

66.   DOLGOV, S. and D. SAVOSTYANOV: 'Alternating Minimal Energy Methods for Linear Systems in Higher Dimensions'. *SIAM Journal on Scientific Computing* (2014), vol. 36(5): A2248–A2271. DOI: `10.1137/140953289` (cit. on pp. 29, 33).

67.   HUBIG, C., I. P. MCCULLOCH, U. SCHOLLWÖCK, and F. A. WOLF: 'Strictly single-site DMRG algorithm with subspace expansion'. *Phys. Rev. B* (2015), vol. 91: p. 155115. DOI: `10.1103/PhysRevB.91.155115` (cit. on pp. 29, 33, 34).

68.   MCCULLOCH, I. P.: *Infinite size density matrix renormalization group, revisited.* arXiv preprint. 2008. eprint: `arXiv:0804.2509[cond-mat.str-el]` (cit. on p. 30).

69.   VIDAL, GUIFRÉ: 'Efficient Classical Simulation of Slightly Entangled Quantum Computations'. *Phys. Rev. Lett.* (2003), vol. 91: p. 147902. DOI: `10.1103/PhysRevLett.91.147902` (cit. on p. 30).

70.   VIDAL, G.: 'Classical Simulation of Infinite-Size Quantum Lattice Systems in One Spatial Dimension'. *Phys. Rev. Lett.* (2007), vol. 98: p. 070201. DOI: `10.1103/PhysRevLett.98.070201` (cit. on p. 30).

71.   PHIEN, HO N., IAN P. MCCULLOCH, and GUIFRÉ VIDAL: 'Fast convergence of imaginary time evolution tensor network algorithms by recycling the environment'. *Phys. Rev. B* (2015), vol. 91: p. 115137. DOI: `10.1103/PhysRevB.91.115137` (cit. on p. 30).

72.   ZALETEL, MICHAEL P., ROGER S. K. MONG, CHRISTOPH KARRASCH, JOEL E. MOORE, and FRANK POLLMANN: 'Time-evolving a matrix product state with long-ranged interactions'. *Phys. Rev. B* (2015), vol. 91: p. 165112. DOI: `10.1103/PhysRevB.91.165112` (cit. on p. 30).

73.   HUBIG, C., J. HAEGEMAN, and U. SCHOLLWÖCK: 'Error estimates for extrapolations with matrix-product states'. *Phys. Rev. B* (2018), vol. 97: p. 045125. DOI: `10.1103/PhysRevB.97.045125` (cit. on pp. 34, 35).

74.   MCCULLOCH, I. P. and M. GULÁCSI: 'The non-Abelian density matrix renormalization group algorithm'. *Europhysics Letters (EPL)* (2002), vol. 57(6): pp. 852–858. DOI: `10.1209/epl/i2002-00393-0` (cit. on p. 43).

75.   MCCULLOCH, I. P.: 'From density-matrix renormalization group to matrix product states'. *Journal of Statistical Mechanics: Theory and Experiment* (2007), vol. 2007(10): P10014–P10014. DOI: `10.1088/1742-5468/2007/10/p10014` (cit. on pp. 43, 65, 72).

76.   WEICHSELBAUM, ANDREAS: 'Non-abelian symmetries in tensor networks: A quantum symmetry space approach'. *Annals of Physics* (2012), vol. 327(12): pp. 2972–3047. ISSN: 0003-4916. DOI: `https://doi.org/10.1016/j.aop.2012.07.009` (cit. on pp. 43, 57, 65).

77. Hubig, Claudius: 'Abelian and non-abelian symmetries in infinite projected entangled pair states'. *SciPost Phys.* (2018), vol. 5: p. 47. DOI: 10.21468/SciPostPhys.5.5.047 (cit. on p. 43).

78. Schmoll, Philipp, Sukhbinder Singh, Matteo Rizzi, and Roman Orus: *A programming guide for tensor networks with global $SU(2)$ symmetry.* arXiv preprint. 2018. eprint: arXiv:1809.08180[cond-mat.str-el] (cit. on pp. 43, 72).

79. Hall, Brian C.: *Lie Groups, Lie Algebras, and Representations. An Elementary Introduction.* Ed. by Axler, Sheldon and Kenneth Ribet. 2nd ed. Heidelberg New York Dordrecht London: Springer Cham, 2015. ISBN: 978-3-319-13466-6 (cit. on pp. 43, 51, 53).

80. Jeevanjee, Nadir: *An Introduction to Tensors and Group Theory for Physicists.* 2nd ed. Heidelberg New York Dordrecht London: Springer Cham, 2015. ISBN: 978-3-319-14793-2 (cit. on pp. 43, 49).

81. Regge, T.: 'Symmetry properties of Clebsch-Gordon's coefficients'. *Il Nuovo Cimento (1955-1965)* (1958), vol. 10(3): pp. 544–545. ISSN: 1827-6121. DOI: 10.1007/BF02859841 (cit. on p. 57).

82. Biedenharn, L.C. and J.D. Louck: 'Angular Momentum in Quantum Physics'. *Encyclopedia of Mathematics and its Applications.* Vol. 8. Ed. by Rota, Gian-Carlo. Reading, Massachusetts: Addison-Wesley Publishing Company, 1981. ISBN: 0-201-13507-8 (cit. on pp. 58, 59).

83. Varshalovich, D.A., A.N Moskalev, and V.K. Khersonskii: *Quantum Theory of Angular Momentum.* 1st ed. Singapore: World Scientific Publishing Co. Pte. Ltd., 1988. ISBN: 9971-50-107-4 (cit. on pp. 58, 59).

84. Racah, Giulio: 'Theory of Complex Spectra. II'. *Phys. Rev.* (1942), vol. 62: pp. 438–462. DOI: 10.1103/PhysRev.62.438 (cit. on p. 58).

85. Racah, Giulio: 'Theory of Complex Spectra. III'. *Phys. Rev.* (1943), vol. 63: pp. 367–382. DOI: 10.1103/PhysRev.63.367 (cit. on p. 58).

86. Bargmann, V.: 'On the Representations of the Rotation Group'. *Rev. Mod. Phys.* (1962), vol. 34: pp. 829–845. DOI: 10.1103/RevModPhys.34.829 (cit. on p. 58).

87. Biedenharn, L.C. and J.D. Louck: 'The Racah-Wigner algebra in quantum theory'. *Encyclopedia of Mathematics and its Applications.* Vol. 9. Ed. by Rota, Gian-Carlo. Reading, Massachusetts: Addison-Wesley Publishing Company, 1981. ISBN: 0-201-13508-6 (cit. on p. 60).

88. Noether, Emmy: 'Invariante Variationsprobleme.' German. *Nachr. Ges. Wiss. Göttingen, Math.-Phys. Kl.* (1918), vol. 1918: pp. 235–257 (cit. on p. 62).

89. Wigner, Eugene Paul: *Group theory and its application to the quantum mechanics of atomic spectra.* Vol. 5. New York: Academic Press, 1959: pp. 233–236 (cit. on p. 63).

90. Essler, Fabian H. L., Holger Frahm, Frank Gohmann, Andreas Klumper, and Vladimir E. Korepin: *The One-Dimensional Hubbard Model.* Cambridge University Press, 2005. ISBN: 0-521-80262-8 (cit. on p. 70).

91. YANG, CHEN NING: 'η pairing and off-diagonal long-range order in a Hubbard model'. *Phys. Rev. Lett.* (1989), vol. 63: pp. 2144–2147. DOI: `10.1103/PhysRevLett.63.2144` (cit. on p. 70).

92. ZHANG, SHOUCHENG: 'Pseudospin symmetry and new collective modes of the Hubbard model'. *Phys. Rev. Lett.* (1990), vol. 65: pp. 120–122. DOI: `10.1103/PhysRevLett.65.120` (cit. on p. 70).

93. KONDO, JUN: 'Resistance Minimum in Dilute Magnetic Alloys'. *Progress of Theoretical Physics* (1964), vol. 32(1): pp. 37–49. ISSN: 0033-068X. DOI: `10.1143/PTP.32.37` (cit. on pp. 75, 84).

94. SCHRIEFFER, J. R. and P. A. WOLFF: 'Relation between the Anderson and Kondo Hamiltonians'. *Phys. Rev.* (1966), vol. 149: pp. 491–492. DOI: `10.1103/PhysRev.149.491` (cit. on p. 76).

95. COLEMAN, PIERS: *Handbook of Magnetism and Advanced Magnetic Materials.* Ed. by KRONMUELLER, HELMUT and STUART PARKIN. Vol. 1. Amsterdam: John Wiley and Sons, 2007: pp. 95–148 (cit. on p. 77).

96. LANDAU, L.D.: 'The Theory of a Fermi liquid'. *JETP* (1956), vol. 3: p. 920 (cit. on p. 77).

97. STEWART, G. R., Z. FISK, and M. S. WIRE: 'New Ce Heavy-Fermion System: CeCu$_6$'. *Phys. Rev. B* (1984), vol. 30: pp. 482–484. DOI: `10.1103/PhysRevB.30.482` (cit. on p. 77).

98. WANG, LE et al.: 'Heavy fermion behavior in the quasi-one-dimensional Kondo lattice CeCo2Ga8'. *npj Quantum Materials* (2017), vol. 2(1): p. 36. ISSN: 2397-4648. DOI: `10.1038/s41535-017-0040-9` (cit. on pp. 77, 78).

99. CHENG, KANGQIAO, LE WANG, YUANJI XU, FENG YANG, HAIPENG ZHU, JIEZUN KE, XIUFANG LU, ZHENGCAI XIA, JUNFENG WANG, YOUGUO SHI, YIFENG YANG, and YONGKANG LUO: 'Realization of Kondo chain in CeCo$_2$Ga$_8$'. *Phys. Rev. Materials* (2019), vol. 3: p. 021402. DOI: `10.1103/PhysRevMaterials.3.021402` (cit. on p. 77).

100. MENTH, A., E. BUEHLER, and T. H. GEBALLE: 'Magnetic and Semiconducting Properties of SmB$_6$'. *Phys. Rev. Lett.* (1969), vol. 22: pp. 295–297. DOI: `10.1103/PhysRevLett.22.295` (cit. on p. 77).

101. HUNDLEY, M. F., P. C. CANFIELD, J. D. THOMPSON, Z. FISK, and J. M. LAWRENCE: 'Hybridization gap in Ce$_3$Bi$_4$Pt$_3$'. *Phys. Rev. B* (1990), vol. 42: pp. 6842–6845. DOI: `10.1103/PhysRevB.42.6842` (cit. on p. 77).

102. GERMANN, A., NIGAM, A. K., DUTZI, J., SCHRÖDER, A., and LÖHNEYSEN, H. V.: 'Magnetic ordering in the heavy-fermion alloys CeCu$_{6-x}$Au$_x$ and CeCu$_{6-x}$Ag$_x$'. *J. Phys. Colloques* (1988), vol. 49(C8): pp. C8-755-C8–756. DOI: `https://doi.org/10.1051/jphyscol:19888340` (cit. on p. 77).

103. STEGLICH, F., J. AARTS, C. D. BREDL, W. LIEKE, D. MESCHEDE, W. FRANZ, and H. SCHÄFER: 'Superconductivity in the Presence of Strong Pauli Paramagnetism: CeCu$_2$Si$_2$'. *Phys. Rev. Lett.* (1979), vol. 43: pp. 1892–1896. DOI: `10.1103/PhysRevLett.43.1892` (cit. on pp. 77, 115).

104. Löhneysen, H.v., A. Schröder, T. Trappmann, and M. Welsch: 'Evolution of magnetic ordering in CeCu6xAux heavy-fermion alloys'. *Journal of Magnetism and Magnetic Materials* (1992), vol. 108(1): pp. 45–46. ISSN: 0304-8853. DOI: https://doi.org/10.1016/0304-8853(92)91341-P (cit. on pp. 77, 78).

105. lebarski, Andrzej and Jozef Spaek: 'Universal Scaling and a Novel Quantum Critical Behavior of $CeRhSb_{1-x}Sn_x$'. *Phys. Rev. Lett.* (2005), vol. 95: p. 046402. DOI: 10.1103/PhysRevLett.95.046402 (cit. on p. 77).

106. Barla, A., J. Derr, J. P. Sanchez, B. Salce, G. Lapertot, B. P. Doyle, R. Rüffer, R. Lengsdorf, M. M. Abd-Elmeguid, and J. Flouquet: 'High-Pressure Ground State of SmB_6: Electronic Conduction and Long Range Magnetic Order'. *Phys. Rev. Lett.* (2005), vol. 94: p. 166401. DOI: 10.1103/PhysRevLett.94.166401 (cit. on pp. 77, 78).

107. Jaime, Marcelo, Roman Movshovich, Gregory R. Stewart, Ward P. Beyermann, Mariano Gomez Berisso, Michael F. Hundley, Paul C. Canfield, and John L. Sarrao: 'Closing the spin gap in the Kondo insulator Ce3Bi4Pt3 at high magnetic fields'. *Nature* (2000), vol. 405(6783): pp. 160–163. ISSN: 1476-4687. DOI: 10.1038/35012027 (cit. on p. 77).

108. Löhneysen, H. v., T. Pietrus, G. Portisch, H. G. Schlager, A. Schröder, M. Sieck, and T. Trappmann: 'Non-Fermi-liquid behavior in a heavy-fermion alloy at a magnetic instability'. *Phys. Rev. Lett.* (1994), vol. 72: pp. 3262–3265. DOI: 10.1103/PhysRevLett.72.3262 (cit. on pp. 77, 78).

109. White, B.D., J.D. Thompson, and M.B. Maple: 'Unconventional superconductivity in heavy-fermion compounds'. *Physica C: Superconductivity and its Applications* (2015), vol. 514. Superconducting Materials: Conventional, Unconventional and Undetermined: pp. 246–278. ISSN: 0921-4534. DOI: https://doi.org/10.1016/j.physc.2015.02.044 (cit. on pp. 77, 132).

110. Steglich, Frank and Steffen Wirth: 'Foundations of heavy-fermion superconductivity: lattice Kondo effect and Mott physics'. *Reports on Progress in Physics* (2016), vol. 79(8): p. 084502. DOI: 10.1088/0034-4885/79/8/084502 (cit. on p. 77).

111. Coleman, Piers: '$\frac{1}{N}$ expansion for the Kondo lattice'. *Phys. Rev. B* (1983), vol. 28: pp. 5255–5262. DOI: 10.1103/PhysRevB.28.5255 (cit. on p. 78).

112. Read, N. and D.M. Newns: 'A new functional integral formalism for the degenerate Anderson model'. *Journal of Physics C: Solid State Physics* (1983), vol. 16(29): pp. L1055–L1060. DOI: 10.1088/0022-3719/16/29/007 (cit. on p. 78).

113. Coleman, Piers: 'New approach to the mixed-valence problem'. *Phys. Rev. B* (1984), vol. 29: pp. 3035–3044. DOI: 10.1103/PhysRevB.29.3035 (cit. on p. 78).

114. Tsunetsugu, Hirokazu, Manfred Sigrist, and Kazuo Ueda: 'The ground-state phase diagram of the one-dimensional Kondo lattice model'. *Rev. Mod. Phys.* (1997), vol. 69: pp. 809–864. DOI: 10.1103/RevModPhys.69.809 (cit. on pp. 78, 79, 88, 95, 115, 116, 120, 129).

115. Mcculloch, I.P., A. Juozapavicius, A. Rosengren, and M. Gulácsi: 'Ferromagnetism in Kondo lattice models'. *Philosophical Magazine Letters* (2001), vol. 81(12): pp. 869–875. DOI: 10.1080/09500830110092390 (cit. on pp. 79, 116).

116. McCulloch, I. P., A. Juozapavicius, A. Rosengren, and M. Gulacsi: 'Localized spin ordering in Kondo lattice models'. *Phys. Rev. B* (2002), vol. 65: p. 052410. DOI: 10.1103/PhysRevB.65.052410 (cit. on pp. 79, 116, 117).

117. Peters, Robert and Norio Kawakami: 'Ferromagnetic state in the one-dimensional Kondo lattice model'. *Phys. Rev. B* (2012), vol. 86: p. 165107. DOI: 10.1103/PhysRevB.86.165107 (cit. on pp. 79, 116, 132).

118. Khait, Ilia, Patrick Azaria, Claudius Hubig, Ulrich Schollwöck, and Assa Auerbach: 'Doped Kondo chain, a heavy Luttinger liquid'. *Proceedings of the National Academy of Sciences* (2018), vol. 115(20): pp. 5140–5144. ISSN: 0027-8424. DOI: 10.1073/pnas.1719374115 (cit. on pp. 79, 116).

119. Xavier, J. C., E. Novais, and E. Miranda: 'Small Fermi surface in the one-dimensional Kondo lattice model'. *Phys. Rev. B* (2002), vol. 65: p. 214406. DOI: 10.1103/PhysRevB.65.214406 (cit. on p. 79).

120. Xavier, J. C., R. G. Pereira, E. Miranda, and I. Affleck: 'Dimerization Induced by the RKKY Interaction'. *Phys. Rev. Lett.* (2003), vol. 90: p. 247204. DOI: 10.1103/PhysRevLett.90.247204 (cit. on pp. 79, 117, 126).

121. Honner, Graeme and Miklós Gulácsi: 'One-Dimensional Kondo Lattice at Partial Band Filling'. *Phys. Rev. Lett.* (1997), vol. 78: pp. 2180–2183. DOI: 10.1103/PhysRevLett.78.2180 (cit. on pp. 79, 131).

122. Honner, Graeme and Miklós Gulácsi: 'Ordering of localized moments in Kondo lattice models'. *Phys. Rev. B* (1998), vol. 58: pp. 2662–2677. DOI: 10.1103/PhysRevB.58.2662 (cit. on pp. 79, 131).

123. *, Miklós Gulácsi: 'The one-dimensional Kondo lattice model at partial band filling'. *Advances in Physics* (2004), vol. 53(7): pp. 769–937. DOI: 10.1080/00018730412331313997 (cit. on p. 79).

124. Assaad, F. F.: 'Quantum Monte Carlo Simulations of the Half-Filled Two-Dimensional Kondo Lattice Model'. *Phys. Rev. Lett.* (1999), vol. 83: pp. 796–799. DOI: 10.1103/PhysRevLett.83.796 (cit. on p. 79).

125. Hayami, Satoru, Masafumi Udagawa, and Yukitoshi Motome: 'Partial Disorder in the Periodic Anderson Model on a Triangular Lattice'. *Journal of the Physical Society of Japan* (2011), vol. 80(7): p. 073704. DOI: 10.1143/JPSJ.80.073704 (cit. on p. 79).

126. Hayami, Satoru, Masafumi Udagawa, and Yukitoshi Motome: 'Partial Disorder and MetalInsulator Transition in the Periodic Anderson Model on a Triangular Lattice'. *Journal of the Physical Society of Japan* (2012), vol. 81(10): p. 103707. DOI: 10.1143/JPSJ.81.103707 (cit. on p. 79).

127. Aulbach, Maximilian W., Fakher F. Assaad, and Michael Potthoff: 'Dynamical mean-field study of partial Kondo screening in the periodic Anderson model on the triangular lattice'. *Phys. Rev. B* (2015), vol. 92: p. 235131. DOI: 10.1103/PhysRevB.92.235131 (cit. on p. 79).

128. Sato, Toshihiro, Fakher F. Assaad, and Tarun Grover: 'Quantum Monte Carlo Simulation of Frustrated Kondo Lattice Models'. *Phys. Rev. Lett.* (2018), vol. 120: p. 107201. DOI: 10.1103/PhysRevLett.120.107201 (cit. on p. 79).

129. WOLFF, P. A.: 'Spin Susceptibility of an Electron Gas'. *Phys. Rev.* (1960), vol. 120: pp. 814–819. DOI: 10.1103/PhysRev.120.814 (cit. on p. 83).

130. WOLFF, P. A.: 'Nuclear Relaxation as a Probe of Electron Spin Correlation'. *Phys. Rev.* (1963), vol. 129: pp. 84–90. DOI: 10.1103/PhysRev.129.84 (cit. on p. 83).

131. ZIENER, C. H., S. GLUTSCH, and F. BECHSTEDT: 'RKKY interaction in semiconductors: Effects of magnetic field and screening'. *Phys. Rev. B* (2004), vol. 70: p. 075205. DOI: 10.1103/PhysRevB.70.075205 (cit. on p. 83).

132. COLEMAN, PIERS: 'Heavy Fermions and the Kondo Lattice: A 21st Century Perspective'. *Many-Body Physics: From Kondo to Hubbard.* Vol. 5. Ed. by PAVARINI, EVA, ERIK KOCH, and PIERS COLEMAN. Forschungszentrum Jülich GmbH Institute for Advanced Simulation, 2015. ISBN: 978-3-95806-074-6 (cit. on p. 84).

133. HAAS, W.J. de, J. de BOER, and G.J. van dën BERG: 'The electrical resistance of gold, copper and lead at low temperatures'. *Physica* (1934), vol. 1(7): pp. 1115–1124. ISSN: 0031-8914. DOI: https://doi.org/10.1016/S0031-8914(34)80310-2 (cit. on p. 84).

134. SHIBATA, NAOKAZU, TOMOTOSHI NISHINO, KAZUO UEDA, and CHIKARA ISHII: 'Spin and charge gaps in the one-dimensional Kondo-lattice model with Coulomb interaction between conduction electrons'. *Phys. Rev. B* (1996), vol. 53: R8828–R8831. DOI: 10.1103/PhysRevB.53.R8828 (cit. on p. 89).

135. HE, HUAN and GUIFRE VIDAL: 'Disentangling theorem and monogamy for entanglement negativity'. *Phys. Rev. A* (2015), vol. 91: p. 012339. DOI: 10.1103/PhysRevA.91.012339 (cit. on p. 99).

136. LANDAU, D. P.: 'Finite-size behavior of the Ising square lattice'. *Phys. Rev. B* (1976), vol. 13: pp. 2997–3011. DOI: 10.1103/PhysRevB.13.2997 (cit. on pp. 103, 157).

137. STANLEY, H. EUGENE: 'Scaling, universality, and renormalization: Three pillars of modern critical phenomena'. *Rev. Mod. Phys.* (1999), vol. 71: S358–S366. DOI: 10.1103/RevModPhys.71.S358 (cit. on pp. 103, 157).

138. OTSUKA, YUICHI, SEIJI YUNOKI, and SANDRO SORELLA: 'Universal Quantum Criticality in the Metal-Insulator Transition of Two-Dimensional Interacting Dirac Electrons'. *Phys. Rev. X* (2016), vol. 6: p. 011029. DOI: 10.1103/PhysRevX.6.011029 (cit. on pp. 103, 157).

139. LIEB, ELLIOTT, THEODORE SCHULTZ, and DANIEL MATTIS: 'Two soluble models of an antiferromagnetic chain'. *Annals of Physics* (1961), vol. 16(3): pp. 407–466. ISSN: 0003-4916. DOI: https://doi.org/10.1016/0003-4916(61)90115-4 (cit. on p. 108).

140. OSHIKAWA, MASAKI: 'Commensurability, Excitation Gap, and Topology in Quantum Many-Particle Systems on a Periodic Lattice'. *Phys. Rev. Lett.* (2000), vol. 84: pp. 1535–1538. DOI: 10.1103/PhysRevLett.84.1535 (cit. on p. 108).

141. SAREMI, SAEED: 'RKKY in half-filled bipartite lattices: Graphene as an example'. *Phys. Rev. B* (2007), vol. 76: p. 184430. DOI: 10.1103/PhysRevB.76.184430 (cit. on p. 109).

142. BUNDER, J. E. and HSIU-HAU LIN: 'Ruderman-Kittel-Kasuya-Yosida interactions on a bipartite lattice'. *Phys. Rev. B* (2009), vol. 80: p. 153414. DOI: 10.1103/PhysRevB.80.153414 (cit. on p. 109).

143. PESCHKE, MATTHIAS, LENA-MARIE WOELK, and MICHAEL POTTHOFF: 'Phase diagram of the Kondo model on the zigzag ladder'. *Phys. Rev. B* (2019), vol. 99: p. 085140. DOI: 10.1103/PhysRevB.99.085140 (cit. on p. 114).

144. HALDANE, F. D. M.: ''Luttinger liquid theory' of one-dimensional quantum fluids. I. Properties of the Luttinger model and their extension to the general 1D interacting spinless Fermi gas'. *Journal of Physics C: Solid State Physics* (1981), vol. 14(19): pp. 2585–2609. DOI: 10.1088/0022-3719/14/19/010 (cit. on p. 115).

145. SIGRIST, MANFRED, HIROKAZU TSUNETSUGA, and KAZUO UEDA: 'Rigorous results for the one-electron Kondo-lattice model'. *Phys. Rev. Lett.* (1991), vol. 67: pp. 2211–2214. DOI: 10.1103/PhysRevLett.67.2211 (cit. on p. 116).

146. SIGRIST, MANFRED, KAZUO UEDA, and HIROKAZU TSUNETSUGU: 'Ferromagnetism of the Kondo lattice in the low-carrier-concentration limit'. *Phys. Rev. B* (1992), vol. 46: pp. 175–183. DOI: 10.1103/PhysRevB.46.175 (cit. on p. 116).

147. ZENER, CLARENCE: 'Interaction between the *d*-Shells in the Transition Metals. II. Ferromagnetic Compounds of Manganese with Perovskite Structure'. *Phys. Rev.* (1951), vol. 82: pp. 403–405. DOI: 10.1103/PhysRev.82.403 (cit. on p. 116).

148. SHIBATA, NAOKAZU, KAZUO UEDA, TOMOTOSHI NISHINO, and CHIKARA ISHII: 'Friedel oscillations in the one-dimensional Kondo lattice model'. *Phys. Rev. B* (1996), vol. 54: pp. 13495–13498. DOI: 10.1103/PhysRevB.54.13495 (cit. on p. 116).

149. SHIBATA, NAOKAZU, ALEXEI TSVELIK, and KAZUO UEDA: 'One-dimensional Kondo lattice model as a Tomonaga-Luttinger liquid'. *Phys. Rev. B* (1997), vol. 56: pp. 330–334. DOI: 10.1103/PhysRevB.56.330 (cit. on p. 116).

150. BASYLKO, S. A., P. H. LUNDOW, and A. ROSENGREN: 'One-dimensional Kondo lattice model studied through numerical diagonalization'. *Phys. Rev. B* (2008), vol. 77: p. 073103. DOI: 10.1103/PhysRevB.77.073103 (cit. on p. 116).

151. XAVIER, J. C. and E. MIRANDA: 'One-dimensional Kondo lattice model at quarter filling'. *Phys. Rev. B* (2008), vol. 78: p. 144406. DOI: 10.1103/PhysRevB.78.144406 (cit. on p. 117).

152. HUANG, YIXUAN, D. N. SHENG, and C. S. TING: *Charge Density Wave in a Doped Kondo Chain.* arXiv preprint. 2019. eprint: arXiv:1901.05643[cond-mat.str-el] (cit. on p. 117).

153. DAUL, S. and R. M. NOACK: 'Ferromagnetic transition and phase diagram of the one-dimensional Hubbard model with next-nearest-neighbor hopping'. *Phys. Rev. B* (1998), vol. 58: pp. 2635–2650. DOI: 10.1103/PhysRevB.58.2635 (cit. on pp. 118, 120).

154. LACROIX, C.: 'Some exact results for the Kondo lattice with infinite exchange interaction'. *Solid State Communications* (1985), vol. 54(11): pp. 991–994. ISSN: 0038-1098. DOI: http://dx.doi.org/10.1016/0038-1098(85)90171-1 (cit. on p. 119).

155. SHIBA, HIROYUKI and MASAO OGATA: 'Correlation functions in one-dimensional large-U Hubbard model: Zero-field and Finite-field Cases'. *International Journal of Modern Physics B* (1991), vol. 05(01n02): pp. 31–44. DOI: 10.1142/S0217979291000031 (cit. on p. 120).

156. UEDA, KAZUO, TOMOTOSHI NISHINO, and HIROKAZU TSUNETSUGU: 'Large Fermi surface of the one-dimensional Kondo lattice model'. *Phys. Rev. B* (1994), vol. 50: pp. 612–615. DOI: `10.1103/PhysRevB.50.612` (cit. on pp. 121, 123).

157. SIGRIST, MANFRED, HIROKAZU TSUNETSUGU, KAZUO UEDA, and T. M. RICE: 'Ferromagnetism in the strong-coupling regime of the one-dimensional Kondo-lattice model'. *Phys. Rev. B* (1992), vol. 46: pp. 13838–13846. DOI: `10.1103/PhysRevB.46.13838` (cit. on p. 121).

158. ITOI, CHIGAK and SHAOJIN QIN: 'Strongly reduced gap in the zigzag spin chain with a ferromagnetic interchain coupling'. *Phys. Rev. B* (2001), vol. 63: p. 224423. DOI: `10.1103/PhysRevB.63.224423` (cit. on p. 126).

159. FABRIZIO, M.: 'Role of transverse hopping in a two-coupled-chains model'. *Phys. Rev. B* (1993), vol. 48: pp. 15838–15860. DOI: `10.1103/PhysRevB.48.15838` (cit. on p. 131).

160. BALENTS, LEON and MATTHEW P. A. FISHER: 'Weak-coupling phase diagram of the two-chain Hubbard model'. *Phys. Rev. B* (1996), vol. 53: pp. 12133–12141. DOI: `10.1103/PhysRevB.53.12133` (cit. on p. 131).

161. FABRIZIO, MICHELE: 'Superconductivity from doping a spin-liquid insulator: A simple one-dimensional example'. *Phys. Rev. B* (1996), vol. 54: pp. 10054–10060. DOI: `10.1103/PhysRevB.54.10054` (cit. on p. 131).

162. WEISSE, ALEXANDER and HOLGER FEHSKE: 'Chebyshev expansion techniques'. *Computational Many-Particle Physics*. Springer, 2008. Chap. 19: pp. 545–577 (cit. on p. 132).

163. LANDAETA, J. F., D. SUBERO, D. CATALÁ, S. V. TAYLOR, N. KIMURA, R. SETTAI, Y. ṅUKI, M. SIGRIST, and I. BONALDE: 'Unconventional superconductivity and quantum criticality in the heavy fermions CeIrSi$_3$ and CeRhSi$_3$'. *Phys. Rev. B* (2018), vol. 97: p. 104513. DOI: `10.1103/PhysRevB.97.104513` (cit. on p. 132).

164. SHIMIZU, YUSEI, DANIEL BRAITHWAITE, DAI AOKI, BERNARD SALCE, and JEAN-PASCAL BRISON: 'Spin-Triplet p-Wave Superconductivity Revealed under High Pressure in UBe$_{13}$'. *Phys. Rev. Lett.* (2019), vol. 122: p. 067001. DOI: `10.1103/PhysRevLett.122.067001` (cit. on p. 132).

165. SONDHI, S. L., S. M. GIRVIN, J. P. CARINI, and D. SHAHAR: 'Continuous quantum phase transitions'. *Rev. Mod. Phys.* (1997), vol. 69: pp. 315–333. DOI: `10.1103/RevModPhys.69.315` (cit. on p. 157).

166. VOJTA, MATTHIAS: 'Quantum phase transitions'. *Reports on Progress in Physics* (2003), vol. 66(12): pp. 2069–2110. DOI: `10.1088/0034-4885/66/12/r01` (cit. on p. 157).

167. FISHER, MICHAEL E. and MICHAEL N. BARBER: 'Scaling Theory for Finite-Size Effects in the Critical Region'. *Phys. Rev. Lett.* (1972), vol. 28: pp. 1516–1519. DOI: `10.1103/PhysRevLett.28.1516` (cit. on p. 157).

168. CAMPOSTRINI, MASSIMO, ANDREA PELISSETTO, and ETTORE VICARI: 'Finite-size scaling at quantum transitions'. *Phys. Rev. B* (2014), vol. 89: p. 094516. DOI: `10.1103/PhysRevB.89.094516` (cit. on p. 157).

169. ROTA, GIAN-CARLO, ed.: *Encyclopedia of Mathematics and its Applications*. Reading, Massachusetts: Addison-Wesley Publishing Company, 1976.

List of Publications

Some parts of this thesis have been published previously as refereed journal articles. In particular, the results in Chap. 6 are published in two articles by the American Physical Society. Some figures are directly taken from these publications but permissions were obtained from the publisher.

Pupblications at the American Physical Society

PESCHKE, MATTHIAS, ROMAN RAUSCH, and MICHAEL POTTHOFF: 'Frustrated quantum magnetism in the Kondo lattice on the zigzag ladder'. *Phys. Rev. B* (2018), vol. 97: p. 115124. DOI: 10.1103/PhysRevB.97.115124.

PESCHKE, MATTHIAS, LENA-MARIE WOELK, and MICHAEL POTTHOFF: 'Phase diagram of the Kondo model on the zigzag ladder'. *Phys. Rev. B* (2019), vol. 99: p. 085140. DOI: 10.1103/PhysRevB.99.085140.

Eidestattliche Erklärung / Declaration on oath

Hiermit versichere ich an Eides statt, die vorliegende Dissertationsschrift selbst verfasst und keine anderen als die angegebenen Hilfsmittel und Quellen benutzt zu haben.

I hereby declare, on oath, that I have written the present dissertation by my own and have not used other than the acknowledged resources and aids.

Hamburg, April 30, 2019   Matthias Peschke

Danksagung

A Matrix decompositions (QR and SVD)

Singular value decomposition

The singular value decomposition (SVD) is a specific decomposition of an $n \times m$ matrix $\boldsymbol{M}$ over the complex numbers $\mathbb{C}$:

$$\boldsymbol{M} = \boldsymbol{U}\boldsymbol{\Sigma}\boldsymbol{V}^\dagger, \tag{A.1}$$

where $\boldsymbol{U}$ is an $n \times n$ unitary matrix and $\boldsymbol{V}$ is a $m \times m$ unitary matrix, i.e. $\boldsymbol{U}^\dagger\boldsymbol{U} = \boldsymbol{U}\boldsymbol{U}^\dagger = \mathbb{1}$ and $\boldsymbol{V}^\dagger\boldsymbol{V} = \boldsymbol{V}\boldsymbol{V}^\dagger = \mathbb{1}$. $\boldsymbol{\Sigma}$ is a rectangular $n \times m$ matrix with positive entries $\Sigma_{11} \geq \Sigma_{22} \geq \cdots \geq \Sigma_{min(n,m)min(n.m)} > 0$ on the diagonal and zeros otherwise. The diagonal entries of $\boldsymbol{\Sigma}$ are called the *singular values* of $\boldsymbol{M}$ and they are uniquely determined by the matrix $\boldsymbol{M}$. The same is not true in general for the unitary matrices $\boldsymbol{U}$ and $\boldsymbol{V}$. The squares of the singular values are the eigenvalues of $\boldsymbol{M}^\dagger\boldsymbol{M}$ and $\boldsymbol{M}\boldsymbol{M}^\dagger$ as can be verified simple. For example for $\boldsymbol{M}^\dagger\boldsymbol{M}$:

$$\boldsymbol{M}^\dagger\boldsymbol{M} = \boldsymbol{V}\boldsymbol{\Sigma}\boldsymbol{U}^\dagger\boldsymbol{U}\boldsymbol{\Sigma}\boldsymbol{V}^\dagger = \boldsymbol{V}\boldsymbol{\Sigma}^2\boldsymbol{V}^\dagger \tag{A.2}$$

Eq. (A.2) shows also that $\boldsymbol{V}$ are the orthonormal eigenvectors of $\boldsymbol{M}^\dagger\boldsymbol{M}$. Similarly, $\boldsymbol{U}$ builds the orthonormal eigenvectors of $\boldsymbol{M}\boldsymbol{M}^\dagger$. Since $\boldsymbol{M}^\dagger\boldsymbol{M}$ is positive definite and Hermitian, it has strictly positive eigenvalues so that also the singular values needs to be positive. For a rectangular matrix $\boldsymbol{M}$ with $n > m$, one can obtain a thin SVD. One therefore restricts the rectangular matrix $\boldsymbol{\Sigma}$ to a $m \times m$ diagonal matrix and discards the other zero-elements. That requires that $\boldsymbol{U}$ is only build from the first m columns and hence is an $n \times m$ isometry instead of an $n \times n$ unitary matrix.

The SVD of a matrix $\boldsymbol{M}$ appears in the optimization problem of approximating a matrix M of rank k by a matrix $\tilde{\boldsymbol{M}}$ of rank $r < k$. The optimal choice for $\tilde{\boldsymbol{M}}$ is obtained by taking only the r largest singular values in the SVD of $\boldsymbol{M}$:

$$\tilde{\boldsymbol{M}} = \boldsymbol{U}_r\boldsymbol{\Sigma}_r\boldsymbol{V}_r^\dagger, \tag{A.3}$$

where U is an $n \times r$ isometry and V an $r \times m$ isometry. This procedure can also be applied as a compression algorithm. Here, one can think for example on an image which is represented as an $N \times N$ matrix where N^2 is the number of pixels. Each entry could be the grey-scale value ranging from 0 to 255. This picture requires $N^2 \cdot \frac{\text{bytes}}{\text{pixel}}$ of memory. After a singular value decomposition, one compress the picture by throwing away all singular values smaller than a given threshold ε and retaining only χ singular values. The remaining memory scales then as $N \times \chi$ instead of N^2. For $\chi \ll N$, this compression can be very efficient.

The ability for the compression of information makes the SVD very useful for the DMRG algorithm or more generally for any tensor-network approach. Here, the compression is used for the wave-function of a physical system.

QR decomposition

The QR decomposition of a complex $n \times m$ matrix $\boldsymbol{M}$ with $n \geq m$ is the following factorization:

$$\boldsymbol{M} = \boldsymbol{Q}\boldsymbol{R}, \tag{A.4}$$

where $\boldsymbol{Q}$ is a unitary $n \times n$ matrix and $\boldsymbol{R}$ has an upper triangular structure of size $n \times m$, i.e. $\boldsymbol{R}$ is non zero only for elements at or above the main diagonal. In particular, the $n - m$ bottom rows are entirely zero. For this reason, it is useful to partition $\boldsymbol{Q}$ and $\boldsymbol{R}$:

$$\boldsymbol{M} = \begin{bmatrix} \boldsymbol{Q}_1 & \boldsymbol{Q}_2 \end{bmatrix} \begin{bmatrix} \boldsymbol{R} \\ \boldsymbol{0} \end{bmatrix} = \boldsymbol{Q}_1 \boldsymbol{R} \tag{A.5}$$

In this formulation, $\boldsymbol{Q}_1$ is an $n \times m$ matrix which fulfil $\boldsymbol{Q}_1^\dagger \boldsymbol{Q}_1 = \mathbb{1}$ but $\boldsymbol{Q}_1 \boldsymbol{Q}_1^\dagger \neq \mathbb{1}$, i.e. $\boldsymbol{Q}_1$ is an isometry. $\boldsymbol{R}$ is an $m \times m$ upper triangular matrix and $\boldsymbol{Q}_2$ is an isometry of size $(n - m) \times m$. In fact this decomposition is in general not unique but at least the matrices $\boldsymbol{R}$ and $\boldsymbol{Q}_1$ can be made unique by the convention that the diagonal of $\boldsymbol{R}$ is positive. With this convention, the QR decomposition is unique for square matrices. For rectangular matrices, the matrix $\boldsymbol{Q}_2$ cannot be determined uniquely. Within a *thin* QR decomposition, the matrix $\boldsymbol{Q}_2$ get not calculated at all. In a *full* QR decomposition, the matrix $\boldsymbol{Q}_2$ delivers an orthonormal basis of the null space of $\boldsymbol{M}$. The QR decomposition can be related to the SVD by identifying $\boldsymbol{R} = \boldsymbol{\Sigma}\boldsymbol{V}^\dagger$. The key advantage of a QR decomposition in the DMRG context is that it delivers a left or right orthonormalization of the A-tensors with less computational cost. However, one does not have access to the singular values and hence no ability for a truncation of the basis. Because of that, the QR decomposition is only useful if truncation is not required.

The definition above required $n > m$. In the case of $m > n$, one can define an analogue LQ decomposition. In numerical libraries, it is convenient to implement only the QR decomposition. For a LQ decomposition of the matrix $\boldsymbol{M}$ one can then simply apply a QR decomposition to $\boldsymbol{M}^\dagger$ and afterwards take the adjoint of both $\boldsymbol{R}$ and $\boldsymbol{Q}$.

B Further $SU(2)$ symmetric algorithms

B.1 2-site A-tensor

For a two-site DMRG optimization step, one needs to combine two adjacent site-tensors $A(l)$ and $A(l+1)$ into a composite object B. When working with reduced matrix-elements, one needs an extra coefficient for this product. As intensively discussed in Sec. 4.5, the contraction of the two A-tensors decomposes into a reduced part and a CGc part. In the case of the product of two A-tensors, the CGc part reads:

$$\Gamma_{i,\sigma\to j}^{I,\Sigma\to J} = \sum_{\sigma_1,\sigma_2,i'} \Gamma_{i,\sigma_1\to i'}^{I,\Sigma_1\to I'} \Gamma_{i',\sigma_2\to j}^{I',\Sigma_2\to J} \Gamma_{\sigma_1\sigma_2\to\sigma}^{\Sigma_1\Sigma_2\to\Sigma} \tag{B.1}$$

One can multiply Eq. (B.1) by $\Gamma_{i,\sigma\to j'}^{I,\Sigma\to J'}$ and sum over i and σ so that the left side becomes $\delta_{JJ'}\delta_{jj'}$. The product of four CGc on the right side can be identified with the recoupling coefficient from Eq. (4.45). The recoupling coefficient is closely related to a Wigner $6j$-symbol (Eq. (4.46)). In summary one obtains:

$$B_{I\alpha_I,J\alpha_J}^{\Sigma(\Sigma_1;\Sigma_2),(\alpha_{\Sigma_1}\alpha_{\Sigma_2})} = \sum_{I'\alpha_{I'}} \begin{Bmatrix} I & \Sigma_1 & I' \\ \Sigma_2 & J & \Sigma \end{Bmatrix} (-1)^{I+\Sigma_1+\Sigma_2+J}\sqrt{(2I'+1)(2\Sigma+1)} A_{I\alpha_I,I'\alpha_{I'}}^{\Sigma_1,\alpha_{\Sigma_1}} A_{I'\alpha_{I'},J\alpha_J}^{\Sigma_2,\alpha_{\Sigma_2}} \tag{B.2}$$

B.2 Product of a W-tensor with an A-tensor

For the evaluation of the action of an MPO $O[\{W\}]$ onto an MPS $|\Psi[\{A\}]\rangle$, one needs to evaluate the contraction of a W-tensor with an A-tensor over the physical index σ which leads to the site-tensor B of the new MPS $|\Phi[\{B\}]\rangle$. Writing out the CGc part of this contraction, one immediately arrives at the following equation:

$$\Gamma_{j,\sigma_1\to j'}^{J,\Sigma_1\to J'} = \sum_{\sigma_2,i,a,i',a',m} \Gamma_{i,\sigma_2\to i'}^{I,\Sigma_2\to I'} \Gamma_{\sigma_2,m\to\sigma_1}^{\Sigma_2,k\to\Sigma_1} \Gamma_{a,m\to a'}^{A,k\to A'} \Gamma_{ia\to j}^{IA\to J} \Gamma_{i'a'\to j'}^{I'A'\to J'} \tag{B.3}$$

By the usual orthogonality relation for the CGc, one can shift the CGc from the left side to the right side of Eq. (B.3). The resulting product of six CGc fits exactly definition of the recoupling coefficient for four angular momenta as introduced in Eq. (4.45). The final expression for the contraction of the reduced matrix elements becomes then:

$$B_{J(I;A)(\alpha_I\alpha_A),J'(I';A')(\alpha_{I'}\alpha_{A'})}^{\Sigma_1,\alpha_{\Sigma_1}} = \sum_{\Sigma_2\alpha_{\Sigma_2},k} \begin{bmatrix} I & \Sigma_2 & I' \\ A & k & A' \\ J & \Sigma_1 & J' \end{bmatrix} A_{I\alpha_I,I'\alpha_{I'}}^{\Sigma_2,\alpha_{\Sigma_2}} W_{A\alpha_A;A'\alpha_{A'}}^{[k]\Sigma_1\alpha_{\Sigma_1};\Sigma_2\alpha_{\Sigma_2}} \tag{B.4}$$

In Eq. (B.4), one needs to combine the degeneracy indices α_I and α_A properly. The same is true for the indices $\alpha_{I'}$ and $\alpha_{A'}$.

C Finite-size scaling analysis

Phases of matter and transitions between different phases are fundamental properties of physical systems. From the theoretical point of view, phase transitions are discontinuities in the equations of state for the corresponding system. These discontinuities can only emerge in the thermodynamic limit. In finite systems, they are regularized. Hence, a finite-size scaling analysis needs to be applied if only finite-size calculations are available.

Thermal phase-transitions are transitions at a critical temperature $T = T_c$. On the contrary, quantum phase transitions (QPT) occur at $T = 0$ at specific values $g = g_c$ for a model parameter g. The critical parameter g_c defines a quantum critical point (QCP). The behaviour of the system in the vicinity of the QCP is believed to be universal [165, 166]. However, it is known that different universality classes exists. The classes differ by critical exponents which describe the behaviour of central quantities like the order parameter, the correlation length, etc.. The correlation length ξ , e.g., diverges at the QCP with the critical exponent ν:

$$\xi \propto (g - g_c)^{-\nu} \tag{C.1}$$

The critical exponent which describes the divergence of the susceptibility χ is γ:

$$\chi \propto (g - g_c)^{-\gamma} \tag{C.2}$$

As described above, these critical behaviour is only expected in the thermodynamic limit and is regularized in finite systems. A quite general finite-size scaling procedure is the *data collapse* method [136–138]. The central equations can be derived for example for the susceptibility χ. The combination of Eq. (C.1) and Eq. (C.2) gives:

$$\chi \propto \xi^{\frac{\gamma}{\nu}} \tag{C.3}$$

In a system of size L, the correlation length ξ is bounded by the system size L. That means if $L \ll \xi$, one can replace ξ by L in the finite system and obtains:

$$\chi_L \propto L^{\frac{\gamma}{\nu}} \tag{C.4}$$

On the contrary if $L \gg \xi$, the finite-size effects are expected to be negligible and $\chi_L = \chi$ for χ as in Eq. (C.3). The basic assumption of the data collapse method is now that the finite-size effects of χ can be absorbed in a function $\tilde{f}(x)$ where $x = \frac{L}{\xi}$ is a dimensionless parameter [167, 168]:

$$\chi_L = \xi^{\frac{\gamma}{\nu}} \tilde{f}\left(\frac{L}{\xi}\right) \tag{C.5}$$

The function $\tilde{f}$ is called *scaling function*. The function is unknown except in the limits $x \ll 1$ and $x \gg 1$. In these cases, $\tilde{f}$ behaves as discussed above. It is convenient, to redefine the

scaling function as:

$$f(x) = x^{-\gamma}\tilde{f}(x^{\nu}) \tag{C.6}$$

The reason is that with definition one obtains for χ_L

$$\chi_L = L^{\frac{\gamma}{\nu}} f\left(L^{\frac{1}{\nu}}\xi^{\nu}\right), \tag{C.7}$$

i.e. the argument is ξ^{ν} which is proportional to $g - g_c$ (Eq. (C.1)). When plotting $\chi_L L^{-\frac{\gamma}{\nu}}$ against $L^{\frac{1}{\nu}}(g - g_c)$ for various system sizes L one expects L-independent curves if the correct values for ν, γ and g_cn are known. The data collapse method can be used to determine the critical exponents and the QCP by searching for the best collapse.